Templated Electrodeposition for Nanostructured Photovoltaic Applications

Harry James Beeson

Selwyn College

University of Cambridge

A dissertation submitted for the degree of

Doctor of Philosophy

20th July 2016

Declaration

This dissertation is the result of my own work and includes nothing which is the outcome of work done in collaboration except as specified in the text.

It is not substantially the same as any dissertation that I have submitted, or, is being concurrently submitted for a degree or diploma or other qualification at the University of Cambridge or any other University or similar institution.

It does not exceed the prescribed word limit for the Physics and Chemistry Degree Committee, namely 60,000 words.

Acknowledgements

I would firstly like to thank two people without whom this project would never have happened. First of all, I thank my supervisor Prof Ulli Steiner for giving me the opportunity to work in his group and for supporting both my PhD project and my fellowship with Parliament, as well as our annual group winterschools. I am lucky to have had a supervisor who recognises the completeness of the PhD experience. Secondly, I thank Dr Maik Scherer, who first proposed the gyroid solar cell project and did much of the preliminary work with gyroid-forming diblock copolymer templates, and who was a great source of guidance and encouragement during my first year in the laboratory.

Several people helped me with specific parts of my work as I completed my PhD. I would like to thank Dr Mike Price for his help with transient absorption measurements, for his continued interest in the gyroid project and his early help guiding me around the Optoelectronics group. I would also like to thank Dr Alessandro Sepe for his help in conducting and analysing GIWAXS measurements and Luis Pazos-Outón for co-ordinating the back-contact perovskite solar cell project.

Additionally, I gratefully acknowledge funding from the EPSRC and the Nano-DTC covering my studentship at Cambridge, including my fellowship with the Parliamentary Office of Science and Technology, and from the UK-India Education and Research Initiative for funding my visit to IIT Delhi. Dr Aga Iwasiewicz-Wabnig and Dr Karishma Jain have been fantastic co-ordinators for the Nano-DTC, and I thank Dr Shery Huang and Dr Adam Robinson for being great mentors during my first-year projects. I would also like to thank Suman Shakya, Dr Shahab Ahmad, Dr G. Vijaya Prakash and the rest of the Nanophotonics group at IIT Delhi for making me feel so welcome during my stay in India.

The PhD experience was also hugely enriched, both academically and personally, by the people I met along the way. I am grateful for the friendships formed in Optoelectronics, Nanophotonics and the Thin Films & Interfaces groups, especially the core Cambridge-based team of Jonathan Lim, Raphael Dehmel, Karl Gödel, Tobey Wenzel and Jamie Dolan. The extended Romsey Terrace crew of Andy Salmon, Sarah Pearce, David Russell and Halie Rando provided all-important laughter throughout my PhD and will perhaps be what I miss most when I leave Cambridge.

Finally, I would like to thank my family for encouraging me in everything I've done with all their love and support over the years, and more recently Claire Davis for being a great reason to get out of the lab and for keeping me smiling throughout the PhD (and for waiting to graduate with me!).

Publications

Work conducted during the course of my PhD, including my first year with the NanoDTC, has led to the following publications:

1. *"Spectroscopic Characterization of Protein-Wrapped Single-Wall Nanotubes and Quantification of Their Cellular Uptake in Multiple Cell Generations".*

Cristina Bertulli, **Harry J. Beeson**, Tawfique Hasan and Y.Y. Shery Huang.

Nanotechnology, **24**, 265102 (2013)

2. *"Strong Photocurrent from Two-Dimensional Excitons in Solution-Processed Stacked Perovskite Semiconductor Sheets".*

Shahab Ahmad, Pawan K. Kanaujia, **Harry J. Beeson**, Antonio Abate, Felix Deschler, Dan Credgington, Ullrich Steiner, G. Vijaya Prakash and Jeremy J. Baumberg.

ACS Applied Materials and Interfaces, **7**, p. 25227–25236 (2015)

3. *"Photon recycling in lead-iodide perovskite solar cells".*

Luis M. Pazos-Outón, Monika Szumilo, Robin Lamboll, Johannes M. Richter, Micaela Crespo-Quesada, Mojtaba Abdi-Jalebi, **Harry J. Beeson**, Milan Vrucinic, Mejd Alsari, Henry J. Snaith, Bruno Ehrler, Richard H. Friend and Felix Deschler.

Science, **351**, p. 1430 – 1433 (2016)

4. *"Fabrication and Characterisation of a Gyroid-Structured Organic Solar Cell"*

Harry J. Beeson, Michael B. Price, Maik R.J. Scherer, Alessandro Sepe and Ullrich Steiner

In Preparation

Summary: Templated Electrodeposition for Nanostructured Photovoltaic Applications

Harry Beeson

This thesis explores the use of templated electrodeposition for the fabrication of nanostructured ‘next-generation’ solar cells. The main project investigates the electropolymerisation of polythiophene around gyroid-structured templates to give organic, bulk heterojunction solar cells with a well-defined, regular donor:acceptor nanostructure. There are three broad motivations for this project: investigating the suitability of templated electropolymerisation for fabricating optoelectronic devices with precisely-controlled nanostructure; preparing organic solar cells with well-defined structure to aid further investigation of their operation; and assessing the suitability of the gyroid bulk heterojunction structure for high-performance solar cells. Additional, briefer projects investigate electrodeposition for the fabrication of perovskite-based solar cells.

Chapter 1 gives an introduction to next-generation solar cells and the motivation for the projects described in the thesis. **Chapter 2** provides a background to organic and perovskite solar cells, as well as the microphase-separated gyroid morphology used for templating. Then **Chapter 3** describes the main experimental methods used in this thesis, in particular the analysis of molecular ordering in polythiophene films based upon their visible absorption spectra.

Chapter 4 covers initial experiments on untemplated electropolymerisation of polythiophene, with a focus on the extent to which the molecular- and micron-scale polymer morphology can be influenced by the electropolymerisation conditions. **Chapter 5** describes the combination of this electropolymerisation with gyroid-structured templates formed *via* microphase-separation, along with the subsequent steps required to complete fabrication of a functioning gyroid-structured organic solar cell. Characterisation of the optoelectronic and device properties of such gyroid-structured solar cells is then described in **Chapter 6**. The projects addressing perovskite-based solar cells are covered in **Chapter 7**. Electropolymerisation of poly(3,4-ethylenedioxythiophene) (PEDOT) is used to fabricate hole-selective contacts for back-contact perovskite solar cells. Electrodeposition methods are also explored for deposition of the perovskite material itself, based upon electrodeposition of lead dioxide followed by *in situ* conversion to lead iodide and finally methylammonium lead iodide perovskite.

Finally, **Chapter 8** summarises the work conducted in this thesis, and provides a conclusion along with suggestions for further work.

Contents

Chapter 1

Introduction

There are strong social, political and economic reasons to search for new sources of energy. Globally, energy consumption is observed to correlate with gross domestic product (figure 1.1(a)), a simple proxy for economic productivity and standard of living. As developing countries industrialise, and standards of living rise around the world, the demand for energy seems set to rise, even as efforts grow for improving efficiencies. At the same time, traditional sources of energy face growing opposition and finite resources (although ‘proved’ fossil fuel reserves are still growing [1]). The Intergovernmental Panel on Climate Change report clear evidence of the human influence on recent climate change, and cite greenhouse gas emission as being ‘extremely likely’ to be the dominant cause of observed global warming [2]. Atmospheric carbon dioxide concentrations have increased dramatically in the past 250 years, a time period that closely matches the Industrial Age (figure 1.1(b)). Along with changing land use (arising principally due to agriculture and deforestation), the Royal Society identify the burning of fossil fuels as a main contributor to climate change [3].

The 2015 United Nations Climate Change Conference agreed to limit temperature rises to ‘well below 2°C’ [4], and the UK Climate Change Act commits the UK to reducing its greenhouse gas emissions by 80% compared to 1990 levels, by 2050 [5]. Both the UN and successive UK governments have made the development and adoption of renewable energy sources major components of these efforts [4, 6, 7]. These factors combined have driven an enormous research effort investigating the potential for alternative energy sources, both to provide a new source for increased power generation, and as a 'cleaner' alternative source of energy to replace carbon-intense sources like fossil fuels.

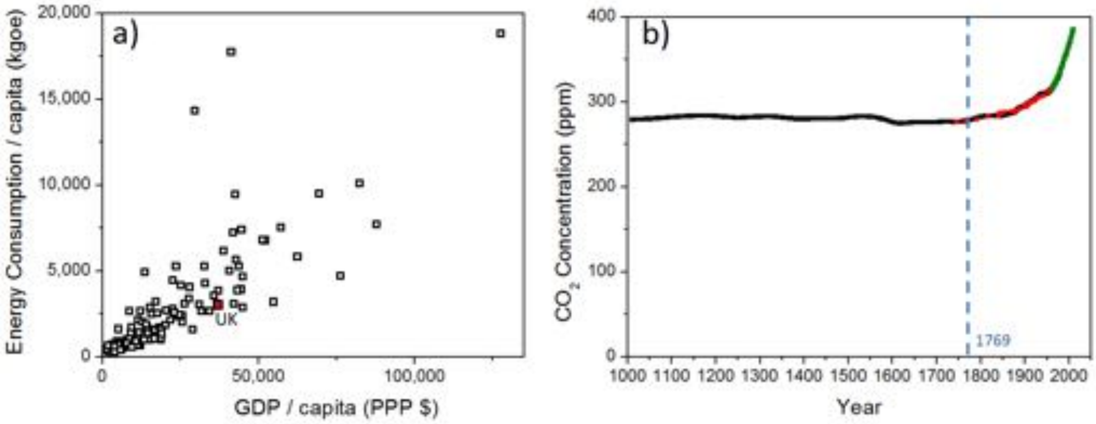

Figure 1.1: Graphs showing a) the correlation between GDP and energy consumption around the world, and b) historic CO_2 concentrations in the atmosphere (1769 marks the invention of the steam engine). The GDP uses purchasing-power parity dollars; energy consumption per capita is given in kilograms of oil equivalent. Figure (b) uses data measured directly since 1958, and extracted from ice cores up to 1977. Data for graphs taken from references [8–13].

The total solar power incident upon the Earth is of order 10^{17} W [14], ten thousand times greater than our total current energy consumption [1]. Even with atmospheric absorption, thermodynamic constraints on maximum possible efficiencies and the diffuse coverage of incident sunlight, there is serious potential for solar power to contribute significantly to our total energy consumption. At the very least, solar power can be expected to play an important role alongside other technologies such as carbon capture and storage, nuclear power, wind power, biomass power, tidal and hydroelectric power.

Commerically available solar cells are currently made using inorganic materials, mostly crystalline silicon, but also amorphous silicon, cadmium telluride and copper indium gallium selenide [15]. However, this requires energy- and cost-intensive processing, making solar power expensive and reducing its beneficial impact for the environment. 'Next-generation' solar cells aim to use easily-processable materials to improve upon conventional silicon cells in manufacturability, flexibility, weight and cost [16–18]. Even amidst falling silicon panel prices, the relative ease-of-manufacture of new-generation solar cells could be beneficial for high-throughput, low-capital mass-manufacture [19]. Light, flexible solar cells would also allow new, niche applications for which existing technologies are unsuitable. Among the technologies being developed as next-generation solar cells are organic solar cells and perovskite solar cells [20], the focus of this thesis. Both technologies require further development before being ready for mainstream commercialisation.

The main obstacles facing these next-generation solar cells are low power conversion efficiencies (organic solar cells) and poor device lifetimes (both organic and perovskite solar cells). The complete working mechanisms underlying both technologies are also not fully understood, with obvious implications for further development. Procedures for improving device lifetimes include introducing a protective, oxygen- and water-scavenging buffer layer [21], and encapsulating devices in glass or transparent film coatings [22, 23]. For organic solar cells, such procedures yield upper bounds on lifetime of order 10,000 hours [24], or a few years, although they can compromise the initial advantages of the organic materials. Early-stage commercial manufacturers of organic solar cells claim that using small molecules rather than polymers as the organic component can substantially increase the lifetime to beyond 25 years [15]. However, research thus far has primarily focused upon improving power conversion efficiency, and progress in this area over the last decade has been impressive (see figure 1.2 [20]). This has been chiefly as a result of developments in materials and cell morphology.

During the development of organic solar cells, the importance of the active layer morphology for performance has become clear. The first organic photovoltaic cell consisted of a monolayer of magnesium phthalocyanine sandwiched between a conducting glass electrode and an oxidised layer of tetramethyl p-phenylenediamine [26]. A large improvement in efficiency was achieved upon evaporating a perylene derivative on top of a copper phthalocyanine electron donor to give a bilayer device [27]. This promoted exciton dissociation by combining two organic, semiconducting materials with different ionisation potentials and electron affinities. This success led naturally to the development of bulk heterojunction cells, in which the two materials are intimately mixed within the

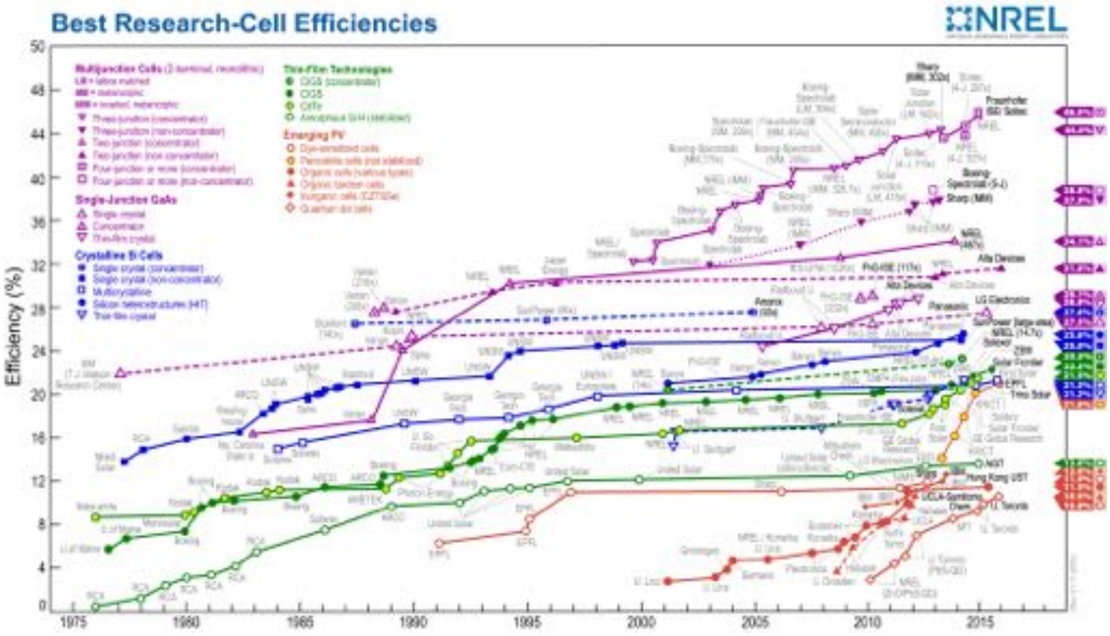

Figure 1.2: NREL chart of record efficiencies in different types of research solar cells [20]. Organic cells are represented by the red, filled circles and triangles. It is worth noting that the maximum theoretical efficiency of a single bandgap semiconductor device is 34 % [25].

active region of the cell [28, 29]. Strategies for influencing, investigating and optimising the exact nature of the bulk heterojunction morphology have driven much of the improvements in power conversion efficiencies since [30, 31]. The highest organic solar cell efficiency certified thus far is 11.5 %, based on conjugated polymers with highly temperature-dependent aggregation properties, allowing solubility in non-halogenated solvents, and facile control of the morphology [32]. Optimal device performance was achieved in devices with small (∼ 40 nm width), pure donor/acceptor domains, and face-on polymer chain orientation both at the polymer:fullerene interfaces and at the substrate.

The vast majority of investigation and development of polymer solar cell morphologies has used variation in materials and solution processing parameters, along with techniques such as using solvent additives and thermal or solvent annealing, to indirectly control the morphology, allowing tailoring of characteristic properties of the random bulk heterojunction structures formed rather than precise control. This is understandable given the relevance to anticipated roll-to-roll production methods, but limits the range and control of morphologies achievable and complicates analysis. In contrast, the main project in this thesis aims to directly control the heterojunction morphology *via* templated electrodeposition. The specific morphology targeted is the gyroid structure, a periodic, regular structure in all three dimensions, which is conceptually well-suited to solar cell operation with pure, bicontinuous domains. Macroscopic areas of gyroid-structured polymer films with nanoscale unit cell size can be realised through microphase separation of carefully controlled diblock coplymer blends. The theoretical gyroid structure and its physical fabrication are described in more detail in chapters 2 and 5. Despite templated electropolymerisation being unlikely to be used in large scale manufacture of organic solar cells, successful utilisation to achieve gyroid-structured solar cells could be a useful model system for investigating organic solar cell operation given a well-defined morphology, and might also be useful for assessing new materials independently of film morphology. Additionally, assessment of the efficacy of gyroid structure in organic solar cells might motivate further research efforts aiming to synthesise conjugated diblock copolymers that can directly form gyroid-structured solar cells *via* solution-processing. Such approaches are complicated by the difficulty in synthesising asymmetrical, difunctional copolymers [33], and by the intrinsic rigidity of conjugated polymers that favour microphase-separated interfaces of low curvature [34], although there has been success with non-gyroid morphologies [35].

Templated electrodeposition will also be investigated for application in perovskite solar cells. Electropolymerisation combined with templated contacts can provide interdigitated, selective electrodes for back-contact perovskite devices. Back-contact designs have previously led to efficiency and manufacturing improvements in conventional solar cells [36], so are worth investigating with perovskite devices as their efficiencies approach those of crystalline silicon. Electrodeposition of the perovskite material itself provides an alternative fabrication technique which may lend itself better to mass manufacturing, and also allows morphological control as demonstrated with organic solar cells.

This thesis therefore aims to investigate new fabrication routes for organic and perovskite solar cells, in particular focusing upon electrochemical deposition routes that allow morphology to be well-controlled down to the nanoscale. This should in turn allow investigation of the effect of this morphology upon performance, offer improved understanding of the working mechanisms in organic photovoltaics, and perhaps provide proof-of-principle for strategies targeting ideal morphologies. Although the gyroid structure has been studied theoretically for use in organic photovoltaics [37], and physically achieved in a solid-state dye-sensitised solar cell [38], I am not aware of any gyroid-structured, all-organic solar cell being reported previously.

Chapter 2

Background and Theory

2.1 Organic Electronics

The macroscopic transport of electrical charge to give electrical conduction is most usually associated with highly crystalline materials in which atoms in a crystalline lattice lead to delocalised electron systems and conventional bandstructures. Such materials include the archetypal conductor copper, and semiconductors such as silicon and gallium arsenide.

The discovery that polymers could also be made electrically conducting or semiconducting was awarded the Nobel Prize in Chemistry in 2000 [39]. Fundamentally, the conduction again appears due to a system of delocalised electrons. This delocalised system results from alternating sp^2 and sp^3 carbon bonds running down the 'backbone' of the polymer, usually consisting of a chain of cyclic molecules (see figure 2.1). The π electron wavefunctions in the carbon double bonds overlap with neighbouring double bonds to give delocalisation along the polymer chain. It is worth noting, however, that the delocalisation in such polymers is on a far smaller lengthscale than in metallic conductors.

Besides conjugated polymers, the other important class of organic electronic materials are small organic molecules [40, 41]. These are still characterised by many π-bonds to give electron delocalisation, and charge transport is afforded by effective crystalline stacking. Molecules tend to be more thermally stable than the polymers [40]. This may allow longer device lifetimes [15], and also facilitates evaporation deposition, which is the standard deposition method for such materials. However, polymers are easier to render soluble through chemical addition of side-groups, allowing deposition by solution-processing [40]. Solution processing is especially attractive for cheap, high-throughput, large-scale manufacture. Unless specified, the focus for the rest of this thesis is conjugated polymers, though many of the features described willl be applicable to all conducting organic materials.

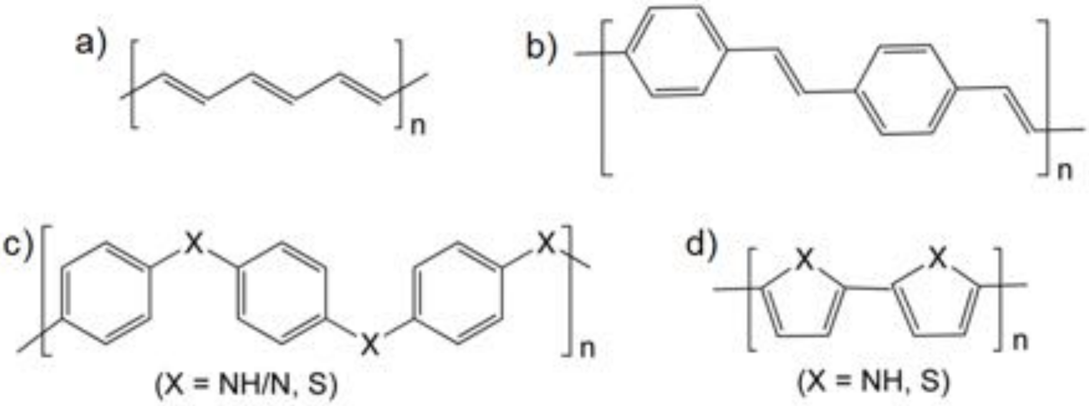

Figure 2.1: Examples of intrinsically conducting polymers, (a) polyacetylene, (b) polyphenylene vinylene, (c) polyaniline (X=NH/N) and polyphenylene sulfide (X=S), and (d) polypyrrole (X=NH) and polythiophene (X=S). Reproduced from Wikimedia Commons.

The double bonds in conducting polymers are relatively readily oxidised, after which the oxidised monomer unit is positively charged. Typically, the ionised monomer has a different equilibrium geometry to its neutral state [42]. Hence there is a change in energy relating to structural deformation as well as electronic charge. Provided the energy 'cost' of distorting the polymer structure is lower than the ionisation energy 'saved' in adopting the equilibrium structure of the ionised monomer, it is energetcially favourable for the ionisation to be associated with a structural deformation and hence localised, at least to within a few (~ 4) monomer units [43]. The localised distortion to the neutral polymer configuration generates an electrostatic polarisation field that opposes the introduced charge. This distortion and its screening field can be thought of as a quasi-particle, which is correspondingly known as a 'polaron' [42]. High polaron concentrations lead eventually to the formation of bipolarons, spinless distortions incorporating two units of charge rather than the singly-charged, spin-$^1/_2$ polarons. It is the movement of these polarons and bipolarons through conjugated polymer films that give them their conductivity.

2.1.1 Polymer Conductivity

Delocalisation in metals and conventional semiconductors extends in principle over the entire material. By contrast, polymer films consist of very large numbers of molecular chains, with disorder disrupting both intra-chain and inter-chain delocalisation. Deviation fom the infinitely-long, perfectly planarised conjugated polymer chain can arise in a variety of ways, including linkage defects, finite chain lengths, kinks and hydrogenated monomer units. 'Linkage defects' in polythiophene correspond to monomer units not bound to each other at their α sites (the carbon atoms adjacent to the sulphur in the thiophene ring, see figure 2.2(a)). Polythiophene chains bend within the polymer plane at α-β' linkages, while twisting out of the plane will occur at β-β' linkages [44, 45]. Both of these defects disrupt the conjugation down the chain. For substituted polythiophenes, such as poly(3-hexylthiophene) (P3HT), the relative positions of the alkyl chains also affects the stacking patterns adopted by the chains in a polymer film. Depending upon which β positions contain the alkyl chain, monomers can be arranged in head-head, head-tail or tail-tail arrangements (as shown in figure 2.2(d)). The proportion of head-tail coupling in a polymer is known as its 'regioregularity'. Regioregularity has been observed to strongly influence polymer stacking in spin-coated films, with crystallinity only readily observed for samples with high regioregularity [46].

Disruption to the π electron delocalisation means that macroscopic charge transport is mediated by 'hopping' of polarons and bipolarons from one segment of delocalisation to an adjacent segment, whether on the same molecule or an adjacent one [47]. This hopping mechanism differs from the displacement of the Fermi distribution of carriers found in metals, severely reducing organic charge carrier mobility. A semi-classical expression for the hopping transition rate, based upon the Miller-Abrahams transition theory [48], is given below:

$$k_{ij} = k_0 \beta e^{-2\frac{|\mathbf{r}_j - \mathbf{r}_i|}{\alpha}}, \quad \beta = \begin{cases} e^{\frac{E_j - E_i}{k_b T}} & \text{if } E_j > E_i \\ 1 & \text{if } E_j < E_i \end{cases}$$

where k_{ij} is the hopping rate from the ith site to the jth site, k_0 is a constant, β is a Boltzmann term relating to the energy difference $(E_j - E_i)$ between the two sites, $\mathbf{r}_i$ is the position of the ith site, and α parameterises the extent of wavefunction overlap between adjacent sites [49]. As such, the packing of the polymer chains has a strong influence on the hopping between molecules and hence the macroscopic charge transport. Intermolecular hopping occurs most readily between adjacent molecules with closely-packed π-π stacking, since this allows considerable overlap of the π molecular orbitals [50]. Correspondingly, intermolecular charge transport improves with local molecular ordering. In real films, good intermolecular ordering extends only within finite crystalline regions, with individual crystallites rarely extending beyond micrometre lengthscales. These crystallites are generally embedded within an amorphous polymer matrix, which can make up anything from 45 – 100% of the film [46, 51, 52].

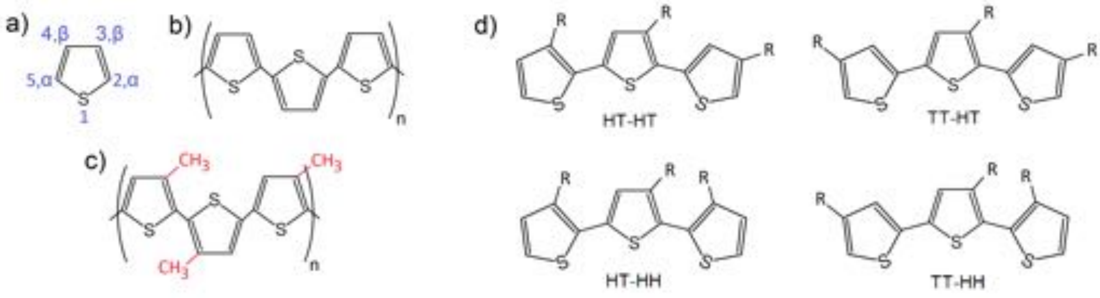

Figure 2.2: Schematic showing the different coupling arrangements possible in polythiophenes. a) Monomers units can be coupled at their α or β sites. b) Polythiophene, and c) Poly(3-methylthiophene), the two conjugated polymers used in this thesis, both shown here with ideal α-α′ linkages. d) Substituted thiophenes can adopt head-tail, head-head or tail-tail structures; since each monomer is ideally linked to two neighbouring monomers, four different triad structures are possible for each monomer site, namely HT-HT, TT-HT, HT-HH and TT-HH.

Since macroscopic conductivity will depend upon charge transport down individual chains, between neighbouring chains and from crystallite to crystallite, it varies substantially with order within the film on several lengthscales. This complexity, along with the variety of fabrication and characterisation techniques used with polymer films, has led to conductivity in conjugated polymer films not being completely understood. For example, high crystallinity is generally associated with good charge transport due to the improved molecular state overlap. However, spin-coated films of P3HT with varying molecular weights have repeatedly shown higher mobility in high molecular weight films, despite significantly greater crystallinity in the low molecular weight films [53–55]. This has separately been attributed to longer chains facilitating inter-crystallite transport despite inferior intra-crystallite ordering (see figure 2.3) [50, 54], or higher molecular weights promoting longer conjugation in amorphous regions despite fewer, smaller crystallites [55]. Pingel *et al.* measured local, nanoscopic mobility and macroscopic mobility using pulse-radiolysis time-resolved microwave conductivity (PR-TRMC) and field-effect transitor mobility measurements respectively. They found that the local mobility increased only slightly with increasing molecular weight, but that macroscopic mobility increased dramatically with increasing molecular weight [56]. Indeed, temperature-dependent mobility measurements suggest that thermal activation energies for local and macroscopic transport are comparable for high molecular weights, but diverge for medium and low molecular weights, suggesting that grain boundaries do not substantially restrict transport in high molecular weight films, but significantly affect transport at lower molecular weights.

The dominant influences on the measured conductivity also depend upon the method of measurement, which relates to the anticipated device the polymer film will be used in. Charge moblity can be measured *via* time-of-flight experiments, PR-TRMC, space-charge limited currents (SCLC) and in thin film transistor architectures. Time-of-flight experiments require very thick films, whereas PR-TRMC only measures conductivity over very small charge transport distances. Mobilities measured in thin film transistors are obviously relevant to operation of those devices, but are frequently orders of magnitude higher than those measured in other devices [50]. This is because higher charge densities are generally used in transistors than in optoelectronics devices, and because in transistors, current flows only within a very thin film layer near the electrodes, where substrate-induced molecular orientation can be very important in determining

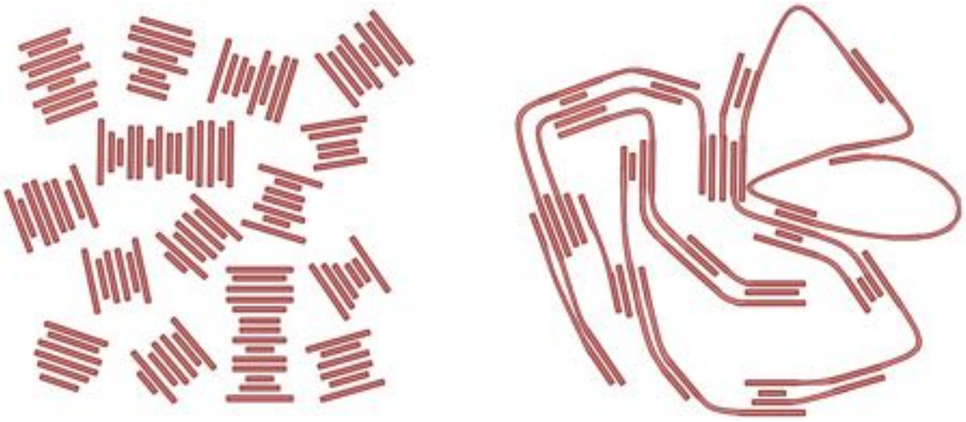

Figure 2.3: Diagram illustrating the potential for more crystalline films (left) to exhibit inferior conductivity than less crystalline films (right) due to poorer inter-crystallite transport. Only crystalline and inter-crystallite polymer chains are shown, with amorphous region chains omitted for clarity.

mobility. The anisotropy of polythiophene, with different molecular overlap down the chain, along the π-π stacking direction and along the coplanar stacking direction (especially with alkylated polythiophenes) clearly indicates that the distribution of chain orientations through the film will also influence charge transport. Space-charge limited current measurements yield measurements of bulk mobility through the film perpendicular to the electrodes, which is generally of more relvance to solar cells. However, the varying internal field makes it much more difficult to assess the field dependency of the mobility.

2.1.2 The Operating Principles of an Organic Solar Cell

The semiconducting nature of un-doped conjugated polymers allows their use in a variety of electronic and optoelectronic devices, such as transistors, light-emitting diodes and solar cells. This thesis focuses upon the latter application. The complete mechanism for photocurrent generation in organic solar cells may be broken down into four fundamental steps [40] (see figure 2.4). These four steps are (i) photon absorption and exciton generation, (ii) exciton diffusion, (iii) exciton dissociation, and (iv) charge migration to the electrodes; each are explained more fully below.

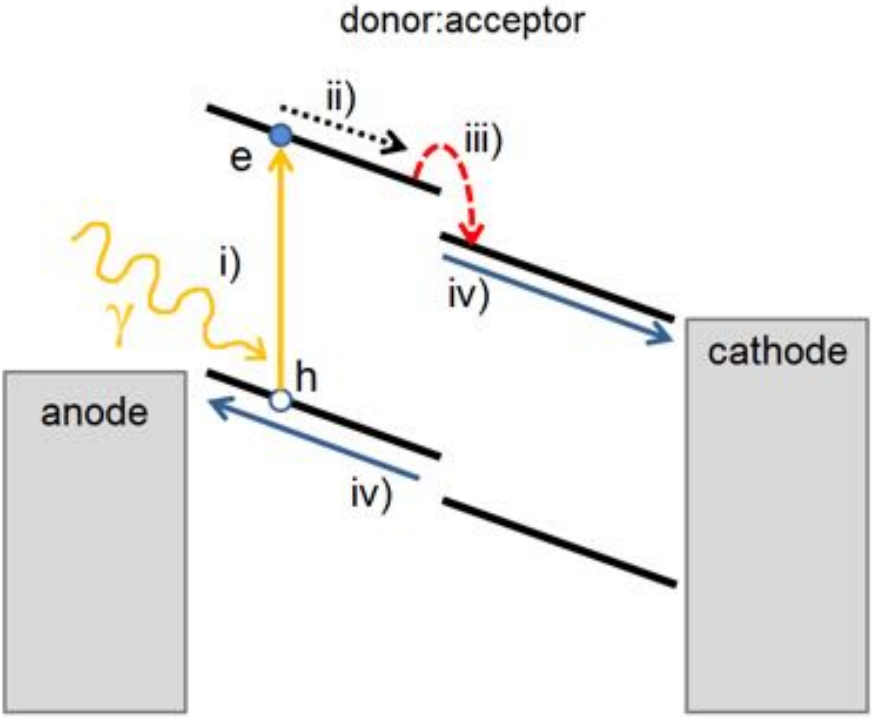

Figure 2.4: A summary of the four main organic photovoltaic processes: (i) Photon absorption and exciton excitation, (ii) exciton diffusion, (iii) exciton dissociation and (iv) charge transport to the electrodes.

Photon Absorption

The full photonic absorption process differs between organic and inorganic solar cells in two key ways. Delocalisation is more restricted in organic materials, and their van der Waals intermolecular forces are weaker than the covalent bonding of crystalline inorganic materials, so the relevant energy states for optoelectronic absorption and emission are much closer to the individual molecular states than the valence and conduction bands of inorganic semiconductors [57]. Hence absorption of a photon by an organic material excites an electron from a localised π bond to the LUMO π^* state, generating a correlated electron-hole pair, *i.e.* an exciton. Additionally, having lower dielectric constants, Coulombic attraction is less well-screened in organic materials leading to more tightly-bound ($E_B > k_BT$) Frenkel excitons rather than transient ($E_B < k_BT$) Wannier-Mott excitons (excitonic effects can generally be ignored at room temperature in inorganic semiconductors [58]). Thus the dominant excited species in organic solar cells are neutral excitons rather than free charge carriers [59, 60], although it should be noted that there is evidence of some direct polaron formation in thin organic films [61, 62].

Conjugated polymers tend to have high absorption coefficients, thus relatively thin films (on the order of 100 nm) can absorb a significant fraction of sunlight [40]. This helps counter the low mobilities found in these materials. The significant geometric relaxations of excited states in conjugated polymers also affords them relatively wideband absorption spectra [58].

Exciton Diffusion

Once an exciton is generated in the absorbing semiconducting polymer, it can move through the material by hopping from one conjugated unit to an adjacent one, either on the same polymer or in a neighbouring one [63]. Being uncharged, there is no preferred direction for the exciton hopping motion, and it can be well-approximated by a simple diffusion model [63, 64].

As shown in figure 2.5, there are several relaxation processes that diminish the exciton population. These processes may either be largely internal to the excited molecule ('unimolecular' processes), or may involve states in neighbouring molecules ('bimolecular' processes) [57]. The dominant recombination process is generally unimolecular $S_1 \rightarrow S_0$ relaxation in which the excited electron falls back down from the π^* state to the π state, annihilating with its 'own' hole. This can be either radiative, resulting in emission of a photon, or non-radiatiative, where the excitation energy is dispersed by phonons. Intersystem crossing, mediated by spin-orbit coupling, allows conversion of singlet excitons into triplets with integer spin. Conversion back to the ground-state ($T_1 \rightarrow S_0$) can also be accompanied by radiative or non-radiative emission. Exciton recombination can also take place at impurity or defect trapping sites. A typical bimolecular process is exciton-exciton fusion, whereby two excitons meet and the excitonic energy is transferred from one to the other, leaving just one exciton that rapidly relaxes back towards the S_1 state [57]. Exciton-exciton fusion can be distinguished from unimolecular relaxation since it is non-linear - its rate varies with the square of exciton density at any point.

Typically, excitons in conjugated polymers have diffusion lengths of order 10 – 20 nm [41, 63] after which, on average, they will have recombined *via* one of the

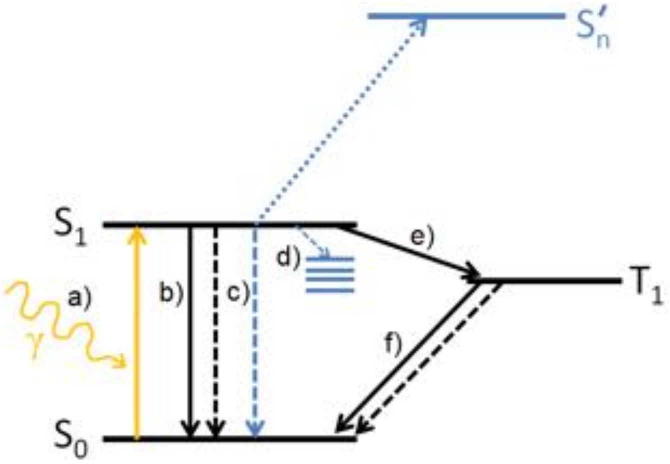

Figure 2.5: A schematic summary of the primary exciton recombination processes: (a) $S_1 \leftarrow S_0$ excitation by absorption of a photon, (b) radiative and non-radiative $S_1 \rightarrow S_0$ relaxation, (c) exciton-exciton fusion, (d) trapping by defect or impurity states, (e) intersystem crossing and (f) $T_1 \rightarrow S_0$ relaxation. Radiative processes are represented by filled lines and non-radiative processes by dotted lines; unimolecular processes/states are black and bimolecular processes/states are blue. The S'_n state is an excited state on a neighbouring molecule.

processes described above. If any charge is to be extracted from the excitons, they must therefore be dissociated before recombination occurs.

Exciton Dissociation

Given the strong binding energies of excitons in organic materials, a strong driving 'force' is needed to dissociate them. This is most readily generated at the interface between two materials with different ionisation potentials. The difference in quasi-Fermi levels in the two materials provides an effective electric field ($\mathbf{E} = -\nabla V$), with it being energetically favourable for electrons to move to the material with the greatest electron affinity (the electron-acceptor) and for holes to move to the material with the smallest ionisation potential (the electron-donor). For brevity, these two materials are usually referred to simply as the acceptor and donor. In the discussion that follows, we assume the transfer of an electron, but dissociation may equally well happen *via* transfer of the hole; this is a mostly analagous process.

The exact processes involved in exciton dissociation in OPV materials are not yet fully understood [58], and it is clear that the simplistic view of simply requiring materials with offset HOMO/LUMO levels is not fully accurate [65]. First of all, the offset in energy must be greater than the exciton binding energy to ensure energetic favourability. Secondly, the dissociated state must be lower in energy than a simple transfer of the exciton between the two materials. Finally, it seems that an intermediate ‘charge transfer’ state exists between the initial intramolecular exciton and fully free polarons [58, 65]. This charge transfer state consists of an electron-hole pair localised on separate molecules, but still Coulombically-bound to each other. It is not clear what mechanism provides the energy to overcome this binding and fully separate the charges. Propositions include phonon-assistance, disordered dipole presence at the interface, preferential exciton transfer to excited rather than ground charge transfer states and built-in fields from asymmetric electrodes. Whatever the mechanism for this second dissociation step, it must be faster than the competing recombination process (in which the donated electron relaxes back to the donor HOMO level) for efficient charge separation to occur. Indeed, the rapid timescales of charge dissociation after exciton generation ($\lesssim 50-100\,\mathrm{fs}$) imply that delocalised states play an important role, although there are contrasting views on whether the exciton or polaron states are delocalised [66, 67].

Charge Transport

If an exciton dissociates at the donor:acceptor interface, n- and p-type polarons will be produced either side of the interface on their respective materials. These propagate *via* hopping as described in section 2.1.1. Charge transport to the electrodes is driven by two different processes, namely drift and diffusion. Drift occurs as a result of the built-in field in the device caused by the choice of electrodes with different work functions, and usually dominates in the thin film active regions found in organic solar cells [40]. Diffusion moves charges away from high concentrations near the interface into the bulk of the relevant phase, and ultimately towards the electrode. Such charge transport is a complicated balance between material properties and morpholgy, and so cannot be simply described for a general system.

Recombination is a problem for polarons as well as excitons, and can be categorised into geminate recombination (annihilation of an electron with its corresponding excitonic hole) or bimolecular recombination (annihilation with a different charge partner or trapping site). Unfortunately, the dense donor:acceptor interfaces beneficial for exciton dissociation can increase polaron recombination.

2.1.3 Current Nanostructures in All-Organic Solar Cells

From the above discussion of the processes involved in organic conduction and organic photovoltaic systems, it is clear that morphology plays an important role in device performance. An intimate blend of donor:acceptor materials is required to provide efficient dissociation of photogenerated excitons (though can lead to increased geminate and non-geminate recombination of free charge carriers), and connectivity and molecular ordering throughout the active region affects the charge extraction to the electrodes. The importance of morphology has been borne out by the developments in device architectures which have enabled the improvement of device performance.

The history of monolayer, bilayer and eventually bulk heterojunction solar cells was described in the introduction. Currently, much research focuses upon investigating and optimising bulk heterojunction morphologies. As a result of the commercial relevance, most of this research has focused upon simple techniques that are compatible with spin-coating or reel-to-reel printing, such as material choice, solvent choice [68], thermal annealing [69] and solvent additives [70]. More strictly-controlled morphologies have not been the subject of as much investigation; some important examples are briefly described below and are represented in figure 2.6.

As an improvement upon simple bilayer devices, the interface between the two layers can be intentionally ‘roughened’ to increase the interfacial contact area. This can be achieved, for example, by thermal treatment of specific copolymers [77] or by carefully controlled electropolymerisation [71], each followed by deposition of the second material. The electropolymerisation process is an interesting alternative to the more commonly-used techniques of solvent processing and evaporation, and is in particular relevant for template-based device architectures as will be seen later. The randomly nanostructured bilayer interface achieved through this method yielded impressive PCEs of 3.0 % under 2.5 Suns

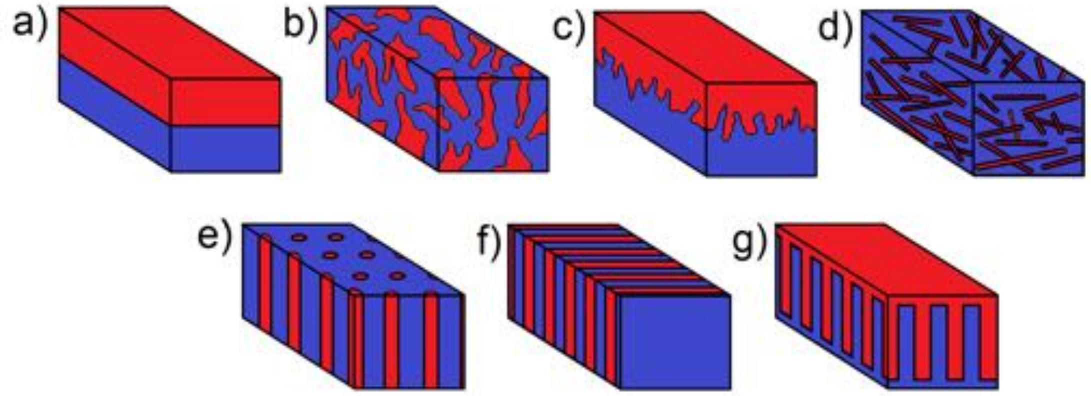

Figure 2.6: Schematic representations of the active region morphologies achieved so far: (a) bilayer [27] (b) bulk heterojunction [29] (c) 'roughened' bilayer [71] (d) nanowires [72] (e) nanorods [73] (f) lamellae [35, 74, 75] and (g) interdigitated fingers [76]. In general, the features are intended to be of a comparable lengthscale to the exciton diffusion length (of order 10 nm), though this is not always achievable.

illumination.

A further degree of morphology control can be achieved by pre-forming elements of the structure in the polymer blend prior to spin-coating it. This approach has been investigated with poly(3-alkylthiophene) nanowires of varying aspect ratios, assembled before mixing with phenyl-C_{61}-butyric acid methyl ester (PCBM) and spin-coating [72]. Transmission electron microscopy and atomic force microscopy showed the nanowires still intact in the fabricated device, mostly ordered parallel to the electrodes. Performance improved with increasing aspect ratio though it is not clear why; perhaps longer wires simply result in fewer isolated regions.

P3HT nanorods perpendicular to the electrode contacts have been fabricated by back-filling anodic aluminium oxide templates with molten P3HT [73]. The resultant nanorods had 50 nm diameter, 100 nm separation and 150 nm length. Solar cells were fabricated by etching away the template and evaporating on C_{60}, yielding a seven-fold improvement upon efficiency compared to bilayer devices. This was thought to be as a result of improved charge mobility in the P3HT rods. This mobility enhancement disappears for lower pore diameters, preventing smaller rods (better-matched with the exciton diffusion length) being used and limiting further performance enhancements. Polymer nanorods are also susceptible to collapse or coalescence, making such morphologies difficult to obtain, especially with more densely-packed rods.

Lamellar structures perpendicular to the substrate surface have been obtained in a P3HT:C_{60} blend. These were achieved *via* microphase separation in a P3HT:PLA diblock copolymer, followed by selective PLA etching and subsequent dip-coating with C_{60} [74]. However, no solar cells were ever successfully fabricated from this technique. It is speculated that the problem was doping of the P3HT during dip-coating, since the C_{60} could only be dissolved in basic water ($\mathrm{pH} \geqslant 8$) [78]. However, solar cells with a similar lamellar structure have been successfully fabricated by Lin *et al.* [75]. Here, diblock copolymers consisting of two polythiophene derivatives (P3HT and P3TODT) were synthesised and spin-coated with bis-PCBA to form bulk heterojunction devices. The copolymer microphase-separated to give the lamellar structure, while the fullerene was selectively incorporated into the P3TODT phase due to advantageous hydrogen bonding. However, although these devices showed better high-temperature stability, their performance was inferior to standard P3HT:PCBM blends. This could be due to the large polythiophene:fullerene content ratio, use of non-standard materials, moisture absorption by the P3TODT or interfacial issues at the polymer:electrode interface.

Vertical lamellar structures have also been obtained directly from microphase separation of purely donor:acceptor diblock copolymers, without an insulating component as is usually needed to guide the phase separation [35]. Annealing the copolymer blend to maximise phase separation led to a threefold increase in power conversion efficiency to 3.1 % as compared to simple bulk heterojunction blends of the two materials. This is a significant performance for a non-fullerene device (the copolymer was P3HT-*b*-PFTBT) and results from a much-enhanced short circuit current. However, rather than morphology, this improvement was attributed more to efficient donor:acceptor transfer due to the covalent bond linking the two components. As described in chapter 1, the rigidity of conjugated polymers favours microphase separated interfaces with low curvature [34], making direct fabrication of gyroid-structured donor:acceptor copolymer films challenging.

An alternative approach to imposing structure upon organic solar cells is nanoimprint lithography, a recent review of which is given by Yang *et al.* [79]. In particular, this technique focuses upon the fabrication of well-defined, interdigitated bilayers allowing horizontal exciton diffusion to be decoupled from vertical absorption and charge transport. Double imprinting uses a silicon mould to imprint the first material, and subsequently uses that as the 'mould' to imprint into the second material, ensuring good interfacial contact between the two materials [76]. The efficiency of P3HT:PCBM blends in this specific example increased with decreasing pillar width up to a maximum of 3.25 % for 25 nm pillars.

2.1.4 Perovskite Solar Cells

An alternative to organic materials in thin-film, solution-processable solar cells emerged from dye-sensitised solar cell architectures in 2012, when mesoporous TiO_2 and Al_2O_3 scaffolds were coated with methylammonium lead halide perovskite and filled with a solid-state hole transport layer to yield devices with up to 10.9% power conversion efficiency [80, 81]. The improved performance with the insulating alumina scaffold suggested that the perovskite acted both as an efficient light absorber and electron conduction medium, and subsequent fabrication of highly-performing planar architectures confirmed this [82]. Since then, improvements in materials and solution processing have led to better energy alignment at the device's interfaces and larger perovskite grain sizes, culminating in power conversion efficiencies above 22% [20, 83–86]. The combination of good charge transport and weak exciton binding in the perovskite material implies that bulk heterojunction nanostructures are unlikely to be useful for photovoltaic performance, although well-controlled nanostructure may be advantageous for light-emitting or lasing applications.

Although perovskite devices already seem able to compete with commercially-available silicon-based devices on efficiency, there are currently serious problems with their long-term stability. Replacing the organic hole transport materials with metal oxide layers that have inherent stability and impermeability to ambient moisture has shown some success in extending device lifetimes to up to thousands of hours (*i.e.* several months) [87–89], as has cross-linking adjacent perovskite grains to slow decomposition [90]. A secondary concern is the presence of lead and its issues with toxicity, motivating research into alternatives such as tin-based perovskites [91].

2.2 The Gyroid Structure

2.2.1 The Theoretical Gyroid Structure

The gyroid surface was first described conceptually by Schoen in 1970 [92]. Mathematically, it is an infinitely connected, triply periodic minimal surface and has I$4_1$32 symmetry with a body-centred cubic Bravais lattice [92, 93]. The gyroid surface separates two continuous, non-intersecting 'networks' in space [94]. A schematic image of the gyroid surface is shown in figure 2.7(a).

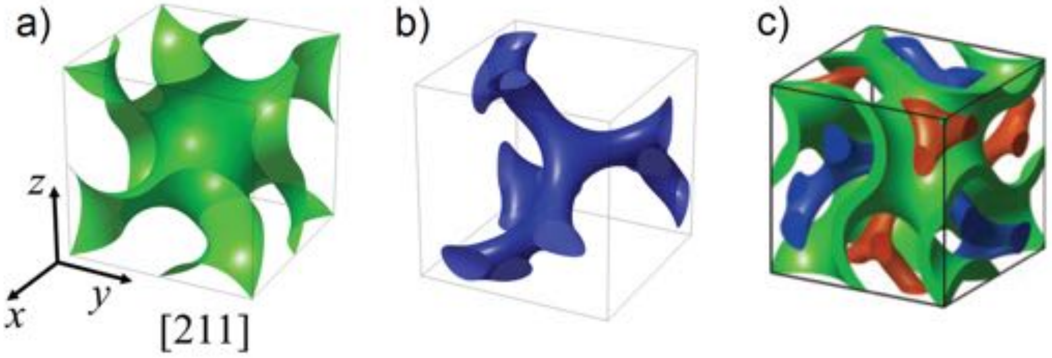

Figure 2.7: Simulated images of gyroid structures, adapted from references [93] and [95]. Figure (a) shows the single gyroid surface (green), which divides space into two separate regions. Increasing the value of w in equation 2.1 leads to surfaces enclosing single gyroids, as illustrated in figure (b). Setting $w = \pm t$ effectively gives the gyroid surface finite thickness, dividing space into two interpenetrating single gyroids with inverse symmetry, as illustrated in figure (c).

The gyroid surface can usefully be approximated by all points that satisfy the following trigonometric equation:

$$\sin(kx)\cos(ky) + \sin(ky)\cos(kz) + \sin(kz)\cos(kx) = \pm w \qquad (2.1)$$

where k=$2\pi/a$, a is the lattice parameter and $w = 0$ for the gyroid surface. Closely related structures with Ia$\bar{3}$d symmetry can be obtained for alternative values of w between 0 and $\sqrt{2}$. Increasing w increases the mean curvature from zero, and shifts the surface into one of the two interpenetrating networks such that the relative volume ratios of the two networks change. The volume enclosed by the resulting surface is known as a 'single gyroid', an example of which is depicted in figure 2.7(b). Setting $w = \pm t$ gives two such structures with inverted symmetry, separated by a gyroid-like surface with finite thickness; this thickness is determined by the value of t. The combined structure is known as a 'double gyroid', and is shown in figure 2.7(c). The double gyroid is composed of three continuous phases – the thickened gyroid surface and the two interpenetrating single gyroids – although it is confusingly referred to as both 'bicontinuous' and 'tricontinuous' by different authors [94]. The single and double gyroid structures are practically interesting because they can be physically realised on a nanoscale during the phase separation of diblock and triblock copolymers [93, 96].

2.2.2 Phase Separation

Phase separation is the process by which the components of a polymer blend adopt structure with separate regions of each component, or 'phase'. This separation is thermodynamically driven, with the system tending towards structures that minimise the free energy of mixing. The minimal free energy configuration balances minimisation of the interfacial energy between domains of the two phases and maximisation of entropy:

$$F = U - TS$$

As is generally the case, entropic considerations become more important as the temperature increases. The Flory-Huggins theory is a mean-field theory that derives an expression for the internal energy and entropy of mixing for a polymer in solution [97, 98], and can be adapted to the case of a polymer blend [99]. In the case of a blend of two polymers, A and B, with volume fractions, ϕ_A and ϕ_B respectively, the molecular entropy of mixing is given by:

$$S = -k_B(\phi_A \log \phi_A + \phi_B \log \phi_B)$$

To calculate the internal energy of mixing, we now assume that the system consists of a large number of sites that can be each occupied by a statistical ‘segment’ of one of the species present in the blend. If we count the energy of interaction between each site and its z nearest neighbours, letting E_{ij} represent the interfacial energy between two segments of species i and j respectively, and again taking the probability for any site to be occupied by a segment of species i to be ϕ_i, we derive the expression:

$$U_{\mathrm{mix}} = \frac{1}{2} z [(\phi_A^2 - \phi_A) E_{AA} + (\phi_B^2 - \phi_B) E_{BB} + 2\phi_A \phi_B E_{AB}]$$

This expression gives the difference in internal energy, per lattice site, between the completely mixed system and the completely separated system where all interactions are either AA or BB. We expect the energy of a molecule to scale simply with its molecular weight such that the molecular internal energy is NU_{mix}.

Introducing the Flory-Huggins parameter, χ, allows the free energy per molecule to be expressed as:

$$F = (\phi_A \ln \phi_A + \phi_B \ln \phi_B + N\chi\phi_A\phi_B) k_B T,$$

$$\chi = \frac{z}{2k_B T}(2E_{AB} - E_{AA} - E_{BB})$$

Here, χ represents the change in energy achieved upon swapping an A segment for a B segment in an otherwise fully separated system. It is thus a measure of the free energy ‘cost’ of placing dissimilar segments together; positive χ indicates repulsion between dissimilar segments.

Since the volume fractions ϕ_i will be fixed for any given blend, the molecular free energy F (and hence the phase structure of the blend) varies only as $N\chi$, where χ absorbs the temperature dependence of the balance between entropy and internal energy. Hence $N\chi$ is frequently used as a stand-alone parameter describing the thermodynamical driving force behind phase separation [100], and boundaries between different phase separated structures can be drawn onto plots of $N\chi$ against volume fraction.

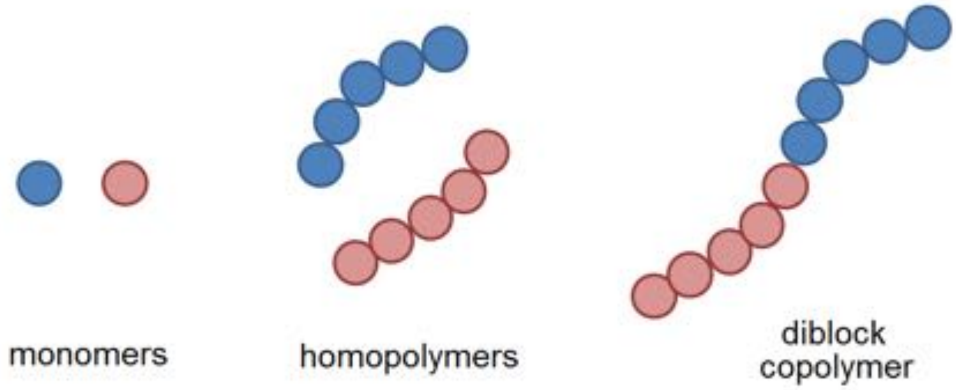

Figure 2.8: Schematic images of two different monomers, their respective homoplymers and a diblock copolymer formed by covalently bonding two homopolymers.

2.2.3 Microphase Separation of Diblock Copolymers

Copolymers consist of multiple monomer species, as opposed to homopolymers which are just chains of a single, repeating monomer unit. Diblock copolymers are copolymers formed from two homopolymers covalently bonded together (see figure 2.8. This covalent bond plays an important role during phase separation of the copolymer blend, since it limits the extent to which the two phases can separate.

Consider a block copolymer blend that would be expected to phase separate according to the simple polymer blend theory presented above. If there is a covalent bond linking the homopolymers A and B, the two phases can only separate as far as the separate homopolymers can extend. Immediately, this consideration shifts the equilibrium structure from macrophase to microphase separation, such as lamellar, cylindrical or spherical structure (as illustrated in figure 2.9).

However, there is a further complication. Clearly, there is an entropic 'cost' to the homopolymers extending away from the covalent bond like this, as there are fewer extended configurations than coiled configurations. We can arrive at a quantitative expression for this entropic contribution by counting the number of possible configurations that give each net chain extension [100, 101]. Consider a polymer made up of N rigid segments of length b_0. In any one dimension, the end of the polymer chain will then be n 'steps' of b_0 away the start of the chain, where n equals the sum of the steps to the right, N_+, minus the number to the left, N_-. Since $N_- = N - N_+$, the number of ways of having a net chain length nb_0 is:

$$W(N,n) = \binom{N}{N_+} = \binom{N}{\frac{N+n}{2}} = \frac{N!}{[(N+n)/2]![(N-n)/2]!}$$

The logarithm of W can be simplified using Stirling's approximation:

$$\ln(W(N,n)) \sim N\ln(2) - \frac{n^2}{2N}$$

Finally, extending to three dimensions gives an expression for the entropy, $S = k_B \ln W$ and hence free energy contribution $-TS$ for a polymer having end-to-end distance R:

$$F(R) = F(0) + \frac{3k_BTR^2}{2Nb_0}$$

The proportionality of $F(R)$ to R^2 gives the interesting result that this entropic consideration leads to a force approximately obeying Hooke's law for an ideal spring.

Equilibrium structures can then be predicted by calculating the interfacial and entropic stretching energies of molecules in different configurations, and finding the unit cell structure that minimises the free energy of mixing. Phase transitions are calculated by determining where the structure with minimal free energy changes. Matsen and Schick formulated a spectral approach within the self-consistent mean field theory, which has allowed the generation of a theoretical phase diagram featuring several complex microphase-separated structures, of which the gyroid is one [100, 102, 103]. Given the complexity of the strutures and the simplifying assumptions made, this theoretical phase diagram agrees well with the empirically-derived one [104], as shown in figure 2.9.

2.2.4 The Physical Gyroid Structure

As presented in the discussion and phase diagrams above, the gyroid structure is physically realisable *via* the microphase separation of diblock copolymer blends.

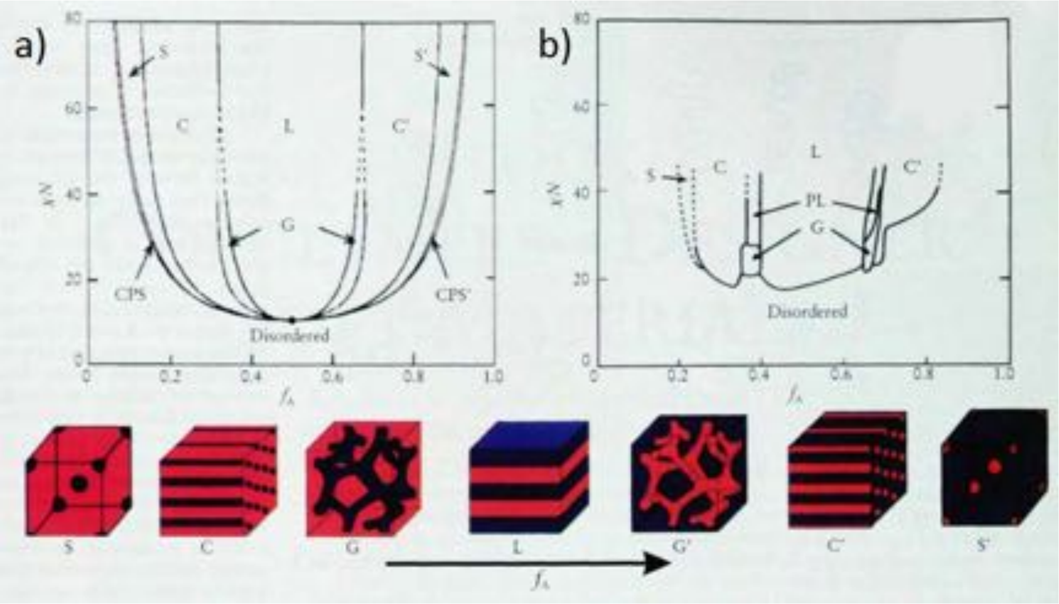

Figure 2.9: The phase diagram for diblock copolymer blends as a function of material fraction and $N\chi$, from (a) self-consistent mean-field theory, and (b) empirical observation [100, 103, 104].

This was first achieved experimentally by Hajduk *et al.* [96], and has since been achieved in blends of at least 28 different diblock and triblock copolymers [105]. However, it has generally been found that all-conjugated diblock copolymers have too stiff ‘backbones’ for such morphologies to form during microphase separation [37]. The lengthscale over which the gyroid features form can be tuned to some extent by varying the molecular weight of the polymers used, although this requires a corresponding decrease in χ in order to reach the same value of $N\chi$ on the phase diagram. Decreasing χ requires increasing the temperature of the blend, and this can only be done up to the point where the polymers used will start to degrade.

Characterisation of the gyroid structure can comprise simple comparisons of scanning electron microscopy (SEM) and transmission electron microscopy (TEM) images to computer generated images [106, 107], or grazing incidence small angle X-ray scattering (GISAXS) for more quantitative bulk analysis [38, 108]. It should be noted that double gyroid structures formed from diblock copolymer blends are generally contracted slightly in the direction perpendicular to the substrate, so that the unit cell is not quite cubic [109].

In addition to being a physically realisable, regular, periodic nanostructure with high surface area to volume ratio, the gyroid structure is also the only microphase-separated structure that is fully self-supporting. Hence selective etching of one of the material phases does not cause the remaining structure to collapse. This enables the mesoporous structures formed by the different material phases to be used as templates, and allows the gyroid structure to be replicated in materials beyond diblock copolymers (for example *via* electrodeposition [38, 106, 110] or atomic layer deposition [111].

2.2.5 The Gyroid Structure in Organic Solar Cells

Beyond its useful properties regarding use as a template for electrodeposition or electropolymerisation, nanoscale gyroid structure has attractive properties specific to organic solar cells. A nanoscale donor:acceptor gyroid would have a very dense interface with mean phase separation potentially comparable to the exciton diffusion length for efficient dissociation. Additionally, the gyroid is a bicontinuous structure so all points on either one of the materials would be connected to the electrode, aiding charge collection. Finally, it is a regular structure so its features will be well-defined, homogenous and reproducible.

These relevant properties have led to previous studies on the gyroid structure for use in organic solar cells. Kimber *et al.* simulated exciton generation, dissociation and charge transport in gyroids compared to random blend structure and vertical rods [37]. In fact, they found that geminate recombination was a much greater issue for the twisting gyroid morphology compared to vertical rods aligned with the drift field across the active region, and that the improvement upon randomly-ordered blends was minimal. However, they noted that this would be heavily dependent upon materials properties such as dissociation, hopping and recombination rates (PFB:F8BT was their test case).

Additionally, an organic-inorganic hybrid device with gyroid structure has previously been fabricated [38]. Here, the large internal surface area of the gyroid structure was used to maximise the coverage of the sensitising dye, yielding efficiencies of 1.7% which was competitive with fully-optimised nanoparticle-based devices of the same thickness. However, to the best of my knowledge, an all-organic gyroid-structured solar cell has not been reported in the literature.

Chapter 3

Experimental Techniques

This chapter covers introductions to the general experimental methods used in this thesis; specific experimental details are included in later chapters prior to their results.

3.1 Scanning Electron Microscopy

Fundamentally, a scanning electron microscope (SEM) works by scanning a tightly-focused electron beam across the surface of a sample and measuring the secondary electron signal resulting from the interaction of the beam with the sample. The probe electrons are generated with a field-emission gun, and are accelerated and shaped using electromagnets to form a tightly-focused (few nanometres diameter at focal point), high energy ($\sim 1-10\,\mathrm{keV}$) beam. The detector collects secondary electrons ejected from inelastic collisions between the beam and the sample to determine a current as a function of beam position across the sample. For a given material, the number of secondary electrons ejected is esssentially dependent upon the surface area the beam impinges upon, and hence the angle of incidence of the beam onto the sample, allowing a map of the surface topology to be drawn up from the beam position and secondary electron current. Throughout this thesis, a Leo 1530VP SEM system is used with an in-lens, secondary electron detector.

Samples must be sufficiently conductive to prevent charging as a result of the incident beam. Hence all samples were sputter-coated with a gold/palladium alloy layer a few nanometres thick. This should render the sample surface conductive without distorting the morphology. An alloy of gold and palladium was chosen due to gold's high conductivity and paladium's ability to prevent gold 'islands' forming, allowing continuous films to be deposited down to nanometre thickness.

3.2 Atomic Force Microscopy

Atomic force microscopy (AFM) is another technique for characterisation of nanoscale surface topography. Whereas SEM allows rapid visual information over potentially large areas and a range of lengthscales, AFM tends to be more quantitative, but is usually slower to carry out. The basic setup consists of a sharp tip on the end of a cantilever that is dragged across the surface of a sample by a piezoelectric navigation system. A laser beam reflects off the cantilever and onto a photodetector to measure (and amplify) the cantilever deflection, and hence the height of the tip. The sub-nanometre resolution of the piezoelectric motors combined with the amplification of the cantilever deflection by the laser measurement system means that AFM can, in principle, deliver measurements of surface topography with atomic precision.

The two principle modes of operation are 'contact mode' and 'tapping mode'. In contact mode, the piezoelectric system scans the cantilever across the sample and adjusts the cantilever height to maintain a set cantilever deflection. The surface topography is then inferred from the the set height required as a function of scanning position across the sample. In tapping mode, the cantilever is set into oscillation, and the height of the cantilever adjusted to maintain constant amplitude of oscillation. Tapping mode generally delivers greater resolution and less sample damage, but slower operation times.

The atomic force microscopy (AFM) system used throughout this thesis was a Dimension 3100 with a NanoScope SPM control module. All data was taken in tapping mode. Data processing was conducted using Gwyddion [112], with each horizontal scan line in any given scan set to have the same median height, in order to negate substrate slopes and errors introduced by scanner 'bow'.

3.3 Visible Absorption Analysis of Molecular Ordering

The absorption spectrum of a conjugated molecule depends upon its internal conformation and its interactions with surrounding molecules. Since both of these depend upon the spatial configuration of the molecules in a polymer film, inferences about the molecular ordering in a polymer film can be made based upon its absorption spectrum [113, 114].

The absorption of isolated conjugated molecules generally peaks in the visible range as a result of their π double carbon bonds (the π-π^* bonding and anti-bonding splitting is weaker than σ-σ^* splitting, which tends to correspond to energies in the ultraviolet spectrum [115]). Experiments with molecules suspended in solvent mixtures with varying temperatures or good/poor solvent ratios demonstrate red-shifting peak absorption and the appearance of fine structure as the polymer chains planarise and extend from coil- to rod-like conformations, as shown in figure 3.1(a). It is worth noting that aggregation accompanies the transition to rod-like conformations, but that the independence of the observed absorption behaviour from polymer concentration indicates that intrachain effects dominate the change in absorption, rather than interchain interactions arising from aggregation [116].

The red-shift observed as a result of the transition from coil-like to rod-like conformations arises from the increased conjugation down the chain that this conformation affords. Kinks and twists between adjacent thiophene units on a polymer chain disrupt the π-orbital overlap and effectively break the polymer up into connected oligomers of different conjugation lengths [120]. A simple treatment of the π electrons as non-interacting 'particles in a box' predicts the $S_1 \leftarrow S_0$ transition energy to scale as $^1/_L$, the effective conjugation length, as spatial confinement decreases [115]. Indeed, absorption spectra taken for oligothiophenes of varying lengths follow this simple $^1/_L$ scaling very reliably, at least over the range of short chain lengths measured (one to seven thiophene units) [121].

The multiple peaks present in the fine structure of the planarised chains arise from excitation to different nuclear vibronic energy levels. Rather than being stationary, the atomic nuclei in the molecule oscillate around their equilibrium positions. This nuclear motion is composed of various different modes, for exam-

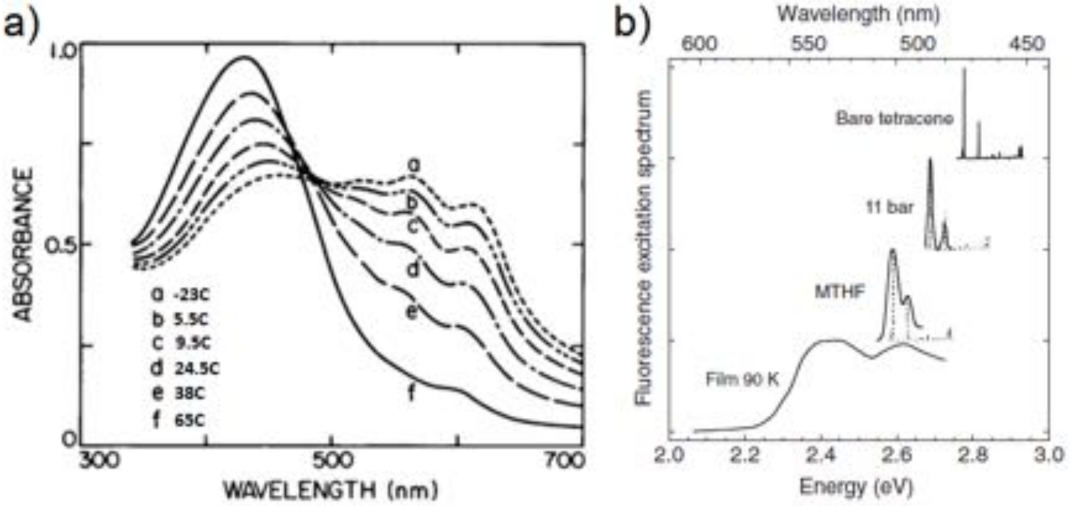

Figure 3.1: a) The shifting absorption spectrum of P3HT in solutions at different temperatures [116]. As the temperature decreases, the polymer undergoes a coil- to rod-like conformational transition, red-shifting the absorption and causing fine structure to appear in the spectrum. b) Fluorescence excitation spectra of tetracene at very low and low vapour pressure in argon, in a methyltetrahydrofuran glass and as a solid-state film [115,117–119]. As the environments surrounding each molecule become more varied across the sample, the vibronic peaks broaden.

ple C=C stretching or C-H in-plane bending modes, each with their own frequency ω_i and corresponding energy $(\nu + {}^1/_2)\hbar\omega_i$. At room temperature, the nuclei are in their vibronic ground-states ($\nu = 0$), but since photoexcitation of the electronic states happens on much shorter timescales than nuclear relaxation, the photoexcitation can cause transitions to excited vibronic states ($\nu \geqslant 0$). The photoexcitation transitions and resultant absorption spectrum for a typical sample of non-interacting conjugated molecules are shown in figure 3.2.

Although a completely isolated molecule (experimentally approximated by dilute vapour-phase molecules in inert gases [122]) has very sharp vibronic peaks, in most experimental setups the conjugated molecule will be surrounded by some interacting environment; the variation in the local environment around each molecule causes these peaks to broaden (see figure 3.1(b)). Additionally, the variation in effective conjugation lengths present in a polymer film leads to statistical broadening of the absorption peaks. Variation in conjugation length is expected to be greater in amorphous polymer films compared to ordered crystallites, hence the featureless absorption in the coil-like phase in figure 3.1(a) [56, 123]. The ${}^{1}/_{L}$ dependence of $S_1 \leftarrow S_0$ transition energies additionally indicates that variation in conjugation lengths causes greater variation in transition energy for shorter chain lengths, further enhancing the broadening in amorphous or non-aggregated polymer regions with short conjugation lengths.

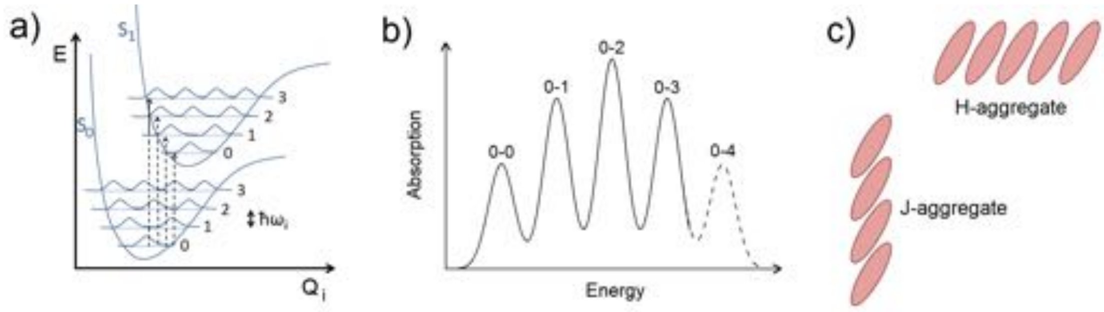

Figure 3.2: Diagrams showing (a) vibronic transitions in absorption, (b) the resulting spectrum (with peaks from higher transitions in dashes), plus (c) a schematic representation of H-aggregate compared to J-aggregate stacking [124]. The variable Q_i in the left-hand diagram is the reciprocal vector space of a nuclear vibrational mode; note that the excited electronic state (S_1) has a different nuclear vibronic ground-state, and hence is displaced in the x-direction compared to the electronic ground state S_0.

Interactions between conjugated molecules will also affect the overall absorption spectrum. As molecules approach each other during aggregation, the interaction between them will form bands from the individual molecular states. A simple treatment [115, 125] for a pair of identical molecules expresses the two-molecule Hamiltonian as:

$$\hat{H} = \hat{H}_1 + \hat{H}_2 + V_{12}$$

where $\hat{H}_{1,2}$ are the Hamiltonians for the individual molecules and V_{12} is the interaction perturbation. This interaction perturbation is the Coulomb interaction between the two molecules (often approximated by the point-dipole approximation, the case where two dipoles are separated by a distance considerably larger than the dipole moments themselves). The overall two-molecule state can be approximated as a linear combination of the two individual molecular states, giving:

$$|\Psi_g\!>= |\Psi_1\!>|\Psi_2\!> \quad \text{and} \quad |\Psi_{E_\pm}\!> = \frac{1}{\sqrt{2}}\,(|\Psi_1^*\!>|\Psi_2\!> \pm |\Psi_1\!>|\Psi_2^*\!>)$$

for the ground and symmetric/antisymmetric excited two-molecule states respectively, where $|\Psi_i\!>$ and $|\Psi_i^*\!>$ are the single-molecule ground and excited states respectively. The two-molecule ground state is offset from the sum of the individual ground state energies by the van der Waals interaction, given by the term $D =<\Psi_1\Psi_2|V_{12}|\Psi_1\Psi_2>$. This is a stabilising term that lowers the two-molecule ground state energy compared to two isolated molecules, which is why the gas- to solid-phase transition occurs in the first place. The energy of the excited two-molecule state, as well as being offset by a van der Waals interaction, is additionally split by the off-diagonal element of the interaction perturbation, $\pm\beta = \pm\!<\!\Psi_1^*\Psi_2|V_{12}|\Psi_1\Psi_2^*\!>$. This term may loosely be thought of as the energy arising from the interaction between the charge overlap of one excited molecule and one ground state molecule with the dipole moments of the two molecules. Extending this model from two molecules to an infinitely long stack of molecules, the split states extend into an exciton band of bandwidth 4β [115].

The transition dipole moment for the two-molecule system is given by $\boldsymbol{\mu}_\pm = <\!\Psi_g|e\mathbf{r}|\Psi_{E_\pm}\!> = \frac{1}{\sqrt{2}}(\boldsymbol{\mu_1} \pm \boldsymbol{\mu_2})$, where $\boldsymbol{\mu_i}$ are the individual molecule transition dipoles, $\boldsymbol{\mu_i} =<\Psi_i|e\mathbf{r}|\Psi_i^*>$ [115]. Hence the oscillator strength for transitions depends upon the vector sum of the individual moleculear transition dipole moments, and thus the relative orientation of the two molecules. In 'H-aggregates', the molecules tend to stack in a co-planar manner (see figure 3.2), and the E_+ excited state has the strongest transition dipole moment while the E_- has zero transition dipole moment. The reverse is true for 'J-aggregates', which tend to stack in a colinear manner. For perfectly ordered films, this means that transitions only occur to the top (bottom) of the exciton bands for H- (J-)aggregates. Although disorder in the film will weaken these selection rules to some extent, overall the vibronic absorption peaks are not broadened significantly by the formation of exciton bands.

These principles have been developed by Frank Spano into a theoretical framework giving the optical spectra of H-aggregating polymers with coplanar, lamellar packing and weak excitonic coupling (and specifically regioregular P3HT) [113, 114]. The excitations are considered to be Frenkel excitons, with an electronically and vibrationally excited molecule surrounded by vibrationally, but not electronically, excited molecules [114]. Indeed this technique has been used by several authors to assess molecular ordering in P3HT and P3HT:PCBM films [51, 56, 126–128]. Since the conjugated π-electron system that leads to the visible absorption spectrum is the same in both P3HT and unsubstituted polythiophene, this analysis should be approximately applicable to PT films too. The C=C stretching mode that is taken to be dominant is present in both materials, and a variety of spectroscopic methods have shown that unsubstituted and alkylated polythiophenes materials have very similar photoexcited bandstructures [129]. Furthermore, the alkyl chains of P3HT have a very small dipole moment, meaning their absence should not have much effect on the intermolecular interactions. The main two potential sources of discrepancy are the molecular packing pattern and the intermolecular spacing. Spano considered the case of coplanar, lamellar stacking, which P3HT is known to adopt. Although powder samples of chemically synthesised polythiophene have been found to adopt a herringbone arrangement with two molecules per unit cell [52, 130], electropolymerised films of polythiophene show a strong molecular orientation preference relative to the substrate, implying a lamellar structure [131–133]. This dependency on preparation method is not unreasonable, especially given the electrolyte counterions that are incorporated into electropolymerised films. However, the intermolecular separations within these stacking patterns are likely to be different for P3HT and unsubstituted polythiophene. The separation in the plane of the chains will be substantially smaller given the lack of alkyl side-chains, and the π-π stacking distance could be slightly affected too. Packing of electropolymerised films will depend upon the electropolymerisation conditions, especially the electrolyte counter-ion, but X-ray diffractometry has reported distances of 3.5 Å and 5.0 Å for polythiophene (electropolymerised with tetrafluoroborate counter ion) [132] compared to 3.8 Å and 16.4 Å for P3HT [134] in the π-π and coplanar directions respectively. These differences could induce some discrepancies between Spano's theoretical model and experimental results for electropoymerised polythiophene films.

The condition of weak excitonic coupling means that the nuclear vibrational energies are greater than the exciton coupling between adjacent molecules, so that the spectral shape of absorption arises from the vibronic bands. The excitonic interactions then modify this vibronic spectrum from the case of an isolated molecule, mostly affecting the relative intensities of each vibronic peak. Following Spano's treatment, the absorption, A, is modelled as:

$$A \propto \sum_{m=0}^{\infty} \frac{e^{-S} S^{m}}{m!} \left(1 - \frac{W e^{-S}}{2E_p} \sum_{n \neq m} \frac{S^{n}}{n!(n-m)}\right)^{2} \exp\left(-\frac{(E - E_{00} - mE_p - {}^{1}\!/_{2} W S^{m} e^{-S})^{2}}{2\sigma^{2}}\right)$$

where S is the Huang-Rhys factor, E_p is the phonon energy of the C=C symmetric stretch (taken as a representative sole vibrational mode), n and m are vibronic modes, E_{00} is the energy of the π-π^{*} transition between both lowest vibrational levels, W is the exciton bandwidth and σ is the energetic disorder fitting parameter [56, 113, 135]. Photoluminescence and absorption spectra of very dilute P3HT solutions (where interchain interactions can be neglected) can be fit with Franck-Condon profiles to yield a value for S of 1.00 [136]. Similarly, Raman spectroscopy and vibrational calculations give a value for E_p of 1440 cm^{-1}, or 179 meV [137]. Using $S = 1$ and considering only the first five vibrational modes (the factor ${}^{1}\!/_{m!}$ drops beneath ${}^{1}\!/_{100}$ for $m \geq 5$), the expression for the absorption can be simplified to:

$$A \propto \sum_{m=0}^{4} \frac{1}{m!} \left(1 - \frac{W}{2eE_p} \sum_{n \neq m} \frac{1}{n!(n-m)}\right)^{2} \exp\left(-\frac{(E - E_{00} - mE_p - {}^{W}\!/_{2e})^{2}}{2\sigma^{2}}\right) \qquad (3.1)$$

Note that the symbol e in equation 3.1 denotes the mathematical number, not the electronic charge. For simplicity, the broadening is assumed to be Gaussian, with the same standard deviation, σ, for each vibronic peak [136]. This broadening arises from the energetic disorder introduced by torsional defects, kinks and chemical defects in the polymer chains [113]. The variable E_{00}, the energy of the 0-0 $S_1 \leftarrow S_0$ transition, is dependent upon the effective conjugation length dominating the absorption, but varies only weakly with conjugation length for long conjugation [121], so should be relatively constant across different crystallites.

The final variable is W, the exciton bandwidth. As described previously in this section, this results from the strength of intermolecular interactions between an excited molecule and neighbouring ground-state molecules. It depends upon the inter-molecular separation, and conjugation lengths on the individual molecules [138, 139]. The interaction, and hence bandwidth, decreases with increasing intermolecular separation as would be expected. For very short conjugation lengths, the transition dipoles of neighbouring molecules are separated by more than the dipole length, allowing the point dipole approximation to be made. In this regime, the dipole moments scale with N, the number of thiophene units in the conjugated segment, and $W \propto N$ [139]. For longer conjugation lengths, the point dipole approximation breaks down. Instead, the two molecules can be treated as a series of dipole moments on each thiophene unit [140]. Using the general expression for the energy of two aligned dipoles separated by a distance r at an angle θ to the dipole orientation, $U = \frac{1}{4\pi\varepsilon_0}[\mathbf{p_1} \cdot \mathbf{p_2} - 3(\mathbf{p_1} \cdot \hat{\mathbf{r}})(\mathbf{p_2} \cdot \hat{\mathbf{r}})]$, it is clear that dipole combinations reduce the interaction energy for $\cos^2\theta > {}^1\!/_3$, *i.e.* for moments separated by large distances perpendicular to the π-stacking axis [139, 141]. For long conjugation lengths, $W \propto {}^1\!/_N$ [139].

Figure 3.3 compares theoretical and experimental relationships between the exciton bandwidth, W, and the number of repeat thiophene units in a conjugated segment, N. Experimental data from Westenhoff *et al.* [142] and Apperloo *et al.* [143] have been extracted from absorption spectra of aggregated end-capped oligothiophenes with defined lengths, while data from Crossland *et al.* [144] comes from absorption spectra of spin-coated P3HT films, in which crystallite widths were measured with AFM to estimate conjugation lengths. The first theoretical curve shown in figure 3.3 uses the expression derived by Beljonne *et al.* with the fitting parameters derived by Clark [139, 145]. This fits the data relatively well, but uses a value for the π-π separation of 1.1 Å, which seems unphysically small. The second theoretical curve models an infinite one-dimensional stack of oligothiophene chains with the intermediate neglect of differential overlap method, including non-nearest neighbour interactions and dielectric screening [138]. Despite their differences, all the experimental and theoretical data agree with the prediction for W to decrease with conjugation length for all but the shortest conjugation lengths.

A further, simple relationship between W and N has been fit to the experi-

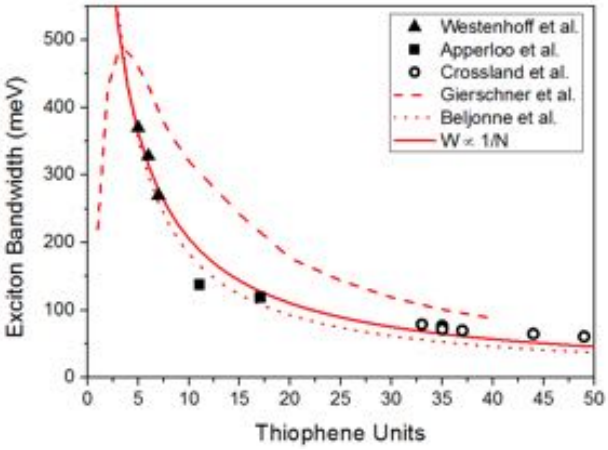

Figure 3.3: Graph showing experimental data (from different sources [142–144]) and theoretical fits to this data (using published models [138,139] and the simple inverse relationship used in the rest of this thesis) of the relationship between exciton bandwidth and the number of thiophene units in a conjugated segment.

mental data shown in figure 3.3 to allow for approximate conversion of values for W deduced from absorption spectra to effective conjugation lengths, N. Using the expectation for W to be inversely proportional to N for large N [139], the equation $W = \frac{k}{N-N_0}$, with k and N_0 as fitting parameters, was fitted to the data and is shown as the solid red line in figure 3.3. This relationship will be used henceforth in this thesis, with the understanding that the values for N so-derived are approximate. A length of 3.9 Å per thiophene unit down the chain is assumed for conversion of N to lengths in nm [146].

3.4 X-Ray Scattering

The correspondance of X-ray wavelengths to the intermolecular distances in polymer films make them a useful probe of polymer structure. For the thin film samples investigated in this thesis, grazing incidence diffractrometry is used, measuring samples in reflection rather than transmission, as shown in figure 3.4. In this setup, the incident X-ray beam strikes the sample at a very shallow angle (ideally beneath the critical angle of the substrate), allowing significant path length through the sample, but confining scattering to the film of interest and not the substrate [147]. Intense (or, more accurately, *brilliant*) beams with very low divergence are required for good angular resolution, so experiments are typically conducted at synchotron beamlines, where such X-ray sources can be prepared. A two-dimensional scattering map can be drawn up, with scattered intensities measured as a function of scattering angles (or reciprocal vectors) in the y- and z-axes, as indicated in figure 3.4. This allows measurement of crystal orientation relative to the film normal as well as crystal spacing and intensity [148].

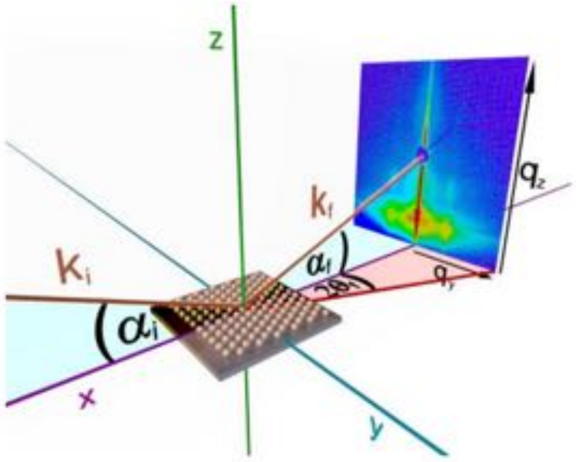

Figure 3.4: Representative diagram of a grazing incidence diffractometry setup, taken from reference [149]. The incident X-ray beam, k_i, strikes the film at an angle α_i and is scattered onto a two-dimensional detector at an angle of α_f from the horizontal and $2\theta_f$ from the incident axis, yielding the scattering vector k_f. The reciprocal dimensions q_z and q_y measure the scattering direction in the two respective directions.

At the most basic level, intense scattering is expected wherever periodic structures present in the film satisfy the Bragg condition $n\lambda = 2d\sin\theta$, where n is the diffraction order 1, 2, 3 etc., λ is the X-ray wavelength, θ is the scattering angle and d is the spacing of the periodic structure off which the signal is scattering [150]. Thus a peak in intensity at a certain scattering vector implies the presence of a periodic structure with a given orientation and spacing, with the peak intensity giving a measure of the how widespread that structure is in the sample and the peak width corresponding to the size distribution of individual crystallites.

By altering the position and type of detector, small or large scattering angles can be accurately detected. The two corresponding techniques are called grazing incidence small angle X-ray scattering (GISAXS) and grazing incidence wide angle X-ray scattering (GIWAXS) respectively. Since these measurements refer to reciprocal space, GISAXS is used to measure features substantially larger than the X-ray wavelength ($\sim 1\,\mathrm{nm} - 1\,\mu\mathrm{m}$) and GIWAXS is used to measure features on a similar lengthscale to the X-ray wavelength ($\sim 0.1 - 10\,\text{Å}$) [147,151]. In the context of polymer solar cells, GISAXS typically gives information about the donor:acceptor phase separation in the film, while GIWAXS gives information about the polymer crystallinity. GIWAXS is used in this thesis, and all such measurements were performed by Dr Alessandro Sepe.

3.5 Photoluminescence Spectroscopy

Photoluminescence quantum efficiency (PLQE) is measured using monochromatic laser excitation of a sample within an integrating sphere. The integrating sphere completely disperses all light incident upon its interior surface, so that all angular dependence in the illumination is lost. In effect, this means that all light from a light source in the sphere is redistributed isotropically over the whole surface of the sphere, independently of the angular dependence of the emission. Hence the full emission can be calculated by measuring the output from a small gap in the sphere surface and scaling by the solid angle this gap covers.

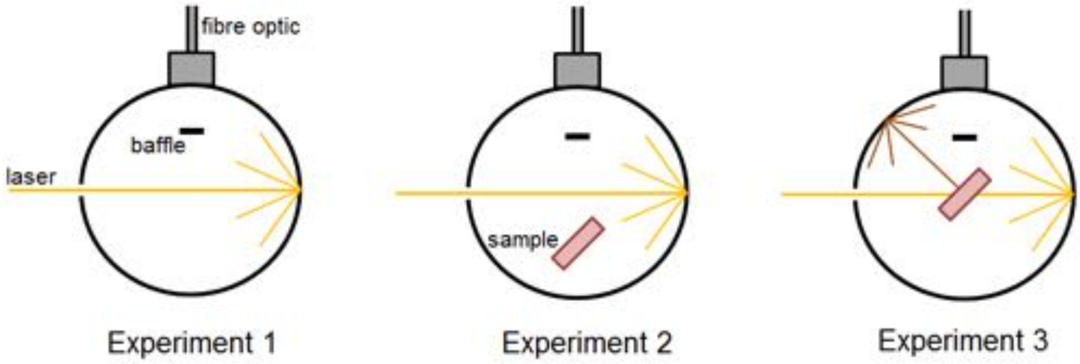

Figure 3.5: Figure illustrating the three steps of taking PLQE measurements. Experiment 1 measures the incident intensity, experiment 2 the absorbed and subsequently emitted scattered light, and experiment 3 the emission from directly absorbed light.

As shown in figure 3.5, the experiment is run in three configurations to make the PLQE measurement. First, the laser illuminates the empty sphere and the detector records the total illumination count. Next, the sample is placed inside the integrating sphere but offset from the incident laser. Finally, the sample is placed such that the laser is incident upon it. The PLQE is then determined by comparisons of the photon count at the excitation wavelength (unabsorbed light) and the photon count at longer wavelengths (emitted light) for each case. A good description of the detailed calculations are given by de Mello *et al.* [152], but, in brief, the second step gives a measure of the light scattered from the sphere back onto the sample, and how much emission this causes. This allows deconvolution of the scattered and absorbed light during direct illumination of the sample . This method requires as little overlap between excitation and emission wavelengths as possible, so that the two can be distinguished by wavelength and to minimise re-absorption of emitted light.

3.6 Transient Absorption Spectroscopy

Transient absorption spectroscopy uses laser pulses to measure how the absorption spectrum of a sample evolves after photoexcitation back to its equilibrium state. A representative setup is illustrated schematically in figure 3.6. Two pulses are used for each measurement - a monochromatic ‘pump’ pulse that excites the sample above its π-π^* transition energy, and a broadband ‘probe’ pulse whose transmission through the sample is used to measure the sample’s absorption spectrum. By varying the delay between the arrival of the pump and probe pulses, absorption spectra can be taken as a function of time after excitation. The temporal resolution is limited principally by the duration of the laser pulses used, and can commonly reach femtosecond timescales (‘ultrafast transient absorption spectroscopy’) [153]. For such short pulses, the pump and probe beams are generated from the same initial laser pulse.

The recorded signal is usually expressed as the change in the sample’s transmission after excitation, normalised by the steady-state transmission:

$$\frac{\Delta T}{T} = \frac{T_{\text{Pump-On}} - T_{\text{Pump-Off}}}{T_{\text{Pump-Off}}}$$

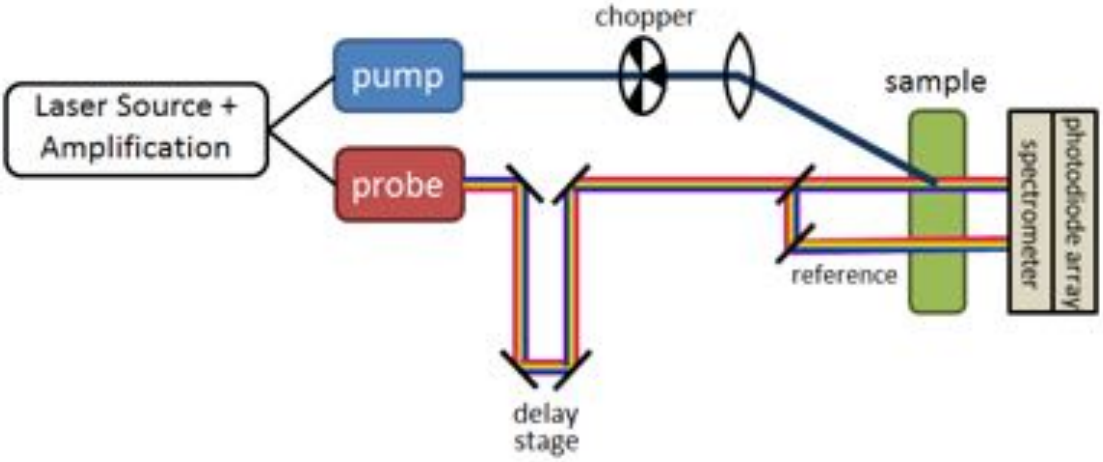

Figure 3.6: Schematic representation of the transient absorption spectroscopy setup. A broadband probe beam strikes the sample at a controllable delay after a monochromatic pump beam, allowing measurement of the sample's absorption spectrum as a function of time after photoexcitation.

where T represents transmission, and 'Pump-On' and 'Pump-Off' represent the transmission after photoexcitation and in the steady-state respectively. This value, $\frac{\Delta T}{T}$, is measured both spectrally and as a function of delay between pump excitation and probe transmission.

There are three principle spectral features commonly observed during transient absorption spectroscopy, namely ground state bleaching, stimulated emission and photoinduced absorption [153]. Derivative features such as electro-absorption or many-body phenomena can also be observed, but are not considered here.

Ground-state bleaching occurs when the pump beam excites electrons from the ground state to excited states, depopulating the ground state and hence reducing the absorption of the probe beam by ground-state electrons. This increases transmission relative to steady-state, resulting in a positive signal, and occurs in the same spectral region as peaks in the steady-state absorption spectrum.

If the probe beam frequency matches an optically active transition between an excited state and the ground state, it can stimulate the transition and cause emission of an additional photon to the probe photon. This also registers as an increase in transmission from the steady-state, and hence gives a positive signal.

Stimulated emission usually has a very similar profile to the photolumiescence spectrum, although it can overlap with photoinduced absorption signals.

Just as ground-state bleaching arises from depopulation of the ground-state, the pump beam populates excited states which can then absorb the probe beam to be excited to yet higher states. This results in decreased transmission compared to steady-state, and hence is detected as a negative signal. This phenomenon is known as photoinduced absorption, and is typically observed at sub-bandgap energies.

3.7 Space-Charge Limited Current Measurements

Consider an infinitely large film of thickness L sandwiched between two metal contacts held at a potential difference of V, as shown in figure 3.7. In the simplest case of the film being a vacuum, Gauss's law tells us that $\nabla \cdot \mathbf{E} = {}^{\rho}/_{\varepsilon_0} = 0$. Given that the film is much wider than it is thick, we can assume that $\mathbf{E}$ doesn't vary in the y- or z-directions so that we get $\frac{\mathrm{d}E}{\mathrm{d}x} = 0$, *i.e.* $E(x)$ is constant too. Since V is the integral $\int_{x=0}^{x=L} E \mathrm{d}x = EL$, we arrive simply at $E = {}^{V}/_{L}$. No current flows through the vacuum.

If instead the film is an insulating dielectric, the voltage will induce a polarisation of the bound charges in the film, so more work will be required to charge the electrodes to achieve the same voltage. However, the film is still electrically neutral and, though polarised, the net charge density will be balanced at all points in the film, so again $\nabla \cdot \mathbf{E} = 0$ and the field is the same as for a vacuum, $E = {}^{V}/_{L}$. There are no free charges and no current flows.

For a conductor, there are free charges spread through the film. Nevertheless, the overall film is neutral, the charges are balanced, and $\nabla \cdot \mathbf{E} = 0$. Again, $E = {}^{V}/_{L}$, but now this results in a current flowing, $J = \sigma E = \frac{\sigma}{L} V$, which is constant throughout the film. This is essentially Ohm's law. Note that the existence of the current does not contradict the statement that the charge density is zero throughout the film – the moving charges that constitute the current are balanced by stationary counter-charges at all points.

We now turn to the case of a semi-conducting film. A strong enough voltage will eventually lead to charges from the electrodes being injected into the film, leading to a current flowing due to the resultant electric field. Unlike in the

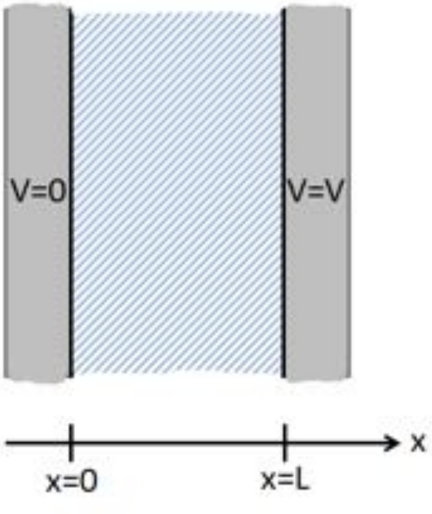

Figure 3.7: An infintely wide film of thickness, L, is sandwiched between two contacts held at a potential of 0 and V respectively. The field and current in the film are considered for various different film materials.

conductor, whose free charges were inherent to the material and hence balanced by stationary charges, these injected charges are 'surplus' free charges so $\nabla\cdot\mathbf{D} = \rho_f \neq 0$ and assuming linear, isotropic, homogeneous polarisability so that $\mathbf{D} = \varepsilon\mathbf{E}$, we obtain:

$$\nabla \cdot \mathbf{E} = \frac{\rho_f}{\varepsilon} \longrightarrow \frac{\mathrm{d}E}{\mathrm{d}x} = \frac{ne}{\varepsilon}$$

where n is the free charge density and ε is the permittivity of the semiconductor. It is clear that the electric field does now vary through the film. However, by continuity, the net current will be constant in the film, and is the sum of drift and diffusion currents:

$$J = nev_d - eD\frac{\mathrm{d}n}{\mathrm{d}x} = ne\mu E - eD\frac{\mathrm{d}n}{\mathrm{d}x}$$

where v_d is the drift velocity of the charges through the film, μ is the charge mobility in the film and D is the coefficient of diffusion. Using Einstein's relation $eD = k_BT\mu$ [154], it can be seen that diffusion is negligible compared to drift currents when $eV \gg k_BT$, which at room temperature is obtained for voltages substantially greater than 25 mV [155]. Neglecting diffusion, substituting for n and re-arranging gives:

$$J = \varepsilon\mu E \frac{\mathrm{d}E}{\mathrm{d}x}$$

From this, $E(x)$ can be found by integrating with respect to x (remembering that J is constant):

$$Jx + k = {}^{1}\!/_{2}\mu\varepsilon E^2$$

where k is the constant of integration. Assuming that $E(x = 0) = 0$ (this is not true if the contacts are not Ohmic, but approximately holds provided any injection barrier extends into the film by much less than the film thickness [155]), the constant of integration is zero and we arrive at:

$$E(x) = \sqrt{\frac{2Jx}{\mu\varepsilon}}$$

Finally, this can be integrated from $x = 0$ to $x = L$ to derive the voltage, V, in relation to the resultant current:

$$V = \int_{x=0}^{x=L} E(x)\,\mathrm{d}x = \sqrt{\frac{8JL^3}{9\varepsilon\mu}}$$

Re-arranging this expression to find the current, we obtain:

$$J = \frac{9\varepsilon\mu V^2}{8L^3} \tag{3.2}$$

Hence measuring the current as a function of applied voltage allows extraction of the value for the charge mobility, μ. This technique has been used to detemine mobilities in a variety of materials, including conjugated polymer films [53]. Other methods for measuring mobility do exist, for example time-of-flight measurements or characterisation of thin film transistors built from the relevant material, but these are less applicable to the bulk mobility of charges perpendicular to the substrates through a thin film, as is relevant in solar cells.

The current calculated in equation 3.2 is known as the space-charge limited current, since the electric field driving it is limited by the build-up of injected charges around the electrode that form a charged region opposing the field of the applied voltage. Note that in the vacuum considered originally, a strong enough voltage can also cause field emission of charges from the electrode into the vacuum, yielding similar results as for the semiconducting film (although the current does not reach a drift velocity in vacuum, changing the voltage dependency to $V^{3/2}$).

3.8 Solar Cell Characterisation

A variety of important properties relevant to solar cells can be deduced by measuring the current output of the device as a function of the potential across its electrodes, both with and without illumination. Figure 3.8 demonstrates a representative voltage-current measurement typical of solar cells, combined with bandstructures illustrating the internal field of the device under different applied potentials. For simplicity, throughout this discussion the active layer of the solar cell is represented as a single semiconductor, with band levels given by the HOMO of the donor and the LUMO of the acceptor respectively.

As the device materials are brought together to build the solar cell, the Fermi levels of the two metal electrodes equilibrate, generating a 'built-in' electric field that is essentially constant throughout the active layer. In the dark, and under zero applied potential, the device is in equilibrium and no net current flows. The drift current induced by the built-in field balances the opposite diffusion current resulting from the different intrinsic Fermi levels in the two electrodes.

Significant current only flows under dark conditions once the applied potential is strong enough to inject charge carriers from the electrodes into the active layer of the solar cell. The metal contacts act as a reservoir of electrons and holes, but the semiconductor bandstructure only allows hole injection into the HOMO and electron injection into the LUMO. Since the materials will generally be chosen so that the anode (cathode) work function closely matches the HOMO (LUMO), this means that charge injection is limited to holes from the anode into the HOMO, and electrons from the cathode into the LUMO. This asymmetry gives the solar cell diodic behaviour, with significant injection only under applied potentials opposite to, and greater than, the built-in potential. Unlike in conventional semiconductors, where Schottky barriers typically form at the semiconductor:metal interface, electric-field dependent injection indicates that field emission tunnelling

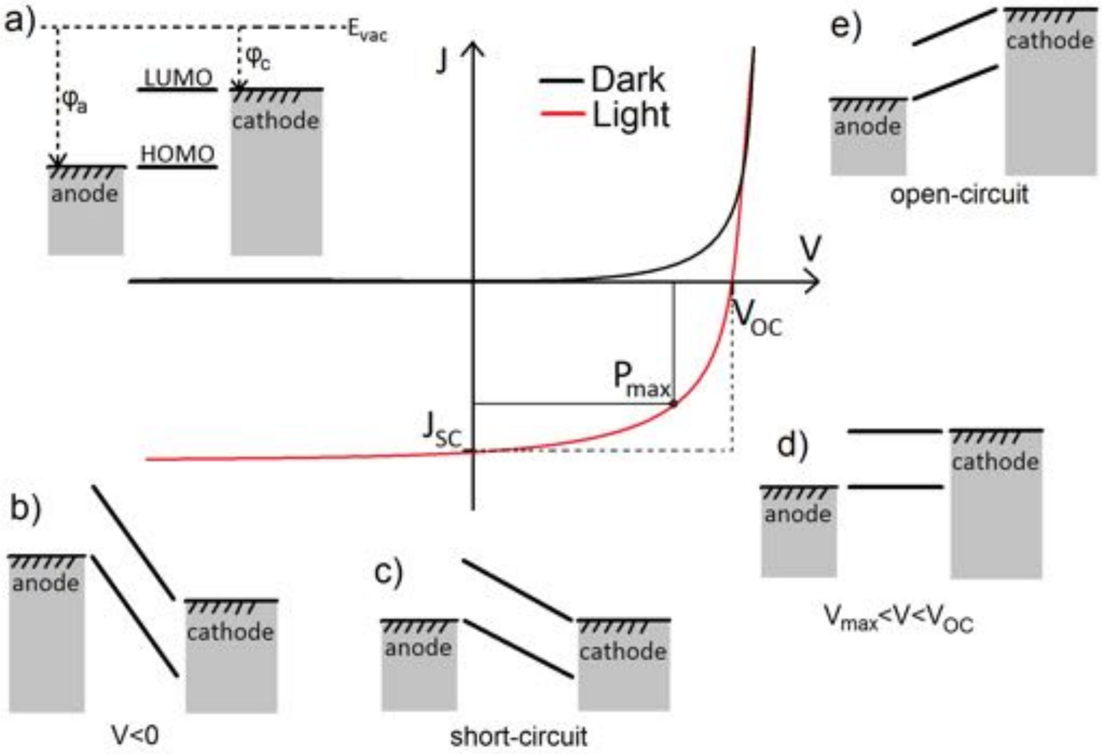

Figure 3.8: Representative J-V curve for an organic solar cell, surrounded by bandstructure diagrams before the materials are in contact (a), and under different applied potentials (b – e). The maximum power conversion occurs for the greatest simultaneous product of J and V, denoted $P_{\max}$ on the diagram.

is responsible for charge injection at polymer:metal interfaces [156]. Following Fowler-Nordheim tunneling theory, the injection current varies approximately exponentially with the effective field at the polymer:electrode interface [156,157], leading to the sharp growth in current at sufficient forward potentials.

Illuminating the device simply adds a photocurrent to the existing drift and diffusion dark currents. Under short-circuit conditions, the built-in field sweeps the photogenerated carriers to the electrodes, generating a short-circuit current density, J_{SC}. Applying a reverse potential reinforces the built-in field, increasing the current slightly as it reduces photogenerated charge losses to traps and other resistance. Applying a forward potential diminishes the built-in field, until the internal field is zero. Diffusion of photogenerated charges will still generate some net current, but at open-circuit voltage (V_{OC}) conditions, this diffusion is balanced by drift currents and the net current is zero. Even more positive potentials sweep photogenerated charges against the built-in field direction, and allow injected currents as in dark conditions, leading to a strong positive current. Between short-circuit and open-circuit, the device generates power given by the product $J \times V$. The maximum power point $P_{\mathrm{max}} = J_{\mathrm{max}} V_{\mathrm{max}}$ hence falls between J_{SC} and V_{OC}, with the ratio $J_{\mathrm{max}} V_{\mathrm{max}} / J_{\mathrm{SC}} V_{\mathrm{OC}}$ known as the fill factor. Evidently, a higher fill factor corresponds to better power conversion efficiencies. Good fill factors are achieved when photocarrier trapping and recombination are low, so that a diminished built-in potential is still efficient at sweeping photogenerated charges to the electrodes.

A second common characterisation technique for solar cells is to measure the external quantum efficiency (EQE) of the device. This is a measure of the number of charges extracted per photon absorbed, and is usually spectrally resolved. The general EQE setup is shown in figure 3.9. A monochromator varies the wavelength of light incident upon the device, which is split before reaching the device so as to illuminate a photodetector at the same time as the solar cell. This photodetector is pre-calibrated (by running the experiment with the solar cell replaced by a second photodetector) so that the incident photon flux upon the device can be measured simultaneously with its extracted current. Typically, this measurement is conducted with the device at short-circuit, but any desired potential can easily be applied.

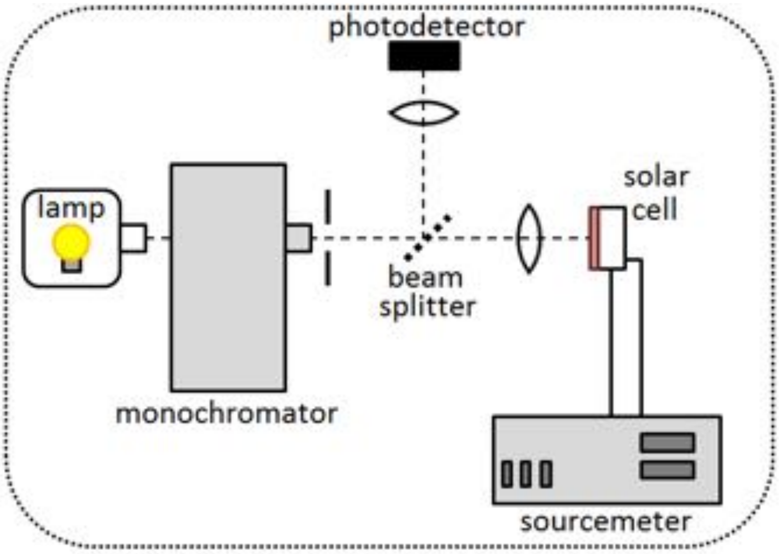

Figure 3.9: Schematic of the general EQE setup. By comparing the current output with the incident photon flux, the external quantum eficiency of a solar cell can be measured.

Chapter 4

Electropolymerisation of Thiophenes in Ionic Liquids

4.1 Introduction

Generally, polymer-based solar cells are fabricated using solution-processing techniques, mostly spin-coating [40]. However, conjugated polymers may also be deposited by electropolymerisation of monomers from solution onto an appropriate conducting substrate [158]. Indeed, several reports describe functioning solar cells employing electropolymerised polythiophenes as a donor material [159–163], with power conversion efficiencies ranging between 0.1 and 1.5% under standard illumination conditions (Gao *et al.* achieved 3.0% conversion efficiency under 2.5 Sun illumination [71]). The attraction of electropolymerisation as a deposition route for polymer solar cells in this thesis is its compatibility with templated deposition to allow direct control over the nanostructure of the polymer film. Although some of the previous reports of electropolymerised poythiophene solar cells attempted to indirectly control the polymer morphology through the deposition parameters, none used a templating approach to directly control the morphology.

Polythiophene can be electropolymerised from a variety of solvents, but the intention to ultimately polymerise around the gyroid templates used in this project restricts the choice of solvents to those that are compatible with the template material. These templates are described in more detail in chapter 5, and consist of poly(4-fluorostyrene-*r*-styrene). The dissolution or swelling of this material in the majority of organic solvents motivated the use of ionic liquid electrolytes, since many of these were found to be compatible with the templates.

This chapter focuses on electropolymerisation without templates. With regard to use in solar cell devices, film coverage and molecular ordering were of particular interest. A brief review of the electropolymerisation process and previous investigations into the influence of experimental conditions on film morphology is given, before a presentation of the results obtained in this project.

4.2 Background

4.2.1 Electropolymerisation of Conjugated Polymers

The standard electrochemical procedure for synthesis of conjugated polymers is anodic polymerisation. Although the exact details are still debated, the basic process is depicted in figure 4.1, and described as follows [164, 165]. Neutral monomers in solution are oxidised to their radical cation form at the anode. Since charge transfer occurs much faster than diffusion, a high concentration of monomer cations is maintained at the anode surface for potentials above the oxidation potential. These monomer cations couple to give di-hydro dimer cations (also termed 'σ-intermediates' [166]), which subsequently lose two protons and re-aromatise to yield dimers. It is now well-established that dimerisation occurs between two cations, rather than involving a neutral monomer or a (neutral) deprotonated cation [165,167,168]. Given the lower oxidation potential of dimers compared to monomers, these dimers will be in their oxidised state. Oxidised dimers can then 'dimerise' again to form tetramers, and so on, forming ever longer oligomers. Since reactivity decreases with chain length, longer oligomers have slower coupling and de-protonation rate constants than shorter chains [169, 170]. This makes it much more likely for a monomer to couple with another monomer rather than an oligomer, and extrapolating this trend makes it seem likely that oligomers of the same size preferentially couple, rather than monomers joining growing polymer chains [165, 167]. The observation of a relatively long-lived intermediate σ-dimer implies that deprotonation is the rate-limiting step at each stage of oligomerisation [166]. Beneath a certain de-protonation rate, the σ-coupled chains are essentially stable and no further oligomerisation occurs,

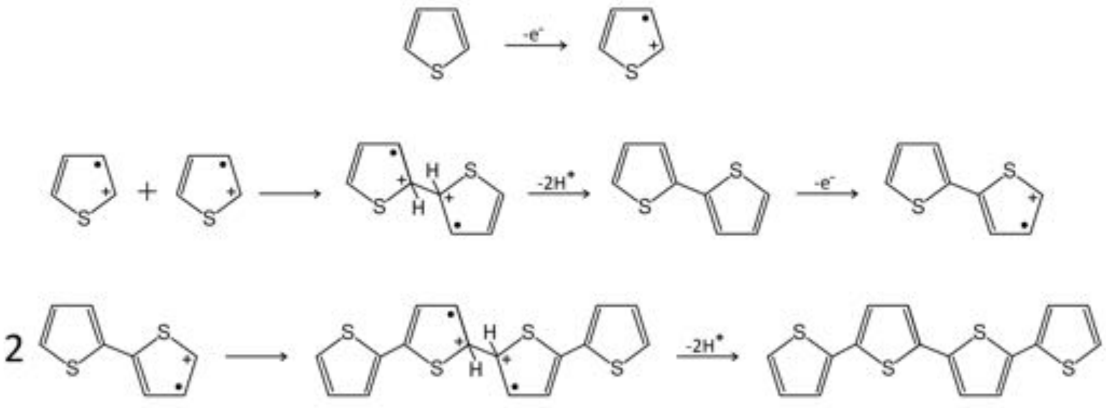

Figure 4.1: Schematic indicating the proposed polymerisation process of polythiophene. Oligomerisation proceeds *via* successive oxidation, coupling and de-protonation steps.

ultimately limiting the chain length that can be reached in solution.

Provided sufficient de-protonation can occur, the charged oligomers are sufficiently stable in the solution, and charged oligomers have a reasonable chance of interacting before diffusing away, the molecular weight of the oligomers can eventually exceed the solubility limit, causing precipitation out of solution onto the anode. Thus nucleation and growth of the polymer film begins. Investigation into the nucleation and growth mechanisms of electropolymerisation has mostly been based upon mechanisms observed in the electrodeposition of metals. However, metal electrodeposition is a far simpler process than elecropolymerisation because it involves just one redox reaction, namely the reduction of metal ions at the electrode surface, whereas multiple species and steps are involved in electropolymerisation. A variety of nucleation and growth mechanisms have been observed during electropolymerisation, including instantaneous nucleation (growth only from initially-formed nuclei) and progressive nucleation (continuous formation of nucleation sites during polymerisation), with two-dimensional and three-dimensional growth out from the nuclei [171]. These observed mechanisms can occur simultaneously, with relative dominance depending strongly upon experimental conditions including monomer concentration, electrolyte solution and electrode surface and morphology [165, 171, 172].

Polymerisation processes can continue once oligomers have been deposited onto the electrode surface. This has been investigated *via* 'solid-state' electropolymerisation experiments, using oligomers dip-coated or sublimated onto electrodes as an initial film and polymerising them potentiodynamically [173, 174]. This method simplifies analysis by removing solution-based reactions, and the effects of potential on processes such as diffusion. Such oligomers can grow to longer chain lengths, and also start cross-linking with each other [174, 175]. With higher applied potential, the average linkages per monomer unit were observed to increase, eventually to beyond two per unit, indicating cross-linking between molecules at their β sites. This occurs as higher potentials charge oligomers to higher cationic states, for example octathiophene goes through neutral, dicationic, tricationic and up to hexacationic states with increasing applied potential [174].

4.2.2 Molecular Ordering in Electropolymerised Polymers

As discussed in chapter 2, the physical properties of a polymer film can depend strongly upon the molecular ordering in the film. In particular, charge mobility through the device will be affected by morphology. The complex relationship between morphology and conductivity, as well as the interdependency of numerous experimental conditions and oligomerisation steps during electropolymerisation make it difficult to elucidate optimal electropolymerisation conditions. In any case, these may be specific to the exact electropolymerisation setup used. Nevertheless, some trends in the effect of electropolymerisation conditions upon morphology and conductivity have emerged.

Important parameters to control during electropolymerisation include the electrochemical technique and chemicals used, the electropolymerisation potential, the monomer concentration and the temperature. Galvanostatic (constant current) electropolymerisation has been observed to give smoother, more uniform films compared to potentiostatic (constant potential) electropolymerisation due to the reduced impact of inhomogeneities on the electrode surface [164, 176]. Potentiodynamic (systematically varying potential) techniques have also yielded smooth films on account of new growth nuclei forming during each voltage cycle, preferentially occurring at sites of slower previous growth [177]. The cycling potential in potentiodynamic growth also repeatedly switches the polymer film between its doped and de-doped states (for more information see section 4.2.4). The resulting insertion and removal of doping counter-ions concurrently causes swelling and de-swelling of the film [178], and has been associated with inferior polymer ordering [165, 175], although this may be confounded by cycling to high potentials in the same reports.

The choice of precursor, solvent and electrolyte can determine if polymerisation occurs at all. There are even some highly reactive monomers that can only ever form soluble oligomers, never polymer films [166]. Solvents must have a large enough dielectric constant to allow ionic conductivity, and a wide enough electrochemical window to withstand the high potentials often used during electropolymerisation [164]. The electrolyte anion also plays an important role in electropolymerisation. Good electron-donor anions can form 'ion pairs' with oligomers of intermediate charging levels, avoiding neutral and over-oxidised molecules unable to polymerise, and significantly facilitating coupling by reducing Coulombic repulsion [179]. Water content in organic solvents has been found to facilitate electropolymerisation of polypyrrole due to its basicity enabling de-protonation [180], but is known to impair electropolymerisation of polythiophene [164, 181]. Additionally, surfactants added to the electrochemical bath are capable of reducing the monomer oxidation potential by stabilising the radical cationic monomer and enhancing conductivity in the electrolyte medium, ultimately improving molecular ordering in the polymer deposits [133].

Some effects of high electropolymerisation potential, monomer concentration or temperature have been found to be interchangeable because increasing any of these factors leads to an increasing reactivity and increased rates of polymerisation [182]. With electropolymerisation from organic solvents, such increased polymerisation rates have typically been associated with more disordered molecular stacking and/or worsened conductivity [175, 183–187]. Various explanations for this have been developed. Higher potentials increase charging level and reactivity of oligomers, which can lengthen oligomers in the film, but also encourages linkage defects and cross-linking [174, 175]. Electropolymerised polypyrrole in particular has been found to consist of two distinguishable components, 'PPyI' which has long chain lengths ($32-64$ pyrrole units), poor crystallinity and low conductivity, and 'PPyII' which has short chain lengths ($8-12$ units), high crystallinity and high conductivity [184, 188]. Despite long chain lengths, linkage defects limit the conjugation in PPyI. Electropolymerisation at higher potentials or temperatures increases the proportion of PPyI deposited (very high potentials yield highly cross-linked ‘PPyIII’). Higher temperatures have also been found to worsen conductivity despite yielding longer chain lengths by encouraging cross-linking [185,186], which was explained by faster de-protonation at higher temperatures enabling more linkage defects. Furthermore, high monomer concentrations were found to reduce the conjugation in resulting electropolymerised films, and thus impair their conductivity [187]. This was explained in terms of increasing concentrations favouring oligomerisation in solution rather than direct chain growth of monomers onto the initally-deposited polymer. Since α-α' linkages become less dominant with oligomer length, polymer growth one monomer at a time was thought to reduce the chance of linkage defects. However, the chain propagation mechanism is no longer regarded as an accurate description of polymer growth. Increased reaction rates can also decrease the pH at the electrode during deposition, since protons are released upon each coupling reaction and will diffuse into the bulk solution at a set rate. Overly acidic conditions are known to hydrogenate thiophene units [189], yielding polymer films with disrupted conjugation [132, 190]. Another simple factor favouring slower growth could simply be that a faster deposition rate leaves the system less able to organise into a well-stacked film.

Atomic force microscopy and its variations (Kelvin probe force microscopy and current-sensing atomic force microscopy) have also revealed that crystallinity and conductivity is not homogeneous throughout electropolymerised films [191, 192]. Instead, higher crystallinity was found in the nuclei of electropolymerised polythiophene films, with lower crystallinity in the surrounding material. It was hypothesised that longer oligomer chains (which have lower solubilities) reach their saturation concentration sooner than shorter oligomer chains and hence form the nuclei, with shorter oligomers filling the remaining regions during later electrodeposition. During electropolymerisation, the morphology shifts from small, highly crystalline grains to larger grains with a larger amorphous component, situated at the periphery of the grains.

4.2.3 Electropolymerisation from Ionic Liquids

Despite the substantial body of literature examining electropolymerisation of conjugated polymers, this has mostly been conducted in aqueous or organic solvents.

There are two important differences between these and ionic liquids. Firstly, the physical properties of ionic liquids are quite different from aqueous or organic solvents, including a tendency to be more viscous and less conductive. For example, low temperatures during electropolymerisation in ionic liquids have been associated with problems of high viscosity and low diffusion, whereas electropolymerised film properties are generally improved by low temperatures during electropolymerisation from organic solvents [176]. The nucleophilicity of ionic liquids is also very low, meaning highly-charged cations are more stable in these media [165]. Secondly, no electrolyte is required in an ionic liquid, meaning among other things that the anion of the ionic liquid itself dopes the polymer during electropolymerisation, rather than the electrolyte chosen for aqueous or organic solvents.

4.2.4 Doping and De-Doping of Conjugated Polymers

The charged species involved in the electropolymerisation process cause counter-ions from the electrochemical solution to be incorporated into the deposited film. The redox behaviour of conjugated polymers enable charge to be shuttled between these incorporated counter-ions and the polymer after (as well as during) deposition, changing the polymer's oxidation state. The transition between oxidised and neutral forms of the polymer can be controlled through application of an external potential, in which case the process is known as 'doping' and 'de-doping'. The counter-ions do not necessarily leave the film during de-doping, especially if they are relatively bulky ($\gtrsim 5-6\,\text{Å}$ [158]). Indeed insertion of oppositely-charged counter-dopant ions may be induced by de-doping. Under ambient conditions, both states of polythiophene and derivatives are relatively stable so the doping state is essentially permanent until actively changed [193].

Despite the higher conductivity of doped conjugated polymer films, the inter-bandgap states formed upon doping act as recombination centres which hinder performance in photovoltaic devices [71]. Hence most reports of electropolymerised PT solar cells use fully de-doped films, although a detailed study found that a low level of doping was actually beneficial [159]. Conventional devices employing spin-coated P3HT do not contain dopants and hence these films are in their fully neutral ('de-doped') state.

4.3 Experimental Methods

4.3.1 Electrochemical Setup

Polythiophenes were electropolymerised using a three electrode setup with ionic liquid electrolytes, as shown in figure 4.2 (a). The whole setup was contained in an argon glovebox atmosphere, and was controlled with a CH Instruments 600C electrochemical workstation. Electropolymerisation took place at the working electrode, generally 2.2 mm thick glass substrates coated with fluorine-doped tin oxide (FTO). A platinum foil counter electrode was used. Standard reference electrodes such as the saturated calomel electrode, or silver/silver chloride reference electrode are not suitable for use with non-aqueous media [194], and could contaminate the experiment and glovebox with water. Often pseudo-reference electrodes such as silver or platinum wires are used with non-aqueous media, but these were found to be very unstable, with voltage variations of up to 500 mV. This is not unexpected, since pseudo-reference electrode potentials depend upon impurities and oxide layers on the electrodes [195, 196]. Hence a more stable reference elctrode was used, following a previously-reported setup [197]. This reference electrode consisted of a silver wire immersed in 10 mM silver bis(trifluoromethylsulfonyl)imide in BmimTFSI, contained in a sealed glass capillary with a glass frit at the end to allow electrical conductivity, but minimise ion transport. Adding 0.05 M ferrocene to the polymerisation solution allowed the reference electrode to be referenced to the Fc/Fc$^+$ redox couple (figure 4.2 (b)), as recommended by IUPAC guidelines for working with non-aqueous reference electrodes [198]. For electropolymerisation from BmimTFSI containing 0.05 M bithiophene, the Fc/Fc$^+$ redox couple equilibrium was found to be -0.395 V.

Two polymer precursors, 2,2′-bithiophene (BT) and 3-methylthiophene (3MT), and four ionic liquids, 1-butyl-3-methylimidazolium bis(trifluoromethylsulfonyl)-imide (BmimTFSI), 1-ethyl-3-methylimidazolium tetrafluoroborate (EmimBF$_4$), 1-ethyl-3-methylimidazolium hexafluorophosphate (EmimPF$_6$), and 1-ethyl-3-methylimidazolium ethyl sulphate (EmimEtSO$_4$) were used. The viscosity and electrical conductivity of these ionic liquids are given in table 4.1, along with those properties for 1 M lithium perchlorate in propylene carbonate, a typical organic solvent mixture for electropolymerisation. Since the physical properties of ionic liquids are heavily influenced by water content in the ppm range [199], the values

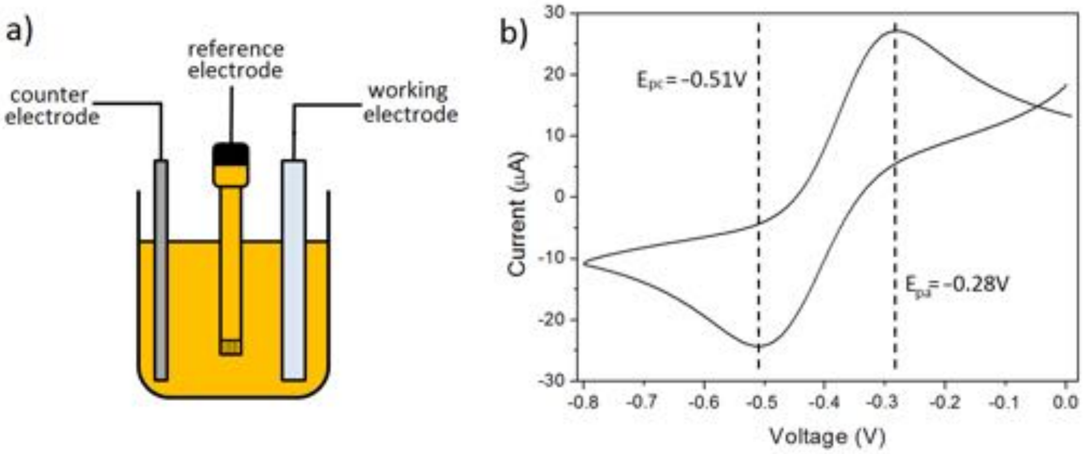

Figure 4.2: a) Schematic diagram of electrochemical setup. A standard three-electrode setup is used, with a platinum foil counter electrode, an Ag/Ag$^+$ reference electrode and the working electrode, typically FTO glass. b) Cyclic voltammogram of the ferrocene redox reaction in a typical deposition solution (0.05 M BT in BmimTFSI), showing peak anodic current at -0.28 V and peak cathodic current at -0.51 V, yielding an equilibrium potential of -0.395 V *vs.* Ag/Ag$^+$ overall.

shown in table 4.1 are indicative rather than absolute.

The ionic liquids were stored and used in an argon atmosphere to avoid contamination with air or water. Additionally, molecular sieves were added to the stock ionic liquid, and the electrochemical baths were bubbled with argon for approximately 15 minutes before each batch of electropolymerisation. Halide impurities can be present in ionic liquids as a result of the synthesis procedure; silver salts (silver nitrate, silver tetrafluoroborate and silver TFSI) were added to a small sample of the ionic liquid to check for precipitation of silver halide salts. Small amounts of precipitate were observed with each silver salt when added to the EmimBF$_4$, EmimPF$_6$ and EmimEtSO$_4$ samples. This precipitate was initially white but darkened with time, and dissolved in ammonia solution to give a clear solution, indicating its identity as silver chloride and hence the presence of chloride impurities in the ionic liquids [206]. By contrast, no precipitation was visible in the BmimTFSI sample even after months, suggesting very low halide impurities.

Prior to electropolymerisation, the FTO substrates were cut to the desired

Solvent	Viscosity (mPa s)		Conductivity (mS/cm)	
BmimTFSI	40	[200]	4.6	[200]
$EmimBF_4$	37	[201]	14	[201]
$EmimEtSO_4$	122	[202]	0.08	[202]
$EmimPF_6$	170	[203]	0.005	[204]
Propylene Carbonate[a]	4	[205]	6	[205]

Table 4.1: Approximate physical properties of ionic liquids and representative molecular solvent system; [a] the properties for propylene carbonate correspond to 1 M $LiClO_4$ electrolyte.

shape and size with a diamond scribe and washed with 'piranha solution', specificly 3 parts sulphuric acid to 1 part hydrogen peroxide, at 90 °C for 10 minutes. This solution reacts violently with most solvents, and extreme caution should be exercised when carrying out this cleaning step. After piranha treatment, the substrates were rinsed with de-ionised water and then sonicated for 10 minutes in de-ionised water before being blown dry with nitrogen.

4.3.2 Visible Absorption Analysis

After electropolymerisation, films were washed with ethanol and dried under a nitrogen stream prior to absorption measurements. The absorption spectra of electropolmyerised films were taken with an HP 8453 UV-Visible ChemStation spectrometer, measuring in transmission. Hence reflection and scattering from the film will also contribute to the detected absorption. As outlined in section 3.3, equation 3.1 was fit to the measured spectra to assess molecular ordering. The fitting parameters were the exciton bandwidth, W, the energetic disorder, σ, and the percentage of the film that is amorphous. The fitting was conducted using the Python function 'curve_fit', a least-squares fitting algorithm [207]. Fitting was conducted over the spectral region between absorption from the amorphous polymer at high energies and significant scattering and reflection at low energies. Following previously reported applications of this method to P3HT, the specific range for fitting was $\sim 2.00-2.30$ eV ($\sim 540-620$ nm) [56].

It is worth noting that absorption was also measured relative to a reference sample, usually bare FTO. For absorption spectra measured of films submerged in 0.1 M aqueous $LiClO_4$, this occasionally resulted in apparently negative absorption for wavelengths greater than ~620 nm. This negative absorption really represents an improved transmission after coating the film with polythiophene, presumably as a result of index matching. This phenomenon has also been reported for P3MT films on thin gold [71] (where its cause was speculated to be optical interference or plasmonic scattering).

4.3.3 Grazing Incidence X-Ray Diffractometry

GIWAXS measurements were performed by Dr Alessandro Sepe at the Adolphe Merkle Institute (University of Fribourg, Switzerland) beamline under vacuum. The scatterless beamline employed the high brilliance Rigaku MicroMax-007HF source, equipped with a rotating Cu-anode. The beam was focused to a size of 500 μm^2 on the sample, with a footprint on the sample averaging over ~ 1 cm in length. A beamstop for the primary beam was employed. An image plate was employed for GIWAXS with a sample-detector distance of 0.1 m. The structural properties of the thin films were studied at incident angles slightly above the critical angle of the nanostructured thin films, allowing the films to be investigated over their full thickness. The samples were moved out of the beam after each measurement to avoid damage from the beam. The q-space calibration was performed by fitting the characteristic scattering signal arising from silver behenate. One-dimensional intensity profiles were extracted from the two-dimensional GIWAXS maps by integrating the signals in the directions parallel and perpendicular to the substrate. The data were also chiefly evaluated by Dr Alessandro Sepe, using Xi-CAM.

4.4 Results and Discussion

4.4.1 Initial Electropolymerisation

The feasibility of electropolymerisation for different precursors and ionic liquids was initially gauged using cyclic voltammetry with a range of precursor concentrations, assessing visible deposition and evidence for polymerisation in the voltammogram (see next section). No polymerisation was achieved for either BT or 3MT precursors in $EmimPF_6$ or $EmimEtSO_4$, at any potential, concentra-

Chemical	BmimTFSI	$\mathrm{EmimBF_4}$	$\mathrm{EmimPF_6}$	$\mathrm{EmimEtSO_4}$
BT	✓	patchy	✗	✗
3MT	patchy[a]	occasional strips	✗	✗

Table 4.2: Summary of electropolymerisation success sith different precursor and ionic liquid combinations. A ✗ indicates no deposition under any conditions tried, a ✓ indicates successful deposition of uniform films under all conditions tried. [a] P3MT films electropolymerised from BmimTFSI were patchy unless high potentials ($\geqslant 0.9\,\mathrm{V}$) or temperatures ($\geqslant 60\,^{\circ}\mathrm{C}$) were used.

tion or temperature tried. Polymerisation of 3MT was very rarely observed with $\mathrm{EmimBF_4}$, and only ever along a thin strip situated where the top of the ionic liquid touched the substrate. Electropolymerisation of BT from $\mathrm{EmimBF_4}$ was more reliable, but still yielded patchy film coverage. By contrast, polymerisation was readily achieved from BmimTFSI. For 3MT, this deposition was patchy across the substrate unless high potentials ($\geqslant 0.9\,\mathrm{V}$) or temperatures ($\geqslant 60\,^{\circ}\mathrm{C}$) were used. Uniform film coverage was possible for all conditions tried with BT from BmimTFSI. These results are summarised in table 4.2.

Since polymerisation depends upon coupling of cationic radicals followed by de-protonation of the resultant oligomer, the solvent system must stabilise cationic oligomers long enough for them to interact with each other, and facilitate the de-protonation step. It could be that $\mathrm{EmimPF_6}$ and $\mathrm{EmimEtSO_4}$ do not satisfy these requirements, or it could be that their high viscosities and low conductivities prevent formation of reasonable concentrations of interacting charged oligomers near enough to the electrode. Previously, poor electron-donor anions, including $\mathrm{PF_6}^-$ and $\mathrm{BF_4}^-$, were found to be unable to support electropolymerisation of 2,2′-bipyrrole whereas strong electron-donor anions could, *via* the formation of stable ‘ion pairs’ with reduced Coulombic repulsion [179].

It is known that water can act as a proton scavenger during electropolymerisation [180]. Being more basic than the oligomers formed during polymerisation, water encourages de-protonation rather than hydrogenation of the coupling products. If this process is required to reach oligomer lengths sufficient for precipitation onto the electrode, the presence of small amounts of water may be necessary to allow film deposition. Hence occasional presence of water impurities may explain the narrow strips of P3MT deposition sometimes observed for polymerisation from EmimBF_4. Such strips of deposition where the solvent surface meets the electrode has been observed before, and also put down to water impurities absorbed from the atmosphere at the surface of the ionic liquid [208]. As mentioned previously, water content is also known to hamper extensive film growth and worsen the resulting film properties [164, 181].

The previously-described interchangeability of high potentials, temperatures and concentrations makes it unsurprising that either high temperatures or high potentials can be used to promote uniform film deposition of P3MT from Bmim TFSI; presumably higher 3MT concentrations would have the same effect, although this wasn't observed for concentrations up to 2 M. The tendency for patchy films at low oligomerisation rates indicates enhanced precipitation onto already-deposited polymer rather than bare electrode. Such nucleated growth has been widely observed in electropolymerisation, with the dominant growth mechanism previously observed to shift from instantaneous to progressive nucleation with increasing potentials, favouring more uniform deposition [171]. The uniform film coverage consistently found for PBT polymerised from BmimTFSI suggests that oligomerisation rates are inherently faster than for 3MT, perhaps because the TFSI^- anion forms ion pairs with oligothiophenes more readily than with oligo(3-methylthiophenes).

Given the versatility and reliability of BT polymerisation from BmimTFSI, this system was used for all further experiments described in this thesis, unless specifically described otherwise. The specific BmimTFSI used here had the added benefit of being the least contaminated with impurities of the ionic liquids received, as described in section 4.3.

4.4.2 Voltammetric Analysis

Typical cyclic voltammograms for thiophene electropolymerisation are given in figure 4.3. These voltammograms show polymerisation of (a) 2,2′-bithiophene, and (b) 3-methylthiophene, in BmimTFSI. The voltammograms shown here match previously reported voltammetry of polythiophene electropolymerisation in ionic liquids [209, 210].

In figure 4.3(a), the current rises sharply at around 0.4 V on the first anodic sweep, before crossing at a lower voltage of around 0.3 V on the return sweep. Al-

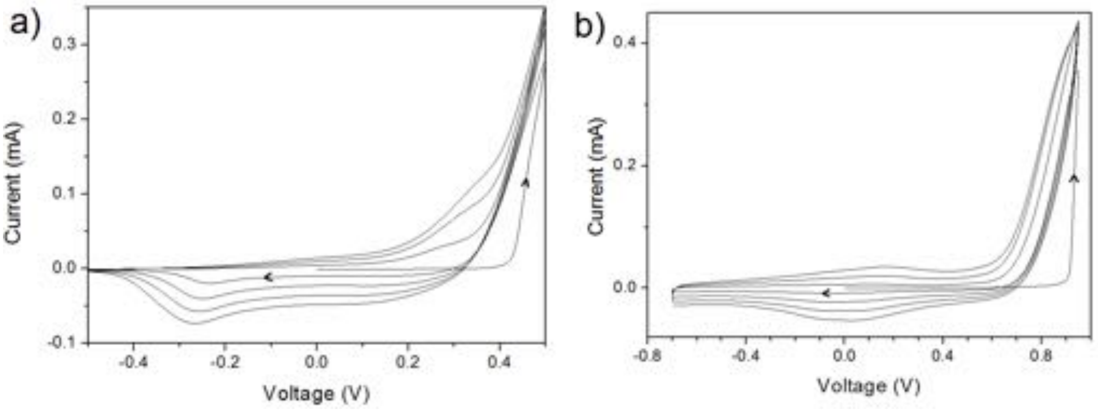

Figure 4.3: Cyclic voltammograms for (a) 0.05 M bithiophene, and (b) 0.02 M 3-methylthiophene, in BmimTFSI, taken between -0.5 V and +0.5 V at 50 mV/s against a Ag/Ag$^+$ reference electrode. Arrows on the first scan label the direction of potential scanning. The trace displays the features typical of thiophene electropolymerisation, namely the ‘redox catalysis’ loop on the first scan, large currents above the precursor oxidation potential, and redox peaks at lower potentials corresponding to doping processes in the polymer film, which grow on sucessive scans as the polymer film thickens.

though this has been previously identified as a nucleation loop resulting from an initial overpotential required for nucleating growth [211], more recent experiments have demonstrated that it is in fact due to so-called ‘redox catalysis’ [209]. In such redox catalysis processes, radical oligomers donate charge to neutral monomers in a homogeneous comproportionation reaction to give radical monomers which can themselves couple and oligomerise (see figure 4.4). This homogeneous oxidation can be far quicker than the heterogeneous oxidation of the monomers at the electrode. Very soon after comproportionation, the oligomer can be heterogeneously oxidised back to its higher oxidation state, contributing to the current measured in the voltammogram. This explains how the current can be higher on the return sweep than the outward sweep (and hence produce trace-crossing), since the oligomers generated on the outward sweep catalyse further monomer oxidation on the reverse sweep. This also increases the reactive monomer concentration at the electrode substantially [209].

Redox catalysis is also responsible for the decreasing potential (from ∼+0.4 V to ∼+0.3 V) of the steep oxidation peak of the bithiophene precursor observed for

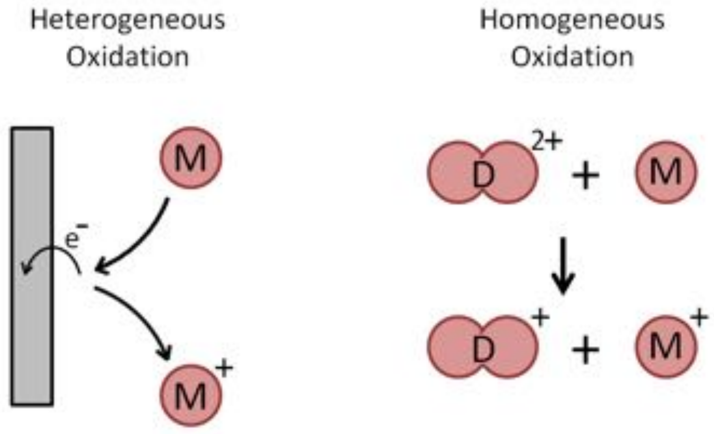

Figure 4.4: Schematics of the different oxidation mechanisms during electropolymerisation. A monomer can either be heterogeneously oxidised at the electrode, or homogeneously oxidised *via* a comproportionation reaction with a doubly-oxidised dimer. The homogeneous reaction can be far quicker than the heterogeneous reaction, leading to the trace-crossing observed in electropolymerisation voltammograms. Note that these processes are not limited to monomers and dimers, but can occur for all lengths of oligomer.

successive anodic sweeps. As the population of oligomers increases, in particular from zero after the first anodic sweep, they increasingly catalyse monomer oxidation. Heterogeneous oxidation of monomers at the electrode cannot take place beneath the monomer oxidation potential ($\sim$+0.4 V), but homogeneous monomer oxidation can take place once the potential reaches the oligomer oxidation potential, which decreases with oligomer length.

The shallower, broader current peaks between around −0.2 V and +0.3 V on the anodic sweep and +0.3 V and −0.4 V on the cathodic sweep correspond to doping and de-doping processes in the deposited polymer film. The current associated with these peaks grows on successive sweeps as the deposited polymer film grows. The breadth of these peaks arises from the variety of oligomer lengths and hence redox potentials present in the solution [165].

The voltammogram of 3MT electropolymerisation shown in figure 4.3(b) exhibits the same qualitative behaviour as for BT electropolymerisation. The only substantial difference is the increase in the initial oxidation potential, from around 0.4 V to 0.9 V.

4.4.3 De-Doping Electropolymerised Thiophenes

Anodic electropolymerisation of polythiophene leaves it in its conducting, doped form, which is unsuitable for use in photovoltaics [71]. The visible absorption analysis developed by Spano and used here to assess film morphology also assumes the polymer is in its neutral state, free of absorption arising from inter-band polaron and bipolaron states. Hence all films were de-doped prior to further characterisation or device fabrication, by applying a potential beneath the reduction potential until the current stabilised around zero. The potential was chosen according to the cathodic reduction peak observed in a cyclic voltammogram of the film. A typical current trace for de-doping is shown in figure 4.5(a), corresponding in this case to a PBT film de-doped at $-0.5\,\mathrm{V}$. A fast initial drop in current is followed by a slower decline, but by 20 s the current has essentially fallen to zero and de-doping is complete. The transition from fast de-doping to slow de-doping could result from the polymer film becoming more compact as dopants are removed from it, slowing the diffusion of dopants at later times [178]. If this is an accurate explanation, this would suggest that at least some of the dopants are removed from the film during de-doping.

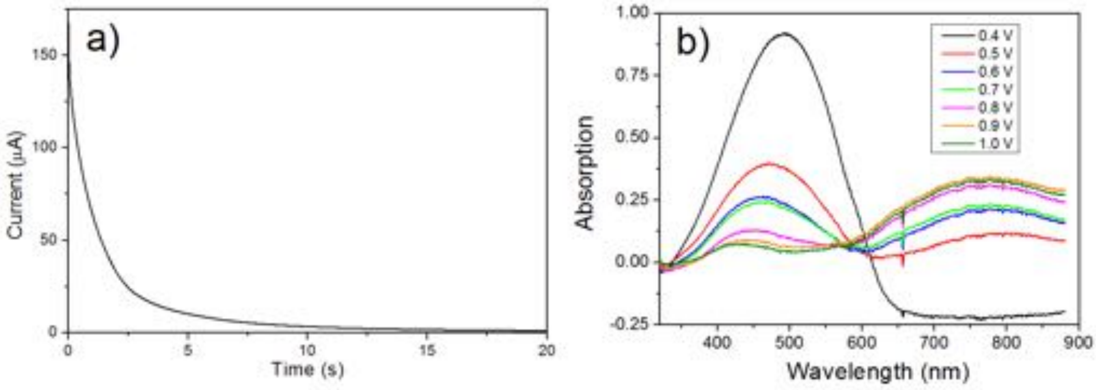

Figure 4.5: a) Typical de-doping current, here corresponding to a PBT film de-doped at $-0.5\,\mathrm{V}$. The current stabilises to zero after a fast initial decrease followed by a slower decline. b) Absorption spectra of a P3MT film as a function of applied potential. The film was submerged in an aqueous $0.1\,\mathrm{M}$ $LiClO_4$ solution, against an Ag/AgCl reference electrode (not the same as the electropolymerisation reference).

The effect of doping upon the polymer bandstructure is readily seen from visible absorption spectra. Figure 4.5(b) shows how the absorption spectrum of a P3MT film changes with applied potential. The film was electropolymerised in BmimTFSI before being washed and transferred to a monomer-free 0.1 M $LiClO_4$ aqueous solution to prevent further polymerisation and facilitate *in situ* absorption measurements. The potentials indicated in the figure correspond to an Ag/AgCl reference electrode. The doping level of the film increases with applied potential, and cycles reversibly as the potential is increased or decreased. No changes to the spectrum were observed for potentials below 0.4 V or above 1.0 V, implying that by 1.0 V, the sample had been fully doped and by 0.4 V, it had been fully de-doped. The apparently negative absorption beyond 620 nm at 0.4 V arises from improved transmission compared to a blank substrate, presumably due to index-matching. The observed spectra match previously reported theoretical and experimental results [212, 213], with a π-π^* transition at 490 nm in the neutral state giving way to lower energy peaks corresponding to absorption to bipolaron states introduced into the polymer bandgap. In fact, two bipolaron states should be present, with absorption around 775 nm and 1770 nm, although the second is outside the range of detection here. The π-π^* peak decreases as the band-edge states with greatest oscillator strength move into the bipolaron states, and blueshifts slightly as the interband bipolaron states widen the bandgap.

4.4.4 Optimising Electropolymerisation Conditions

Visible absorption measurements were used as a covenient way to assess molecular ordering in the electropolymerised films. As an initial trial of this analysis method, absorption spectra of a PBT film electropolymerised potentiostatically at 0.35 V were measured after annealing at different temperatures (the films were cooled to room temperature before the absorption was measured). The spectra and resultant fitting parameters are shown in figure 4.6. Absorption spectra of films annealed up to 250 °C are displayed here; spectra taken at higher temperatures maintain the same spectral shape, but decrease in magnitude indicating the onset of polymer degradation (the samples were annealed in air).

The weaker 0-0 transition (around 600 nm) compared to the 0-1 transition (around 555 nm) in figure 4.6(a) is evidence of H-aggregate behaviour in the PBT

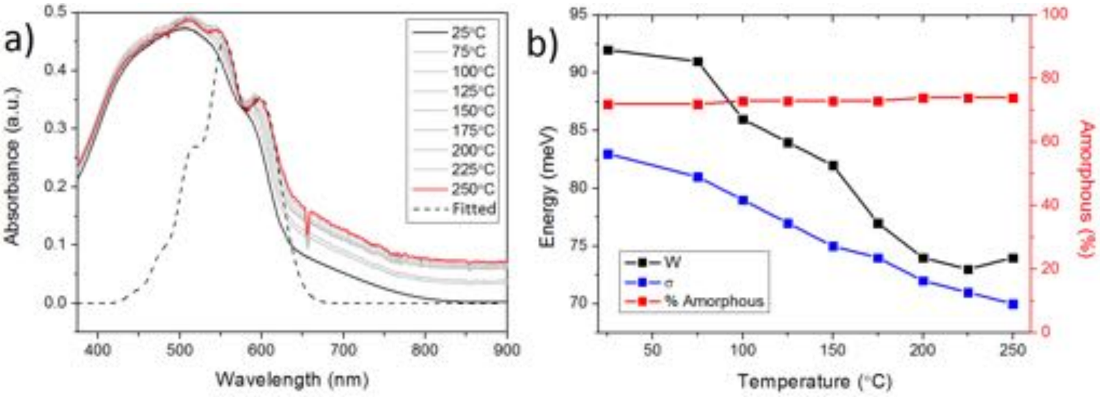

Figure 4.6: a) Absorption spectra of a PBT film deposited at 0.35 V from 0.05 M BT in BmimTFSI, taken after annealing at different temperatures. The fitted spectrum for the film annealed at 250 °C is also shown. b) Chart showing the changes in exciton bandwidth (W), energetic disorder (σ) and proportion of amorphous PBT during annealing, as determined by fitting the absorption spectra to equation 3.1.

films (assuming a Huang-Rhys factor of close to unity, which is expected for the dominant C=C vibrational mode) [114]. The dotted line in figure 4.6(a) shows the best fit of equation 3.1 to the absorption spectrum taken at 250 °C, yielding the fitting parameters recorded in figure 4.6(b). Although there is only a narrow region where this fitted spectrum matches the experimental spectrum, reflection is known to distort the measured absorption at wavelengths longer than the polymer bandgap [214], and absorption from the amorphous parts of the film contributes to absorption at shorter wavelengths (indeed this is how the percentage of the film that is amorphous is calculated) [126], so this narrow region of good fitting is expected and has been consistently observed previously [51, 56, 126].

Thermal annealing provides thermal energy for the polymer film to re-arrange itself into a lower energy equilibrium arrangement, and is routinely used to improve ordering in spin-coated polythiophene films with a kinetically trapped initial morphology [30, 31, 69, 215]. This re-organisation is thought to proceed *via* de-planarisation of the polythiophene chains during annealing [56, 216], induced by twisting of adjacent thiophene units, along with increased molecule mobility, followed by re-organisation towards more crystalline configurations during cooling [46]. Although the alkyl side-chains are thought to play some role in the re-organisation [215], thermal annealing has also led to improved crystallinity in chemically synthesised powder samples of unsubstituted polythiophene [52]. Specifically, conjugation lengths, crystallite dimensions and the relative proportion of crystalline to amorphous polymer have all been found to increase after heat treatment [46, 52, 215].

Figure 4.6 clearly shows red-shifting absorption with increasingly resolved vibronic peaks for increasing annealing temperatures. The fitting parameters show monotonically declining values for W and σ with annealing temperature, other than for W at the very highest annealing temperature. Following the discussion in section 3.3, this corresponds to extending conjugation lengths with a narrowing distribution of lengths across the film. The exciton bandwith decreases from 92 meV to 73 meV, corresponding approximately to an increase in conjugation length from 24 to 31 repeat thiophene units, or 9 nm to 12 nm, using the relationship shown in figure 3.3. Simultaneously, the energetic disorder term decreases from 83 meV to 70 meV. These results are consistent with the thermal annealing of P3AT films spin-coated from a low boiling point solvent, such as chloroform, which has been found to yield films of poor initial crystallinity that improves after annealing [46, 51, 126, 215]. Thermal annealing of P3OT films spin-coated from chloroform was found to extend conjugation lengths from 5.7 nm to 8.6 nm, with a narrower distribution for higher temperatures [215], and a very similar decrease in energetic disorder, from 80 meV to 72 meV was observed during thermal annealing of a P3HT:PCBM film spin-coated from chloroform [51].

The third fitted parameter is the proportion of the film that is amorphous, which is essentially constant throughout the annealing process, increasing slightly from 72 % to 74 %. Combined with the decreasing values for W and σ, this suggests that crystallisation proceeds through the merging of smaller conjugation segments to form larger ones, simultaneously increasing conjugation lengths and decreasing energetic disorder, without affecting the amorphous regions. This has been observed for P3HT aggregating in solution as the concentration of a poor solvent is increased [128], but is atypical for thermal annealing of P3AT films, where crystallites have been observed to grow at the expense of surrounding amorphous regions [30, 51, 215]. The value of $\sim 70\,\%$ is also higher than reported for annealed, spin-coated films of regioregular P3HT, where values in the range of $45-60\,\%$ are more usual [51, 52, 126, 217]. In contrast, regiorandom P3HT is often found to have negligible crystallinity [46]. This points to the first likely cause for the behaviour seen in electropolymerised films of polythiophene. Although there are no side-chains, so regioregularity isn't relevant to PBT, the bithiophene units are free to polymerise at α or β positions (see section 2.1.1). Conjugation is disrupted by α-β' and β-β' links [44, 45], and these defects cannot be removed by thermal annealing. This is known to be a problem in electropolymerised films due to the progression through increasing oligomer size before polymerisation. Initially, α-α' linkages are promoted by the sulphur atom on the thiophene unit, which stabilises the free radical at the α site. However, this stabilisation diminishes with oligomer length, so that the probability of the radical being at the β site increases from $\sim 5\,\%$ for a monomer to $\sim 50\,\%$ for a trimer (although steric hindrances will still favour α-α' linkages) [218, 219].

Another possible cause of the relatively large proportion of amorphous polymer is the influence of the counter-ions that are incorporated into the film during electropolymerisation. For deposition from BmimTFSI, the bulky TFSI ion will be embedded in the PBT, which could disrupt the PBT stacking. Indeed, GIWAXS reveals a broad peak around $1.5\,\text{Å}^{-1}$, corresponding to a π-π stacking separation of 4.4 Å (discussed later, see figure 4.8), larger than the 3.5 Å separation observed in polythiophene electropolymerised with the smaller tetrafluoroborate ion [132]. However, it is not clear why thermal annealing would have no effect on the proportion of amorphous film if the presence of counter-ions were causing this, and de-doping was thought to remove at least some of the dopants from the film.

Next, the evolution of crystallinity throughout the film growth was assessed by examining the absorption spectra for films of different thickness. All samples were electropolymerised potentiostatically at 0.35 V for varying deposition times to give films of different thickness. The absorption spectra and corresponding fitting parameters are shown in figure 4.7. Although the energetic disorder and proportion of amorphous film are unaffected by film thickness, there is a clear variation in exciton bandwidth. As the film thickens, W falls from 149 meV to 60 meV, corresponding to an increase in conjugation from 14 to 38 thiophene units (6 nm to 15 nm). A systematic redshift in peak absorption, from 486 nm to 508 nm, complements this decrease in bandwidth, strengthening the implication that it is due to extending conjugation rather than optical effects.

More can be learnt about the evolution of polymer morphology with film

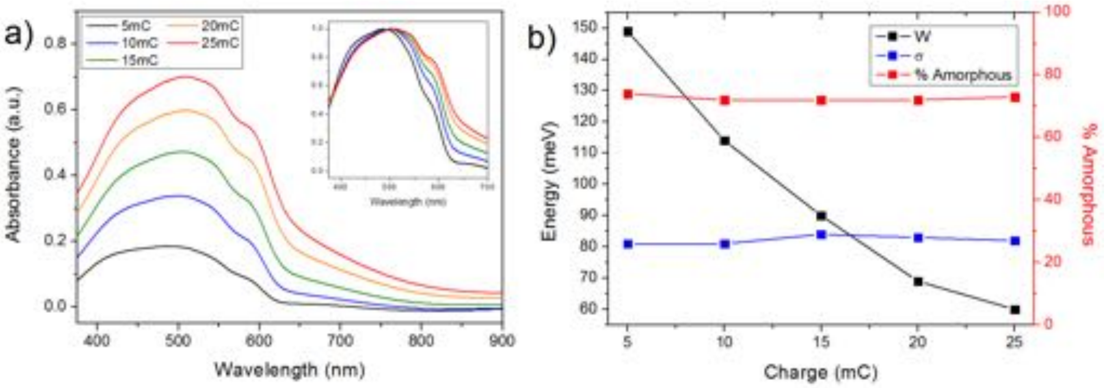

Figure 4.7: a) Absorption spectra for PBT films electropolymerised potentiostatically at 0.35 V, deposited for different lengths of time until the corresponding charge had been consumed, inset shows normalised spectra. b) Fitting parameters - although the energetic disorder, σ, and the proportion of amorphous film are essentially unaffected by film thickness, W decreases sharply for thicker films.

thickness from GIWAXS measurements, which measure mainly the coplanar and π-π stacking in the film (see figure 4.9), and are therefore complementary to the absorption spectrum analysis (W is related to conjugation length, but is not strongly affected by the extent of coplanar stacking, and the variation with π-π stacking diminishes with increased stacking). Hence GIWAXS measurements were performed on the 5 mC, 10 mC and 20 mC films from figure 4.7, as well as a blank FTO reference sample. The spectra were integrated over the q_y and q_z directions (see figure 3.4) to assess in-plane and out-of-plane morphologies respectively. These results are shown in figure 4.8(a) and (b).

There are two main features in the spectra shown in figure 4.8, sharp peaks at 0.38 Å^{-1} and 0.64 Å^{-1} (marked with arrows) and a broad feature around 1.4 Å^{-1}, as well as peaks in the FTO reference at 0.30 Å^{-1} and 0.47 Å^{-1}. Since the FTO peaks do not overlap with any of the film features, they can be ignored. The peaks at 0.38 Å^{-1} and 0.64 Å^{-1} correspond to a stacking distance of 16 Å, the coplanar stacking separation. They are visible only in the 5 mC film, and only in the in-plane direction, indicating edge-on oriented polymer chains (as illustrated in figure 4.9). The broad peak around 1.4 Å^{-1} corresponds to a stacking distance of 4.4 Å, commensurate with the π-π stacking in polythiophene. This peak is visible in all films and all directions, and grows in magnitude with film thick-

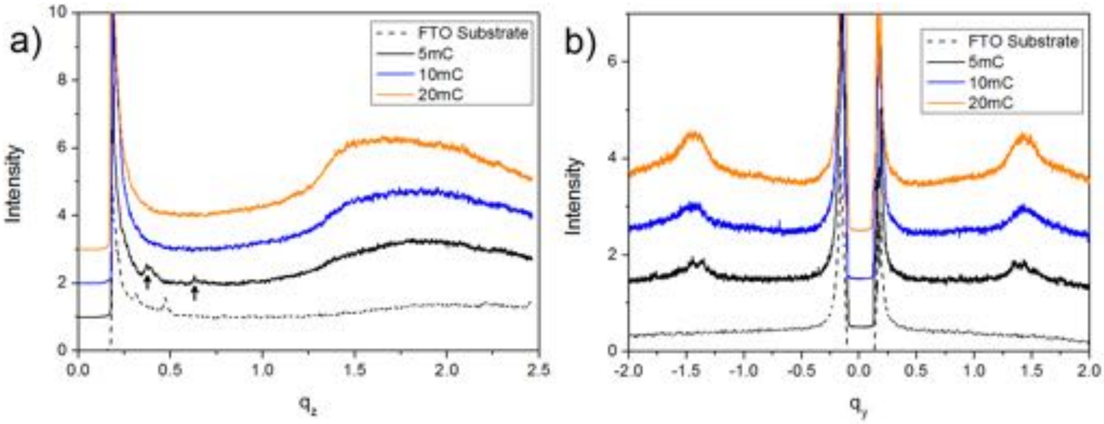

Figure 4.8: Grazing incidence, wide angle X-ray spectra of PBT films electropolymerised potentiostatically at 0.35 V for varying times from BmimTFSI, with a blank FTO substrate for reference. Spectra integrated over the directions (a) parallel, and (b) normal, to the substrate; these signals have been normalised at featureless points in their background signal ($q_z = 0.75$ and $q_y = 0.5$) and offset to aid in visualisation. The broad peak around 1.4 Å^{-1} indicates a π-π stacking separation of 4.4 Å, whereas the sharp peaks around 0.38 Å^{-1} and 0.64 Å^{-1} (marked with arrows) correspond to coplanar stacking of 16 Å. All GIWAXS measurements taken by Dr Alessandro Sepe.

ness. Hence it appears that there is a transition during polymer growth from coplanar stacking with edge-on orientation to isotropically-oriented π-π stacking. Note that previous investigations into spin-coated P3HT films have also found decreasing X-ray signals for coplanar stacking with increasing conjugation lengths as inferred from optical spectroscopy or AFM [54, 55]. However, this was accomanied by an implied increase in amorphous content, which is not observed in the electropolymerised films.

Together with the absorption spectra, the GIWAXS data suggest an evolution in deposited polymer morphology as shown in figure 4.9. Initial film growth is composed of polymer chains with strong coplanar stacking in an edge-on orientation but weak π-π ordering and short conjugation lengths. As the film grows, the coplanar ordering weakens significantly, but π-π ordering improves and the effective conjugation lengths increase. However, the edge-on orientation is lost, giving way to isotropically-oriented crystallites. Perhaps a relaxation in an initial constraint on orientation allows for better crystallinity as the film develops.

This seems to correlate with previous investigations of polymer electropolymerisation, where preferential orientation of the polythiophene chains was observed to be induced at the substrate and slowly diminish with film thickness, giving way to isotropically oriented crystallites (although both effects were dependent upon polymerisation conditions) [177,220,221]. O'Neil *et al.* also investigated polymer morphology and crystallinity at various stages during polymer film growth and reported a transition from highly crystalline, small grains at the beginning of film growth to larger grains containing crystalline cores and amorphous peripheries as the film thickened [192]. Despite the increasing amorphous content, the size of the crystallites still grew with film thickness; the authors didn't comment upon changes in orientation.

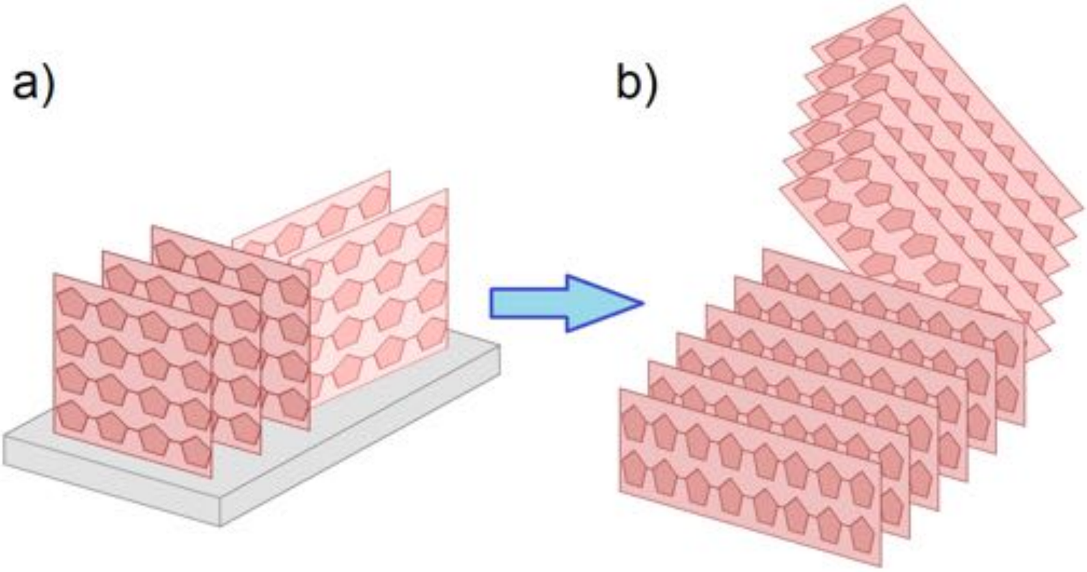

Figure 4.9: Schematic of the proposed transition in deposited polymer morphology as the film thickens. Edge-on stacking near the substrate encourages good coplanar stacking, but results in short conjugation and poor π-π stacking (a). During later deposition in the bulk film, conjugation and π-π stacking increase while coplanar stacking decreases; the crystallite orientation also becomes isotropic (b).

The variation in W is larger than that induced by thermal annealing, and makes clear the need to compare films of similar thicknesses to determine optimal electropolymerisation parameters. For potentiostatic electropolymerisation, this is easily done by controlling the charge consumed during deposition (although changes in electropolymerisation ‘efficiency’ under different conditions does not guarantee this to be sufficient); potentiodynamic electropolymerisation is more difficult to control, but the number of sweep cycles can be varied empirically to obtain similar thicknesses. In either case, the absolute absorption spectra should be compared to ensure similar optical densities across a batch of samples. Although it is impossible to ensure identical film thicknesses across a batch (especially given the variation in oscillator strength and hence absorption with crystallinity [126]), variation was kept as low as reasonably possible, and at least ensured not to vary systematically across the parameter being investigated.

Having established the efficacy of absorption analysis, and learnt the need for comparison between films of comparable thickness, the same procedure was carried out to examine the influence of electropolymerisation conditions upon molecular ordering in the resultant films. The first parameter to be investigated was deposition potential, intially with potentiostatic electropolymerisation. Absorption spectra for PBT films deposited at different potentials are shown in figure 4.10. All films were deposited from 0.05 M BT, until 15 mC had been consumed; variation in peak absorption was minimised and did not vary systematically with deposition potential.

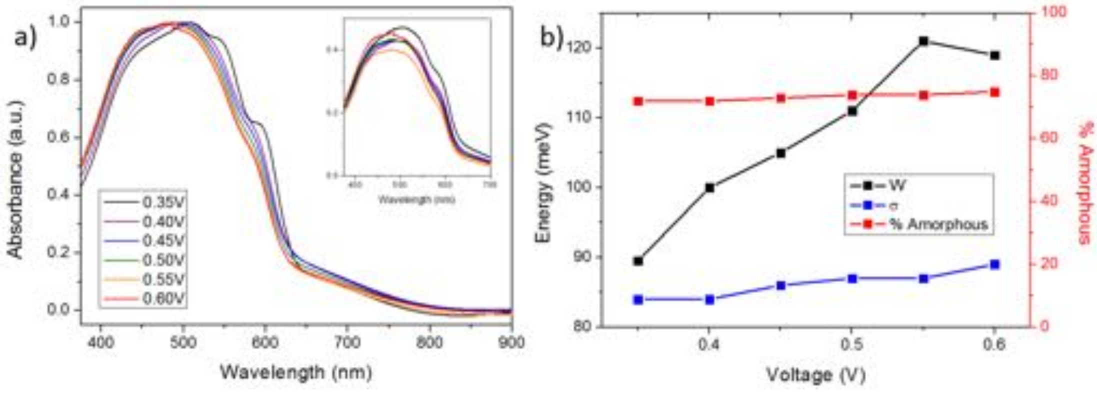

Figure 4.10: a) Normalised UV-vis absorption spectra for PBT films deposited *via* potentiostatic deposition at different potentials until 15 mC had been passed, here from 0.05 M BT in BmimTFSI. The inset shows the un-normalised spectra. b) Fitting parameters as determined by fitting equation 3.1 to the absorption spectra.

Excitonic bandwidth and energetic disorder are both observed to increase with electropolymerisation potential, from 90 meV to 121 meV and from 84 meV to 89 meV respectively. This corresponds to a decrease in conjugation from 25 thiophene units to 20, or 10 nm to 8 nm. Again, the trend in W is matched by the wavelength of peak absorption, which blueshifts from 505 nm to 480 nm with increasing deposition potential. In contrast, the proportion of amorphous film is essentially unchanged, rising from 72 % to 75 %. As discussed in section 4.2.2, high deposition potentials have previously been found to yield decreased film quality across many conjugated polymers and electropolymerisation setups, as determined from properties such as crystallinity, conjugation length and conductivity [165, 175, 213, 221, 222]. Given the complexity of the full electropolymerisation process, and dependence upon a range of different experimental parameters, it is not possible to isolate one specific explanation for this effect of potential, although various possibilites have been outlined in the references given and the description in section 4.2.2. Low potentials have been observed to yield shorter overall chain lengths during electropolymerisation [174, 175], since reactivity decreases with chain length, but this does not appear to affect the effective conjugation measured here.

The same analysis was conducted for film electropolymerised potentiodynamically, as shown in figure 4.11. These films were polymerised between −0.5 V and a different upper voltage for each sample, as indicated in figure 4.11. The scan rate in all cases was 0.2 V/s.

For potentiodynamic electropolymerisation, there is a different relationship between exciton bandwidth and potential. The bandwidth has a minimum of 85 meV at 0.55 V, with lower and higher potentials reaching values of 98 meV and 100 meV respectively. This represents a variation in conjugation between 26 and 22 thiophene units. Although the film polymerised at 0.60 V has a relatively low absolute absorption, it is comparable to the film polymerised at 0.45 V, suggesting that the increased bandwidth at 0.60 V is real, even if the effect is not quite as strong as shown in figure 4.11(b). Other than these two films, the raw spectra are very similar and do not vary systematically with the resultant values of W. An initial increase in conjugation with potential followed by shortening conjugation has been observed before with potentiodynamic electropolymerisation, and can be explained by increased oligomer charging levels and reactivities initally yielding extending chain lengths before causing cross-linking at higher po-

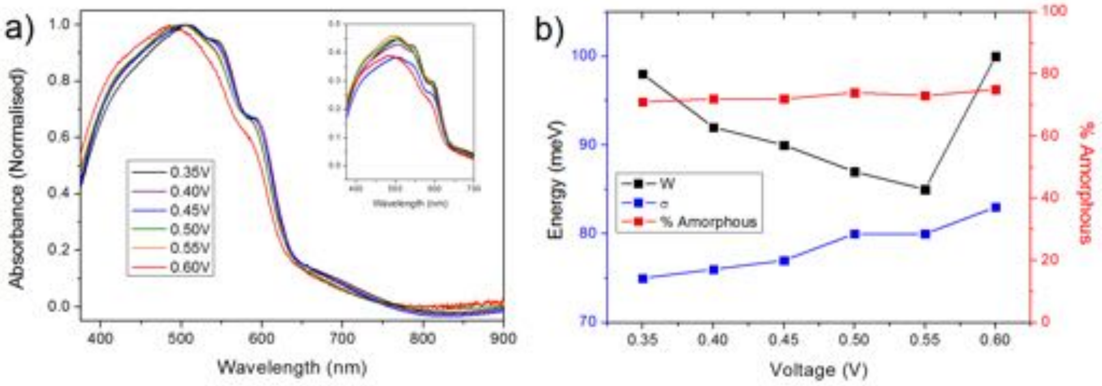

Figure 4.11: a) Absorption spectra and b) fitting parameters for PBT films electropolymerised potentiodynamically. The voltages here indicate the maximum voltage on the scan sweep, all scan rates were 0.2 V/s. The energetic disorder, σ, increases with potential, but the exciton bandwidth, W, decreases before increasing at 0.60 V.

tentials [174, 175]. The energetic disorder increases monotonically with potential, from 75 meV to 83 meV. This could result from higher potentials only enabling extended conjugations *via* merging of adjacent oligomers free from linkage defects, thus increasing variation in conjugation as well as average conjugation length.

The potentiodynamically deposited films are of similar thickness to the potentiostatically deposited films, allowing comparison between the two methods. Potentiodynamic electropolymerisation gives less energetic disorder across all potentials, varying between 75 – 83 meV rather than 84 – 89 meV. Simultaneously, optimal potentiodynamic conditions lead to marginally improved conjugation compared to potentiostatic deposition, reaching 26 thiophene units compared to 25. It is worth considering why the variation in exciton bandwidth as a function of applied potential is different for potentiostatic and potentiodynamic electropolymerisation.

There are two obvious differences between potentiostatic and potentiodynamic electropolymerisation. Firstly, the potential is varying rather than static, and secondly the polymerisation is periodic rather than continuous. The varying potential means that the charging levels of oligomers will vary during polymerisation, and also means that the deposited film cycles through its doped and de-doped state multiple times during the deposition. The periodic polymerisation is, by contrast, a kinetic effect. It is likely to affect diffusion and the relative concentrations of different chemical species in the oxidation region. In order to distinguish between varying polymerisation potentials during deposition and kinetic effects, pulsed electropolymerisation was conducted, with a voltage switching between −0.5 V (the de-doping potential) and 0.5 V (the polymerisation potential). The duration of the pulses was chosen to be comparable to the times for which polymerisation does and doesn't occur during a potentiodynamic scan at 0.2 V/s (namely 1 s at 0.5 V, 2 s at 0 V, 2 s at −0.5 V and 4.5 s at 0 V per pulse cycle). The absorption spectrum of the resulting film is given in figure 4.12(a), along with the fitted spectrum yielding fitting parameters of 85 meV exciton bandwidth, 78 meV energetic disorder and 75 % amorphous content – very similar to the potentiodynamically deposited film and different to the potentiostatically deposited film. Hence varying charging levels don't seem to be responsible for the differences between potentiostatic and potentiodynamic electropolymerisation, leaving either the cycling between doped and de-doped states, or the kinetic effects on diffusion as explanations.

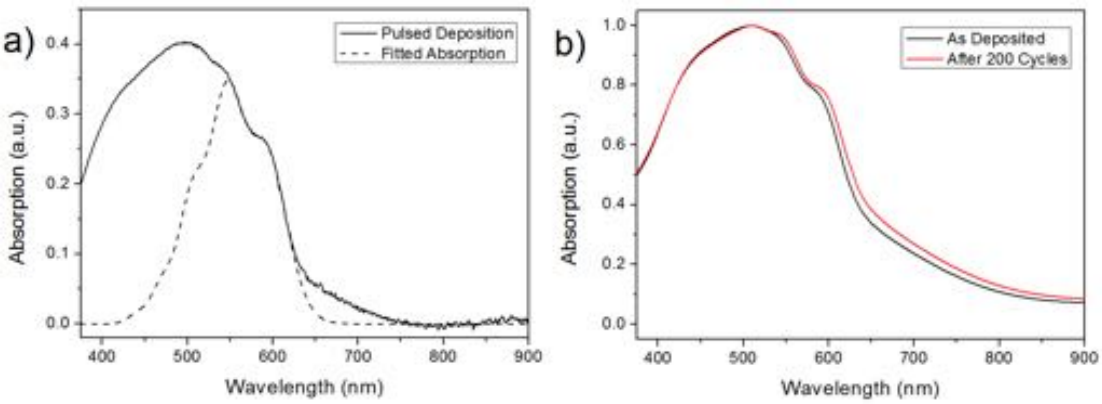

Figure 4.12: a) Experimental and fitted absorption spectrum for a PBT film deposited with pulsed electropolymerisation between −0.5 V and 0.5 V. b) The normalised absorption spectra of a PBT film electropolymerised potentiostatically at 0.35 V, before and after cycling through 200 doping and de-doping cycles. The 0-0 vibronic peak is slightly more prominent after annealing.

Electrochemically cycling conjugated polymers between their doped and de-doped states involves the insertion of counter-ions into and out of the polymer matrix [223]. With bulky counter-ions, reversing the charge can sometimes lead to further incorporation of oppositely-charged ions rather than removal of the bulky ions. In any case, it is hypothesised that doping and de-doping events involve considerable re-organisation within the polymer structure [165,178]. It is possible that this could distort molecular ordering in the film, or provide mobility for the film to adopt a more ordered morphology in a similar fashion to thermal and solvent annealing. In order to explore this further, PBT films were electropolymerised potentiostatically and then cycled multiple times between doping states; low potentiostatic potentials were used to avoid permanent disordering through cross-linking. If some sort of annealing process were induced by the doping cycling, the ordering would be expected to improve after this cycling. Figure 4.12(b) shows the absorption spectra of a PBT film before and after 200 doping/de-doping cycles. The exciton bandwidth decreases from 63 meV to 55 meV after such cycling. It should be noted that conjugation could increase after 'doping annealing' as a result of electrically-induced coupling reactions rather than morphological rearrangement [175, 188]. In either case, the effect does not seem to be large enough to explain the difference observed between potentiostatic and potentiodynamic electropolymerisation. Additionally, if such cycling annealing were a dominant effect, the inverse relationship between W and V would be expected for potentiodynamically electropolymerised films, where more cycles are required at lower voltages to yield films of equivalent thickness.

This evidence suggests that it is predominantly kinetic effects that lead to the different variation in conjugation with deposition potential observed for potentiostatic and potentiodynamic electropolymerisation. Periodic gaps in polymerisation during potentiodynamic electropolymerisation should enhance diffusion of non-equilibrium species, reducing the concentration of oligomers and protons near the electrode. Since short oligomers are likely to diffuse faster than longer oligomers, it could be that this enhanced diffusion favours deposition of long oligomers over shorter ones. However, while this may explain the longer conjugation obtained with potentiodynamic deposition, it doesn't explain the dependency of W on V. Indeed, higher potentials would still be expected to reduce conjugation since both the polymerisation rate and time spent polymerising per cycle increase with potential, which should raise the concentration of short oligomers at the electrode [224]. Instead, it could be that potentiodynamic deposition reduces the proton concentration during polymerisation. Buffered electrodeposition solutions have previously demonstrated impaired conductivity beneath a certain pH, which was speculated to result from hydrogenated monomer units disrupting conjugation [190]. If potentiodynamic electropolymerisation leads to proton concentrations beneath this limit, this could cause the difference in observed relationships between W and V for the two techniques. The initial improvement in conjugation with higher potentials could then be explained by higher reactivities yielding longer oligomers (before cross-linking starts dominating), free of hydrogenation problems induced by the low pH generated during potentiostatic electropolymerisation.

If the proton concentration is responsible for the different behaviours observed for potentiostatic and potentiodynamic electropolymerisation, and it is the enhanced proton diffusion during potentiodynamic deposition that mitigates the hydrogenation effect, then conjugation lengths might be expected to increase if diffusion speeds up. Since the diffusion coefficient of electroactive species in imidazolium-based ionic liquids has been found to significantly increase with temperature [225], this is an easy way to vary the diffusion. Films were thus electropolymerised potentiostatically at 0.35 V at different temperatures. Their morphological properties, as derived from their absorption spectra, are shown figure 4.13(a). As suggested, conjugation improves with increased deposition temperature. The opposite effect of temperature has been observed for organic solvents; it could be that the relative viscosity of ionic liquids makes diffusion of protons a more dominant problem than in organic solvents. The variation in morphological parameters with bithiophene concentration is also shown in figure 4.13(b), where conjugation is observed to shorten with concentration beneath 0.2 M. This is also in agreement with the hypothesis that proton concentration is an important factor in determining conjugation length, since lower concentrations would be expected to slow polymerisation (indeed the time taken to consume 15 mC decreases with concentration) and hence reduce the proton concentration during polymerisation.

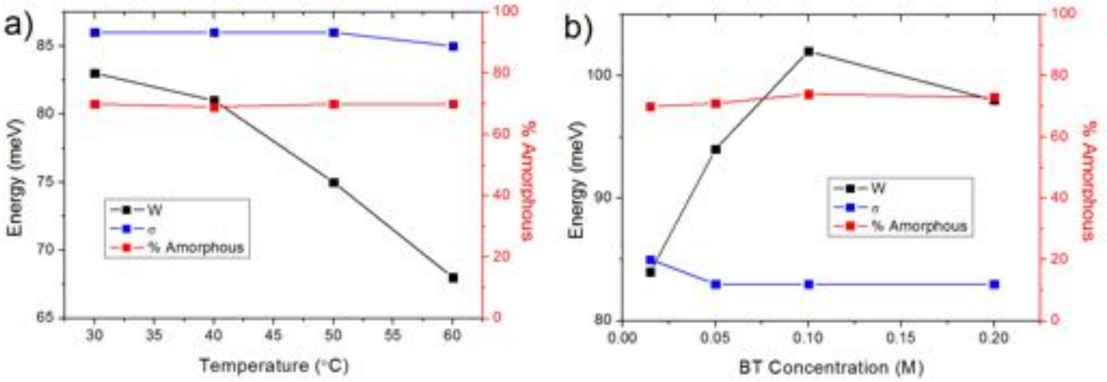

Figure 4.13: Fitting parameters derived from absorption spectra of PBT films electropolymerised potentiostatically from BmimTFSI with different (a) temperatures, and (b) precursor concentrations. Exciton bandwidths decrease with temperature and increase with concentration, up to 0.2 M.

4.4.5 Conclusions

Films of PBT and P3MT were successfully electropolymerised from BmimTFSI and EmimBF$_4$, although only deposition of PBT from BmimTFSI reliably yielded uniform film coverage across a range of experimental conditions.

Visible absorption spectra of these films indicated H-aggregate behaviour, suggesting suitability for analysis with Spano's model for polymer absorption. Using this model to derive exciton bandwidth and energetic disorder in the film during thermal annealing revealed behaviour matching previous reports of thermal annealing, lending further evidence for the applicability of this treatment.

The largest influence on effective conjugation was found to be the film thickness, with thicker films exhibiting significantly longer conjugation. GIWAXS measurements suggested a transition from edge-on oriented chains with short conjugation and little π-π stacking during initial film growth to isotropically-oriented crystallites with longer conjugation and more π-π stacking but much weaker coplanar stacking. This could result from an initial constraint on chain orientation induced by the substrate, which relaxes with increasing film thickness, as has been reported before. The preferential orientation might hinder initial crystallinity, which then improves as the constraint is relaxed.

Films deposited with potentiostatic and potentiodynamic electropolymerisation show different dependencies of exciton bandwidth on deposition potential. The complex interdependency between experimental conditions, electropolymerisation steps and film morphology makes it impossible to identify the exact cause of the observed differences from these results alone, but one explanation could be the effects of pH from protons released during coupling reactions. Optimal polymer conjugation is achieved with potentiodynamic electropolymerisation at intermediate potentials.

Chapter 5

Fabrication of Gyroid-Structured Organic Solar Cells

5.1 Introduction

Having investigated the electropolymerisation of polythiophenes on untemplated substrates, the next step was to produce gyroid-structured polythiophene films and develop a fabrication route to gyroid-structured solar cells. Building upon previous work by Dr Maik Scherer [106, 226], a 'passive' diblock copolymer was used to generate the initial gyroid morphology, which in turn was used as a template for electropolymerisation of gyroid-structured polythiophene. Further fabrication steps led to gyroid-structured, polymer:fullerene heterojunctions.

5.2 Templated Electropolymerisation

A schematic overview of the fabrication process used to obtain gyroid-structured polythiophenes is given in figure 5.1. The gyroid structure was initially realised *via* guided microphase separation in a melt of the block copolymer poly(4-fluorostyrene-*r*-styrene)-*b*-poly($_{\text{D,L}}$-lactide) (PFS-*b*-PLA). The PLA component was then selectively etched to leave the PFS phase as a template for electropolymerisation of the desired polythiophene. Following electropolymerisation, the PFS template was itself selectively dissolved to leave a free-standing polythiophene scaffold with the desired structure. Characterisation of the various steps in this process was performed principally using SEM.

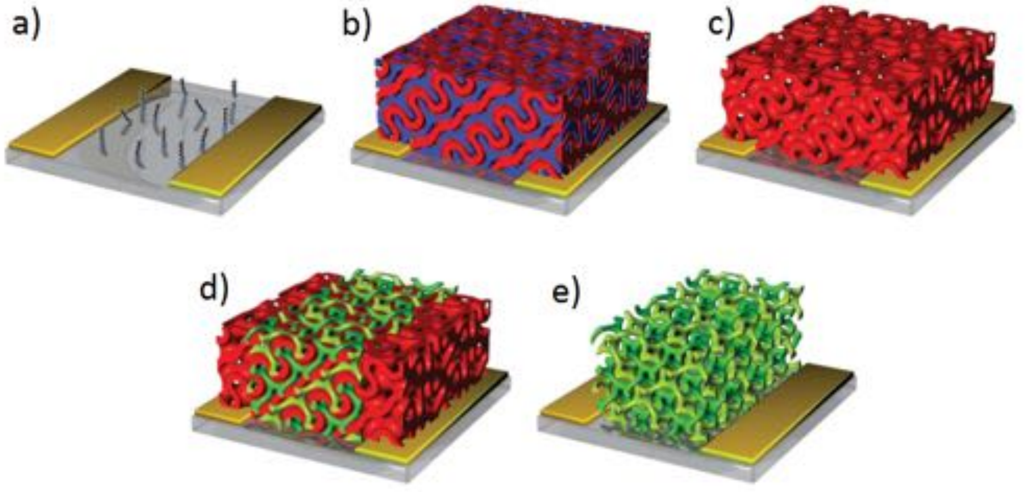

Figure 5.1: A pictorial summary of the fabrication process used to obtain polythiophene gyroids. First, the substrate is cleaned and silanised to provide the surface energy required to seed the gyroid structure (a). Next, the PFS-*b*-PLA blend is spin-coated onto the substrate and annealed to induce the gyroid morphology (b). Subsequently the PLA is selectively etched to leave the PFS template (c). Electropolymerisation is used to replicate the inverse structure of the template with polythiophene (d). Finally, the PFS template is selectively dissolved to yield the free-standing, gyroid-structured polythiophene as desired (e). This figure appears courtesy of Dr Maik Scherer, and is adapted from previously published work [106].

5.2.1 Fabricating the Gyroid Template

The development and optimisation of the techniques described below for fabricating the gyroid template, and the synthesis of the copolymers used to do so, are the work of Dr. Maik Scherer [95, 106, 226]. The protocols used in these publications were used without modification.

The gyroid templates were grown on piranha-etched FTO-coated glass as described in chapter 4. The piranha treatment cleans all organic contaminants from the FTO surface, but also leaves it with a high surface energy. In general, this is unsuitable for growth of the template because it favours contact of the

PLA phase with the substrate surface rather than PFS, seeding lamellar rather than gyroid structure during the microphase separation. Hence the substrate was coated with a partial octyltrichlorosilane monolayer to reduce the surface energy. The cleaned substrates were washed for 10 seconds in a solution of 10 µl octyltrichlorosilane (OTS) in 10 ml anhydrous cyclohexane, after which the water contact angle on the substrate was $59 \pm 5°$. However, the silanisation step was not necessary if small ($\lesssim 1\text{mm}^2$) areas of FTO were defined with SU-8 photoresist, since SU-8 deposition and removal during the photolithographic processing steps seems to appropriately modify the FTO surface.

Having silanised the substrates, blends of the block copolymer PFS-*b*-PLA dissolved in toluene at 10 mg/ml were spin-coated at 350 rpm for 45 seconds. The films were then placed in an oven and heated according to a well-defined heating program (from 90 °C to 150 °C at 150 °C/hour, then from 150 °C to 173 °C at 180 °C/hour, and finally held at 173 °C for 20 minutes). The samples were then quickly removed from the oven and placed onto a large metal plate to cool them quickly and 'freeze' the acquired structure into place.

The cooled, self-assembled films were then submerged in 0.1 M sodium hydroxide in 1:1 (vol) methanol:de-ionised water for between 2-4 hours to selectively etch the PLA phase. After this, the samples were briefly transferred to pure methanol for 5 minutes to wash out the etched PLA. This treatment left the desired PFS template for electropolymerisation, as shown by SEM images such as those in figures 5.2 and 5.3. The specific gyroid structure formed has 37.9% PLA content, unit cell size 41.5 ± 1 nm, strut diameter of 11.0 ± 0.3 nm and a surface area to volume ratio of 161.4 m^{-1} [110].

5.2.2 Assessing Template Replication

The same electrochemical setup was used for templated electropolymerisation as for untemplated electropolymerisation. For initial investigation of templated deposition, 0.05 M 2,2′-bithiophene in BmimTFSI was used at room temperature. Potentiostatic and potentiodynamic electropolymerisation yielded visible film deposition similar to that observed with un-templated deposition. By eye, reasonable film coverage was generally achieved, although deposition over large areas ($\gtrsim 1\,\text{cm}^2$) sometimes displayed apparent variation in thickness.

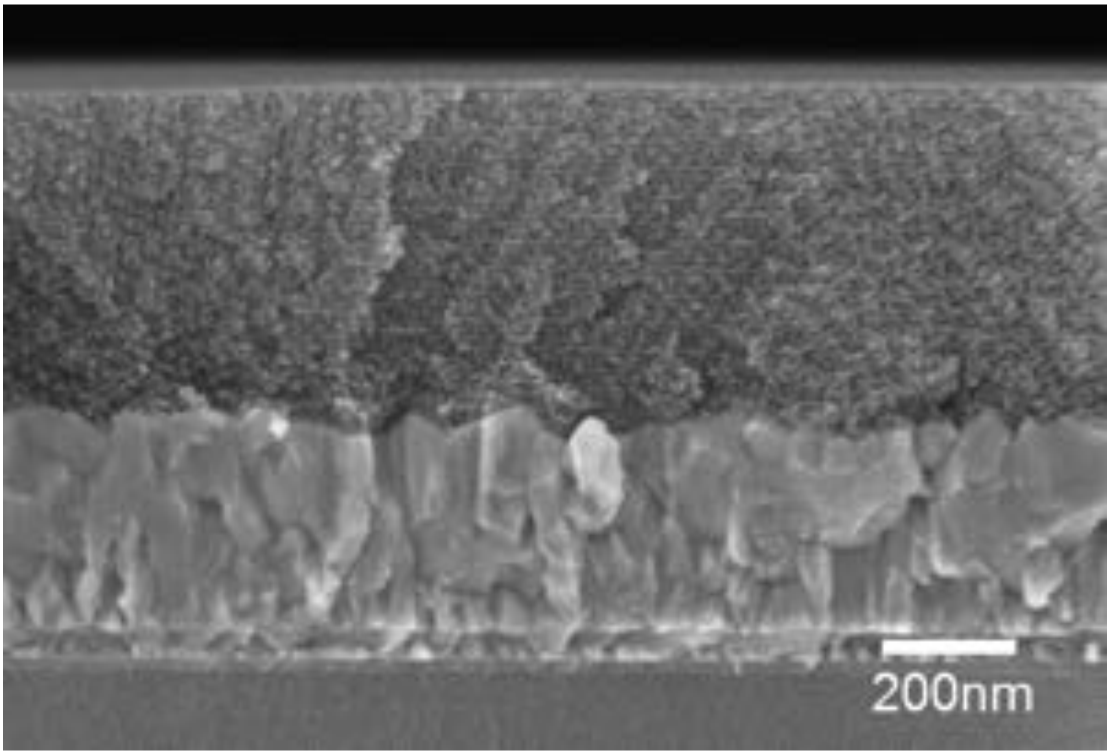

Figure 5.2: SEM cross-sectional image of a fractured polystyrene gyroid template, on top of an FTO-coated glass substrate. This image shows the regular porous gyroid structure throughout the whole film of ∼ 500 nm thickness; thicknesses of a few hundred nanometres to several microns are easily obtainable with different spin-coating conditions.

In order to evaluate template replication after electropolymerisation, the ionic liquid had to be washed from the film and the template selectively removed ready for SEM analysis. Previous work with the same PFS templates for templated electrodeposition of inorganic materials used a 2:1 (vol) mix of diethyl ether: hexane to selectively dissolve the template [95] so this was employed here too. To find a suitable solvent for washing out the ionic liquid, a simple solvent search was conducted in which three ionic liquids were mixed with a variety of solvents and their basic miscibility noted. Solvents that appeared to be miscible with the ionic liquids were re-checked after leaving the mixture to stand to ensure the apparent miscibility wasn't in fact a very fine emulsion. The results of this solvent search are presented in table 5.1.

Initially, 2,2,2-trifluoroethanol (TFE) had not been considered, so acetonitrile

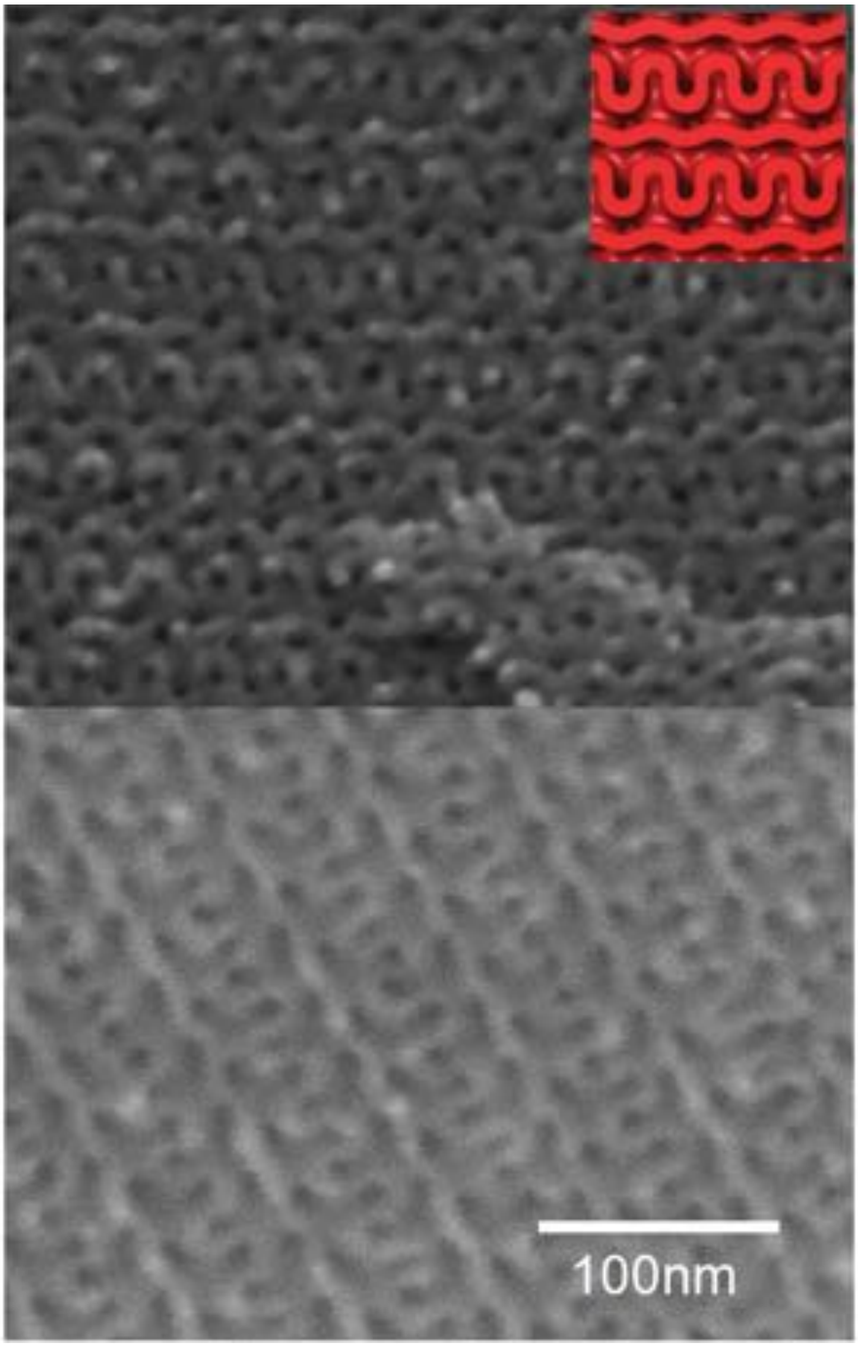

Figure 5.3: High magnification SEM image of the gyroid structure in the polystyrene template, with theoretical simulation of the (211) gyroid plane (inset, reproduced from [106]). Despite the poor resolution, the structure clearly matches the simulated structure, with $\sim 40\,\mathrm{nm}$ period as expected.

Solvent	Ionic Liquid		
	BmimTFSI	$EmimBF_4$	$EmimEtSO_4$
Acetone		✓	
Acetonitrile	✓	✓	
Benzyl Alcohol		✓	
Decyl Alcohol	✗	✗	
Dichloromethane		✓	
Diethyl Ether	✗	✗	✗
Dimethyl Sulphoxide		✓	
Ethanol	✓	✗	$\sim$
Hexane		✗	
1-Hexanol	✗	✗	$\sim$
Methanol	$\sim$		$\sim$
Pentanol	✗	✗	
Propan-2-ol	✗	✗	
2,2,2-Trifluoroethanol	✓	✓	✓
Water	✗	$\sim$	
Xylene	✗		

Table 5.1: A summary of solvent miscibilites with ionic liquids, ticks (✓) indicating miscibility, crosses (✗) indicating immiscibility and tildes ($\sim$) indicating limited miscibility or uncertainty. Not all mixtures were tried, those that weren't have been left blank.

and ethanol were tried following deposition from BmimTFSI, but SEM analysis revealed that these damaged the PT gyroid (see figure 5.4(a)). The first solution to this problem was a solvent exchange of the BmimTFSI for $EmimBF_4$ after electropolymerisation, as this could be washed out with water, in which the gyroid was more stable. Although PBT gyroid structure was observed after this treatment, indicating the success of templated electropolymerisation, the washing step was very temperamental and generally cracked the films (see figure 5.4(b)). This led to a wider solvent search and ultimately the discovery that TFE worked much more reliably. Upon drying, the high surface tension of the TFE cracked the films but this problem was again solved *via* solvent exchange, in which the TFE was washed out with diethyl ether:hexane before being allowed to dry. For this, the films were initially submerged in 2:1 diethyl ether:hexane, before extra hexane was added to bring the ratio to around 1:5 at which point the film was removed and gently dried under a nitrogen stream. An example of the PBT gyroids obtained with the optimised process is shown in figure 5.5.

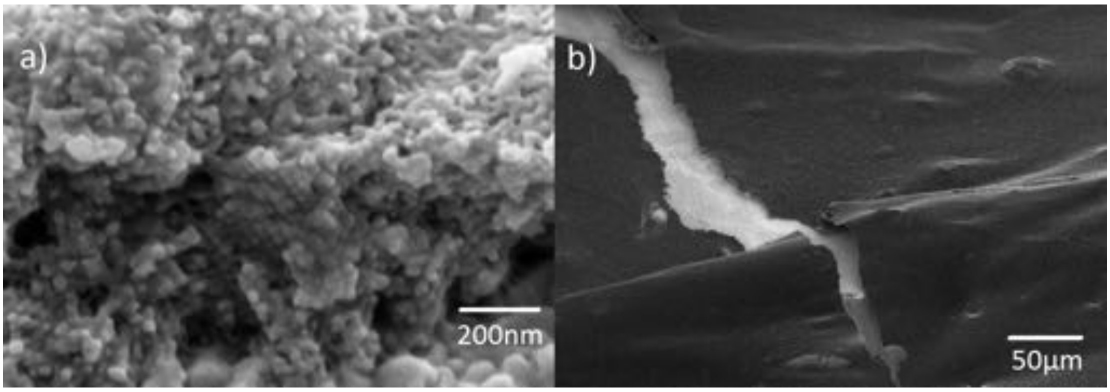

Figure 5.4: Figure (a) shows a PBT film following treatment with acetonitrile that has destroyed the gyroid structure present immediately after electropolymerisation. Figure (b) shows a P3MT film that has cracked following treatment with water.

5.2.3 Large-Scale Film Morphology

As shown in the representative SEM images, templated electropolymerisation followed by washing with TFE and submersion in diethyl ether: hexane yields excellent PBT replication of the gyroid structure. However, the large-scale morphology of the film is also important for use in devices. Film thickness can be influenced by controlling the charge transferred during deposition, although the multi-step process of polymerisation means that there is not a simple linear relationship between the amount of film polymerised and the total charge transferred. Soluble oligomers may diffuse away from the electrode surface before coupling to the polymer film, and the ‘efficiency’ of oxidation is sensitive to the electropolymerisation conditions. Nevertheless, holding the experimental conditions as constant as possible allows reasonable control of film thickness.

For optimal use in solar cell devices, the gyroid film should have complete coverage over the substrate, to avoid pinholes in the film through which leakage current can flow. The film should also preferably be as smooth as possible, so that the film thickness is roughly uniform over the whole device. This is in particular important for measuring space-charge limited currents in thin films to deduce mobility. All films deposited without gyroid templating were found to have a

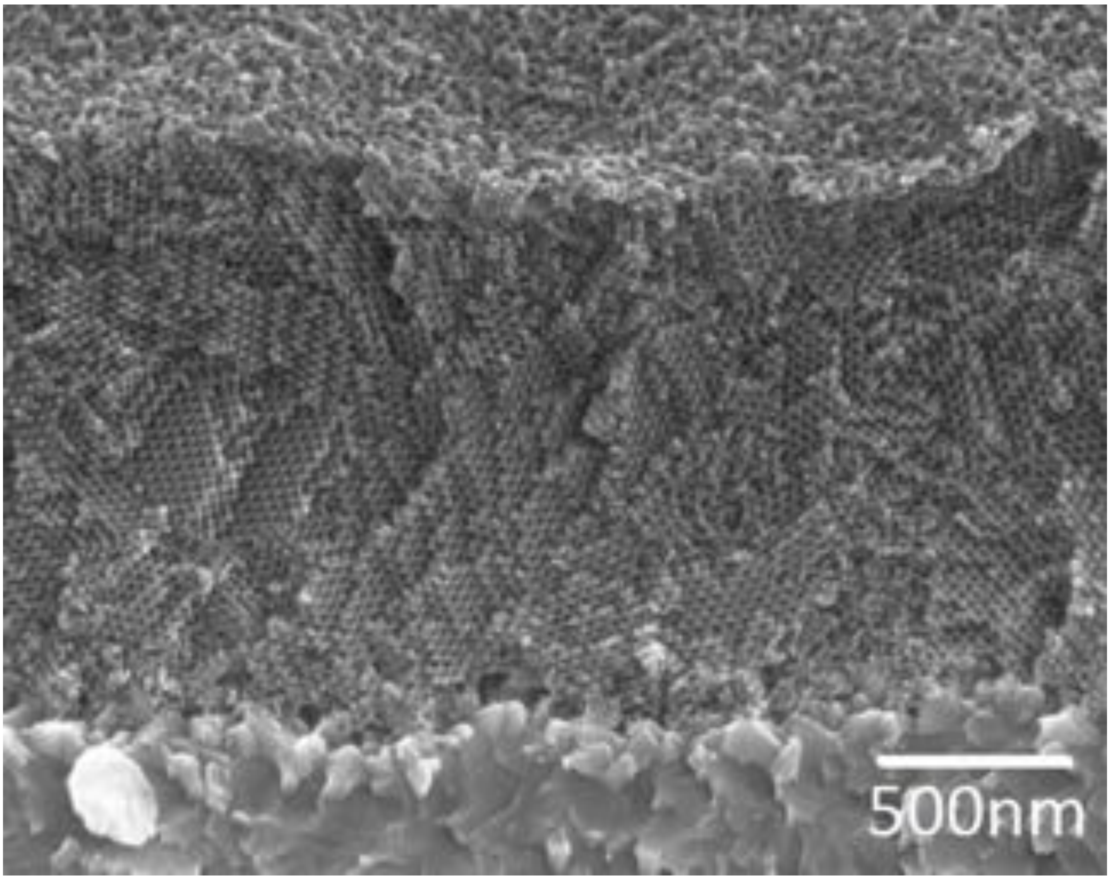

Figure 5.5: PBT gyroid film washed with TFE followed by submersion in a diethyl ether:hexane mixture. Fracturing the film to image the cross-section exerts stress on the film and explains the ‘rugged’ nature of the cross-section.

broadly ‘globular’ morphology (figure 5.6(a)) characteristic of three-dimensional nucleation and growth [211, 227, 228]. This is common for electropolymerised films, including when deposited from ionic liquids [210], however it does not matched the idealised compact, uniform film morphology for devices. It was hoped that the presence of the gyroid template would beneficially improve the large-scale film morphology in this regard.

A variety of electropolymerisation parameters such as monomer concentration, deposition potential, scan rate and temperature were varied but no clear effect was apparent from the qualitative SEM analysis conducted. This task was further complicated by the known progression in morphology as deposition

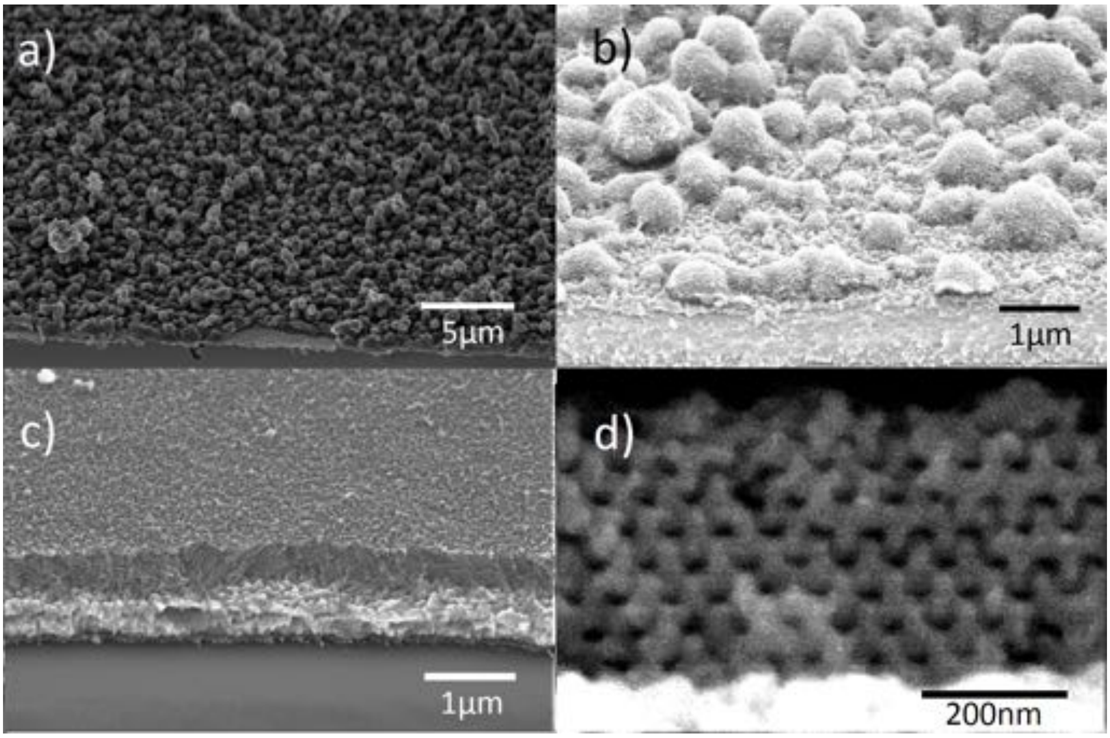

Figure 5.6: Representative SEM images of the different large-scale PBT morphologies obtained. Figure (a) shows typical 3D ‘nucleation and growth’ morphologies obtained with un-templated electropolymerisation. Potentiostatic electropolymerisation with gyroid templating still leads to ‘globular’ morphologies, but with far larger ‘grains’, (b). Figures (c) and (d) show the desired flat, compact film morphologies (incorporating gyroid structure) obtained using templated potentiodynamic electropolymerisation, including for films of thicknesses relevant to solar cell applications (d).

proceeds [171, 210], and the difficulty of precisely controlling film thickness (especially with non-compact morphologies). However, film morphology was consistently and clearly dependent upon the electropolymerisation technique employed. Potentiostatic deposition yielded films with much larger hemi-spherical ‘grains’ than for un-templated deposition, but still very rough for device applications (figure 5.6(b)). By contrast, potentiodynamic electropolymerisation gave rise to flat, compact films incorporating the gyroid structure (figures 5.6 (c) and (d)). Specificly, these films have been deposited with cyclic voltammetry, *i.e.* sweeping between negative and positive potentials and back again at a constant rate.

This is known to promote different nucleation spots on each cycle [177], which could explain the smoother morphology. Brief experimentation with pulsed electropolymerisation seemed to suggest the deposition of flat films too.

The possibility of spin-coating template films of the desired thickness, intentionally depositing polymer films through and beyond the template and then peeling off the overgrowth was explored as a possibility for obtaining flat films of known thickness regardless of electropolymerisation technique. Although investigation of this route was not exhausted, the highly non-uniform growth of potentiostatically electropolymerised films required very thick overgrowth to ensure filling the template fully; peeling such thick films always removed the templated part as well as the overgrowth. Overall, it seems that potentiodynamic electropolymerisation is necessary for the fabrication of devices comparable to standard spin-coated bulk heterojunction morphologies.

5.2.4 Molecular Ordering in Gyroid-Structured Polythiophenes

The gyroid-structured PBT films were now characterised with the same techniques as used for non-templated films in chapter 4. Despite the importance of potentiodynamic electropolymerisation for suitable large-scale film morphology, potentiostatically electropolymerised films can still give information about the templated electropolymerisation process and so were characterised too. The variation in morphology with film thickness was again investigated by measuring the absorption of films electropolymerised potentiostatically at 0.35 V for varying times, as shown in figure 5.7.

Two important results are clear from figure 5.7. Firstly, there is no systematic variation in any of the morphology parameters with film thickness, which instead stay roughly constant. Secondly, the exciton bandwidth values are all substantially higher for gyroid-structured films than for untemplated films ($\sim 160\,\mathrm{meV}$ compared to $\lesssim 100\,\mathrm{meV}$ for similar potentials and thicknesses). Both of these results might be expected given the explanation for the evolution in film morphology with thickness suggested in chapter 4. There, constraints on polymer orientation induced by the substrate were speculated to reduce the polymer's ability to form large crystallites with long conjugation and good π-π stacking.

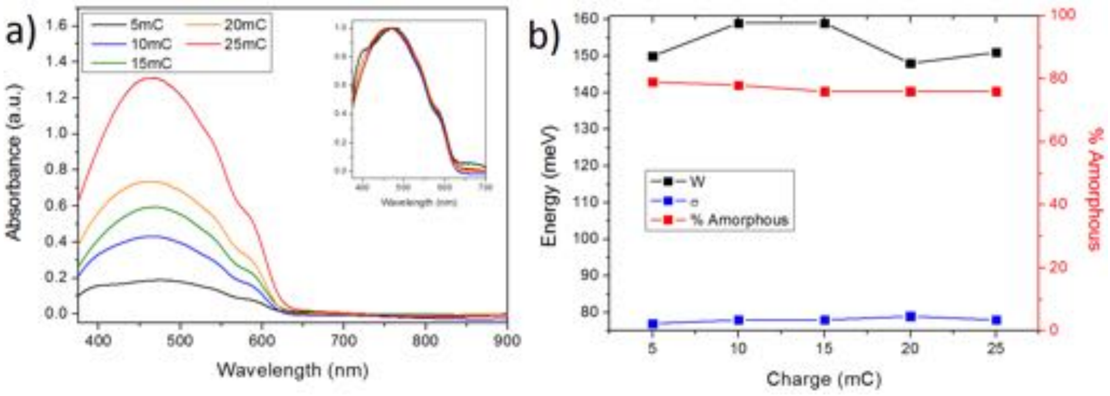

Figure 5.7: Visible absorption spectra of gyroid-structured PBT films electropolymerised at 0.35 V for different durations (inset shows specta normalised to peak absorption). Unlike for untemplated films, there appears to be no systematic variation in conjugation with film thickness.

The presence of the gyroid-structured template will clearly constrain the mesocale morphology significantly, so inferior molecular packing is not un-anticipated. An alternative explanation could be that the template hinders diffusion in the electrodeposition region, which could lead to low pH and poor conjugation induced by hydrogenation, as speculated with potentiostatic electropolymerisation at high potentials. In either case, the need to compare gyroid-structured films of the same thickness is not as great as for untemplated films.

The absorption spectra of PBT films deposited potentiostatically around gyroid templates at different potentials are shown in figure 5.8. The apparent negative absorption at long wavelengths again corresponds to improved transmission compared to a blank FTO reference. Other than the initial increase in exciton bandwidth resulting from deposition at 0.40 V compared to 0.35 V, the conjugation does not seem to vary systematically with electropolymerisation potential, and is substantially higher than observed in untemplated samples. Instead, it averages around 210 meV, corresponding to 10 thiophene units, or 4 nm. This is substantially beneath the 11 nm strut size of the PFS template voids, suggesting that the reduced crystallinity is not directly caused by the template restricting crystallite dimensions. The lower exciton bandwidth observed for the film electropolymerised at 0.35 V is probably a real feature, given that it matches better the bandwidths measured for potentiostatically deposited films in figure 5.7. The slight differences remaining between these films electropolymerised at 0.35 V probably arises from slight differences in monomer concentration and temperatures, given that the films were produced in different batches from different solutions (although both nominally 0.05 M and room temperature). The improved conjugation at the lowest electropolymerisation potential, which will correspond to the slowest rate of electropolymerisation, suggests that problems with diffusion in the presence of the template may be contributing to the inferior conjugation compared to untemplated films.

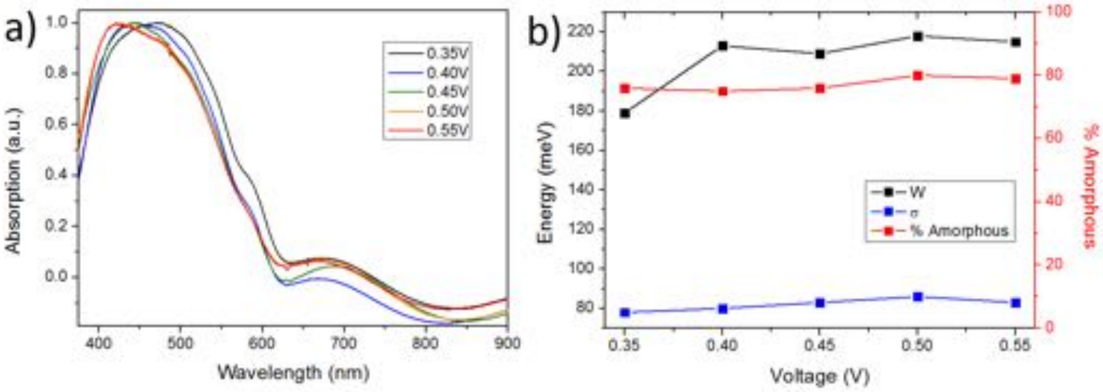

Figure 5.8: a) Absorption spectra and b) fitting parameters for PBT film electropolymerised potentiostatically around gyroid templates. The vibronic features are not as clearly resolved as for untemplated electropolymerisation, and the exciton bandwith is, in particular, very much larger than for untemplated films, indicating less molecular ordering.

Despite large differences in exciton bandwidth for untemplated and gyroid-templated electropolymerisation, the energetic disorder is similar, growing here from 78 meV to 86 meV, compared to 84 − 89 meV for untemplated films. The fact that there are very few chains with long conjugation probably results in the slight decrease in σ. The amorphous content is marginally higher in the gyroid-structured films too, averaging 76 % compared to 73 %, corresponding simply to the inferior crystallinity. Inferior crystallinity is perhaps also the reason for apparently less scattering, allowing the transmission at long wavelengths to be improved relative to blank FTO and untemplated films.

The absorption analysis process was repeated for potentiodynamically electropolymerised films, again deposited at 0.2 V/s between −0.5 V and an upper potential as indicated in figure 5.9. Electropolymerisation up to 0.35 V yields films with slightly inferior conjugation and energetic disorder compared to higher potentials, possibly due to the very large number of cycles required to deposit comparable film thicknesses. Other than this, the influence of potential appears weak, with exciton bandwidths varying between 159 meV and 170 meV and energetic disorder increasing from 77 meV to 79 meV. These values of W are lower than for potentiostatically electropolymerised gyroid-strucured films, potentially due to improved diffusion of protons avoiding extreme pH again. The amorphous content is essentially the same for potentiostatic and potentiodynamic electropolymerisation, again averaging 76 %. Combined with the requirement for smooth polymer films, it is clear that potentiodynamic electropolymerisation is the best technique for gyroidally-structured device fabrication.

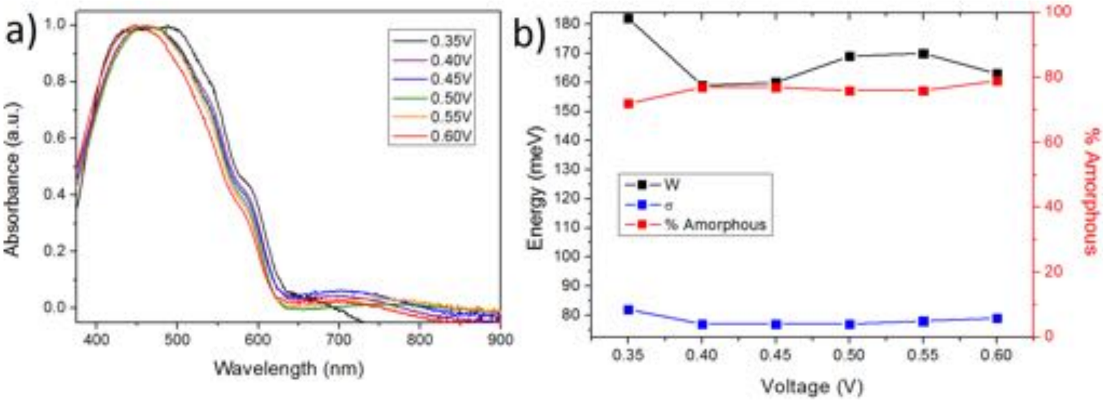

Figure 5.9: a) Absorption spectra and b) fitting parameters for PBT films electropolymerised potentiodynamically around gyroid templates. The voltage displayed in figure (b) indicates the maximum potential of the potentiodynamic scans. There appears to be no systematic variation with potential, with the bandwidth consistently far greater than for untemplated films.

Thermal and solvent annealing are two well-known, widely-used techniques for improving molecular ordering in spin-coated polymer solar cells [31, 69, 144]. As demonstrated in chapter 4, thermally annealing electropolymerised PBT films decreases both the exciton bandwidth and the energetic disorder factor. Hence both techniques were applied to gyroid-structured PBT films to see if molecular ordering could be improved post-electrodeposition, without damaging the gyroid structure. Gyroid-structured PBT films were annealed with the PFS template still in place, and subsequently imaged with the SEM after dissolving the template. The thermal annealing was conducted at 160 °C for 30 minutes, and the solvent annealing was conducted in a hexanethiol or 2-chlorophenol atmosphere whose partial pressure was gradually decreased and replaced with air. Unfortunately, both techniques clearly destroyed the gyroid structure in the PBT films (figure 5.10), so further experimentation with these techniques was abandoned. The destruction of the gyroid structure by such annealing protocols is unsurprising, given that they work by allowing the polymer chains to re-assemble into energetically favourable configurations.

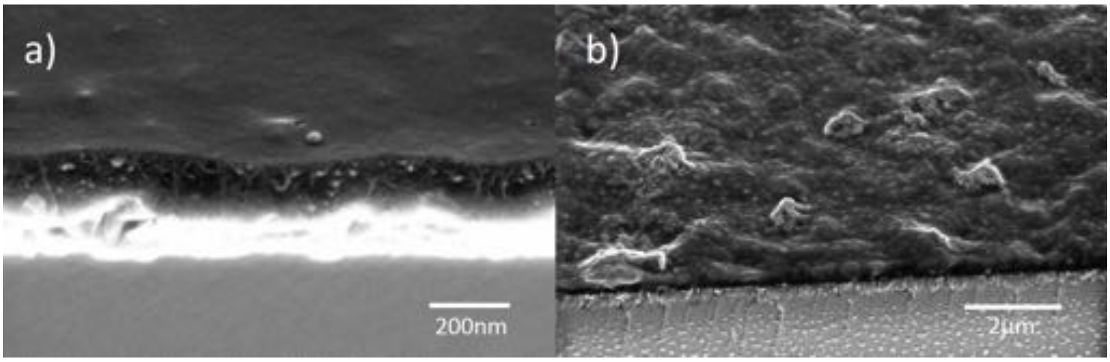

Figure 5.10: SEM images of gyroid-structured PBT films after a) thermal annealing at 160 °C and b) solvent annealing in a 2-chlorophenol atmosphere. The gyroid structure has been clearly destroyed by both annealing techniques.

Overall, it is clear that gyroid-structured films should be electropolymerised potentiodynamically for use in solar cells. The influence of potential on morphology is found to be weak, so maximum voltages of around 0.50 V can be used to fabricate films without very long deposition times. However, even with optimised electropolymerisation conditions, the presence of the gyroid template disrupts the molecular ordering of the PBT considerably. Thermal and solvent annealing are unable to improve ordering without destroying the gyroid structure, so the films must be used as-deposited. Following optimisation of PBT gyroid fabrication, a procedure for back-filling the gyroid pores with an acceptor material had to be established.

5.3 Backfilling Polythiophene Gyroid Structures

Having established optimal procedures for fabrication of gyroid-structured PBT films, the next step was to investigate methods for backfilling the gyroid voids with an electron acceptor material to complete the active layer of a photovoltaic device. Being the standard acceptor material used in combination with polythiophenes, it was intially assumed that PCBM would be the acceptor material, and that some sort of solution-processing technique would be used to backfill the PBT gyroids. Hence an 'orthogonal' solvent sytem was needed which would dissolve PCBM but not affect the PBT gyroid. Given its widespread use, the solubility of PCBM has been relatively well-characterised, especially given its importance to the morphology of spin-coated bulk heterojunctions [229]. Thus a systematic solvent search could be conducted, initially guided by Hansen solubility paramaterisation [230].

Hansen Solubility Parameters

Hansen categorised the intermolecular forces of a solute or solvent into three components, namely atomic dispersion forces, molecular permanent dipole–permanent dipole forces and molecular hydrogen bonding [230]. Following numerical and empirical efforts, many chemicals have now been assigned values for the strengths of these components and hence assigned a position in 'Hansen space', using the three interaction parameters (δ_D, δ_P and δ_H respectively) as co-ordinates. To determine solubility or miscibility from these Hansen solubility parameters, the formalism assumes that 'like seeks like', and that if two materials are located sufficiently close together in Hansen space, they will be miscible. Each solute has a sphere of radius R_0 (determined for each solute separately) around its Hansen position such that it should dissolve in any solvent within the sphere. The distance between the solute and solvent in Hansen space is scaled to give a value R_a, and solubility is predicted if the ratio R_a/R_0 is less than or equal to one [230,231].

Following this formalism, potential orthogonal solvents were identified by finding solvents simultaneously nearest to PCBM and furthest from polythiophene in Hansen space. Solubility parameters could only be found for P3HT [229], but since the alkyl groups are added to improve solubility, the results should be valid for PBT too. The solvents included in the initial solvent search were those identified by Machui *et al.* as being orthogonal between P3HT and PCBM, according to a simple soluble/insoluble test by eye [229], plus a wide database of solvents published by Hansen [230]. Their Hansen solubility parameters are given in table 5.2, along with the weighted relative energy difference between their positions in Hansen space and those of P3HT and PCBM. The difference between these relative energy differences then indicates which solvents should be the 'most' orthogonal.

Guided by these Hansen solubility parameters, the most promising solvents were tested for compatibility with the polythiophene gyroid, namely acetonitrile, carbon disulphide, 2-chlorophenol, dioxane, n-methyl pyrrolidone, quinoline and tetrahydrafuran. To test compatibility, the polythiophene gyroid was imaged under the SEM after washing out the ionic liquid and selectively dissolving the PFS template. This established that a clear gyroid structure was initially present. The sample was then submerged in the solvent for 30 s, dried and replaced under the SEM; an indicative image is shown in figure 5.11.

Unfortunately, this SEM analysis clearly showed that all of these solvents degraded the gyroid structure, despite their predicted orthogonal solubility. It could be that even a minute degree of solubility reveals degradation in such a well-defined structure on such a small lengthscale, or it could be that the solvent induces swelling in the polymer which cannot be fully tolerated by the gyroid. Although the large surface area to volume ratio of nanoscale gyroids is desirable for exciton dissociation in organic solar cells, it makes these films very sensitive to solvent conditions.

Literature Search

Following the failure of Hansen solubility parameters to predict suitable orthogonal solvents, a literature search was conducted to find if any solvents had previously been used for a similar role with the same materials. Bilayer devices fabricated by spin-coating PCBM onto a pre-deposited P3HT layer had reported dichloromethane as dissolving PCBM without affecting P3HT [232]. Accordingly, dichloromethane was tested, but was found to still degrade the gyroid slightly. This is actually because although the P3HT is insoluble in dichloromethane, it swells substantially [233].

Having found no suitable solvent for back-filling PCBM, other acceptor ma-

Solvent	Solubility Parameters (MPa$^{1/2}$)			R_a/R_0		Δ
	δ_D	δ_P	δ_H	P3HT	PCBM	
Acetonitrile	15.3	18.0	6.1	5.28	2.37	2.91
Aniline	20.1	5.8	11.2	2.49	0.62	1.87
Benzaldehyde	19.4	7.4	5.3	1.02	0.64	0.39
Benzene	18.4	0.0	2.0	2.31	0.99	1.32
Benzyl Benzoate	20.0	5.1	5.2	1.11	0.36	0.76
Carbon Disulphide	20.5	0.0	0.6	3.01	1.00	2.02
3-Chloroaniline	20.2	7.3	9.8	2.22	0.62	1.60
2-Chlorophenol	19.0	5.5	13.9	3.21	1.00	2.20
2-Chlorotoluene	19.0	4.9	2.3	1.18	0.78	0.41
3-Chlorotoluene	18.9	3.9	2.9	1.07	0.70	0.37
Cyclohexanone	19.2	6.3	3.3	0.98	0.72	0.26
Diethyl Ether	14.5	2.9	5.1	3.09	1.60	1.49
Dioxane	19.0	1.8	7.4	1.56	0.44	1.12
Dodecane	16.1	0.0	0.0	3.30	1.57	1.73
Hexane	14.9	0.0	0.0	3.85	1.81	2.04
Limonene	17.2	1.8	4.3	1.66	0.96	0.69
α-Methyl Styrene	18.5	2.4	2.4	1.52	0.83	0.69
n-Methyl Pyrrolidone	18.0	12.3	7.2	2.71	1.34	1.38
Quinoline	20.5	5.6	5.7	1.49	0.34	1.15
Styrene	18.6	1.0	4.1	1.66	0.72	0.94
Tetrahydrofuran	15.5	7.2	7.6	2.48	1.40	1.08
Toluene	18.0	1.4	2.0	1.93	0.98	0.94
Trichlorobenzene	20.2	4.2	3.2	1.54	0.54	0.99
1,2-Xylene	17.8	1.0	3.1	1.86	0.94	0.92

Table 5.2: Hansen solubility parameters and weighted distances of each solvent from P3HT and PCBM in Hansen space. The final column gives the difference between the values of R_a/R_0 for P3HT and PCBM, so that the biggest value indicates the prediction for the 'most' orthogonal solvent. All data taken from Machui *et al.* [229] or Hansen [230].

terials were considered. Only three solvents had been established to be perfectly compatible with the polythiophene gyroid: TFE, hexane and diethyl ether. Further experimentation revealed that all alkanes tested were compatible with the gyroid structure, perhaps as a result of their completely non-polar nature. Hence solubility testing of potential acceptors was constrained to TFE, diethyl ether and alkanes. Beyond the ubiquitous use of PCBM, almost all other acceptors

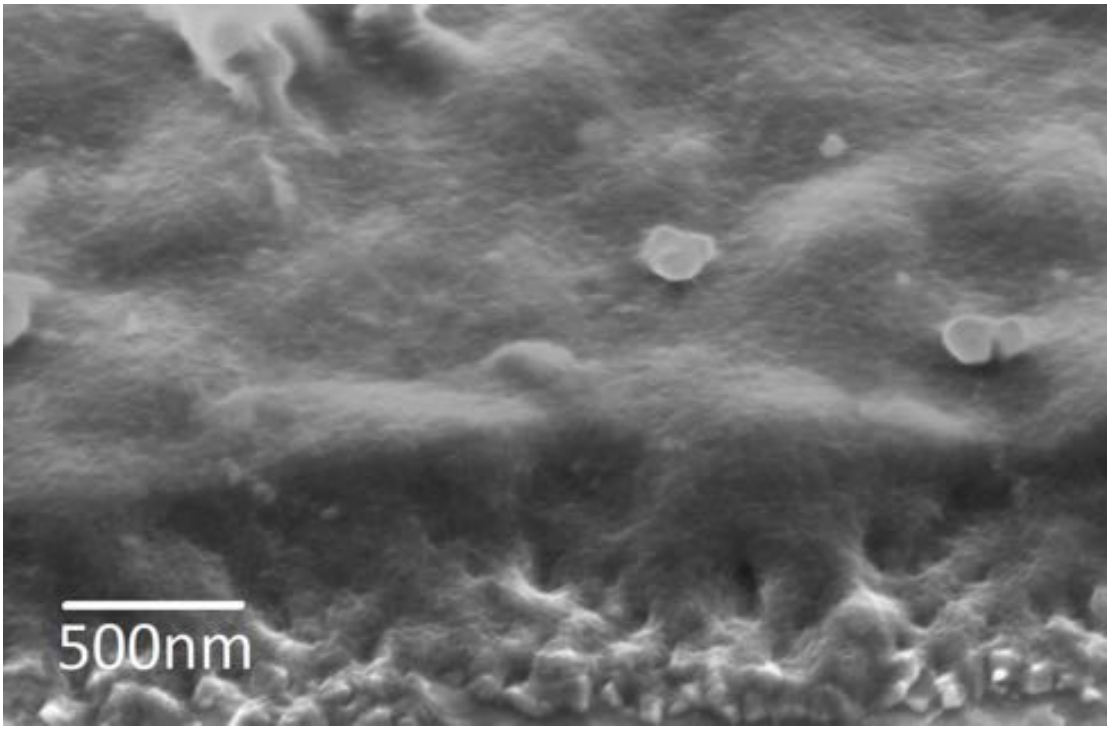

Figure 5.11: Gyroid structure after treatment with aniline, showing clear degradation of the structure. Similar effects were observed after treatment with 2-chlorophenol, acetonitrile, quinoline, chloromethyl methyl ether, dioxane, tetrahydrofuran, dichloromethane, n-methyl pyrrolidone, carbon disulfide and dodecane.

used in conjuction with polythiophene are other fullerene derivatives. Polyhydroxy fullerene had been reported to dissolve in basic ($\mathrm{pH} \geqslant 8$) water and used to back-fill P3HT lamellae [74], so this was tested but found to be insoluble. NaOH dissolved in TFE produced a basic solution but still didn't dissolve the hydroxy fullerene, even up to pH 10. In any case, the authors of the reported work had not been able to use this method to fabricate a working solar cell; they speculated that the basicity of the solution doped the polythiophene [78]. Non-fullerene acceptor materials such as the perylene derivative, N,N-Dioctyl-3,4,9,10-perylenedicarboximide (PTCDI-C8) were also tried, but found to be insoluble too.

More recently-developed fullerene derivatives include indene-based derivatives, namely indene-C_{60} mono-, bis- and tris-adducts (ICMA, ICBA and ICTA respectively) [234]. None of these were soluble in TFE, but ICBA appeared to dissolve at small concentrations in diethyl ether and hexane. Hence ICBA was spin-cast onto the gyroid films from diethyl ether, hexane and a 50:50 (vol) mix of the two. Unfortunately, SEM images of the resulting films showed large clumps of ICBA stuck on top of the gyroid (see figure 5.12). Presumably it had aggregated in solution to form aggregates too large to infiltrate the gyroid pores; passing the solution through a 100 nm filter directly prior to spin-coating did not solve the problem.

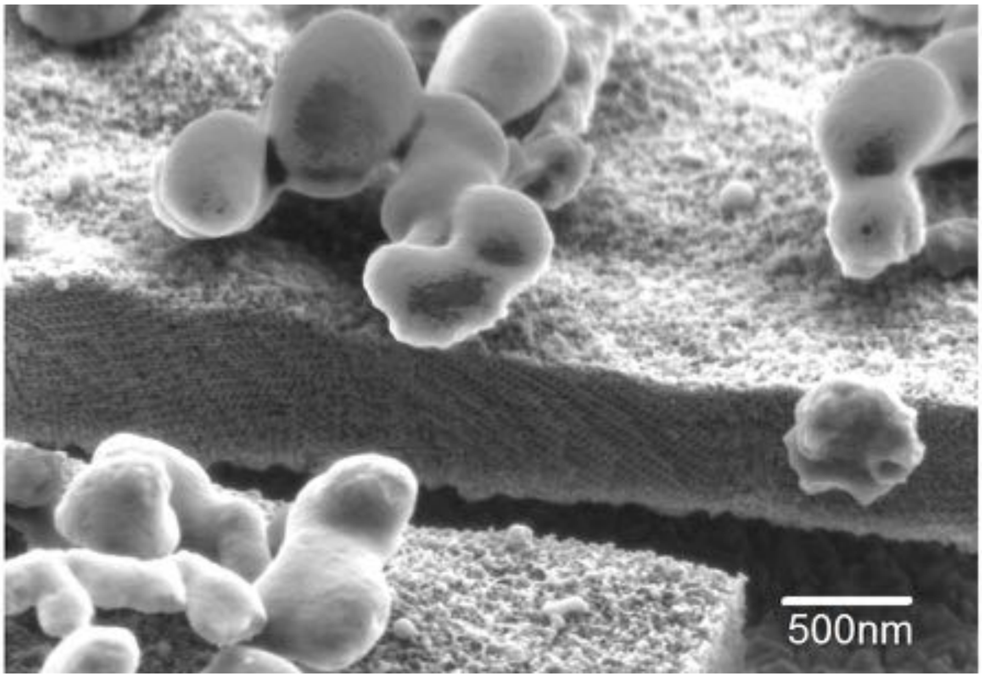

Figure 5.12: Despite appearing to dissolve in hexane and diethyl ether by eye, SEM images of ICBA after drop- and spin-casting indicate that actually, ICBA aggregates in these solvents. These aggregates are too large for infiltration into the gyroid structure.

Motivated by their use as solvent additives to drive fullerene aggregation through selective solubility, alkanethiols were now tried. Promisingly, Lee *et al.* have reported using alkanedithiols to selectively dissolve PCBM after spin-coating P3HT:PCBM blends for morphology analysis with AFM [70]. Ethanedithiol and dodecanethiol were found to dissolve ICBA but degrade the gyroid structure. However, alkanethiols were found to be able to dissolve reasonable concentrations of ICBA even when mixed with large volumes of hexane or diethyl ether. Furthermore, SEM analysis revealed that treatment with 5:1 (vol) mixtures of alkane:alkanethiol cause no gyroid degradation (figure 5.13).

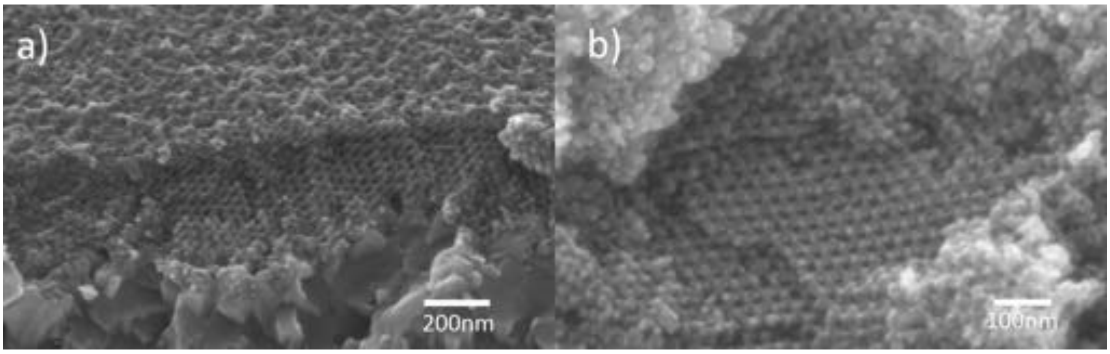

Figure 5.13: SEM images demonstrating un-damaged PBT gyroid structure after submersion in 5:1 (vol) non-thiol:thiol mixtures. Figure (a) shows an intact film after submersion in 5:1 hexane:propanethiol, while figure (b) is a close-up of gyroid structure after submersion in 5:1 hexane:dodecanethiol.

Different methods of filling the gyroid voids with the ICBA from solution were explored. Drop-casting ICBA from dimethyl sulphide:hexane revealed the importance of matching the volatilities of the two solvent components since the dimethyl sulphide was observed to evaporate faster, causing the ICBA to precipitate out of solution. Fortunately, the boiling points of alkanethiols closely match those of alkanes with two additional carbon atoms, enabling identification of a range of solvent pairs with at least comparable volatility (see table 5.3). Even with matched boiling points, drop-casting of ICBA solution on top of the gyroid film left a compact layer of ICBA above the PBT gyroid, without substantially filling the voids (figure 5.14 (a)). Additionally, the solvent pair with the lowest boiling point (5:1 diethyl ether: dimethyl sulphide) cracked the gyroid film (figure 5.14(b)). Hexane:propanethiol yielded the same compact ICBA layer, but did not cause cracking. Presumably the slower evaporation mitigates the effects of surface tension during solvent drying (hexane and diethyl ether have similar surface tensions, so it cannot be surface tension alone). Dynamic light scattering did not reveal any particles larger than 1 nm in these solvent combinations, suggesting that aggregation is not causing the formation of the compact layer. Additionally, the ICBA films are uniform in contrast to the aggregates deposited

Thiol	Non-Thiol	Boiling Points (°C)
Dimethyl Sulphide	Diethyl Ether	38/35
Propanethiol	Hexane	67/69
Butanethiol	Heptane	98/99
Pentanethiol	Octane	126/126
Hexanethiol	Nonane	152/151
Dodecanethiol	-	266

Table 5.3: Relevant solvents and their boiling points. All data at room temperature, from Sigma Aldrich [202].

from pure hexane. Hence submersion was tried rather than drop-casting.

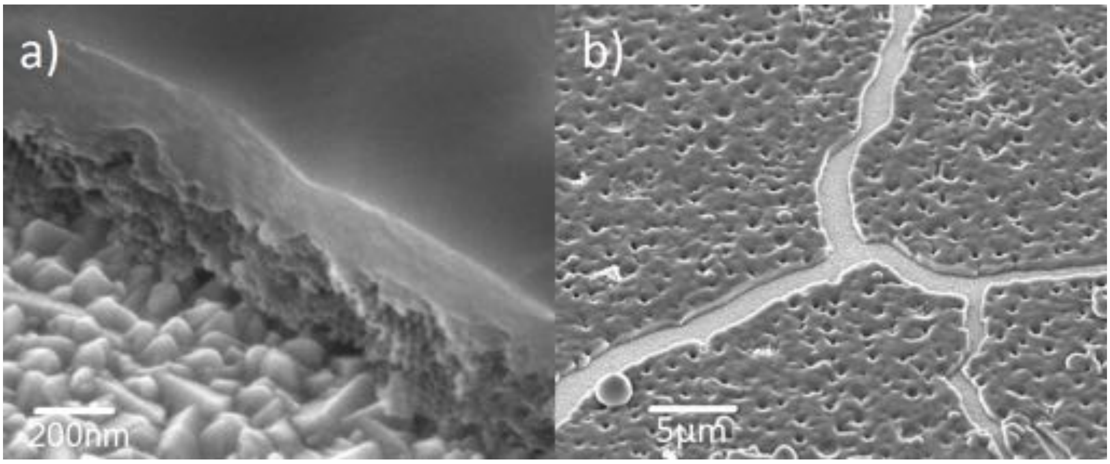

Figure 5.14: a) Drop-casting ICBA from thiol:non-thiol mixed solvents led to compact films of ICBA above intact gyroid films; b) drop-casting from dimethyl sulphide: diethyl ether also cracked the polymer films, but this problem was not observed for slower-evaporating solvent mixtures.

Gyroid films were submerged in ICBA solutions, removed and dried. SEM imaging suggested that drying with a nitrogen gun removed most, if not all, of any fullerene deposited, but slow drying enhanced *via* spinning on a spin-coater at 200 rpm showed the porous gyroid structure starting to clog up. Repeated submersion interspersed with drying built up the fullerene deposition, filling the gyroid structure. In order to shorten this lengthy process and reduce the exposure of the polymer film to different solvents, high ICBA concentrations were desired. Thus ICBA solubility in different alkane:alkanethiol mixtures were investigated.

Saturated ICBA solutions in these solvent combinations were prepared by mixing above-saturation concentrations, waiting for the excess ICBA to settle and removing the saturated supernatant. For a range of alkane:alkanethiol mixing ratios, absorption spectra were taken of these supernatants and compared to calibration spectra of known ICBA concentrations to estimate saturation concentrations. As shown in figure 5.15, ICBA solubility increases with the molecular weight and the mixing ratio of the thiol component.

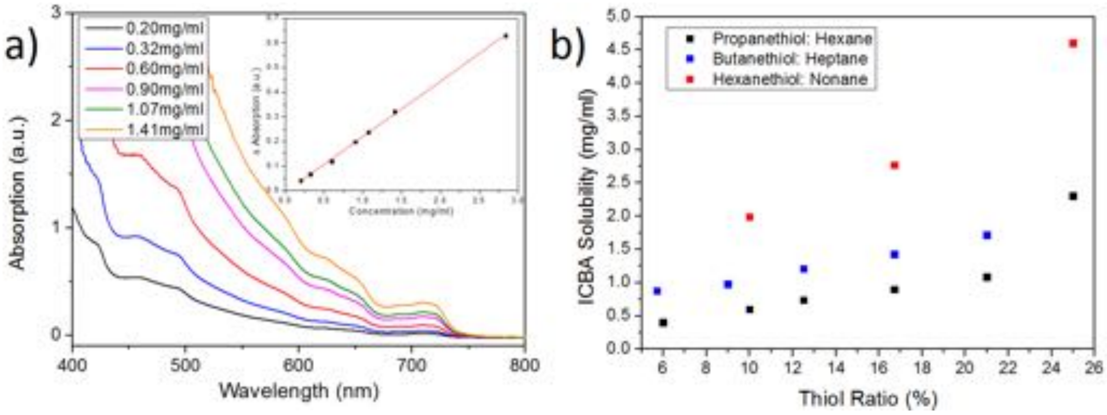

Figure 5.15: a) Absorption spectra of ICBA solutions of known concentration were used to calibrate absorption against concentration, using feature at 710 nm (inset). b) Comparison of absorption spectra with the calibration data allows ICBA saturation concentrations to be estimated for different thiol:non-thiol mixing ratios and molecular weights.

The benefits of high molecular weight and thiol mixing ratio must be balanced against disadvantages. SEM analysis had already shown gyroid films were only stable in mixed non-thiol:thiol solvents up to mixing ratios of 5:1. Higher molecular weight solvents afforded higher ICBA solubility, but became increasingly slow to dry during spin-coating. Eventually, experimentation settled on solutions of 2.5 mg/ml ICBA in 5:1 nonane:hexanethiol as a good compromise for backfilling gyroid films *via* this submersion-spinning process. Figure 5.16 shows SEM images after certain iterations of this process, and demonstrates complete backfilling after five cycles.

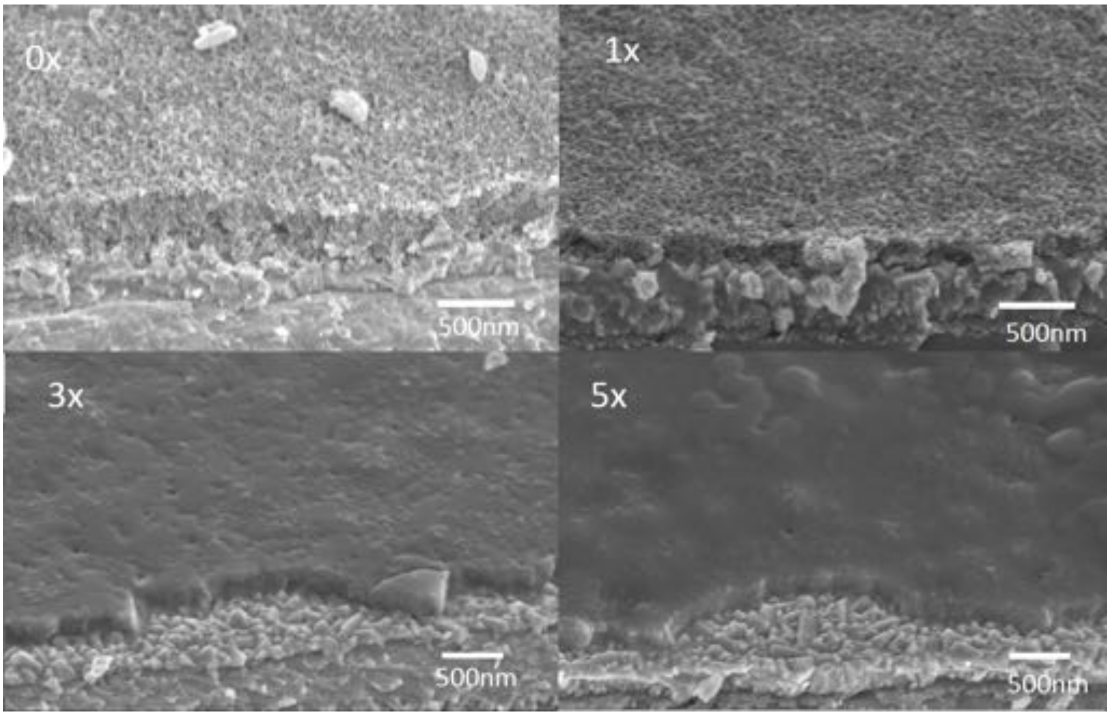

Figure 5.16: SEM images showing the voids in a polybithiophene gyroid being filled with ICBA *via* submersion followed by spin-coating. The different images show the film before backfilling, and after undergoing the process once, three times and five times respectively.

5.4 Conclusions

Gyroid-structured PBT films were succesfully electropolymerised, with 2,2,2-trifluoroethanol, diethyl ether and alkanes identified as compatible solvents for washing and further solution processing that did not destroy the gyroid structure after submersion. Potentiodynamic electropolymerisation was found to give relatively smooth films suitable for use in thin-film devices, and also yield longer conjugation lengths than potentiostatic electropolymerisation. However, the gyroid template consistently led to films with shorter conjugation than found after untemplated electropolymerisation, perhaps due to the mesoscale morphology constraints hampering molecular ordering, or perhaps due to the template slowing diffusion of protons.

A wide range of potential orthogonal solvents were tested for backfilling the PBT gyroid films with fullerene acceptors, but most were found to destroy the gyroid structure. Eventually, mixing alkanethiols with alkanes of similar volatilities allowed backfilling of the gyroid films with an ICBA acceptor. SEM analysis showed that successive submersion steps interspersed with slow spin-drying allowed the gyroid films to be completely filled. Increased solvent molecular weight allowed high concentrations of ICBA, but slowed drying times. Finally, backfilling *via* five steps of submersion in 2.5 mg/ml ICBA in a 5:1 (vol) mixture of nonane:hexanethiol followed by spin-assisted drying was adopted as the backfilling procedure.

Chapter 6

Characterisation of Gyroid-Structured Organic Solar Cells

6.1 Introduction

With fabrication of gyroid-structured all-organic solar cells complete, their electronic properties were characterised and their photovoltaic performance assessed. Besides overall photovoltaic performance, photoluminescence and transient absorption spectroscopy were used to assess exciton photogeneration and subsequent behaviour, and SCLC devices were tested as a measure of charge mobility in the films. Bilayer devices fabricated *via* untemplated electropolymerisation were also characterised for comparison with the morphological properties measured in chapter 4.

6.2 Experimental Methods

6.2.1 Sample Preparation

Gyroid-structured PBT films were electropolymerised potentiodynamically at 0.2 V/s between -0.50 and 0.50 V, on bare FTO-coated glass for spectroscopic measurements and SCLC devices, and on FTO glass coated with titanium dioxide for solar cell devices. The TiO_2 was spin-coated onto the FTO as described in the next paragraph. A 1 s pre-pulse at 0.60 V was applied to the samples deposited on TiO_2 to aid with uniform deposition, given the slightly higher substrate resistivity. Titanium dioxide was chosen as a hole-blocking layer to improve photovoltaic performance; solar cells made without this layer consistently short-circuited. Molybdenum oxide and PEDOT:PSS electron-blocking layers (deposited *via* thermal evaporation and spin-coating respectively) were not used because gyroid templates could not be successfully formed on top of them.

Prior to TiO_2 deposition, the FTO was cleaned with piranha solution as described in chapter 4. Then, 3.18 ml titanium (IV) isopropoxide was mixed in a beaker with 50 ml dry ethanol in an argon-filled glovebox. A second beaker was filled with 900 µl water, 120 µl nitric acid and 50 ml ethanol. The first beaker was removed from the glovebox, emptied into the second beaker and this was shaken vigorously before being filtered through a 0.45 µm PTFE filter. Substrate areas of 28 mm × 28 mm were then immediately spin-coated with 150 µl of the prepared solution at 2000 rpm for 45 s. These substrates were then ramped to 500 °C over 30 minutes and held there for a further 30 minutes, before being left to cool gradually, all in air.

XRD measurements taken for TiO_2 films spin-coated on FTO under these conditions show only FTO peaks, masking the TiO_2 features, hence thicker TiO_2 films were spin-coated using slower spin speeds and used for XRD measurements (figure 6.1(a)). The peak observed at 25.3° is not observed for un-coated reference samples (unlike the other peaks, labelled with asterisks) and matches the main peak of anatase-phase TiO_2 [235]. Brookite-phase TiO_2 also has a peak near 25.3° [236], but should have other peaks of similar intensity which are not observed here, so the spin-coated TiO_2 layer is assumed to be anatase. SEM images of the TiO_2 surface exhibit similar morphology to the bare FTO surface (figure 6.1(b)), and AFM measurements (figure 6.1(c)) reveal a surface roughness, R_a, of 9 nm, only slightly rougher than that measured for bare FTO, with R_a of 5 nm. Ellipsometry of films deposited using the standard spin-coating conditions on flat glass measured a TiO_2 thickness of $\sim$20 nm.

Bilayer solar cells and SCLC devices were fabricated with untemplated electropolymerisation, and used glass substrates coated with indium tin oxide (ITO), spin-coated with PEDOT:PSS (Heraeus Clevios HTL Solar) at 5000 rpm for 45 s

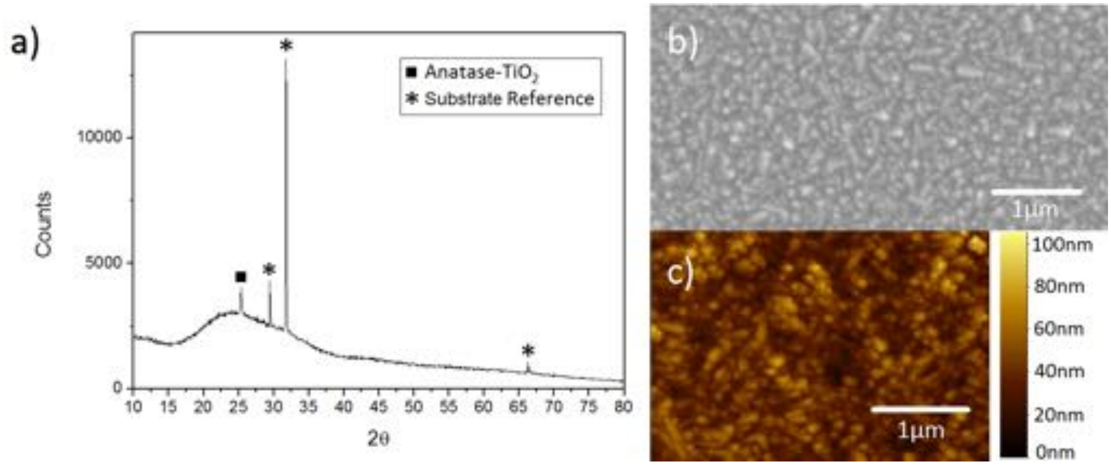

Figure 6.1: a) XRD, b) SEM and c) AFM measurements of a spin-coated, compact TiO_2 layer. The XRD peak at 25.3° is the only peak distinguished from the reference substrate, indicating anatase-phase TiO_2 [235]. The SEM and AFM measurements reveal a granular surface morphology, with surface roughness, R_a, of 9 nm; ellipsometry of similar films on flat glass substrates measured thicknesses of 20 nm.

before being annealed under a nitrogen stream at 230 °C for 20 minutes. These films were deposited using an earlier setup employing a simple silver wire pseudoreference rather than the Ag/Ag^+ reference electrode used in most of this thesis. Comparison between cyclic voltammograms of PBT deposition with both references allows an approximate correlation between the two - for ease of comparison, all potentials are reported relative to the Ag/Ag^+ reference.

Photoluminescence quantum efficiency and transient absorption measurements were taken on gyroid-structured PBT films before and after back-filling with ICBA from a 5:1 nonane:hexanethiol solvent mixture, as described in chapter 5. SEM images revealed a PBT gyroid film thickness of ~500 nm for PLQE measurements and ~250 nm for transient absorption.

Gyroid-structured solar cell devices were also backfilled with ICBA, whereas bilayer devices were spin-coated with 20 mg/ml PCBM in chlorobenzene at 2000 rpm for 30 s. SCLC devices were maintained as pure PBT. The solar cell and SCLC devices were completed by evaporation of an appropriate metal contact through a mask defining rectangular pixels with area 4.5 mm^2 for untemplated films, and circular pixels of 0.5 mm diameter for gyroid-structured films. Evaporation was conducted with a BOC Edwards evaporator, at pressures below $\sim 5 \times 10^{-6}$ mbar and deposition rates around 1 Å/s. Gyroid-structured solar cells and SCLC devices were coated with 10 nm molybdenum oxide followed by 50 nm gold, whereas bilayer solar cells were coated with 20 nm calcium followed by 50 nm aluminium, and bilayer SCLC devices were coated with 50 nm aluminium.

6.2.2 Photoluminescence Spectroscopy

The general PLQE setup was shown in figure 3.5. The inner surface of the integrating sphere and the baffle protecting the output optical fibre were coated with barium sulphate to provide diffuse reflectivity. The input laser wavelength was 405 nm, and measurements were taken over 200 integrations of 25 ms duration. The sample position was adjusted to give the maximum photoluminescence spectrum possible in both setups containing the sample.

6.2.3 Transient Absorption Spectroscopy

The experimental setup used for transient absorption spectoscopy is represented schematically in figure 3.6. A Spectra Physics 'MaiTai' Ti:Sapphire laser was used to generate femtosecond laser pulses. These pulses are time-stretched, pumped and then compressed back to the desired duration. The resultant output is an 800 nm, 100 fs pulsed beam emitting at 1 kHz, split to generate both the pump and probe beams. The pump pulse is sent through a tunable optical parametric amplifier of super-fluorescence and optically chopped at 500 kHz to give pump-on/pump-off modulation. The probe pulse is sent through a non-colinear optical parametric amplifier and a mechanical delay stage before being split further into a probe and reference pulse. The reference beam is used to account for variations from pulse to pulse during sequences of different delays. The pump and probe beams strike the same point on the sample, separated by a time delay controlled with the delay stage, and by the 'magic angle' of $\arccos({}^{1}\!/\!_{\sqrt{3}}) = 54.7°$ to eliminate the influence of dipole orientation in the sample on signal intensity [237]. Beyond the sample, the pump beam meets a beam-stop, while the probe and reference beams are focused onto a PI acton Spectrapro 2150i imaging spectrometer employing two Hammamatsu S3901256G diode arrays. All transient absorption spectroscopy and its data processing was performed by Dr Mike Price.

6.2.4 Current-Voltage Measurements

Solar cell and SCLC devices were measured using a Keithley 2636A source meter setup. AM1.5 solar spectrum illumination was provided by an Abet Technologies Sun2000 solar simulator, calibrated to have output power of 100 mW/cm^2 over the device area. For SCLC experiments, the film thickness must also be known. This was measured using AFM to scan across the edge of the electropolymerised film for untemplated films, and using SEM of film cross-sections for gyroid-structured films.

6.3 Results and Discussion

6.3.1 PLQE Measurements

The photoluminescence spectrum for a gyroid-structured PBT film is shown in figure 6.2, both before ICBA backfilling and after one to six backfilling steps. The initial photoluminescence spectrum clearly displays the 0-0, 0-1 and 0-2 vibrational features observed previously for regioregular P3HT [136], situated here at 620 nm, 670 nm and 735 nm respectively. Comparison between photoluminesence measurements without a sample and with direct and indirect illumination yield a PLQE value for the film of $\sim 0.08\%$, corresponding better to spin-coated regioregular P3HT (PLQE $< 0.5\%$) than regiorandom P3HT (PLQE $\sim 8\%$) [60]. The low value could be influenced by the lack of side-chains as well as lamellar order, as photoluminesence has been observed to increase as a function of side-chain length due to increased exciton confinement [238]. The PBT photoluminescence is unchanged even after submerging the film in 5:1 alkane:alkanethiol solvent mixtures, indicating that this treatment does not damage the optoelectronic properties of the film, as well as its nanostructure.

The effect on the photoluminescence of back-filling the PBT gyroid with ICBA is clear. After the first backfilling step, the PBT photoluminescence is strongly quenched, with the overall PLQE dropping to $\sim 0.02\%$. ICBA itself has weak photoluminescence around 735 nm [239], which is the strongest peak after ICBA backfilling. Subtracting a Gaussian fitted to the ICBA peak after five backfilling steps gives an estimate for PLQE from the PBT alone as 0.01%, yielding a PBT PL quenching of $\sim 85\%$ upon full ICBA backfilling. This quenching is proof of

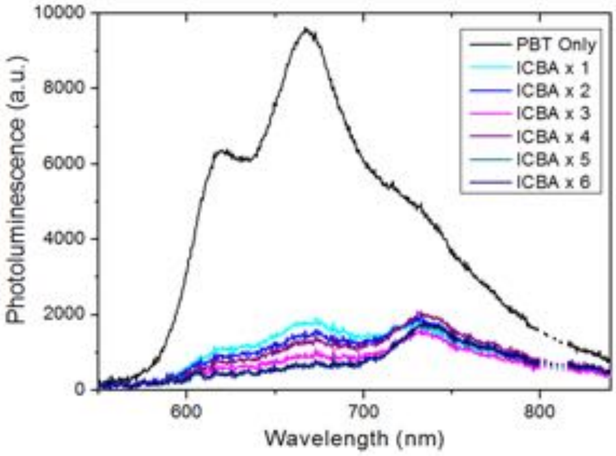

Figure 6.2: Photoluminescence spectra of a gyroid-structured PBT film before backfilling with ICBA, and after one to six backfilling steps. The photoluminescence is quenched upon addition of ICBA, demonstrating molecular contact between PBT and ICBA, and exciton dissociation across their interface. The second harmonic of the laser illumination overlaps the photoluminescence around 810 nm, so the signal here has been removed and the spectra were extrapolated (dotted line).

molecular contact between the two materials, and efficient exciton dissociation at their interface. It is also evidence that the surface of the gyroid structure with 40 nm unit cell size is within the exciton recombination length of the bulk of the gyroid. The small decrease in PLQE for successive backfilling steps after the first one implies that the PBT is almost completely coated with ICBA after the first backfilling treatment.

6.3.2 Transient Absorption Spectroscopy

Transient absorption spectra as a function of wavelength and pump-probe delay are shown in figure 6.3 for the un-filled and filled PBT gyroid films. Ground-state bleaching (GSB) can be seen in both samples, with peaks around 545 nm and 595 nm, matching the 0-0 and 0-1 peaks in steady-state absorption. Stimulated emission (SE) is also apparent in both samples, with peaks at 675 nm and 740 nm, matching the 0-1 and 0-2 photoluminescence peaks. There is probably also a stimulated emission peak matching the 0-0 photoluminescence peak at 620 nm, but this is masked by the tail of the ground-state bleaching. Finally, photoinduced absorption (PIA) is visible above 610 nm, but only with any significance for the backfilled film. Although PIA seems to appear only around 1 ps after photoexcitation, the negative signals at 630 nm and above 790 nm that are already present by 0.25 ps indicate that PIA is present directly after photoexcitation. There were no discernible differences between spectra collected with 1 and 5 µJ/cm^2 pump fluences, suggesting that bimolecular recombination was weak within the fluence range investigated.

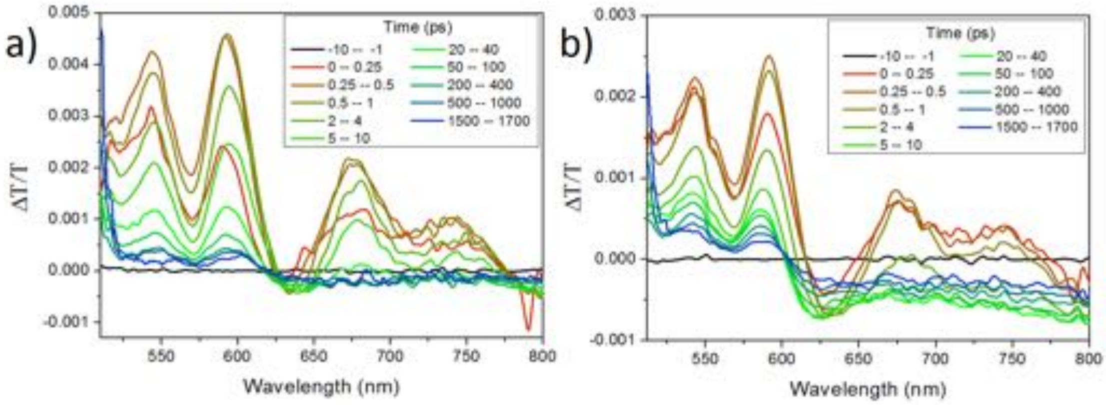

Figure 6.3: Transient absorption spectra for gyroid-structured PBT films (a) before, and (b) after, backfilling with ICBA. Ground-state bleaching can be seen with peaks around 545 nm and 595 nm, while stimulated emission peaks are visible around 675 nm and 740 nm. Photoinduced absorption is also apparent after 1 ps in the backfilled film, between ~ 610 – 800 nm.

The time evolution of the different spectroscopic features is shown more clearly in figure 6.4. Transient absorption signals have been integrated over four spectral regions relating to different transient features (530 – 550 nm, ground-state bleaching; 590 – 610 nm, ground-state bleaching and stimulated emission; 670 – 690 nm, stimulated emission and photoinduced absorption; and 780 –800 nm, photoinduced absorption), and plotted as a function of time after photoexcitation, normalised to the peak value.

As expected, all transient features display a peak before decaying back to the steady state absorption spectrum. The only possible exception is the PIA signal for the sample without ICBA, but looking at the absolute signal in figure 6.3(a) shows that this signal is very small anyway, meaning its normalised signal is

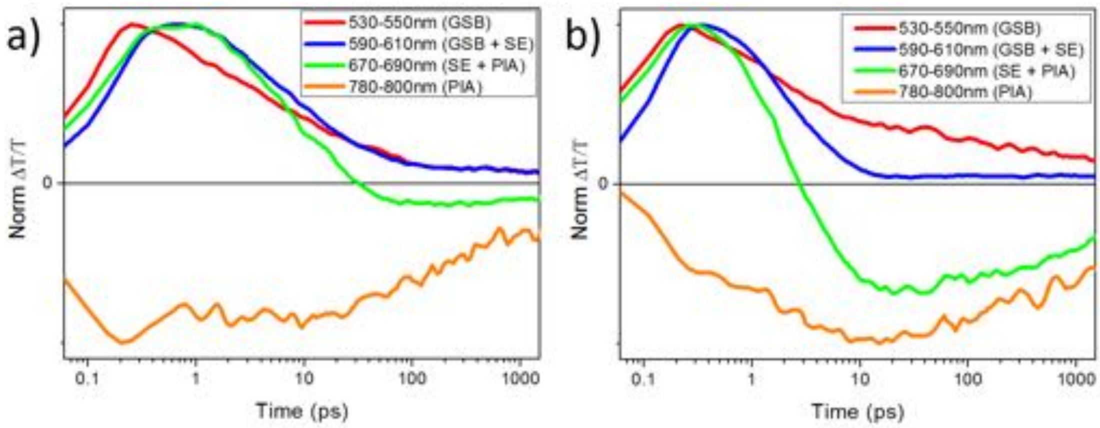

Figure 6.4: Time evolution of different transient features after photoexcitation of gyroid-structured PBT films (a) before, and (b) after, backfilling with ICBA. The signals are normalised to their peak values; the photoinduced absorption of the un-backfilled film is weak, which should be born in mind when looking at its normalised value.

much more susceptible to noise than the others. In both samples, with and without ICBA, the ground-state bleaching between 530 nm and 550 nm peaks after about 0.25 ps. Without ICBA, the two stimulated emission signals peaks slightly later, after 0.7 ps. This is probably a thermalisation effect, with excitons initially excited to the second and higher vibrational states relaxing to the ground vibrational state. With ICBA, these signals peak earlier, around 0.3 – 0.4 ps, which is likely due to faster decay processes. These ICBA-induced faster decay processes are also clear in the evolution of the two signals after they peak. The 590 – 610 nm peak falls to 10% of its peak value after ∼ 150 ps without ICBA, but within 10 ps with ICBA. The 670 – 690 nm peak also decays much faster after the addition of ICBA, although the signal is conflated with the photoinduced absorption making it difficult to determine an exact decay lifetime. The photoinduced absorption for the PBT:ICBA sample peaks after around 10 ps, decaying relatively slowly over the next nanosecond.

The spectral and temporal transient absorption features match previously reported behaviour for standard spin-coated, regioregular P3HT and P3HT:PCBM films [240–242]. As described in chapter 3, the ground state bleach corresponds simply to depopulation of the HOMO states in the polythiophene. In contrast, the stimulated emission corresponds to optically allowed transitions from singlet excitons back to the ground state, and hence has a strength proportional to the singlet exciton population. The PIA around 650 nm has previously been ascribed to bound polaron pairs in P3HT (free polarons induce PIA beyond 1000 nm, which was not measured here) [242]. Correlating the signals with these populations allows the elucidation of photoexcitation and subsequent decay routes.

For the PBT-only sample, the photoexcitation initially de-populates the HOMO levels, generating excitons with a range of vibrational energies. This takes place within ~ 250 fs, with thermalisation relaxing these down to the ground vibrational state within ~ 700 fs. The stimulated emission decays within ~ 100 ps, implying that these singlet excitons have also disappeared in this timeframe. The similar decay rate in the 0-0 ground-state bleach (590 – 610 nm) and 0-1 stimulated emission (670 – 690 nm) implies that the HOMO levels re-populate at the same rate as the singlet excitons depopulate, suggesting a simple $S_1 \rightarrow S_0$ relaxation of singlet excitons back to the ground state; the signals diverge at later times due to the PIA contribution. Although the photoinduced absorption persists for longer timescales, it is a very weak signal. In regioregular P3HT films, a small percentage of 'hot' excitons (those with above-thermal energies) are known to generate polarons rather than relaxing to singlet excitons in the vibrational ground state [242], which is a possible cause of the PIA observed here.

By contrast, the 670 – 690 nm signal decays significantly faster than the 590 – 610 nm signal once ICBA has been added. This implies that the singlet excitons are decaying into another, non-emissive excited species rather than relaxing back to equilibrium. Possible identities are triplet excitons, charge transfer states, bound polarons, trapped polarons or free polarons. The PIA around 650 nm has been attributed to bound polarons [242], but this doesn't rule out the presence of other non-emissive species. Free polarons have been assoicated with PIA beyond 1000 nm, which is beyond the range of these measurements. Pump-push-probe experiments could be used to investigate the relative proportions of trapped and free species [243]. The PIA signal here demonstrates that the bound polarons persist at least on the nanosecond timescale, but measurements were not conducted out to the millisecond timescale characteristic of charge extraction to the electrodes after initial photoexcitation [244].

Overall, these transient absorption measurements demonstrate that excitons are generated in the PBT and, upon addition of ICBA, dissociate into some other excited species. The PIA signal suggests that these species persist at least on the nanosecond timescale. However, the identity of this species cannot be determined, although bound polaron pairs are likely to make up some proportion of them.

6.3.3 Solar Cell Characterisation

Having observed evidence of exciton photogeneration in the PBT and efficient dissociation at the PBT:ICBA interface, solar cells were fabricated and tested. Figure 6.5 shows the characteristics of the best-performing gyroid-structured device. Due to time constraints, very little device optimisation was conducted, most notably with regards to film thickness. Instead the results correspond simply to the best performing device from a few different batches, with a PBT film thickness of roughly 100 – 200 nm as judged by SEM.

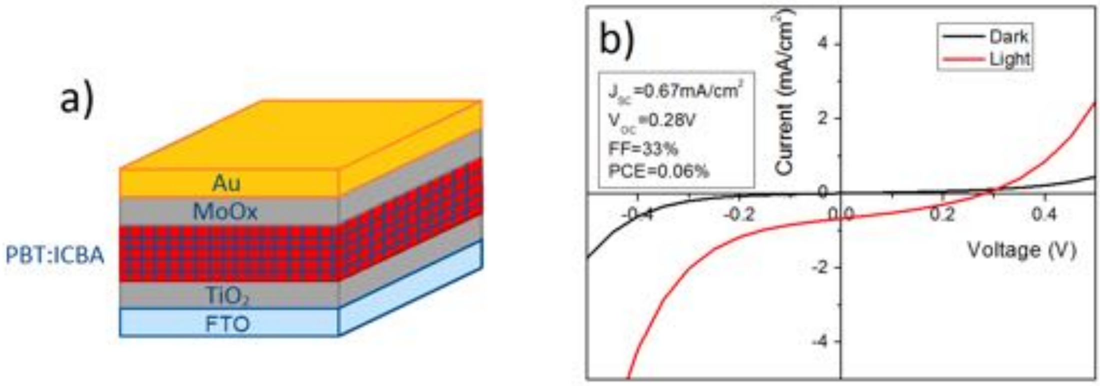

Figure 6.5: a) Schematic of the gyroid-structured PBT:ICBA solar cell. b) Output current density of the best-performing gyroid-structured solar cell as a function of applied potential, with and without AM1.5 solar illumination. The overall power conversion efficiency is 0.06%.

The best-performing gyroid-structured PBT:ICBA solar cell had a short-circuit current density of 0.67 mA/cm^2, an open-circuit voltage of 0.28 V and a fill factor of 33%, leading to an overall power conversion efficiency of 0.06%. This compares poorly to typical P3HT:PCBM efficiencies of ∼ 2 – 5% [31], and at the lower end of previously reported electropolymerised solar cell efficiencies of 0.1 – 1.5% [160, 162]. The inferior performance here seems to arise from all characteristic parameters, as documented in table 6.1.

Device	J_{SC} (mA/cm^2)	V_{OC} (V)	FF (%)	PCE (%)	R_S (Ωcm^2)
Gyroid Device	0.67	0.28	33	0.06	210
Ratcliff *et al.* [159]	3.0	0.5	65	1.0	3
Yu *et al.* [160]	0.4	0.6	42	0.1	250
Nasybulin *et al.* [161]	1.4	0.47	38	0.37	170
Tezuka *et al.* [162]	3.5	0.71	61	1.5	55
Fan *et al.* [163]	0.3	0.81	38	0.3	870
P3HT:PCBM [31,69]	10	0.6	50 – 65	2 – 5	8

Table 6.1: Summary of solar cell performance characteristics of the champion gyroid-structured solar cell in this project, previously reported electropolymerised devices, and common parameters for highly performing spin-coated P3HT:PCBM devices. Where unreported, the series resistance, R_S, was estimated from the gradient of the illuminated J-V curve at open-circuit.

The low short-circuit current density of the gyroid-structured device is in fact typical of electropolymerised devices. Given the short conjugation lengths measured in electropolymerised films in chapters 4 and 5, especially with gyroid structure, this is perhaps unsurprising. As well as permitting more extensive intramolecular transport, long conjugation lengths are compatible with better π-π stacking (as observed from absorption spectroscopy and GIWAXS in chapter 4), and have hence been associated with better inter-chain charge transport and macroscopic mobility [55]. Spin-coated films employed as transistors have demonstrated increasingly voltage-dependent mobilities for films with large exciton bandwidths, which was attributed to wider distributions of trap states in films with short conjugation lengths (the absolute mobilities did not vary systematically with the measured conjugation, but transistor mobilities depend strongly upon the polymer orientation at the substrate surface, which is not specifically measured by the absorption analysis, and is also not as important in solar cell devices) [126]. Hence the poor conjugation in gyroid-templated PBT films would be expected to lead to low current output from the device.

Optimising spin-coated organic solar cell performance has demonstrated the importance of improved crystallinity inducing high carrier mobilities and low series resistances [69]. The series resistance for each of the reported electropolymerised devices was estimated from the current gradient at open circuit, with the results shown in table 6.1. The gyroid-structured device has a series resistance of around 210 Ωcm^2, over twenty times larger than an optimised spin-coated device [69]. Only the electropolymerised devices of Ratcliff *et al.* had a series resistance comparable to spin-coated devices, suggesting that low mobility is indeed a common problem for electropolymerised solar cells.

Besides short conjugation and its implications for poor charge transport in the PBT phase, the ICBA phase may also be hindering the current output of the device. The extent of ICBA backfilling has not been quantified beyond photoluminescence quenching and SEM images showing clogged gyroid pores. It could be that the ICBA packing is not dense enough for efficient, continuous electron transport to the electrodes; it is known that higher fullerene concentrations are needed for efficient charge extraction than for photoluminescence quenching in spin-coated blends [245]. Pure films of ICBA have been found to crystallise less than similar films of PCBM [246], which may be a disadvantage of backfilling with ICBA. Further investigation and optimisation of the ICBA back-filling could be conducted using GIWAXS or calibrated absorption spectroscopy in the near-ultraviolet spectrum, where ICBA absorbs strongly but PBT doesn't.

Simulations of photovoltaic operation in organic solar cells with different donor:acceptor morphologies suggest that the gyroid structure is susceptible to significant geminate recombination as a result of its smooth interface and the intricate morphology frequently requiring charge transport against the device's built-in field in order for dissociated charges to escape each other [37]. However, this result will be dependent upon material-specific rate constants such as charge mobilities and dissociation or recombination rates, which in the simulation study were either chosen to be appropriate to poly(9,9′-dioctylfluorene-co-bis(N,N′-(4,butylphenyl))bis(N,N′-phenyl-1,4-phenylene)diamine):poly(9,9′-dioctylfluorene-co-benzothiadiazole) blends or assumed. Significant geminate recombination in gyroid-structured devices would contribute to the low short-circuit currents observed here. Bimolecular recombination was found to be less of a problem in the simulated gyroid-structured devices, and indeed the fluency independence of the transient spectroscopy results reported in section 6.3.2 suggest that bimolecular recombination is not dominant here.

Low mobility and significant geminate recombination would also account for the low fill factor observed in the gyroid-structured device. Increasing the applied potential towards V_{OC} decreases the effective field inside the device, so if strong fields are needed to overcome poor charge separation and transport, the fill factor will be expected to be low. Indeed, improvements in power conversion efficiency achieved by reducing series resistance in optimised spin-coated devices resulted almost equally from improved fill factor and short-circuit current density [69].

The back-filling procedure used to fabricate the gyroid-structured solar cells seems liable to producing an ICBA capping layer on the PBT film. Unfortunately, SEM images of the film after multiple back-filling steps appear to show such morphology (refer back to figure 5.16). With the inverted cell architecture used here, this could lead to an accumulation of trapped holes at the top contact, forming a region of positive charge opposing the built-in field of the device, and further reducing the fill factor. Similar fill factor behaviour has been seen in standard architecture solar cells where rapidly-evaporated aluminium electrodes formed poor contact with the active layer, leading to a build up of electrons at the contact interface [247]. Under reverse bias, a concentrated population of holes under the ICBA capping layer could induce a strong enough local electric field to allow injection of electrons from the molybdenum oxide into the ICBA, increasing the overall current through the device. This would explain the low ‘breakdown’ voltage in reverse bias.

In contrast to the short-circuit current, the open-circuit voltage of the gyroid-structured device is poor for electropolymerised solar cells. This is in particular surprising given that ICBA has previously been associated with higher open-circuit voltages than PCBM due to its higher LUMO [248]. This is perhaps evidence of pinholes through the device allowing significant leakage currents. Although electropolymerisation might be expected to give full coverage of all electrically active areas of the substrate, short-circuited devices were a recurrent problem (in particular for FTO substrates without a TiO_2 layer), so such pinholes do seem prevalent. Perhaps the electropolymerisation or back-filling technique could be modified to limit the appearance of pinholes. Leakage currents would also contribute to the large reverse-bias current observed in the device.

To complement photovoltaic studies of gyroid-structured films, bilayer devices were also fabricated and tested, with an ITO/PEDOT:PSS/PBT/PCBM/Ca/Al layered structure as shown in figure 6.6(a). Since pulsed electropolymerisation was anecdotally observed to yield the smoothest films (according to SEM images), this was used for deposition of the PBT layers. Pulses of 0.25 s duration at different electropolymerisation potentials were used to build up the PBT layer. AFM measurements indicated approximate PBT thicknesses of 50 nm.

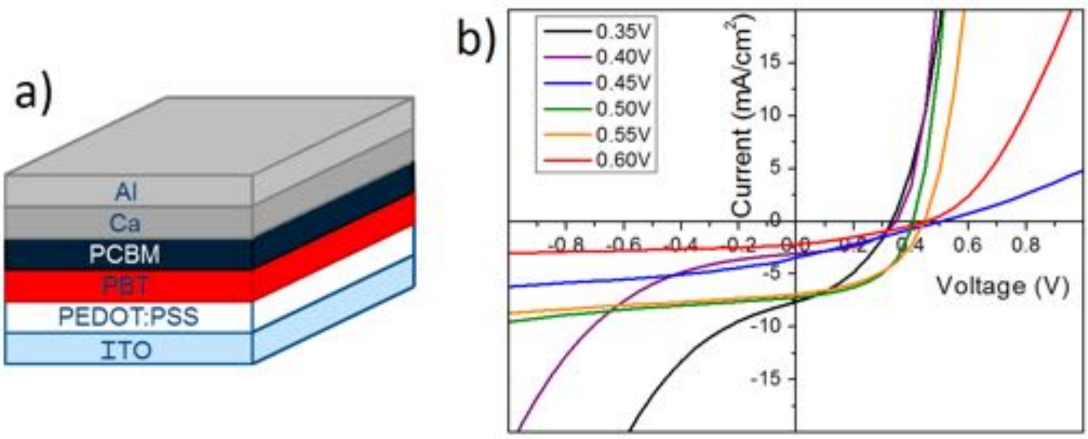

Figure 6.6: a) Schematic of the bilayer PBT:PCBM solar cell. b) Current-voltage behaviour of bilayer devices deposited with pulsed electropolymerisation at different potentials, under AM1.5 illumination (reported potentials approximate).

The bilayer device efficiencies are higher than for the gyroid-structured devices, ranging from 0.31 – 1.49%. The highest efficiency device was fabricated with an intermediate potential, which corresponds with the optimal potential for long conjugation in untemplated, potentiodynamically electropolymerised PBT films as found in chapter 4. Devices fabricated with the lowest electropolymerisation potentials exhibited lower open-circuit voltages and high reverse-bias currents, suggesting a significant presence of pinholes through the active layer. This might result from inhomogeneous substrate conductivity, with low deposition potentials not covering points of high resistance as effectively as higher deposition potentials. The highest electropolymerisation potential yielded a device with low short-circuit current density and high series resistance, suggestive of the problems affecting gyroid-structured devices which were speculated to derive from poor molecular ordering in the PBT. This again correlates with the relationship between conjugation length and deposition potential observed in chapter 4.

The champion bilayer device had a short-circuit current density of 7.2 mA/cm^2, an open-circuit voltage of 0.41 V, a fill factor of 51% and a power conversion efficiency of 1.49%, which equals the highest-performing previously-reported electropolymerised solar cell operating under standard illumination conditions [162]. The gradient of the current-voltage slope at open-circuit indicates a series resistance of $\sim 10\,\Omega\text{cm}^2$, corresponding to optimised spin-coated devices [69]. This is further evidence, along with Ratcliff *et al.* [159], that electropolymerisation can produce conjugated polymer films of sufficient quality to compete with spin-coated P3HT:PCBM devices, at least with untemplated electropolymerisation.

In fact, the champion bilayer device here falls below the optimised P3HT: PCBM power conversion efficiency mostly on account of its open-circuit voltage, which is 0.63 V in the spin-coated device and ranges between 0.47 V and 0.71 V in the previously reported electropolymerised bilayer devices. Judging from the electro-oxidation potential of the monomer, thiophene has a slightly lower HOMO than its alkyl-substituted variants [249, 250], and would therefore be expected to produce a slightly higher V_{OC} than P3HT films. This could be as a result of the polythiophene chain orientation. In chapter 4, the polymer chains were found to be predominantly oriented edge-on in thin electropolymerised films as used in these bilayer devices. This is in contrast to previous reports of polythiophenes electropolymerised from organic solvents, which all report predominantly face-on orientation close to the substrate [177, 220, 221]. Shifting average orientation of P3HT chains from face-on to edge-on has previously been found to decrease the open-circuit voltage in P3HT:PCBM bilayer devices by 0.18 V as the P3HT ionisation energy varies with orientation due to dipole moments along the polymer backbone [251].

6.3.4 Space-Charge Limited Currents

Electropolymerised PBT films without ICBA or PCBM addition were used to measure charge mobility from space-charge limited currents, as has been previously reported for spin-coated P3HT films [53]. However, an important difference between spin-coated and electropolymerised films is the smoothness of the films. Even thin films of electropolymerised PBT have surface roughness, $\mathrm{R_a}$, of up to $\approx 40\,\mathrm{nm}$ according to AFM measurements, whereas it is not unusual for spin-coated polymer films to have surface roughness of $\mathrm{R_a} \leqslant 5\,\mathrm{nm}$. Since the SCLC treatment assumes a uniform film thickness, and indeed the calculated mobility depends upon the third power of the film thickness, rough film surfaces are likely to induce substantial errors. Hence the charge mobilities reported in the following section are only approximate. As for bilayer solar cells, pulsed electropolymerisation was used in an attempt to minimise surface roughness and hence errors in the calculated mobility (the gyroid-structured film was electropolymerised with constantly-varying potential, as with all other gyroid-structured films in this chapter). Film thicknesses were also kept beneath 70 nm, again due to observed improvements in film roughness. Since substantial current is likely to span the polymer film at its thinnest points, where resistance is presumably lowest, the mobilities reported here are likely to represent maximum values.

Figure 6.7(a) shows a representative graph of the square root of current density as a function of voltage applied across a polymer film, with an approximately linear relationship between $\sqrt{J}$ and V indicating the region of space-charge limited current used to deduce charge mobility. Using equation 3.2, the charge mobilities shown in figure 6.7(b) were calculated for untemplated and gyroid-structured PBT films as a function of electropolymerisation potential.

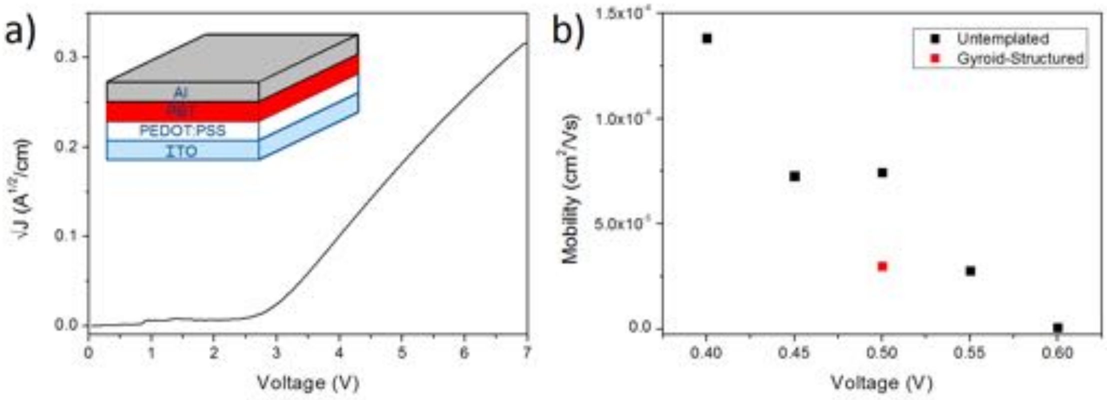

Figure 6.7: a) Graph of $\sqrt{J}$ against applied voltage for a PBT film electropolymerised with pulsed deposition at approximately 0.40 V, with a roughly linear region corresponding to the space-charge limited current. b) SCLC-derived mobilities as a function of deposition potential for electropolymerised PBT films. Note that the deposition potentials shown here are approximate due to the reference electrode used.

Although the mobilities and potentials are only approximate, there is a clear trend for higher electropolymerisation potentials to lead to deposition of films with lower charge mobilities. This appears to correspond closer to the behaviour observed in chapter 4 for conjugation lengths with potentiostatic electropolymerisation rather than potentiodynamic electropolymerisation. The films deposited here are significantly thinner than the films used for visible absorption analysis, which may be one source of this discrepancy, along with the indirect relationship between conjugation lengths and charge mobility.

Regioregular P3HT films with SCLC architecture have been found to have mobilities in the range of $\sim 1 \times 10^{-5} - 5 \times 10^{-4}\,\mathrm{cm^2/Vs}$ depending upon molecular weight [53]. Hence the mobilities measured for the untemplated electropolymerised PBT films fall roughly within the region of low molecular weight, regioregular P3HT. The mobility measured in the gyroid-structured film also lies towards the bottom of this range, with a value lower than the untemplated film deposited with the same deposition potential. This is in agreement with the inferior conjugation and photovoltaic performance observed in gyroid-templated films. It should be remembered that the SCLC measurements presented here are likely to represent an upper limit on the true film mobility.

6.4 Conclusions

Photoluminescence and transient absorption spectroscopy demonstrate efficient exciton generation and dissociation in gyroid-structured PBT:ICBA films. However, photovoltaic performance in gyroid-structured solar cells is poor, with a maximum achieved power conversion efficiency of 0.06%. This is partly attributed to high series resistance in the device, which is a common problem for previously-reported electropolymerised solar cells. High series resistance corresponds with the poor conjugation observed for electropolymerised films in chapters 4 and 5, especially for gyroid-templated deposition. Indeed, bilayer devices fabricated with untemplated polymerisation exhibited better performance, with 1.49% power conversion efficiency and series resistance comparable to spin-coated P3HT:PCBM films.

It is possible that there is scope for considerable improvement in the gyroid-structured device performance. The ICBA backfilling can still be investigated to ascertain and improve the extent of backfilling and fullerene ordering, and to ensure there is no ICBA capping layer above the PBT film. Additionally, PBT film deposition should be optimised to give complete film coverage without pinholes, and films of most suitable thickness. Finally, investigation into all electropolymerisation conditions has not been exhausted. Importantly, the poor device performance measured here is attributed to the constraints of the fabrication procedure, rather than intrinsic problems with the gyroid structure.

Chapter 7

Electrochemical Techniques for Perovskite Solar Cells

This chapter describes two separate projects employing electrochemical techniques for the fabrication of lead halide perovskite solar cells. The first project describes electropolymerisation of poly(3,4-ethylenedioxythiophene) (PEDOT) finger electrodes for back-contact solar cells, and the second investigates perovskite films deposited *via* electrodeposition of a lead oxide precursor.

The first project was carried out as a collaborative effort. My role was to prepare the PEDOT contacts for hole extraction, and this is described in detail; the rest of the project is summarised for completeness but was conducted principally by other people. The second project was conducted myself.

7.1 Back-Contact Perovskite Solar Cells

7.1.1 Background

The recent emergence of lead halide perovskite materials for thin-film photovoltaics fabricated *via* cheap solution-processing techniques is discussed briefly in chapter 2. Until now, perovskite-based devices have generally been based upon organic or dye-sensitised solar cell architectures [252, 253], with the active layer sandwiched between two electrodes, one of which must be transparent (see figure 7.1(a)). As the power conversion efficiencies of perovskite-based devices ap-

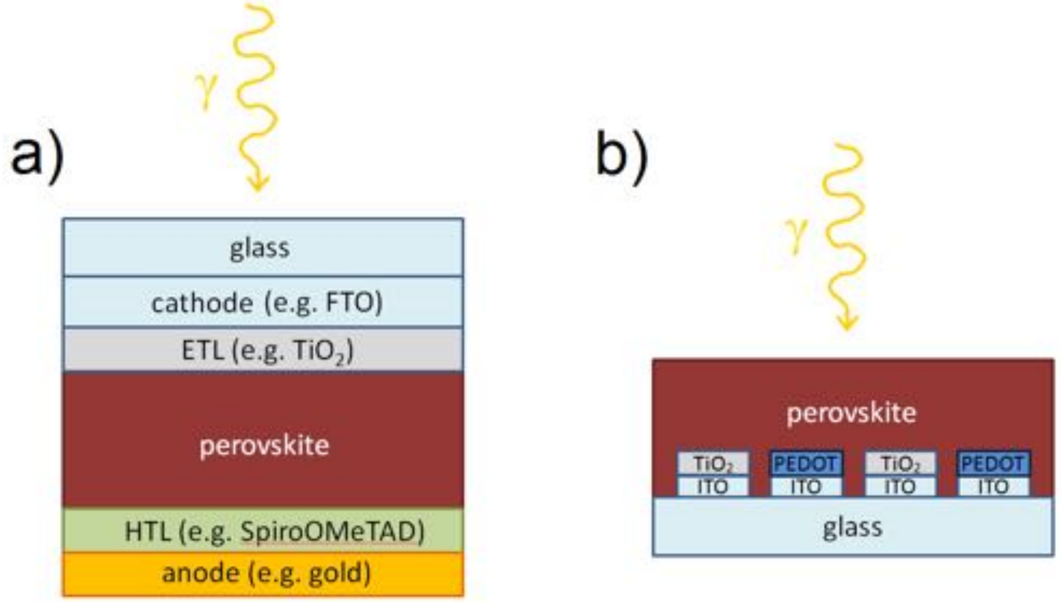

Figure 7.1: Schematic diagrams of a) the conventional ‘sandwich’ architecture, and b) the back-contact architecture for perovskite solar cells. The schematic for the sandwich architecture shows a transparent cathode, an electron transport layer (ETL), a hole transport layer (HTL), and a metal anode, along with common examples of materials used for each of these. The back-contact architecture has alternating, interdigitated cathodes and anodes formed of ITO coated with an electron-selective and hole-selective material (TiO_2 and PEDOT) respectively. Both architectures are designed to be illuminated from above as shown in this figure.

proach those of crystalline silicon-based devices [20, 83], it is worth exploring the fabrication and performance of perovskite solar cells built with the back-contact architectures commonly employed in silicon solar panels [254].

Back-contact architectures, in which both the anode and cathode are positioned between the substrate and the active region of the solar cell (figure 7.1(b)), have several advantages over ‘sandwich’ architectures for use in commercial, large-area solar panels. Most obviously, back-contact designs avoid the placement of any electrical components on one side of the active layer, reducing or avoiding ‘shading’ losses from light being absorbed before reaching the active layer of the device [36, 254]. Although transparent conducting layers are used in sandwich architectures, these still absorb some light; even if a non-conductive encapsulation layer is required for the perovskite active layer, it is likely to have a higher transmission than conducting layers. Placing all of the electronics on the opposite side to that which is illuminated allows each face of the device to be optimised independently, for electronic and optical properties respectively. This advantage is greater for large area panels composed of multipe cells, where metallic interconnects are required between the different cells. In particular, wide interconnects can be used without causing shading, allowing resistive losses in the interconnects to be minimised (differences in thermal exapnsion limits interconnect thickness, the other dimension in which they could expand to reduce resistance) [36]. Additional advantages of containing all interconnect circuitry in one plane include higher cell packing density, simpler manufacture and improved aesthetics [36].

In order to fabricate a back-contact solar cell, interdigitated fingers with alternating charge selectivities are required. Furthermore, the active layer thickness, and separation between fingers must be comparable or smaller than the charge diffusion length in the active region, so that generated charges are on average collected by the contacts rather than recombining. Previous measurements have reported charge diffusion lengths from hundreds of nanometres up to one micrometre in polycrystalline thin film perovskite cells [255, 256], and even millimetres in large, single crystals of perovskite [257]. Lateral diffusion lengths were probed by collaborators in this project to determine optimal interdigitated electrode spacing; this investigation of lateral charge diffusion lengths eventually led to evidence of photon recycling in the perovskite films.

The fabrication strategy in this project uses photolithography to define an interdigitated electrode pattern in ITO on a glass substrate. To provide charge selectivity at the two sets of electrodes, different blocking layer materials need to be deposited to completely cover the alternating electrodes. The difficulty of properly aligning successive layer deposition without registration errors makes electrodeposition of these blocking layers the simplest fabrication route. Electrodeposited TiO_2 was chosen to be the electron-collecting layer, with electropolymerised PEDOT the hole-collecting layer. Hence, electropolymerisation of hole-selective PEDOT covering the desired ITO electrodes was investigated and characterised.

7.1.2 Experimental Methods

Electrodeposition of PEDOT anodes constitutes one part of the fabrication route for back-contact lead halide perovskite solar cells. Full details of the other fabrication and characterisation steps are published elsewhere [258]. Briefly, photolithography was used to define a pattern of interdigitated fingers (4 µm width, 4 µm separation) on an ITO-coated glass substrate. ITO was removed from the exposed spaces between the desired fingers *via* etching with hydrochloric acid, followed by dissolution of the remaining resist with acetone. Subsequently, titanium hydroxide was electrodeposited onto one half of the ITO fingers from an aqueous titanium oxysulphate solution and annealed at 400 °C to yield polycrystalline titanium dioxide. The PEDOT electropolymerisation on the remining ITO fingers was performed at this point, and is discussed further in the main body of this chapter. Finally, a solution of lead acetate and methylammonium iodide in N,N-dimethylformamide was spin-coated on top of the electrodes at 2000 rpm and annealed at 100 °C to give a uniform methylammonium lead iodide perovskite film. A schematic of the fabrication procedure is shown in figure 7.2.

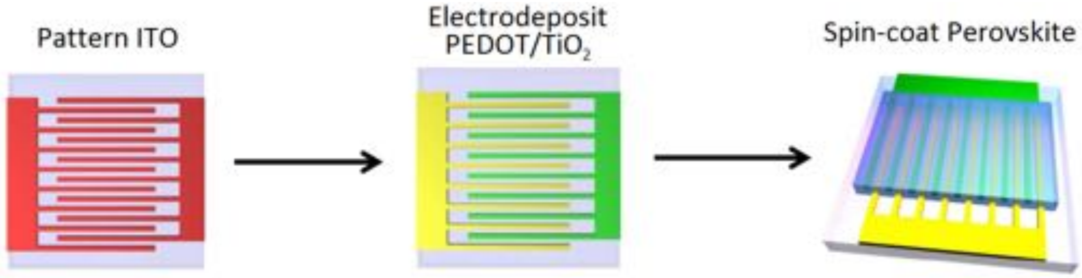

Figure 7.2: Schematic overview of the fabrication process for interdigitated back-contact perovskite solar cells, reproduced from reference [258]. Photolithography and hydrochloric acid etching define interdigitated ITO fingers on a glass substrate. Titanium dioxide and PEDOT layers are then electrodeposited on alternating fingers before a methylammonium lead iodide film is spin-coated on top and annealed to complete the device.

All electropolymerisation was conducted inside a sealed glass chamber containing the appropriate concentrations of EDOT monomer, lithium perchlorate supporting electrolyte and solvent. A three electrode setup was used, with a platinum foil counter electrode, ITO working electrode and a reference electrode which was chosen as a function of the solvent used. For deionised water and methanol mixtures, a saturated calomel reference electrode was used, whereas a silver wire pseudo-reference electrode was used with acetonitrile and propylene carbonate. A ferrocene solution was used to calibrate the silver wire pseudoreference electrode.

7.1.3 Electropolymerisation of PEDOT Anodes

Optimisation of PEDOT Electropolymerisation

Given that templated electropolymerisation was not required for this project, standard aqueous and organic solvents could be used. Initial electropolymeristion was conducted using three commonly reported solvents for PEDOT electropolymerisation, namely acetonitrile [259], propylene carbonate [259] and a 50:50 (vol) mix of de-ionised water and methanol [260]. In each case, 0.02 M EDOT monomer concentration was used. Following the conditions used by Dehmel *et al.* [260], 0.1 M lithium perchlorate was used as the supporting electrolyte for the de-ionised water:methanol mixture and acetonitrile; this was found to give very patchy deposition from propylene carbonate so 0.5 M lithium perchlorate was used with this solvent as this greatly improved coverage (see figure 7.3(b)). This could be due to improved conductivity, which is found to peak around 1 M lithium perchlorate in propylene carbonate [205]. Cyclic voltammetry was used to determine the potential at which polymerisation started, and films were subsequently deposited from each solvent using the lowest potential possible. The cyclic voltammogram for propylene carbonate and normalised absorption spectra for representative dedoped PEDOT films deposited from each solvent are shown in figure 7.3.

The cyclic voltammogram for electropolymerisation of PEDOT from propylene carbonate shown in figure 7.3 corresponds with previously reported voltammetry [261]. As for PBT electropolymerisation, there is a sharp rise in current on the first anodic sweep, at an increased potential compared to the return trace, occurring here at around 1.2 V *vs.* Ag. This overpotential on the first anodic sweep is again a manifestation of redox catalysis, as described in chapter 4. The redox reaction observed around -0.6 V corresponds to doping and de-doping of the conjugated polymer, and is accompanied by a clearly observable change in film colour from pale blue to dark blue or black. The inset of figure 7.3(a) shows

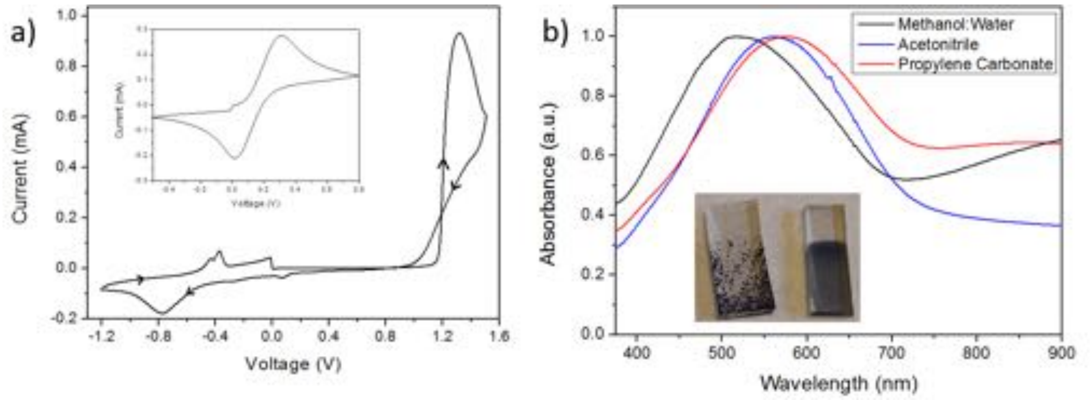

Figure 7.3: a) Cyclic voltammogram showing deposition of PEDOT onto ITO fingers from 0.01 M EDOT, 1.0 M $LiClO_4$ in propylene carbonate. The inset shows a cyclic voltammogram for the ferrocene redox reaction in an identical solution, other than an additional 0.01 M ferrocene. Both experiments were conducted at 50 mV/s. b) Absorption spectra for PEDOT films deposited from the three solvents indicated. The inset shows the improvement in film coverage from increasing the $LiClO_4$ concentration in propylene carbonate from 0.1 M (left) to 0.5 M (right).

the ferrocene/ferrocenium redox couple measured in the same solution used for PEDOT electropolymerisation, with 0.01 M ferrocene added. The anodic peak current occurs at 0.31 V *vs.* Ag and the peak cathodic current occurs at 0.01 V *vs.* Ag, giving an equilibrium potential for the reaction of 0.16 V *vs.* Ag. Having determined this reference potential following IUPAC guidelines [198], all further potentials are given relative to the Ag pseudoreference electrode.

Initial experimentation with PEDOT electropolymerisation revealed deposition of films at rates much faster than had been found for PBT electropolymerisation from ionic liquids. Since thin PEDOT films were required for hole-selectivity without high resistance, this limited deposition timescales to hundreds of milliseconds. Hence potentiodynamic techniques were impractical, and all further electropolymerisation presented here was conducted potentiostatically.

Absorption spectra were taken for films deposited from the three solvents and compared (figure 7.3(b)). Just as for unsubstituted and alyklated polythiophenes, PEDOT is redox-active and can be doped and de-doped. The absorption spectra shown here correspond to films de-doped at -0.8 V, held until the de-doping current stabilised. The spectral absorption profiles are similar for films deposited from all three solvents, but the wavelength of peak absorption increases in the order water:methanol $<$ acetonitrile $<$ propylene carbonate. The single, broad absorption peak of these de-doped films correspond to the π-π^* transition [262]. These peaks are featureless, probably as a result of energetic disorder leading to a distribution of bandgap energies in the film [263]; such absorption spectra are not unusual for electropolymerised PEDOT [259]. The wavelength of this absorption transition has been correlated to chain lengths in EDOT oligomers [264], as well as oligothiophenes [121], implying that redder absorption peaks in conjugated polymer films correspond to longer average conjugation lengths. Hence these spectra are interpreted to report longest PEDOT conjugation lengths for electropolymerisation from propylene carbonate. This agrees with previously reported optimal conjugation for PEDOT electropolymerised from propylene carbonate [259]. Further investigation was therefore conducted using propylene carbonate as the solvent. Given the peak in conductivity at $\sim$1.0 M $LiCl_4$ in propylene carbonate [205], this concentration of electrolyte was used in all subsequent experiments too.

Absorption spectra of de-doped PEDOT films electropolymerised from different EDOT concentrations in propylene carbonate are shown in figure 7.4(a). All of these films were electropolymerised at 1.2 V until 20 mC of charge had passed (over similar deposition areas for each sample). The main difference between the spectra shown here is the absorption strength. Films deposited from the extremes in EDOT concentration show the weakest absorption, with peak absorption measured for 0.01 M EDOT. Since all films were electropolymerised with the same charge consumed, there are three possible explanations for this systematic variation in absorption with monomer concentration. Either electropolymerisation is most ‘efficient’ at 0.01 M EDOT, such that more polymer film is deposited per unit of charge passed, or the polymer film is most structurally robust when deposited from 0.01 M EDOT, so that rinsing the film after deposition leads to the least material washed off, or the polymer that is deposited has greatest intrinsic absorption when electropolymerised from this monomer concentration.

No material was observed to detach from the film during rinsing, so this explanation was rejected. Inefficient electropolymerisation implies that relatively large amounts of charge are transferred to monomers or oligomers that don’t

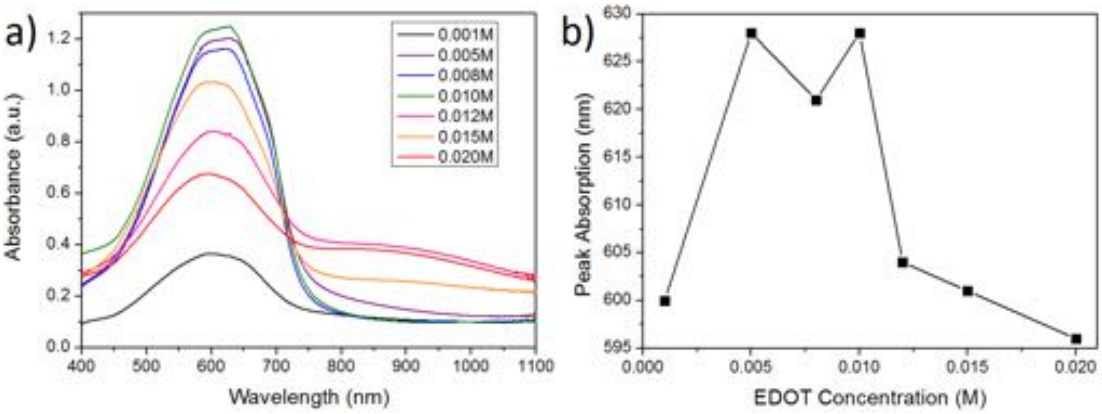

Figure 7.4: a) Absorption spectra of PEDOT films electropolymerised from varying EDOT concentrations and b) variation of peak absorption wavelength with EDOT concentration. The absorption spectra have not been normalised and all correspond to films electropolymerised having passed the same charge.

ultimately become incorporated into the adhered polymer film. Although lower EDOT concentrations might lead to radical oligomers being less likely to couple with other radical oligomers before diffusing away from the polymerisation region, it seems counter-intuitive that high EDOT concentrations would also cause lower electropolymerisation efficiency in this way. Instead, looking at the spectral features of the absorption spectra suggest that the third explanation for varying absorption could be appropriate. The wavelength of peak absorption is found to red-shift for intermediate EDOT concentrations (see figure 7.4(b)). This seems to occur as a result of an increasingly resolved vibronic structure in the absorption spectra, with growing absorption in the redder vibronic peak. In analogy to the polythiophene spectra discussed in earlier chapters, this would suggest decreasing exciton bandwidth and energetic disorder, *i.e.* enhanced crystallinity, for films deposited from the intermediate EDOT concentrations. Oscillator strength, and hence absorption for a given film thickness, is known to increase with crystallinity in spin-coated P3HT films [126], which would explain the observed rise in absorption for films deposited from intermediate EDOT concentrations. Hence intermediate EDOT concentrations were inferred to yield PEDOT films with improved crystallinity after electropolymerisation, and further electropolymerisation was conducted from 0.01 M EDOT solutions.

Having conducted these experiments, the optimised PEDOT electropolymerisation conditions were settled upon. Films were electropolymerised potentiostatically from 0.01 M EDOT in propylene carbonate with 1.0 M $LiClO_4$ supporting electrolyte. Following the results of PBT discussed in earlier chapters, in which low potentiostatic potentials were found to yield better molecular ordering, electropolymerisation was conducted at the lowest potential at which deposition was observed. Following cyclic voltammetry and current-time traces measured with different applied potentials, electropolymerisation was thus conducted at +1.2 V *vs.* Ag.

PEDOT Film Characterisation

Having optimised PEDOT electropolymerisation on standard ITO substrates, film deposition on interdigitated ITO fingers was attempted and characterised. Perovskite solar cells were fabricated as described in the experimental section of this chapter, with a range of PEDOT electropolymersiation, TiO_2 electrodeposition and $CH_3NH_3PbI_3$ perovksite spin-coating parameters. Solar cell performance would depend on the combination of all of these fabrication steps, but given that the initial aim for this project was proof-of-principle, a relatively small variety of deposition parameters were used. The highest power conversion efficiency was achieved for a device with PEDOT electropolymerisation lasting 1.0 s (see section 7.1.4). Characterisation of similarly-deposited PEDOT finger electrodes is described here.

Figure 7.5(a) shows the current-time trace recorded for PEDOT electropolymerisation. There are three distinct current regions. At very short times (< 0.15 s), the current sharply drops. This corresponds to charge bilayer formation in the solution near the electrode. Between ~ 0.15 s and 0.75 s, the current grows to a plateau which continues to the end of the deposition run. This initial current rise occurs as the growing radical monomer population induces redox catalysis, and the growing PEDOT film also increases the exposed surface available for polymerisation. By 0.75 s, the radical monomer and oligomer populations reach steady-state and the current stabilises.

The PEDOT film thickness was measured by atomic force microscopy (AFM). PEDOT was deposited on one half of the interdigitated fingers, alternating with fingers that were left with bare ITO. Tapping mode AFM was used to scan across

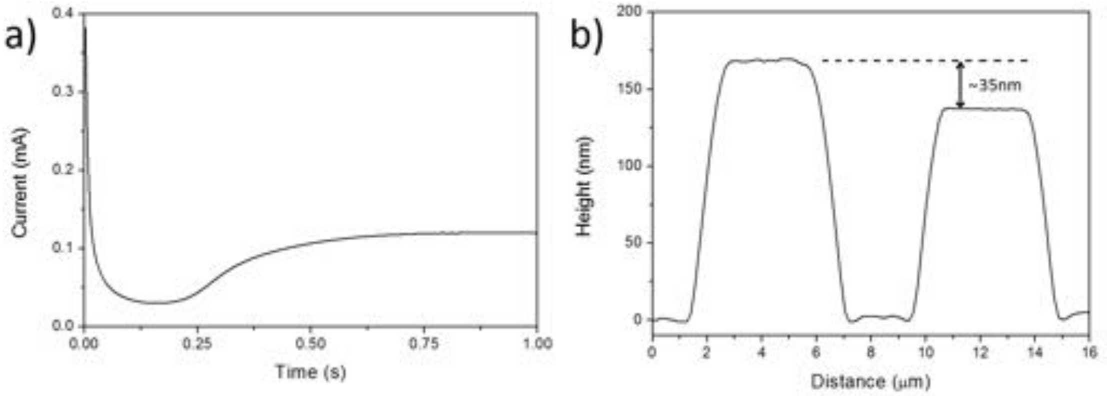

Figure 7.5: a) Current-time trace for deposition of PEDOT onto an ITO finger at 1.2 V *vs.* Ag; b) AFM scan across adjacent ITO fingers, one bare and one with PEDOT coverage, averaged over 5 μm of finger length.

two adjacent fingers. The height recorded aross this profile, averaged over 5 μm of finger length, is shown in figure 7.5(b). Taking the difference in average height between the bare ITO and PEDOT-coated ITO gives a PEDOT thickness of ~ 35 nm.

Scanning electron microscopy (SEM) was also used to image the PEDOT film morphology. Figure 7.6 shows an ITO finger electrode before (a), and after (b) electropolymerisation. Close inspection of the images reveals the rough, granular morphology of the ITO being replaced by a more 'globular' morphology. This PEDOT morphology extends over the whole ITO electrode, suggesting full coverage.

PEDOT Doping

Further characterisation of the electropolymerised PEDOT films was carried out with X-ray photoelectron spectroscopy (XPS) and ultraviolet photoelectron spectroscopy (UPS). Figure 7.7 shows XPS spectra in the S 2p, O 1s and C 1s orbital regions. These spectra were taken for PEDOT films electropolymerised on gold-coated glass slides because films deposited on ITO charged too much during XPS analysis to obtain reasonable measurements.

The S 2p region of the XPS spectrum exhibits a doublet at 162.4 eV and 163.5 eV, corresponding to the S $2p_{3/2}$ and $2p_{1/2}$ features respectively [265]. There is a third feature centred around 165.2 eV, 1.7 eV higher than the main peak at

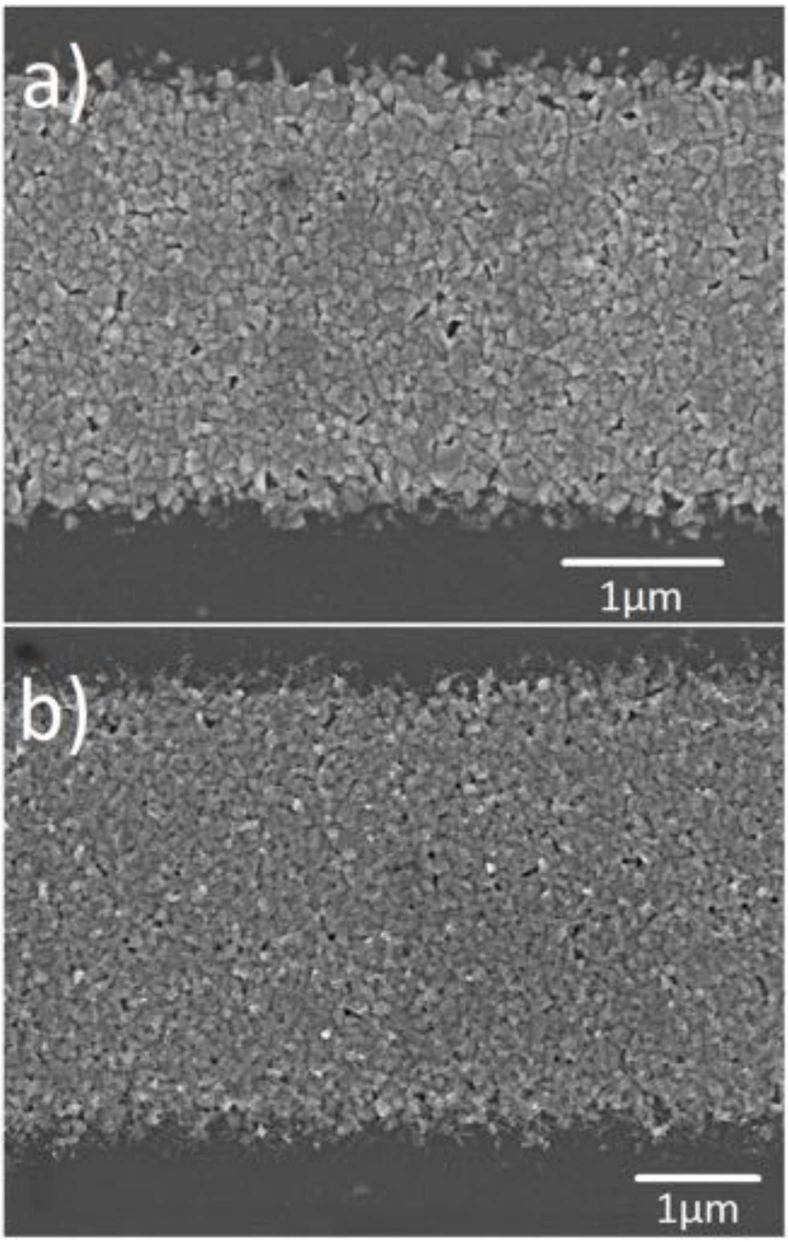

Figure 7.6: SEM images of the ITO finger, a) before and b) after PEDOT deposition. The PEDOT deposition conditions were +1.20 V *vs.* Ag for 1 s from 0.01 M EDOT, 1.0 M $LiClO_4$ in propylene carbonate. Close inspection of the images suggests essentially complete PEDOT coverage.

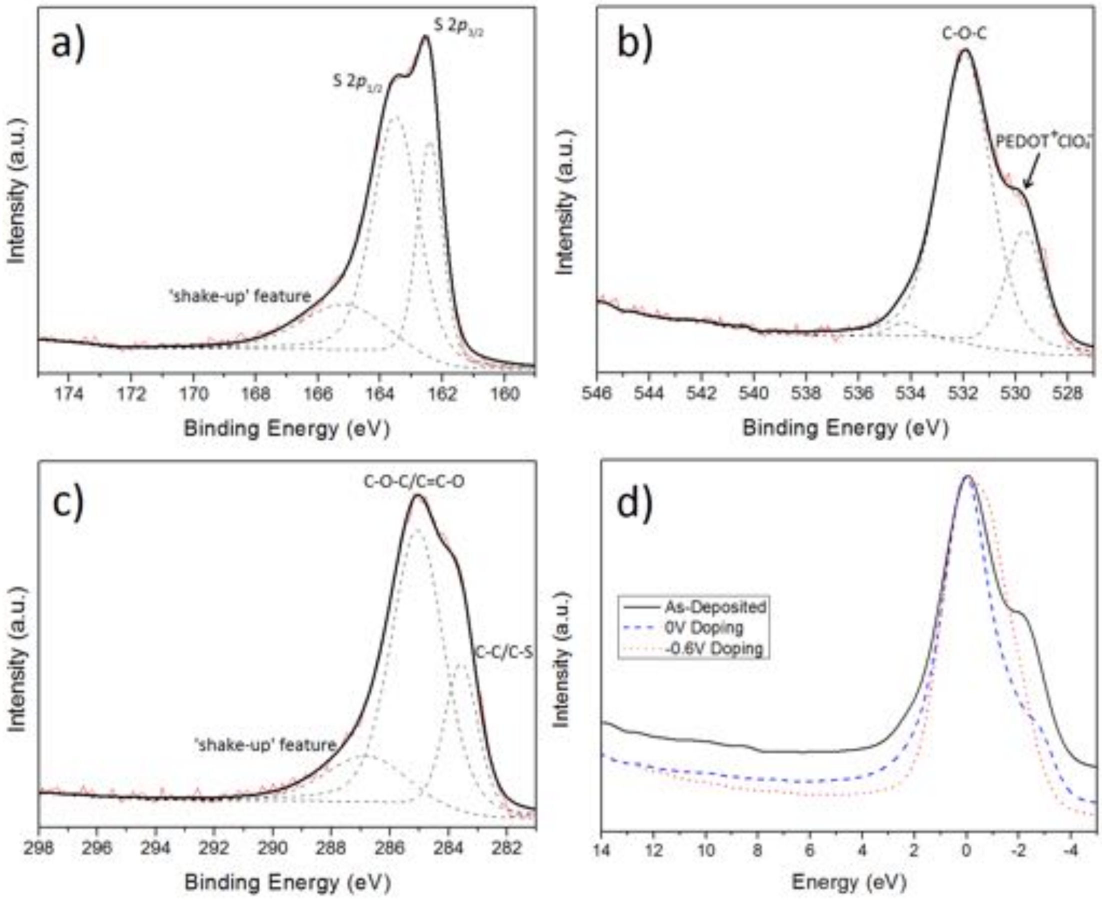

Figure 7.7: XPS spectra of a) S 2p, b) O 1s and c) C 1s orbitals for PEDOT films as-deposited, and d) comparison of O 1s spectra for PEDOT films after de-doping at different potentials.

163.5 eV. This closely matches the π-π^* transition bandgap [266], and hence is likely a shake-up feature (resulting from the photoejected electron losing some energy by exciting a separate electron from the HOMO to the LUMO level) [265].

The O 1s region of the spectrum exhibits three features, namely the main C-O-C peak at 531.9 eV [267], a small peak at 534.3 eV, and a third peak at lower binding energies, which can be attributed to the ClO_4^- counter-ion [267]. Indeed, the magnitude of this third peak signal relative to the first decreases as the PEDOT films are de-doped at increasingly negative potentials after electropolymerisation (see figure 7.7(d); the spectra here have been normalised and the origin set to the peak signal for each trace to account for slight variations in bandgap offset, presumably caused by sample charging). This demonstrates that de-doping the PEDOT film decreases the ionic bonding between the PEDOT and ClO_4 dopants, returning the PEDOT to its neutral, semiconducting state. This de-doping effect was also seen in absorption spectra taken for films de-doped at different potentials, in which absorption at longer wavelengths than the π-π^* transition decreases with de-doping as interband polaron and bipolaron states are removed (not shown here).

The C 1s region of the spectrum shows a main peak at 285.1 eV, which is likely to arise from the C-O-C and C=C-O bonds [267], a second peak at 283.6 eV, which corresponds to C-C and C-S bonds [267], and a shake-up feature at 286.8 eV [267].

Since the PEDOT film is being used as a charge-selective electrode layer, one of its most important properties is its workfunction. Hence ultraviolet photoelectron spectroscopy was carried out for PEDOT films electropolymerised on gold, after de-doping at various potentials to investigate the influence of doping level on the workfunction. The spectra obtained are shown in figure 7.8. Figure 7.8(a) shows the whole UPS spectrum, essentially the range of energies with which photoelectrons are emitted from the sample surface. The highest detected energies (figure 7.8(b)) correspond to photoelectrons that leave the sample surface without any inelastic collisions before reaching the detector. Hence these are emitted with kinetic energies matching the photoexcitation energy, minus the HOMO ionisation energy that they have to overcome to leave the sample surface. The lowest detected energies (figure 7.8(c)) correspond to photoelectrons that only just reach the detector after inelastic collisions, with kinetic energies approaching zero. The whole spectrum is shifted by Fermi level alignment between the sample and the detector (hence all samples exhibiting the same HOMO energy), and by a deliberately-applied potential to separate the signal from secondary eletrons ejected from the detector itself. Hence the absolute values vary, but the PEDOT workfunction can be measured by deducting the difference in HOMO and onset energy from the photoexcitation energy [268]. The PEDOT workfunctions for different de-doping potentials have been calculated in this way, and are shown in figure 7.8(d).

The measured PEDOT workfunctions agree roughly with literature values (which themselves show reasonable variation) [268–270]. For the most part, the variation in workfunction with doping level is also as previously reported, with

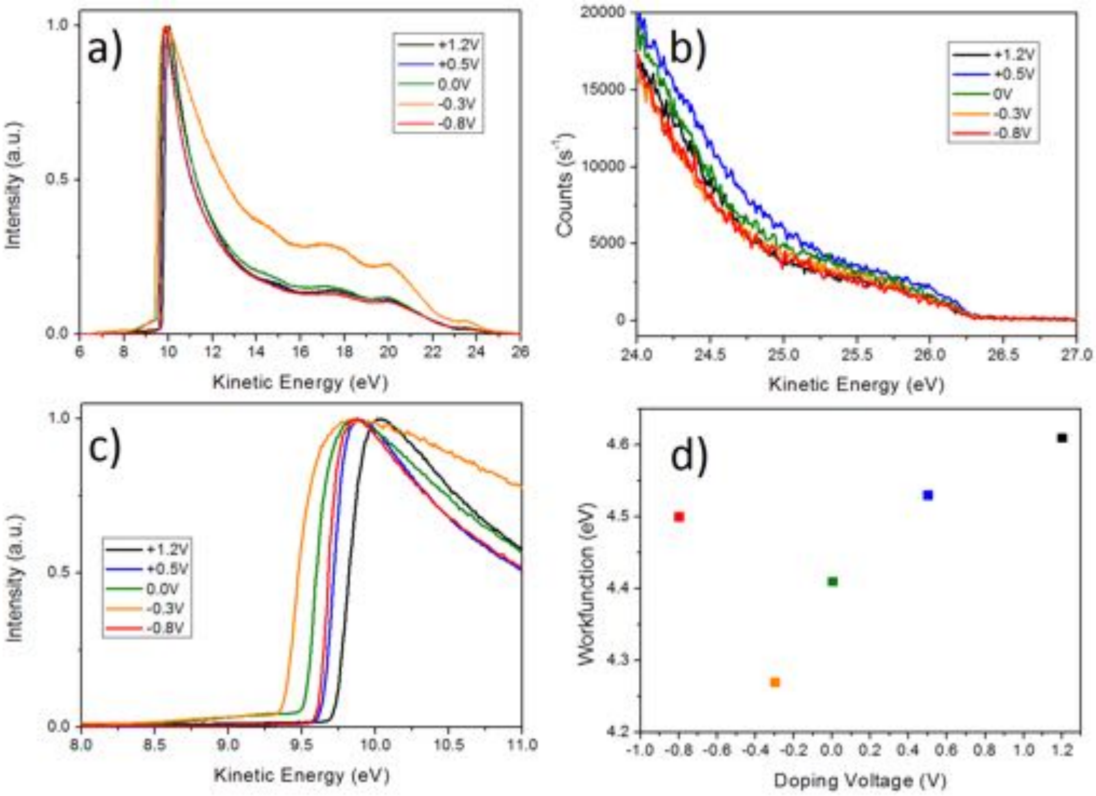

Figure 7.8: Normalised UPS spectra of PEDOT films de-doped at various potentials after electropolymerisation. The full spectra are shown in figure (a), with the HOMO and onset regions displayed in figures (b) and (c) respectively. Figure (d) plots the workfunctions calculated from the difference in HOMO and onset energy, taking into account the 21.2 eV He I α excitation source energy.

increased doping (more positive doping potential) leading to greater workfunctions [271, 272]. It is not known why the fully de-doped film does not follow this trend. Unfortunately, only one measurement was taken for each doping level, so it is not known if this last workfunction is an accurate value or not. Measurement of the workfunction of organic materials is known to be very sensitive to preparation and measurement conditions [273], so there could have been a problem with surface contamination, for example. Alternatively, given the problems that were encountered with charging for films on ITO substrates rather than gold substrates, it could be that the lower conductivity of fully de-doped PEDOT affects the measurement. Previously reported measurements have observed a linear relationship between doping potential and resultant workfunction over the full doping potential range [271, 272]. In any case, it is clear that the workfunction can be continuously tuned within the range of at least 4.2 –4.6 eV *via* electrochemical doping post-deposition. Furthermore, the fully-doped PEDOT-coated electrodes used in the back-contact perovskite solar cells are assumed to have a workfunction of about 4.6 eV.

7.1.4 Back-Contact Lead Halide Perovskite Solar Cells

This section and the next section summarise results obtained with the back-contact pervoskite solar cells employing the PEDOT-coated electrodes described in this chapter thus far. My role was to prepare the PEDOT electrodes, these sections describe work conducted by other members of the collaboration, led by Luis Pazos-Outón, and is included for context and completeness.

As described previously, a narrow range of TiO_2, PEDOT and perovskite deposition parameters were investigated. PEDOT was electropolymerised as described earlier (potentiostatic deposition from 0.01 M EDOT, 1.0 M $LiClO_4$ in propylene carbonate at +1.2 V *vs.* Ag) for 0.25 s, 0.50 s, 0.75 s and 1.0 s. The highest power conversion efficiency recorded for a back-contact device was 0.11 %, obtained with a device using PEDOT electrodes that had been electropolymerised for 1.0 s. The current-voltage trace for this device is shown in figure 7.9(a). Given that this was the longest of the deposition times used, it is not known if extending the deposition time would improve the performance further. In any case, the other fabrication parameters were being varied too, so very few devices were tested with each set of fabrication parameters. Figure 7.9(a) also shows the current-voltage measurement from the highest-performing device fabricated without charge selective layers (*i.e.* perovskite spin-coated on top of the bare ITO interdigitated electrodes). This device produces essentially no photocurrent, demonstrating the clear advantage of charge-selective electrodes. This is to be expected, since without charge selectivity, there is essentially no asymmetry in the device to yield an output voltage.

For the device with selective contacts, the sharp increase in current at voltages more negative than −0.4 V could be evidence of an extraction barrier limiting current output (although it might just be the device shorting due to photo-induced

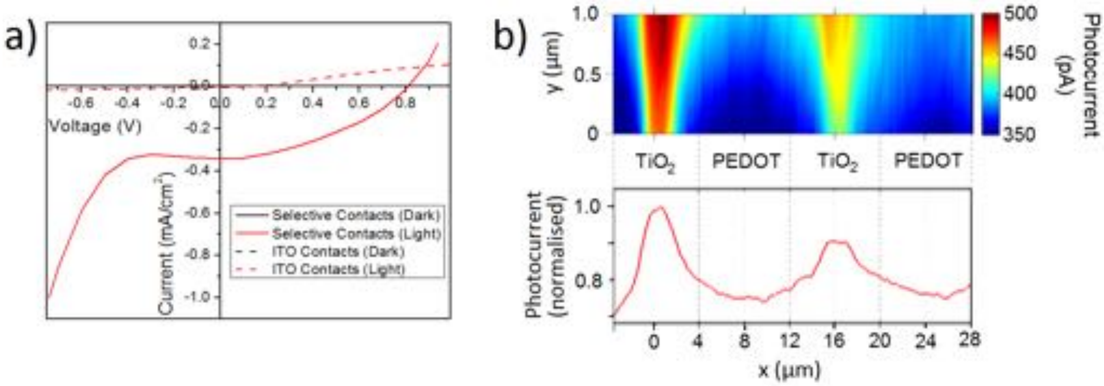

Figure 7.9: a) Current-voltage measurement for best-performing back-contact perovskite solar cells, with and without selective contact layers over ITO. b) Photocurrent map and trace at constant y, measuring current output under localised illumination. Note that the photocurrent axes do not start at zero.

breakdown). Indeed, using confocal microscopy to scan illumination localised with resolution $< 1\,\mu m$ yields a photocurrent map as shown in figure 7.9(b). The photocurrent extracted with illumination over the TiO_2-coated electrodes reaches 500 pA, whereas for illumination over the PEDOT-coated electrodes, the photocurrent doesn't exceed 400 pA (note that the photocurrent axes do not start at zero in figure 7.9(b)). This suggests that the extraction barrier exists at the PEDOT electrode, although this hasn't been investigated further. Fabricating and testing solar cell devices employing PEDOT films with different doping levels (and hence workfunctions) would be a sensible next step. Recently, a back-contact perovskite solar cell employing 2 µm-wide interdigitated fingers (with 2 µm separation) of ZnO-coated ITO and NiO-coated aluminium as electron- and hole-extraction layers respectively reported power conversion efficiencies of 3.2% [274].

7.1.5 Photon Recycling in Lead Halide Perovskites

The back-contact device architecture also led to experiments demonstrating the 'photon recycling' effect in $CH_3NH_3PbI_3$ perovskite films [258]. Confocal microscopy was used to provide localised photoexcitation of the device away from the outer finger electrodes in order to determine lateral charge diffusion lengths, as the relationship between this length and the interdigitated electrode pitch strongly impacts device performance. These experiments revealed that charge extraction was possible even with excitation over 100 µm from the nearest electrodes (see figure 7.10(a)). The observation of excitation propagation (between absorption and charge extraction) over such large distances implies either that charge diffusion lengths also extend over these distances, considerably further than previously reported for polycrystalline thin films [255, 256], or that some other process is extending excitation propagation.

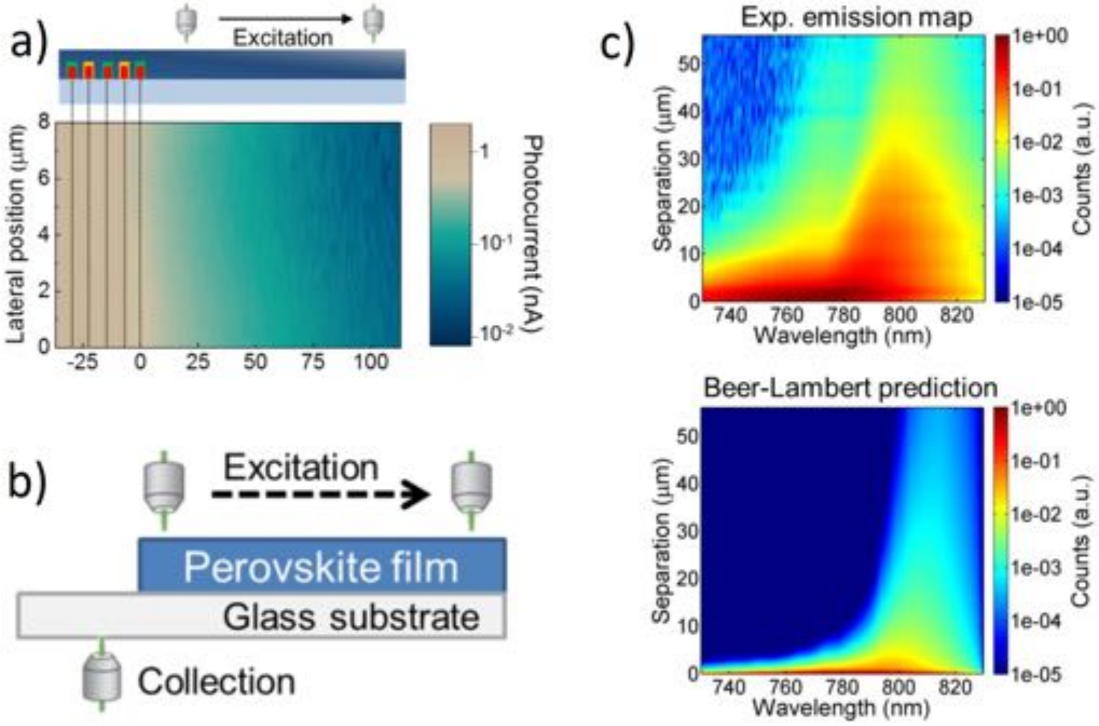

Figure 7.10: a) Photocurrent was collected even with photoexcitation 50 µm away from the electrodes, b) Experimental setup for photoluminescence mapping, c) Comparison between experimental (top) and predicted (bottom) spectral photoluminescence mapping, indicating excitation propagation beyond Beer-Lambert expectations. These diagrams are all adapted from reference [258], and have been prepared by collaborators.

Strong phonon coupling with charge carriers in $CH_3NH_3PbI_3$ perovskite films leads to large homogeneous broadening of the emission spectrum [275], which in combination with a small Stokes shift [275] leads to significant overlap between the emission spectrum and the absorption edge and tail. Combined with low non-radiative decay [276], these properties harbour the potential for significant photon recycling, whereby photoexcited charge carriers recombine and re-emit before being regenerated elsewhere in the film after re-absorption. Such processes allow excitation propagation far beyond charge diffusion lengths. The weak absorption spectrum tail at wavelengths longer than the sharp absorption edge allows the reddest part of the emission to propagate over the largest distances before re-absorption; the emission spectrum is un-affected by excitation energy [275], so excitation propagation *via* this red light does not red-shift successive emissions (the additional energy required is probably provided by phonon-assisted thermalisation).

Evidence for such photon recycling comes from comparison between detected photoluminescence and that anticipated from simple Beer-Lambert absorption as a function of separation between excitation and detection. Spectral absorption coefficients for use in the Beer-Lambert model were extracted from photothermal deflection spectroscopy and photoluminescence excitation spectroscopy, accounting for non-radiative and radiative post-absorption mechanisms respectively. A confocal setup allowing localised excitation and detection was used in combination with thin perovskite films ($\sim$100 nm thick) that wave-guide most photoluminescence emission through the film rather than allowing scattering out of it [258] (see figure 7.10(b)). Placing the detector at the edge of the film captures light waveguided through the film as well as light emitted luminescently at the edge of the film, giving a complete measurement of the internal photon population.

The experimental and theoretical spectra are shown in figure 7.10(c), from which it is clear that Beer-Lambert absorption underestimates the detected outscattered light. In addition to simply underestimating this detected emission, the Beer-Lambert analysis also fails to reproduce the emergence of two spectral peaks, corresponding to gradually red-shifting emission and persistent emission centred around 765 nm. These peaks are interpreted as corresponding to emission waveguided through the film, red-shifted by the absorption spectrum, and intrinsic perovskite emission from recycled photons respectively. This interpretation is corroborated by the photocurrent measurements, with reported charge densities matching those expected from the observed emission centred around 765 nm (for the fluences used here, photoluminescence in organometal perovskites results primarily from bimolecular recombination [276], so the square-root of photoluminescence is expected to correspond to charge density). The persistence of the intrinsic emission spectrum amidst the red-shifting waveguided emission, and its spatial correlation with measured charge densities provide strong evidence for the photon recycling process.

7.2 Perovskite Solar Cell Fabrication *via* Electrodeposition

7.2.1 Background

The solution-processability of perovskite-based solar cells makes them an alternative to organic-based devices in the search for cheap photovoltaics [252, 277, 278]. However, the solvents used (such as N,N-dimethylformamide or γ-butyrolactone) are typically toxic, increasing production costs and potentially limiting the environmental benefits. Additionally, while simple spin-coating techniques have led to very efficient devices, there have been problems with incomplete or inhomogeneous film coverage limiting reproducible performance in simple planar architectures as a result of pinholes in the film providing shunt current paths [279, 280]. Recent progress has been made on this front by controlling crystal growth through the choice of anion in the lead precursor, most notably with lead acetate [281]. Mesoporous scaffolds have also been used to avoid shorting problems, but this complicates device architecture, adding fabrication steps. Single-step spin-coated films typically require an annealing step before crystalline perovskite films are obtained [279, 282]. This again represents an additional fabrication step, which would be expensive for large-scale manufacture. Finally, relatively few publications investigate the large-area devices required for commercialisation [86], so it is worth exploring alternative fabrication routes which may be more amenable to these large areas.

As an alternative to solution-processing techniques, thermal vapour deposition has been used to fabricate simple planar devices with uniform perovskite film coverage and correspondingly high efficiency (15.4 %) [82], but this requires high temperatures and vacuums. Another technique worth exploring for cheap, large-scale manufacture is electrodeposition. This is already used in large-scale manufacturing of silicon solar panels [283], involves little material wastage or toxic solvents, and can yield complete coverage of exposed areas regardless of morphology [284, 285]. Additionally, electrodeposition may allow more control over the morphology of the perovskite part of a device, for example *via* templated techniques such as those shown for polythiophene gyroid and interdigitated structures described earlier in this thesis. Although the large exciton diffusion lengths

($\sim 100\,\mathrm{nm} - 1\,\mu\mathrm{m}$ [255,256]; now shown to be influenced by photon recycling [258]) found in perovskites make it unlikely for bulk heterojunction structures to be beneficial to solar cell performance, well-controlled perovskite morphologies could be beneficial in other applications. For example, grating-like patterns could be useful for fabricating distributed feedback lasers using perovskite gain media [276, 286]. Electrodeposition of the perovskite material combined with a grating template defined by photolithography could in principle allow simple fabrication of such devices. Alternatively, nanostructure-induced exciton confinement could reduce dissociation in perovskite-based LEDs and improve current efficiency [287].

Electrodeposition has been used in the fabrication of a variety of perovskite films, in particular for high-temperature superconductor [288–290], solid oxide fuel cell [291, 292] and dielectric applications [293]. These have typically involved electrodeposition of an amorphous film followed by high temperature annealing, although some direct perovskite electrodeposition has been reported [290]. Organometal halide perovskites have also been fabricated *via* electrodeposition of lead oxide films, followed by chemical conversion to the desired perovskite [294]. However, upon commencement of this research, such electrochemically prepared organometal halide films had been restricted to two-dimensional perovskites (interesting for optical properties as a result of their inherent multiple quantum well structure) rather than the three-dimensional perovskites employed in high-efficiency solar cells.

The aim of this project was therefore to investigate electrodeposition as a technique for fabrication of organometal halide perovskite films. Despite the potential for nanostructured perovskite films, this initial investigation of electrodeposition was limited to planar films, to simplify fabrication and characterisation of the resulting morphology. Hence solar cells were fabricated to assess the performance of electrodeposited films in devices.

7.2.2 Experimental Methods

The fabrication method was developed with reference to the previously-reported fabrication of two-dimensional organometal halide perovskite materials *via* electrodeposition [294]. An overview of the process is given in figure 7.11. First, lead oxide is electrodeposited onto the substrate. This is converted to lead io-

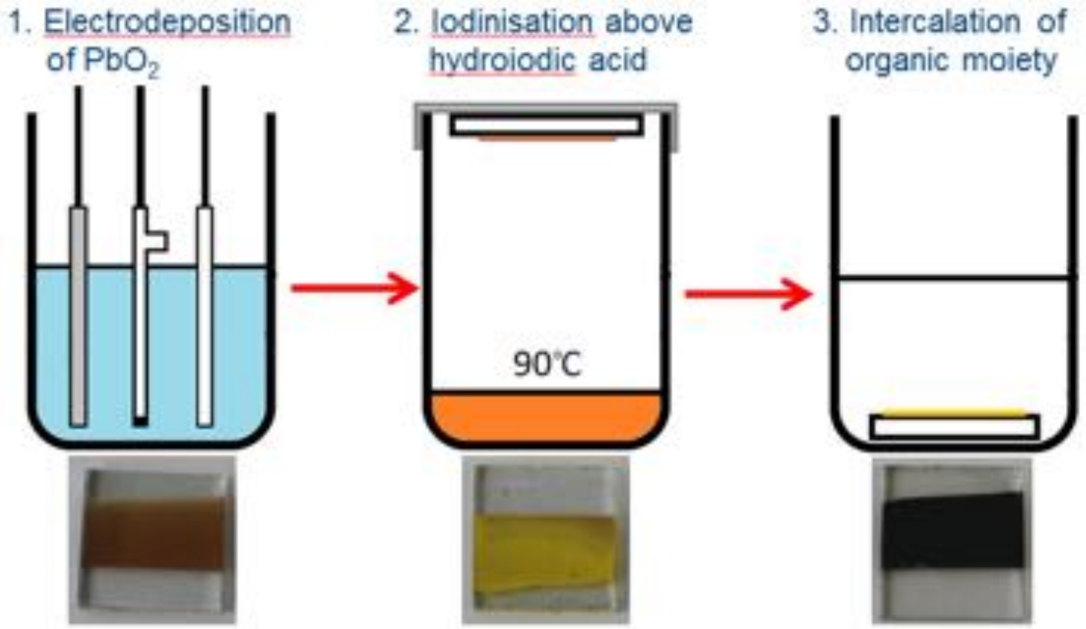

Figure 7.11: An overview of the fabrication process. First, PbO_2 films are electrodeposited onto TiO_2-coated FTO using a three-electrode setup. This PbO_2 film is iodinised to PbI_2 through exposure to hydroiodic acid vapour. Finally, the PbI_2 film is submerged in a methylammoinium iodide solution, converting it to methylammonium lead iodide perovskite. Photographs of the films after each stage are shown beneath the respective diagrams.

dide and then to the desired perovskite material, namely methylammonium lead iodide ($CH_3NH_3PbI_3$). For the fabrication of solar cells, P3HT was spin-coated on top of the perovskite film as a hole transport layer, and gold electrodes were evaporated through a mask for charge collection. In contrast to the fabrication method reported in the literature [294], TiO_2-coated substrates were used with a view to forming an electron-extraction layer in a solar cell architecture. The compact TiO_2 layer was deposited on FTO-coated glass substrates as described in chapter 6.

A standard three-electrode setup was used for electrodeposition. A platinum foil counter electrode and saturated calomel reference electrode were used, with the TiO_2-coated FTO substrate as the working electrode. The electrodeposition bath consisted of equal parts of 0.1 M aqueous sodium acetate and aqueous lead acetate, of which different concentrations were investigated. A representative cyclic voltammogram for lead dioxide deposition is shown in figure 7.12, in this case using 2 mM lead acetate. Potentiostatic deposition at + 1.2 V vs SCE gave a uniform orange/brown film, identified as lead dioxide (see Results and Discussion section). The lead dioxide film was then converted to lead iodide, before further conversion to the desired perovskite film $CH_3NH_3PbI_3$. A variety of iodination and intercalation techniques were tested, and these are also discussed further in the Results and Discussion section.

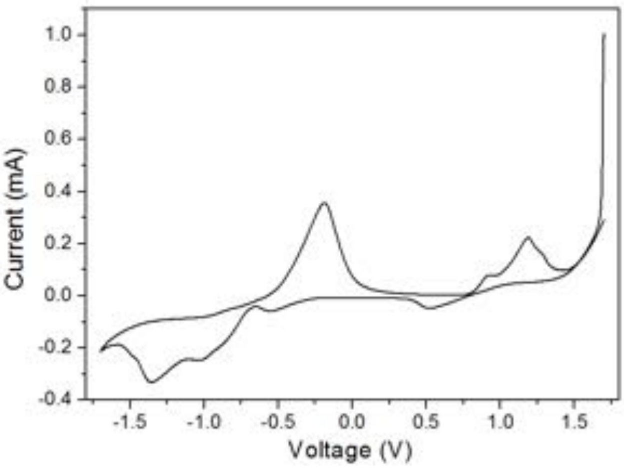

Figure 7.12: Cyclic voltammogram for lead dioxide deposition from equal parts 0.1 M aqueous sodium acetate and 2 mM lead acetate. The scan started at + 1.7 V vs. SCE, and scanned to −1.7 V and back at 10 mV/s. Inset shows a current-time trace for potentiostatic deposition at + 1.2 V vs SCE.

Iodination required either iodine crystals or hydroiodic acid, both of which were simply purchased from Sigma Aldrich. However, intercalation of the lead iodide with the organic moiety to yield perovskite films required methylammonium iodide, which was synthesised in the laboratory using the following procedure. First, absolute ethanol was placed in a sealed round-bottomed flask and bubbled with nitrogen for an hour to remove oxygen. Next, 24 ml of 35% methylamine in absolute ethanol was injected into the ethanol, followed by 10 ml hydroiodic acid (without added stabilisers) injected slowly over the course of ~10 minutes. The ethanol solution was stirred throughout by magnetic stirrer bars, and left stirring and purging with nitrogen for an hour after injection. This should produce methylammonium lead iodide in the ethanol solution, which needs to be extracted and purified. The flask containing the methylammonium iodide solution was attached to a rotary evaporator and partially submerged in a water bath set at 40°C. The ethanol slowly evaporated to leave crystals of methylammonium iodide in the round-bottomed flask . This was repeatedly rinsed with diethyl ether and filtered, until plain white crystals were obtained. Finally, the methylammonium iodide crystals were dissolved in anyhdrous ethanol at 100°C and left to re-crystallise overnight in the freezer.

To complete the solar cell devices, 30 mg/ml P3HT was spin-coated from ortho-dichlorobenzene at 1500 rpm for 45 s. Finally, 80 nm thick gold electrodes were thermally evaporated onto the device through a mask defining pixels.

7.2.3 Results and Discussion

Initial Fabrication and Photovoltaic Performance

First, identification of each intermediate material in the fabrication route was established. XRD spectra taken of the orange/brown films initially obtained from electrodeposition confirmed identification as lead dioxide (see figure 7.13). However, varying the lead acetate concentration in the electrodeposition bath yielded different phases of lead dioxide, namely orthorhombic (also known as α-PbO_2) or rutile (β-PbO_2) phases at high and low lead acetate concentrations respectively. Note that the deposition of lead dioxide differs from the deposition of lead oxide reported by Dwivedi *et al.* [294], despite identical electrodeposition conditions. This suggests a large influence from the substrate on deposition, since the only difference here is the spin-coated TiO_2 substrate compared to their ITO-coated glass substrate.

Cross-sectional SEM images and AFM scans were taken of the lead dioxide films to assess film morphology and thickness in relation to electrodeposition conditions. All films were deposited at + 1.2 V *vs* SCE, until 120 mC of charge had been transferred. Varying lead acetate concentrations demonstrated clear morphological differences between orthorhombic and rutile phase lead dioxide, as shown in figure 7.14. Beneath lead acetate concentrations of around 0.02 M, highly anisotropic, needle-like structures of β-PbO_2 form, with average height deviation (R_a) reaching hundreds of nanometres. Above 0.02 M lead acetate, the morphology shifts to smooth, globular films of α-PbO_2 with average height

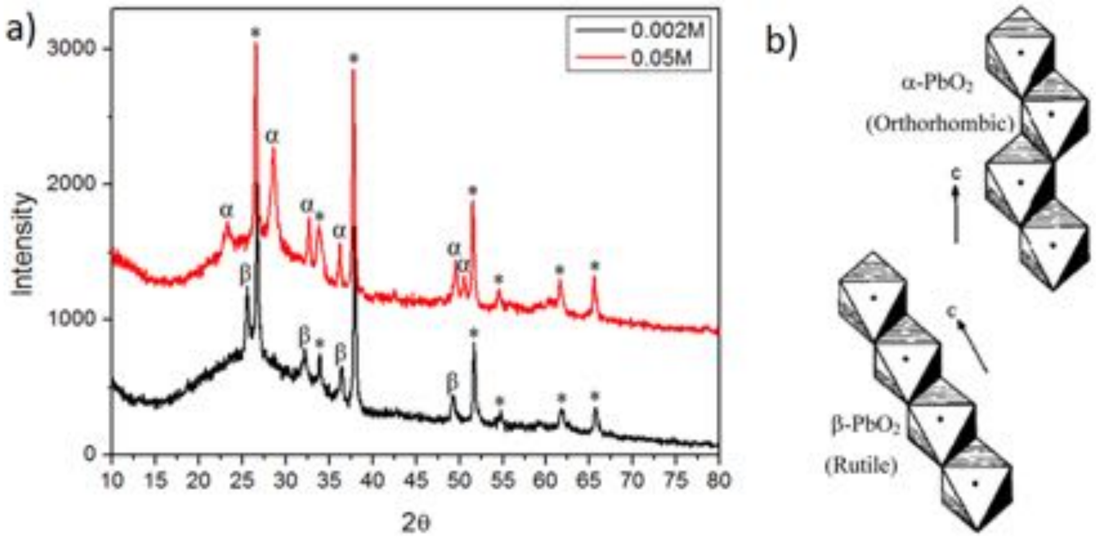

Figure 7.13: a) XRD spectra of lead dioxide films deposited at low (0.002 M, black) and high (0.05 M, red) lead acetate concentrations. The two different concentrations yield apparently pure films of two different crystalline phases of lead dioxide, namely rutile (β-PbO_2) for 0.002 M, and orthorhombic (α-PbO_2) for 0.05 M [295, 296]. The peaks labeled with an asterisk correspond to the FTO/TiO_2 substrate. b) The different PbO_2 phases are presented schematically, reproduced from Li *et al.* [297].

deviation consistently around 20 nm. Since one of the main goals of this project was to fabricate perovskite films of controlled morphology, α-PbO_2 films were chosen for all further investigation as smooth films seem to be more controllable and desirable.

Compact films of lead dioxide were deposited from 0.05 M lead acetate with different values of total charge consumed during the deposition. Cross-sectional SEM images showed that the film thickness increased roughly linearly with the charge density of deposition, as shown in figure 7.14. The line of best fit doesn't quite pass through the origin, but this could be due to, for example, quicker initial film growth. Films are likely to start growing out from nucleation sites, making very thin films patchy and their thicknesses ill-defined. Measuring very thin film thicknesses is not suited to cross-sectional SEM analysis.

With compact films of relatively smooth, thickness-controllable PbO_2 attain-

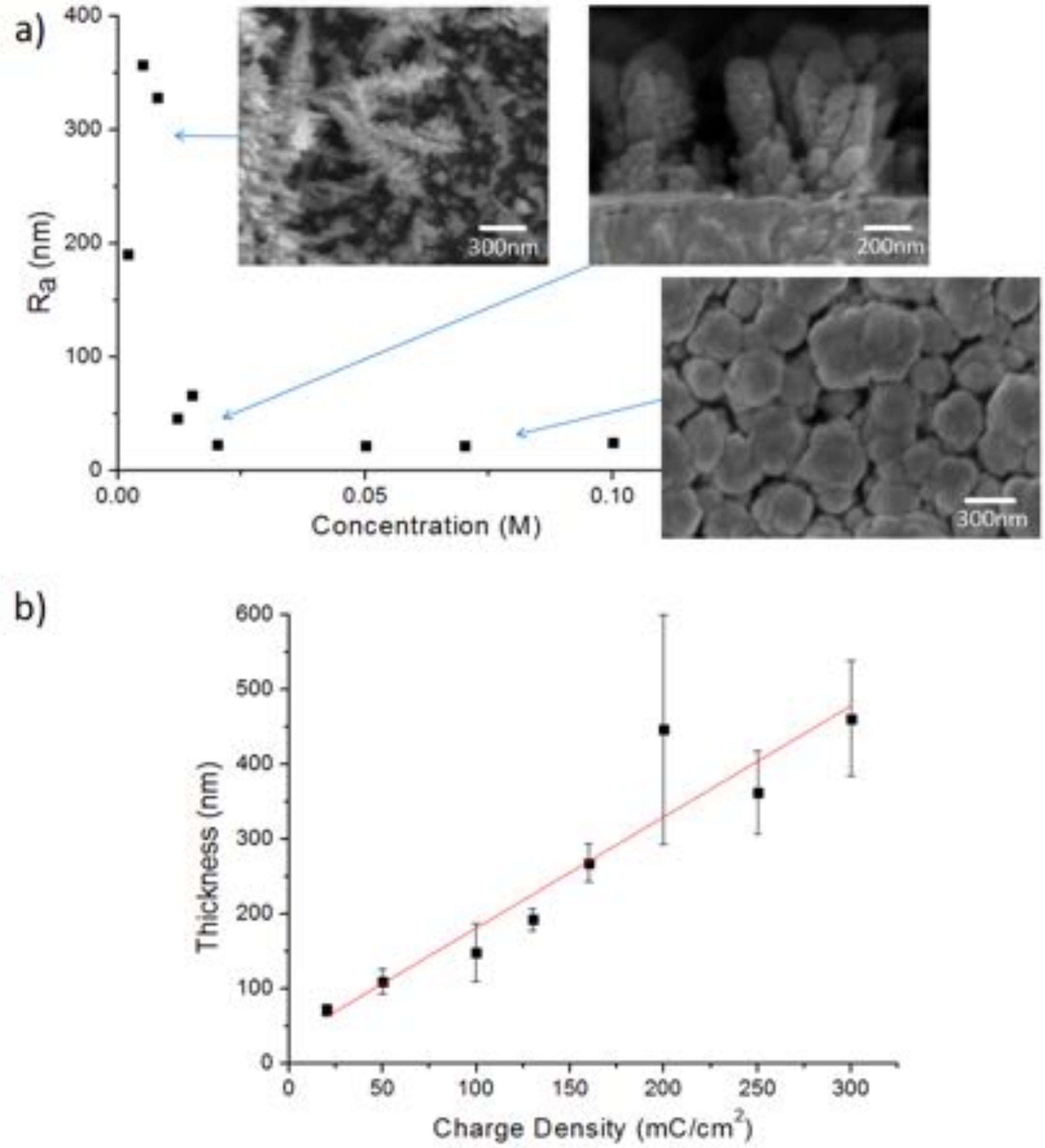

Figure 7.14: a) Average height deviation at the surface of lead dioxide films for different lead acetate concentrations, as measured by AFM. SEM images show the different morphologies obtained at low and high lead acetate concentrations, with a cross-sectional image of an intermediate film. b) The relationship between the thickness of electrodeposited α-PbO_2 film and the density of charge consumed during its deposition. Data points represent the mean thickness measured by cross-sectional SEM analysis across different points on the relevant films, with error bars showing the standard deviation of thicknesses measured.

able, iodination to lead iodide was investigated. Following Dwivedi *et al.* [294], this was first attempted by holding the lead dioxide films above hydroiodic acid, heated to 90°C , as shown in figure 7.11. After several minutes, the film had turned from its initial orange/brown colour to a vivid yellow. XRD measurements taken on the resultant film confirmed its identity as lead iodide, as shown in figure 7.16. Almost all peaks correspond to hexagonal PbI_2, although small peaks around 23° and 68° suggest a minority presence of some other PbI_2 phase. The main additional peak at 23° has been observed previously in lead iodide films spin-coated onto TiO_2 [298]. Importantly, none of the lead dioxide peaks are visible in the XRD spectrum taken after iodination, implying full conversion to lead iodide. However, the iodination process was not well-controlled, as iodination (as judged from the colour change) took variable amounts of time, from seconds to minutes. Additionally, condensation from the hydroiodic acid formed on the film during iodination, which was prone to removing the iodinised film. SEM analysis also revealed a wide range of lead iodide morphologies, as shown in figure 7.15. These ranged from apparently compact films with roughness, R_a, around 75 nm to films with increasingly evident crystallite grain morphology. As these grains become more clearly defined, pinholes in the film also grow, revealing the FTO/TiO_2 substrate beneath. Eventually, very large scale crystalline areas emerge. It is assumed that the morphology proceeds through this range of morphologies as iodination continues, but the difficulty in controlling the procedure and the differences in observable iodination rates makes this difficult to verfiy. XRD measurements seem to routinely show complete conversion from lead dioxide to lead iodide, suggesting that iodination can be halted at the compact film stage without leaving un-converted lead dioxide.

Finally, lead iodide films were converted to methylammonium lead iodide perovskite films by submerging in methylammonium iodide solution. The methylammonium iodide was synthesised as described in the experimental section, and dissolved at 10 mg/ml in isopropyl alcohol, all maintained in an argon atmosphere. The bright yellow lead iodide films changed colour to dark black very quickly upon submersion. XRD measurements confirmed the presence of methylammonium lead iodide perovskite as desired, although some lead iodide peaks were also present, indicating incomplete conversion (see figure 7.16). No thermal annealing step was required to form the black perovskite film.

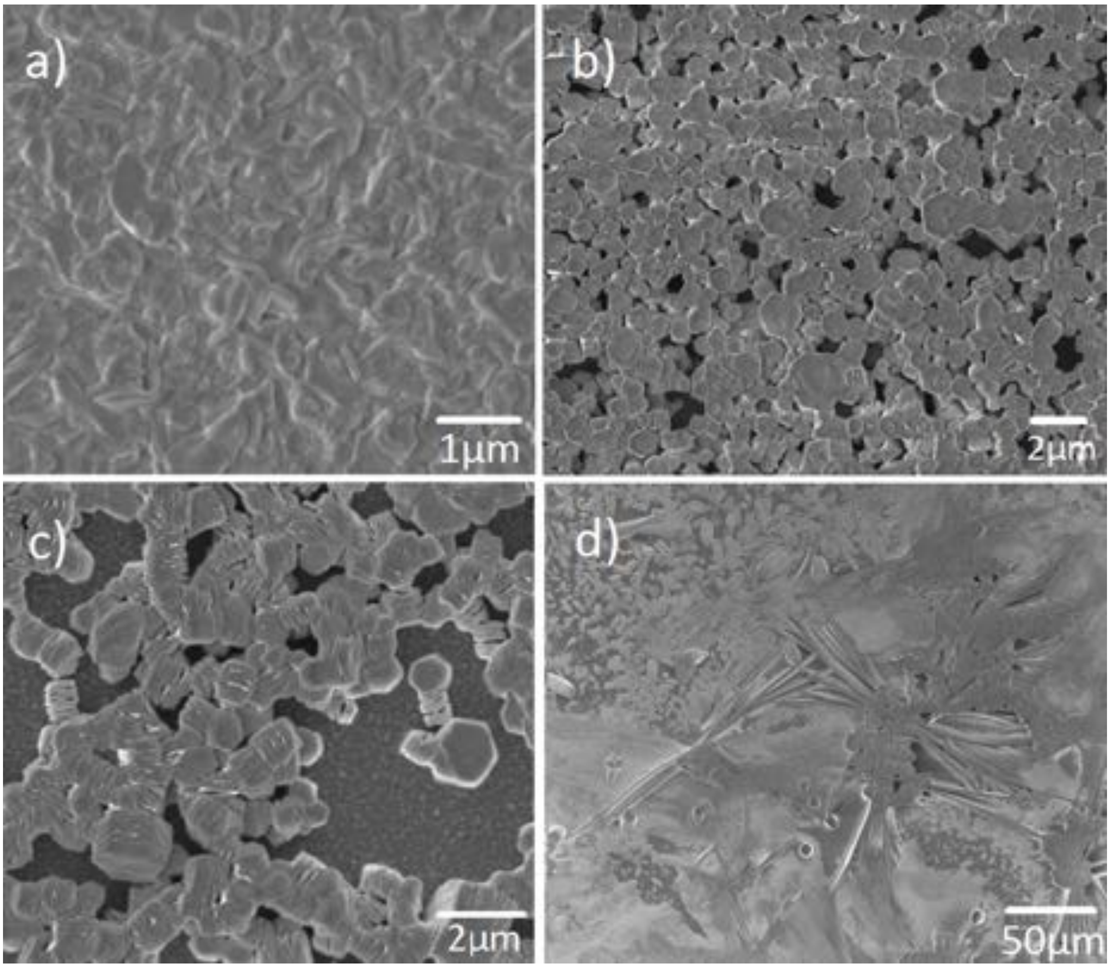

Figure 7.15: A variety of PbI_2 morphologies were observed after iodination of the PbO_2 films with hydroiodic acid. These range from relatively smooth, compact films (a) to increasingly granular films (b), (c) and eventually highly anisotropic, crystalline films with large ($\sim 10\,\mu m$) pinholes. It is assumed that this progression proceeds with increasing iodination, but this is not knwon for sure.

With $CH_3NH_3PbI_3$ obtained, P3HT was spincoated on top and finally gold contacts evaporated to enable measurement of photovoltaic performance. The JV and EQE traces measured for this device are shown in figure 7.17. A power conversion efficiency of 1.2% was recorded, with a low fill factor of 29% playing a large role in reducing the efficiency. The external quantum efficiency was also recorded, with a spectral profile matching the perovskite absorption spectrum

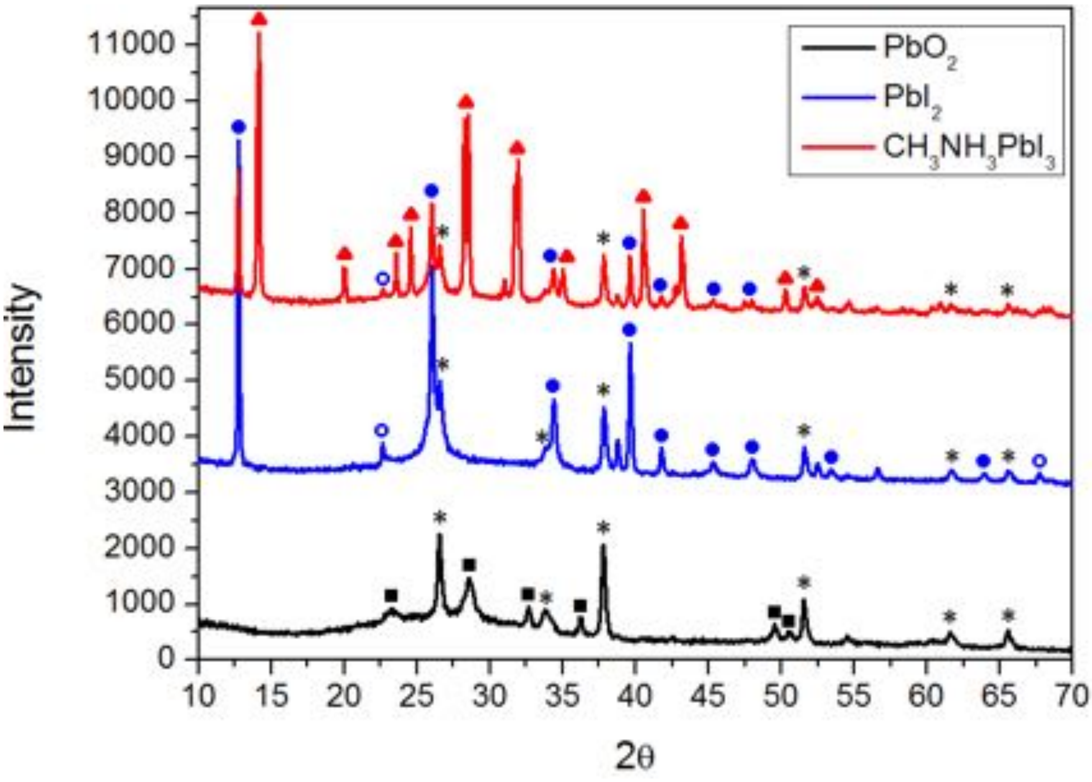

Figure 7.16: XRD spectra for each step of the fabrication route, namely α-PbO_2 (black), PbI_2 (blue) and CH_3NH_3 (red). Peaks are labeled with asterisks (for FTO/TiO_2; referenced from blank substrate spectrum), black squares (α-PbO_2; from [295]), blue dots (hexagonal PbI_2; from [299]), and red triangles ($CH_3NH_3PbI_3$; with reference to Baikie *et al.* [300]). All of the main peaks for hexagonal lead iodide are present [299], and none of the PbO_2 peaks remain for the PbI_2 film. The perovskite film exhibits all $CH_3NH_3PbI_3$ peaks [300], confirming successful fabrication, although PbI_2 peaks indicate that the film has not been completely converted.

and previously reported devices [81]. Given the lack of optimisation, the measured performance is encouraging for the potential of devices fabricated using this electrodeposition method.

Further Investigation of the Fabrication Technique

There are a number of avenues to explore further with regard to improving the power conversion efficiency of such devices. The first should be achieving complete

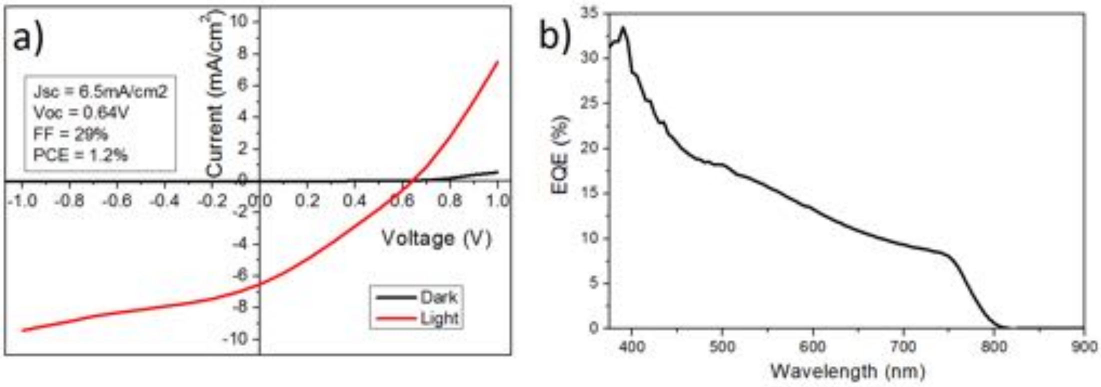

Figure 7.17: a) JV curve and b) external quantum efficiency for prototype $CH_3NH_3PbI_3$ solar cell fabricated *via* electrodeposition. A power conversion efficeincy of 1.2% was recorded. The cell suffers in particular from poor fill factor.

conversion from lead iodide to perovskite, followed by optimisation of the lead iodide and perovskite morphologies.

Initially, lead iodide films were submerged in methylammonium iodide in isopropanol for 20 s to convert to the perovskite. This follows previously reported treatments [298] and corresponded with the immediate change in film colour by eye. However, given the incomplete conversion, intercalation over a period of five hours was attempted. Previous reports have suggested that $CH_3NH_3PbI_3$ does not degrade in such solutions of methylammonium iodide in isopropanol [301], so substantially increasing the submersion time was not expected to pose a problem. Additionally, vapour-assisted solution processing (‘VASP’ [302]) was investigated, using vapour-phase methylammonium iodide rather than dissolved methylammonium iodide to intercalate the organic moiety into the lead iodide film. For this, methylammonium iodide crystals were placed around the sample bearing the lead iodide film and heated to 150 °C for two hours in a nitrogen atmosphere.

The XRD spectra of the resultant perovskite films are shown in figure 7.18. The signals recorded from the three films have been normalised to the main perovskite peak at 14.1° for comparison. These spectra appear to demonstrate improved, but still incomplete, conversion for longer solution-phase intercalation treatment, and almost complete conversion with vapour-phase intercalation. The lead iodide film treated with solution-phase methylammonium iodide for five hours has weaker PbI_2 peaks at 12.7°, 26.0° and 34.4° than the film treated for 20 s, but stronger PbI_2 peaks at 39.6° and 41.8° (there doesn't appear to be much difference between the peaks beyond 45°, but these have very low signals anyway). The increase in some peaks and decrease in others perhaps results from different crystal orientations in the original PbI_2 films, but given the assumption that $CH_3NH_3PbI_3$ doesn't degrade in solution [301], the variation in PbI_2 presence with intercalation time suggests that longer submersion times lead to more complete conversion, although it is not known if complete conversion would ever be achieved. In any case, vapour-phase intercalation seems to yield close to complete conversion, apparent from the very small PbI_2 signal present in the perovskite spectrum.

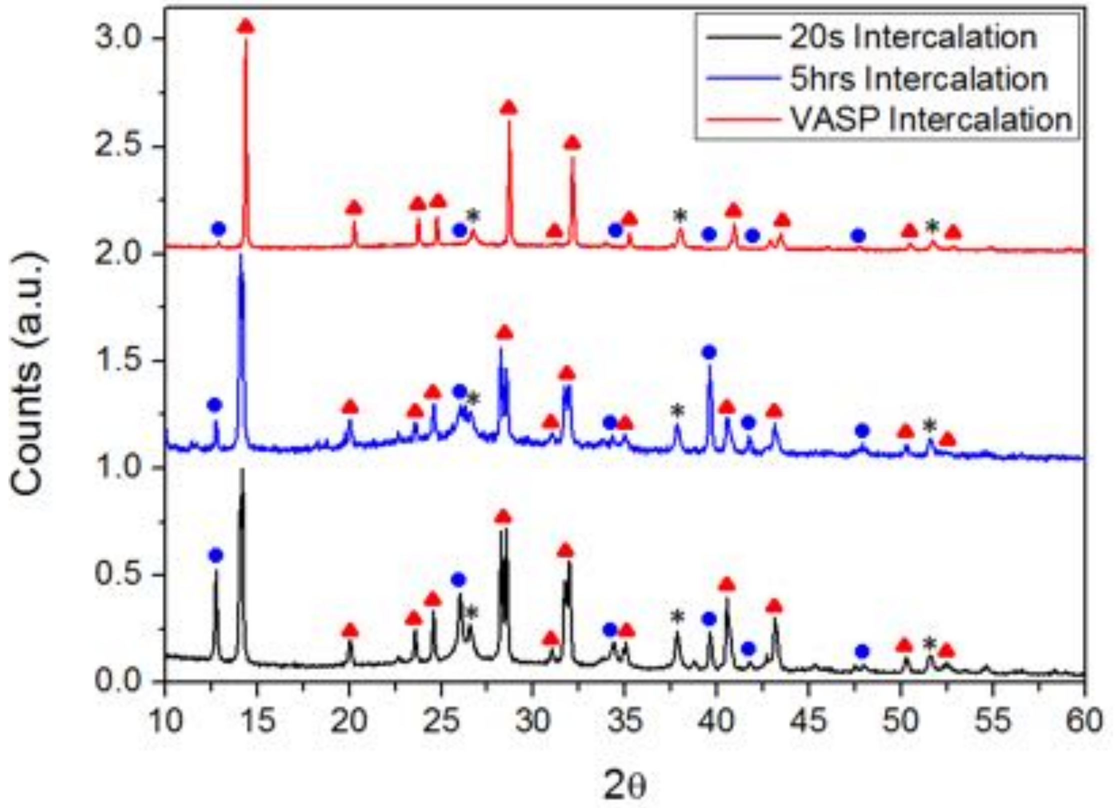

Figure 7.18: Comparison of XRD spectra for perovskite films converted from pure PbI_2 by submersion in 10 mg/ml methylammonium iodide in isopropanol for 20 seconds (black line) or 5 hours (red line).

An additional difference between the vapour- and solution-phase intercalation treatments is the nature of the perovskite peaks observed at 28.6° and 32.2°, which appear as doublets in the solution-treated films but singlets in the vapour-treated films. Although this could signal presence of the cubic, rather than tetragonal, phase in the vapour-treated films, the peak at 23.7° would seem to rule this out [300]. Additionally, the cubic phase has previously been observed at temperatures above the (reversible) transition range of $\sim 54-57$°C [300, 303–305]. Instead, it might be due to better peak resolution in the solution-treated films, whether due to larger crystallite size [306, 307] or simply measurement conditions.

Alternative methods of iodinisation were also explored in an attempt to better control the morphology of the lead iodide films. First, the hydroiodic acid was heated to different temperatures during iodinisation, with higher temperatures leading to quicker iodinisation times. XRD analysis showed virtually identical spectra for all iodinsation temperatures, but AFM detected no simple correspondence between temperature and surface morphology, with roughness, $\mathrm{R_a}$, varying between 70 and 300 nm. As well as iodinisation *via* exposure to hydroiodic acid fumes, lead dioxide films can be iodinised simply through exposure to the vapour from heated iodine crystals. This avoids problems with condensation forming on the film during iodinisation, but can instead lead to formation of iodine crystals on the surface of the film (although these can be removed afterwards by heating). Although the films change colour, they are not as bright yellow by eye as films iodinised with hydroiodic acid, and XRD spectra of the films show markedly weaker $\mathrm{PbI_2}$ peaks compared to the substrate peaks (although the lack of $\mathrm{PbO_2}$ peaks again indicates complete conversion; see figure 7.19(c)). The morphology of the resultant lead iodide films does seem affected by the iodinsation technique too, with SEM images showing smaller, more 'angular' features for iodine-treated compared to hydroioidic acid-treated films (figure 7.19(a) and (b) respectively), and AFM measuring smoother films with $\mathrm{R_a} \sim 40$ nm rather than 75 nm and above. Figure 7.19(d) also shows the perovskite morphology formed after iodinisation with hydroiodic acid and intercalation with vapour-phase methylammonium iodide, probably the optimal fabrication technique used so far. The surface roughness of the perovskite film was measured to be $\mathrm{R_a} \sim 70$ nm.

Using vapour-phase intercalation to obtain almost complete conversion of lead iodide to $\mathrm{CH_3NH_3PbI_3}$ perovskite should allow signifcant enhancement of solar cell performance. Additionally, there seems resaonable scope to investigate differ-

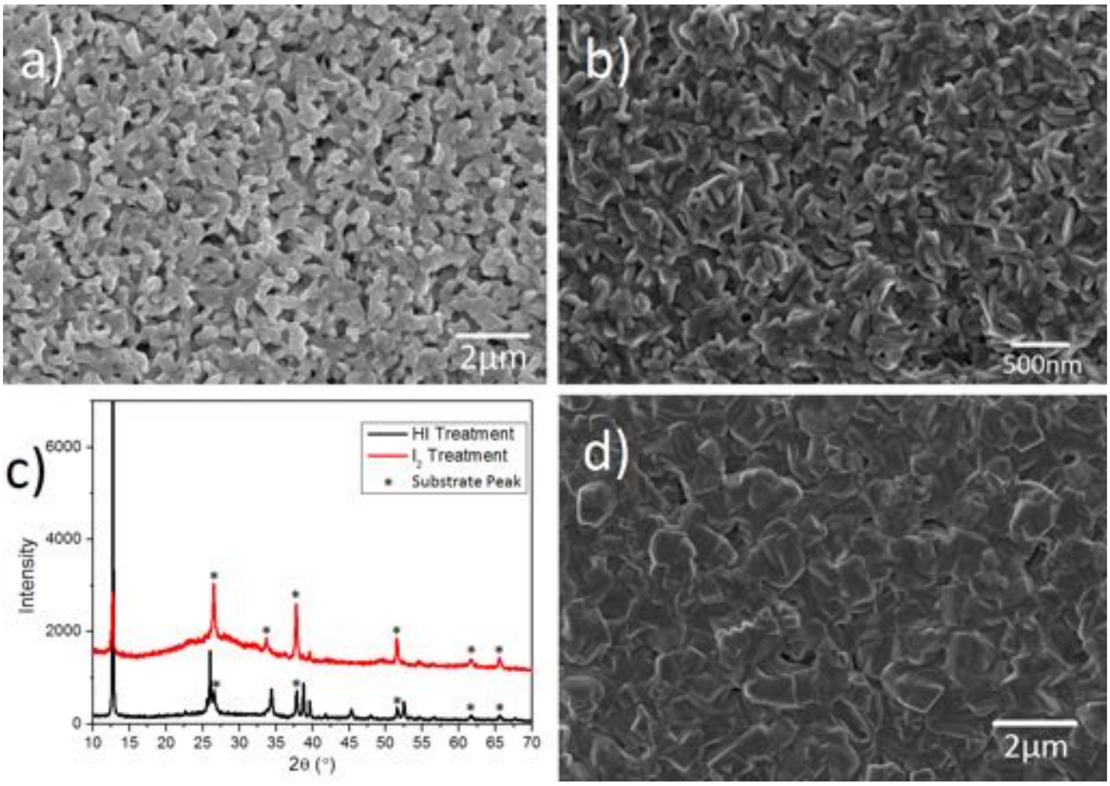

Figure 7.19: Lead iodide morphologies after (a) hydroiodic acid and (b) iodine vapour iodinisation, with comparative XRD spectra of the two films (c). Figure (d) shows perovskite film morphology fabricated with the assumed ‘optimal’ methods of iodinisation with hydroiodic acid followed by vapour-phase methylammonium iodide intercalation.

ent iodinsation routes to optimise film morphology. Optimisation of other simple parameters such as perovskite thickness, the hole transport layer chosen and hole transport layer thickness could also quickly improve performance. However, this project was not continued further due to time constraints, and in the meantime several publications have reported similar results, with power conversion efficiencies up to 14.6 % [308–310]. In all cases, electrodeposition of lead oxide was used followed by conversion to $CH_3NH_3PbI_3$ films. However, variation within these methods demonstrate the versatility of the technique, with different lead oxide films (PbO or PbO_2), electron-collecting layers (compact or mesoporous TiO_2) and hole-collecting layers (spiro-MeOTAD or carbon paste) used. In particular, iodinsation methods ranged from exposure to heated iodine crystals, to submersion in hydroiodic acid in ethanol, to direct conversion from lead oxide to perovksite by annealing with a spin-coated methylammonium iodide layer directly above the lead oxide [310]. This solid-phase intercalation method, as well as liquid-phase intercalation, was used for conversion to perovskite, but never vapour-phase intercalation. Despite this variation in fabrication routes, reported power conversion efficiencies were above 8% in all cases.

Chapter 8

Conclusions and Future Work

This thesis investigated electrodeposition as a fabrication method for organic and perovskite solar cells. The main project used templated electropolymerisation to produce organic solar cells with well-defined, periodic donor:acceptor nanostructure. Specifically, microphase separation in diblock copolymer blends was used to generate double gyroid structured templates with $\sim 40\,\text{nm}$ unit cell size. Functioning devices with such well-defined, regular nanostructure could facilitate further investigation of the underlying working principles in organic heterojunctions, for example with transient absorption experiments, and highly-performing devices would provide motivation for the development of gyroid-forming donor:acceptor diblock copolymers. Experimentation with electropolymerisation techniques and solvent processing led to the reliable fabrication of relatively smooth, uniform thickness gyroid-structured polythiophene films. Backfilling these films with the fullerene acceptor ICBA and coating with evaporated electrodes gave functioning photovoltaic devices, with a maximum observed power conversion efficiency of 0.06%. This is lower than conventional spin-coated organic solar cells, whose efficiencies can reach $5-10\%$.

Reasonable exciton generation and dissociation in the gyroid-structured devices are implied by both efficient photoluminescence quenching upon addition of the ICBA acceptor and transient absorption measurements. This suggests that charge extraction rather than generation is the limiting factor for photovoltaic performance. Indeed, absorption spectrum measurements indicate that the gyroid-structured polythiophene exhibits significantly shorter conjugation lengths than polythiophene electropolymerised without a template. Short conjugation lengths have previously been associated with poor molecular ordering and inferior charge mobility [51, 55, 126]. However, poor charge extraction may not necessarily be caused by poor free charge mobility; other potential causes include strongly bound polaron pairs across the donor:acceptor interface, trap sites in the organic film or extraction barriers at the electrode contacts. Experiments involving pump-push-probe transient absorption measurements [243] or current-voltage measurements under varying illumination intensities [311] are examples of further work that could elucidate the processes limiting charge transport and/or extraction.

Importantly, short conjugation lengths are not necessarily inherent to the gyroid-structure, as they could simply result from the templated electropolymerisation procedure. Various potentially important electropolymerisation parameters were varied to investigate their effect upon conjugation, both with and without templates. Deposition technique and voltage appeared to have a significant effect on conjugation for untemplated electropolymerisation, and bilayer devices fabricated under the optimised conditions achieved power conversion efficiencies of up to 1.49%, close to the maximum previously reported value of 1.5% for electropolymerised bilayer devices. In contrast, little effect was observed from varying conditions for templated deposition. However, investigation of the full range of electropolymerisation parameters has certainly not been exhausted. In particular, substituted thiophene monomers beyond 3-methylthiophene could be tested. One obvious area for further work would be to investigate how conjugation varies with the unit cell size of the gyroid template. The work in this thesis was conducted with a constant unit cell size, but altering the molecular weight of the diblock copolymer changes this lengthscale (the increase in required annealing temperature with molecular weight places an upper limit on the unit cell size attainable given the decomposition temperatures of the diblock copolymers). There is a limit to how much you can enlarge the unit cell before recombination losses would become too great, however.

Additional projects included examination of electrochemical techniques for the fabrication of perovskite solar cells. Initial investigations into electrodeposition of lead oxide for *in situ* conversion to lead halide perovskite demonstrated the feasibility of this material conversion, and reasonable photovoltaic performance suggests potential for fabrication of highly-performing devices. This has since been confirmed with recently published similar work [308–310]. This could be useful as an alternative fabrication method for large-scale solar panels or for avoiding the use of toxic solvents. However, the significant morphological changes occuring between iodinisation and intercalation steps suggest that templated electrodeposition would not be able to produce precisely-controlled perovskite morphologies, as had also been intended. Additionally, PEDOT films were electropolymerised onto alternating interdigitated ITO electrodes for the fabrication of back-contact spin-coated perovskite solar cells. Again, functioning devices were obtained, but with low power conversion efficiencies. Photocurrent mapping suggests one issue could be limited charge extraction at the PEDOT-coated electrodes, which could be investigated further by varying the PEDOT doping level and investigating subsequent photovoltaic performance. Recently, back-contact perovskite devices with 3.2% efficiency have been developed using nickel oxide as the hole extraction layer [274].

In conclusion, templated electrodeposition allows fabrication of macroscopic films with precise nanostructure. In particular, gyroid-structured organic solar cells were successfully fabricated using diblock copolymer templates and electropolymerisation, followed by solvent processing. However, templated electropolymerisation appeared to produce polymer films with short conjugation lengths and poor molecular order. This could explain the poor photovoltaic performance of the obtained gyroid-structured solar cells despite their reasonable excitonic generation and dissociation, as demonstrated by efficient photoluminescence quenching and transient absorption measurements.

Glossary

AFM	Atomic force microscopy
Bmim	1-Butyl-3-methylimidazolium
CV	Cyclic voltammetry
Emim	1-Ethyl-3-methylimidazolium
$EtSO_4$	Ethyl sulphate
EQE	External quantum efficiency
GSB	Ground-state bleaching
HOMO	Highest occupied molecular orbital
ICBA	Indene-C_{60} bis-adduct
J_{SC}	Short-circuit current
LUMO	Lowest unoccupied molecular orbital
OPV	Organic photovoltaics
PCBM	Phenyl-C_{61}-butyric acid methyl ester

PEDOT	Poly(3,4-ethylenedioxythiophene)
PFS	Poly(4-fluorostyrene-*r*-styrene)
PIA	Photoinduced absorption
PLA	Polylactic acid
PLQE	Photoluminescence quantum efficiency
PR-TRMC	Pulse-radiolysis time-resolved microwave conductivity
PBT	Polybithiophene
P3HT	Poly-3-hexylthiophene
P3MT	Poly-3-methylthiophene
SE	Stimulated emission
SCE	Saturated calomel electrode
SEM	Scanning electron microscopy
TFE	2,2,2-Trifluoroethanol
TFSI	bis(trifluoromethylsulfonyl)imide
$\mathbf{V_{OC}}$	Open-circuit voltage
XRD	X-Ray diffractometry

References

[1] British Petroleum. *BP Statistical Review of World Energy June 2015.* Technical report, British Petroleum (2015) 1, 2

[2] Intergovernmental Panel on Climate Change. *Fifth Assessment Report: Summary for Policymakers* (2014) 1

[3] The Royal Society. *Climate change: a summary of the science* (2010) 1

[4] United Nations Framework Convention on Climate Change Parties. *The Paris Agreement* (2015) 1

[5] UK Parliament. *Climate Change Act 2008* (2008) 1

[6] HM Government. *The UK Low Carbon Transition Plan* (2009) 1

[7] HM Government Department of Energy & Climate Change. *UK Renewable Energy Roadmap* (2011) 1

[8] United Nations Development Program. *Human Development Report 2015* (2015) 2

[9] The World Bank. *Energy Use Data* (2012) 2

[10] D.J.C. MacKay. *Sustainable Energy - Without the Hot Air*, (UIT Cambridge, 2008) 2

[11] C. Keeling and T. Whorf. *Atmospheric* CO_2 *records from sites in the SIO air sampling network.* In: *Trends: A Compendium of Data on Climate Change*, (US Department of Energy, 2005) 2

[12] A. Neftel, H. Friedli, E. Moor, H. Lötscher, H. Oeschger, U. Siegenthaler and B. Stauffer. *Historical CO_2 record from the Siple station ice core.* In: *Trends: A Compendium of Data on Climate Change*, (US Department of Energy, 1994) 2

[13] D. Etheridge, L. Steele, R. Langenfelds, R. Francey, J.-M. Barnola and V. Morgan. *Historical CO_2 records from the Law Dome DE08, DE08-2, and DSS ice cores.* In: *Trends: A Compendium of Data on Climate Change*, (US Department of Energy, 1994) 2

[14] J. Marshall and R.A. Plumb. *Atmosphere, Ocean and Climate Dynamics*, (Academic Press,2007) 2

[15] Heliatek GmbH. *http://www.heliatek.com/en/heliafilm/technical-data* (2016) 2, 3, 7

[16] G. Dennler and N.S. Saraciftci. *Flexible Conjugated Polymer-Based Plastic Solar Cells: From Basics to Applications.* Thin Solid Films, (2005) 3

[17] M.A. Green, A. Ho-Baillie and H.J. Snaith. *The emergence of perovskite solar cells.* Nature Photonics, (2014): 506–514 3

[18] M. Kaltenbrunner, G. Adam, E.D. Głowacki, M. Drack, R. Schwödiauer, L. Leonat, D.H. Apaydin, H. Groiss, M.C. Scharber, M.S. White, N.S. Saraciftci and S. Bauer. *Flexible high power-per-weight perovskite solar cells with chromium oxidemetal contacts for improved stability in air.* Nature Materials, 14 (2015): 1032–1039 3

[19] G. Dennler and C.J. Brabec. *Organic Photovoltaics*, (Wiley, 2009), chapter 20 - Socio-Economic Impact of Low-Cost PV Technologies 3

[20] National Renewable Energy Laboratory. *NREL Research Cell Efficiency Records Chart* 3, 4, 20, 126

[21] K. Lee, J.Y. Kim, S.H. Park, S.H. Kim, S. Cho and A.J. Heeger. *Air-Stable Polymer Electronic Devices.* Advanced Materials, 19 (2007): 2445–2449 3

[22] G. Dennler, C. Lungenschmied, H. Neugebauer, N.S. Sariciftci and A. Labouret. *Flexible, conjugated polymer-fullerene-based bulk-heterojunction solar cells: Basics, encapsulation, and integration.* Journal of Material Research, 20 (2005): 3224–3233 3

[23] L. Moro, N. Rutherford, R.J. Visser, J.A. Hauch, C. Klepek, P. Denk, P. Schilinsky and C.J. Brabec. *Barix multilayer barrier technology for organic solar cells.* Proceedings of SPIE, 6334 (2006) 3

[24] S.A. Gevorgyan, M.V. Madsen, H.F. Dam, M. Jørgensen, C.J. Fell, K.F. Anderson, B.C. Duck, A. Mescheloff, E.A. Katz, A. Elschner, R. Roesch, H. Hoppe, M. Hermenau, M. Riede and F.C. Krebs. *Interlaboratory outdoor stability studies of flexible roll-to-roll coated organic photovoltaic modules: Stability over 10,000 h.* Solar Energy Materials & Solar Cells, 116 (2013): 187–196 3

[25] W. Shockley and H.J. Queisser. . Journal of Applied Physics, 32 (1961) 4

[26] D. Kearns and M. Calvin. *Photovoltaic Effect and Photoconductivity in Laminated Organic Systems.* Journal of Chemical Physics, 29 (1958): 950–951 3

[27] C.W. Tang. *Two-layer organic photovoltaic cell.* Applied Physics Letters, 48 (1986): 183–185 3, 18

[28] J.J.M. Halls, C.A. Walsh, N.C. Greenham, E.A. Marseglia, R.H. Friend, S.C. Moratti and A.B. Holmes. *Efficient photodiodes from interpenetrating polymer networks.* Nature, 376 (1995): 498–500 4

[29] G. Yu, J. Gao, J.C. Hummelen, F. Wudl and A.J. Heeger. *Polymer Photovoltaic Cells: Enhanced Efficiencies via a Network of Internal Donor-Acceptor Heterojunctions.* Science, 270 (1995): 1789–1791 4, 18

[30] Y. Huang, E.J. Kramer, A.J. Heeger and G.C. Bazan. *Bulk Heterojunction Solar Cells: Morphology and Performance Relationships.* Chemical Reviews, 114 (2014): 7006–7043 4, 68, 69

[31] M.T. Dang, L. Hirsch and G. Wantz. *P3HT:PCBM, Best Seller in Polymer Photovoltaic Research.* Advanced Materials, 23 (2011): 3597–3602 4, 68, 95, 116, 117

[32] J. Zhao, Y. Li, G. Yang, J. Jiang, H. Lin, H. Ade, W. Ma and H. Yan. *Efficient organic solar cells processed from hydrocarbon solvents.* Nature Energy, 1 (2016): 15027 4

[33] S.-Y. Ku, M.A. Brady, N.D. Treat, J.E. Cochran, M.J. Robb, E.J. Kramer, M.L. Chabinyc and C.J. Hawker. *A Modular Strategy for Fully Conjugated Donor-Acceptor Block Copolymers.* Journal of the American Chemical Society, 134 (2012): 16040–16046 5

[34] U. Scherf, S. Adamczyk, A. Gutacker and N. Koenen. *All-Conjugated, Rod-Rod Block Copolymers – Generation and Self-Assembly Properties.* Macromolecular Rapid Communications, 30 (2009): 1059–1065 5, 19

[35] C. Guo, Y.-H. Lin, M.D. Witman, K.A. Smith, C. Wang, A. Hexemer, J. Strzalka, E.D. Gomez and R. Verduzco. *Conjugated Block Copolymer Photovoltaics with near 3 % Efficiency through Microphase Separation.* Nano Letters, 13 (2013): 2957–2963 5, 18, 19

[36] E. van Kerschaver and G. Beaucarne. *Back-contact solar cells: A review.* Progress in Photovoltaics Research and Applications, 14 (2006): 107–123 5, 127

[37] R.G.E. Kimber, A.B. Walker, G.E. Schröder-Turk and D.J. Cleaver. *Bicontinuous minimal surface nanostructures for polymer blend solar cells.* Physical Chemistry Chemical Physics, 12 (2009): 844–851 6, 26, 27, 118

[38] E.J.W. Crossland, M. Kamperman, M. Nedelcu, C. Ducati, U. Wiesner, D.M. Smilgies, G.E.S. Toombes, M.A. Hillmyer, S. Ludwigs, U. Steiner and H.J. Snaith. *A Bicontinuous Double Gyroid Hybrid Solar Cell.* Nano Letters, 9 (2008) 6, 26, 27

[39] A.J. Heeger. *Semiconducting and Metallic Polymers: The Fourth Generation of Polymeric Materials* (2001). Nobel Lecture 7

[40] H. Hoppe and N.S. Sariciftci. *Organic solar cells: An overview.* Journal of Materials Research, 19 (2004): 1924–1945 7, 8, 12, 14, 16, 51

[41] S. Günes, H. Neugebauer and N.S. Saraciftci. *Conjugated Poymer-Based Organic Solar Cells.* Chemical Review, 107 (2007) 7, 14

[42] J.L. Brédas and G.B. Street. *Polarons, Bipolarons, and Solitons in Conducting Polymers.* Accounts of Chemical Research, 18 (1985): 309–315 8

[43] M.S. Freund and B.A. Deore. *Self-Doped Conducting Polymers*, (Wiley, 2007) 8

[44] D.A. dos Santos and J.L. Brédas. *Influence of polymerization irregularities on the electronic properties of polythiophene.* Journal of Chemical Physics, 95 (1991): 6567–6575 9, 70

[45] H. Fujimoto, U. Nagashima, H. Inokuchi, K. Seki, Y. Cao, H. Nakahara, J. Nakayama, M. Hoshiro and K. Fukuda. *Ultraviolet photoemission study of oligothiophenes: π-band evolution and geometries.* Journal of Chemical Physics, 92 (1990): 4077–4092 9, 70

[46] S. Hugger, R. Thomann, T. Heinzel and T. Thurn-Albrecht. *Semicrystalline morphology in thin films of poly(3-hexlthiophene).* Colloid and Polymer Science, 282 (2004): 932–938 9, 10, 68, 69

[47] K. Asadi, A.J. Kronemeijer, T. Cramer, L.J.A. Koster, P.W.M. Blom and D.M. de Leeuw. *Polaron hopping mediated by nuclear tunnelling in semiconducting polymers at high carrier density.* Nature Communications, 4 (2013): 1710 9

[48] A. Miller and E. Abrahams. *Impurity conduction at low concentrations.* Physical Review, 120 (1960): 645–755 9

[49] H. Bässler. *Charge Transport in Disordered Organic Photoconductors.* Physica Status Solidi B, 175 (1993): 15–56 10

[50] R.J. Kline and M.D. McGehee. *Morphology and Charge Transport in Conjugated Polymers.* Journal of Macromolecular Science, Part C: Polymer Reviews, 46 (2006): 27–45 10, 11

[51] S.T. Turner, P. Pingel, R. Steyrleuthner, E.J.W. Crossland, S. Ludwigs and D. Neher. *Quantitative Analysis of Bulk Heterojunction Films Using Linear Absorption Spectroscopy and Solar Cell Performance.* Advanced Functional Materials, 21 (2011): 4640–4652 10, 35, 68, 69, 160

[52] Z. Mo, K.-B. Lee, Y.B. Moon, M. Kobayashi, A.J. Heeger and F. Wudl. *X-ray Scattering from Polythiophene: Crystallinity and Crystallographic Structure.* Macromolecules, 18 (1985): 1972–1977 10, 35, 69

[53] C. Goh, R.J. Kline, M.D. McGehee, E.N. Kadnikova and J.M.J. Fréchet. *Molecular-weight-dependent mobilities in regioregular poly(3-hexylthiophene) diodes.* Applied Physics Letters, 86 (2005): 122110 11, 45, 121, 123

[54] R.J. Kline, M.D. McGehee, E.N. Kadnikova, J. Liu and J.M.J. Fréchet. *Controlling the Field-Effect Mobility of Regioregular Polythiophene by Changing the Molecular Weight.* Advanced Materials, 15 (2003): 1519–1522 11, 72

[55] A. Zen, J. Pflaum, S. Hirschmann, W. Zhuang, F. Jaiser, U. Asawapirom, J.P. Rabe, U. Scherf and D. Neher. *Effect of Molecular Weight and Annealing of Poly(3-hexylthiophene)s on the Performance of Organic Field-Effect Transistors.* Advanced Functional Materials, 14 (2004): 757–764 11, 72, 117, 160

[56] P. Pingel, A. Zen, R.D. Abellón, F.C. Grozema, L.D.A. Siebbeles and D. Neher. *Temperature-Resolved Local and Macroscopic Charge Carrier Transport in Thin P3HT Layers.* Advanced Functional Materials, 20 (2010): 2286–2295 11, 33, 35, 36, 60, 68

[57] M. Pope and C.E. Swenberg. *Electronic processes in organic crystals*, (Oxford University Press, 1999) 13, 14

[58] B. Kippelen and J.-L. Brédas. *Organic photovoltaics.* Energy and Environmental Science, 2 (2009): 241–332 14, 16

[59] N.C. Greenham, I.D.W. Samuel, G.R. Hayes, R.T. Phillips, Y.A.R.R. Kessener, S.C. Moratti, A.B. Holmes and R.H. Friend. *Measurement of*

absolute photoluminescence quantum efficiencies in conjugated polymers. Chemical Physics Letters 14

[60] X.M. Jiang, R. Österbacka, O. Korovyanko, C.P. An, B. Horovitz, R.A.J. Janssen and Z.V. Vardeny. *Spectroscopic Studies of Photoexcitations in Regioregular and Regiorandom Polythiophene Films.* Advanced Functional Materials, 12 (2002): 587–597 14, 111

[61] P.B. Miranda, D. Moses and A.J. Heeger. *Ultrafast photogeneration of charged polarons in conjugated polymers.* Physical Review B, 64 (2001) 14

[62] S. Cook, A. Furube and R. Katoh. *Analysis of the excited states of regioregular polythiophene P3HT.* Energy & Environmental Science, 1 (2008): 294–299 14

[63] A. Haugeneder, M. Neges, C. Kallinger, W. Spirkl, U. Lemmer, J. Feldmann, U. Scherf, E. Harth, A. Gügel and K. Müllen. *Exciton diffusion and dissociation in conjugated polymer/fullerene blends and heterostructures.* Physical Review B, 59 (1999) 14

[64] J.-L. Brédas, J.E. Norton, J. Cornil and V. Coropceanu. *Molecular Understanding of Organic Solar Cells: The Challenges.* Accounts of Chemical Research, 42 (2009): 1691–1699 14

[65] S.-S. Sun and N.S. Sariciftci. *Organic Photovoltaics: Mechanisms, Materials and Devices*, (CRC Press, 2005) 16

[66] L.G. Kaake, D. Moses and A.J. Heeger. *Coherence and Uncertainty in Nanostructured Organic Photovoltaics.* The Journal of Physical Chemistry Letters, 4 (2013): 2264–2268 16

[67] S. Gélinas, A. Rao, A. Kumar, S.L. Smith, A.W. Chin, J. Clark, T.S. van der Poll, G.C. Bazan and R.H. Friend. *Ultrafast Long-Range Charge Separation in Organic Semiconductor Photovoltaic Diodes.* Science, 343 (2014): 512–516 16

[68] M.A. Ruderer, S. Guo, R. Meier, H.-Y. Chiang, V. Körstgens, J. Wiedersich, J. Perlich, S.V. Roth and P. Müller-Buschbaum. *Solvent-Induced Mor-*

phology in Polymer-Based Systems for Organic Photovoltaics. Advanced Functional Materials, 21 (2011): 3382–3391 17

[69] W. Ma, C. Yang, X. Gong, K. Lee and A.J. Heeger. *Thermally Stable, Efficient Polymer Solar Cells with Nanoscale Control of the Interpenetrating Network Morphology.* Advanced Functional Materials, 15 (2005): 1617–1622 17, 68, 95, 117, 118, 119, 121

[70] J.K. Lee, W.L. Ma, C.J. Brabec, J. Yuen, J.S. Moon, J.Y. Kim, K. Lee, G.C. Bazan and A.J. Heeger. *Processing Additives for Improved Efficiency from Bulk Heterojunction Solar Cells.* Journal of the American Chemical Society, 130 (2008): 3619–3623 17, 101

[71] H. Gao, Y. Chen and Y. Luo. *Three-dimensional nano-networked P3MT/PCBM solar cells.* Nanotechnology, 22 (2011) 17, 18, 51, 57, 61, 66

[72] G. Ren, P.-T. Wu and S.A. Jenekhe. *Solar Cells Based on Block Copolymer Semiconductor Nanowires: Effects of Nanowire Aspect Ratio.* ACS Nano, 5 (2011): 376–384 18

[73] J.S. Kim, Y. Park, D.Y. Lee, J.H. Lee, J.H. Park, J.K. Kim and K. Cho. *Poly(3-hexylthiophene) Nanorods with Aligned Chain Orientation for Organic Photovoltaics.* Advanced Functional Materials, 20 (2010): 540–545 18

[74] I. Botiz and S.B. Darling. *Self-Assembly of Poly(3-hexylthiophene)*-block-*polylactide Block Copolymer and Subsequent Incorporation of Electron Acceptor Material.* Macromolecules, 42 (2009): 8211–8217 18, 19, 100

[75] Y. Lin, J.A. Lim, Q. Wei, S.C.B. Mannsfeld, A.L. Briseno and J.J. Watkins. *Cooperative Assembly of Hydrogen-Bonded Diblock Copolythiophene/Fullerene Blends for Photovoltaic Devices with Well-Defined Morphologies and Enhanced Stability.* Chemistry of Materials, 24 (2012): 622–632 18, 19

[76] X. He, F. Gao, G. Tu, D.G. Hasko, S. Hüttner, N.C. Greenham, U. Steiner, R.H. Friend and W.T.S. Huck. *Formation of Well-Ordered Heterojunctions*

in Polymer:PCBM Photovoltaic Devices. Advanced Functional Materials, 21 (2011): 139–146 18, 20

[77] D. Kekuda, J.-H. Huang, K.-C. Ho and C.-W. Chu. *Modulation of Donor-Acceptor Interface through Thermal Treatment for Efficient Bilayer Organic Solar Cells.* Journal of Physical Chemistry, 114 (2010): 2764–2768 17

[78] S.B. Darling. Private Communication 19, 100

[79] Y. Yang, K. Mielczarek, M. Aryal, A. Zakhidov and W. Hu. *Nanoimprinted Polymer Solar Cell.* ACS Nano, 6 (2012): 2877–2892 20

[80] H.-S. Kim, C.-R. Lee, J.-H. Im, K.-B. Lee, T. Moehl, A. Marchioro, S.-J. Moon, R. Humphry-Baker, J.-H. Yum, J.E. Moser, M. Grätzel and N.-G. Park. *Lead Iodide Perovskite Sensitized All-Solid-State Submicron Thin Film Mesoscopic Solar Cell with Efficiency Exceeding 9%.* Scientific Reports, 2 (2012): 591 20

[81] M. Lee, J. Teuscher, T. Miyasaka, T.N. Murakami and H.J. Snaith. *Efficient Hybrid Solar Cells Based on Meso-Superstructured Organometal Halide Perovskites.* Science, 338 (2012): 643–647 20, 153

[82] M. Liu, M.B. Jonhston and H.J. Snaith. *Efficient planar heterojunction perovskite solar cells by vapour deposition.* Nature, 501 (2013): 395–398 20, 144

[83] H. Zhou, Q. Chen, G. Li, S. Luo, T.-B. Song, H.-S. Duan, Z. Hong, J. You, Y. Liu and Y. Yang. *Interface engineering of highly efficient perovskite solar cells.* Science, 345 (2014): 542–546 20, 126

[84] J.P.C. Baena, L. Steier, W. Tress, M. Saliba, S. Neutzner, T. Matsui, F. Giordano, T.J. Jacobsson, A.R.S. Kandada, S.M. Zakeeruddin, A. Petrozza, A. Abate, M.K. Nazeeruddin, M. Grätzel and A. Hagfeldt. *Highly efficient planar perovskite solar cells through band alignment engineering.* Energy & Environmental Science, 8 (2015): 2928–2934 20

[85] W. Nie, H. Tsai, R. Asadpour, J.-C. Blancon, A.J. Neukirch, G. Gupta, J.J. Crochet, M. Chhowalla, S. Tretiak, M.A. Alam, H.-S. Wang and

A.D. Mohite. *High-efficiency solution-processed perovskite solar cells with millimeter-scale grains.* Science, 347 (2015): 522–525 20

[86] M. Yang, Y. Zhou, Y. Zeng, C.-S. Jiang, N.P. Padture and K. Zhu. *Square-Centimeter Solution-Processed Planar $CH_3NH_3PbI_3$ Perovskite Solar Cells with Efficiency Exceeding 15%.* Advanced Materials, 27 (2015): 6363–6370 20, 144

[87] A. Mei, X. Li, L. Liu, Z. Ku, T. Liu, Y. Rong, M. Xu, M. Hu, J. Chen, Y. Yang, M. Grätzel and H. Han. *A hole-conductor-free, fully printable mesoscopic perovskite solar cell with high stability.* Science, 345 (2015): 295–298 20

[88] X. Li, M. Tschumi, H. Han, S.S. Babkair, R.A. Alzubaydi, A.A. Ansari, S.S. Habib, M.K. Nazeeruddin, S.M. Zakeeruddin and M. Grätzel. *Outdoor Performance and Stability under Elevated Temperatures and Long-Term Light Soaking of Triple-Layer Mesoporous Perovskite Photovoltaics.* Energy Technology, 3 (2015): 551–555 20

[89] J. You, L. Meng, T.-B. Song, T.-F. Guo, Y. Yang, W.-H. Chang, Z. Hong, H. Chen, H. Zhou, Q. Chen, Y. Liu, N. De Marco and Y. Yang. *Improved air stability of perovskite solar cells via solution-processed metal oxide transport layers.* Nature Nanotechnology, (2016): 75–81 20

[90] X. Li, M.I. Dar, C. Yi, J. Luo, M. Tschumi, S.M. Zakeeruddin, M.K. Nazeeruddin, H. Han and M. Grätzel. *Improved performance and stability of perovskite solar cells by crystal crosslinking with alkylphosphonic acid ω-ammonium chlorides.* Nature Chemistry, 7 (2015): 703–711 20

[91] N.K. Noel, S.D. Stranks, A. Abate, C. Wehrenfennig, S. Guarnera, A.-A. Haghighirad, A. Sadhanala, G.E. Eperon, S.K. Pathak, M.B. Johnston, A. Petrozza, L.M. Herz and H.J. Snaith. *Lead-free organicinorganic tin halide perovskites for photovoltaic applications.* Energy & Environmental Science, 7 (2014): 3061–3068 21

[92] A.H. Schoen. *Infinite Periodic Minimal Surfaces without Self-Intersections.* Technical report, NASA (1970) 21

[93] J.A. Dolan, B.D. Wilts, S. Vignolini, J.J. Baumberg, U. Steiner and T.D. Wilkinson. *Optical Properties of Gyroid Structured Materials: From Photonic Crystals to Metamaterials.* Advanced Optical Materials, 3 (2015): 12–32 21, 22

[94] V.N. Urade, T.-C. Wei, M.P. Tate, J.D. Kowalski and H.W. Hillhouse. *Nanofabrication of Double-Gyroid Thin Films.* Chemistry of Materials, 19 (2007): 768–777 21, 22

[95] M.R.J. Scherer. *Synthesis and Applications of Double-Gyroid Structured Functional Materials.* Ph.D. thesis, University of Cambridge (2012) 21, 84, 86

[96] D.A. Hajduk, P.E. Harper, S.M. Gruner, C.C. Honeker, G. Kim, E.L. Thomas and L.J. Fetters. *The Gyroid: A New Equilibrium Morphology in Weakly Segregated Diblock Copolymers.* Macromolecules, 27 (1994) 22, 26

[97] P.J. Flory. *Thermodynamics of High Polymer Solutions.* Journal of Chemical Physics, 10 (1942): 51–61 22

[98] M.L. Huggins. *Solutions of Long Chain Compounds.* Journal of Chemical Physics, 9 (1941): 440 22

[99] P.J. Flory. *The Principles of Polymer Chemistry*, (Cornell University Press, 1953) 22

[100] F.S. Bates and G.H. Fredrickson. *Block Copolymers - Designer Soft Materials.* Physics Today, 52 (1999): 32–38 23, 24, 25, 26

[101] T.P.J. Knowles. *Chemistry at small lengthscales*, (Chemistry Department, University of Cambridge, 2012), chapter 3 24

[102] M.W. Matsen and M. Schick. *Stable and Unstable Phases of a Diblock Copolymer Melt.* Physical Review Letters, 72 (1994): 2660–2663 25

[103] M.W. Matsen and F.S. Bates. *Unifying Weak- and Strong-Segregation Block Copolymer Theories.* Macromolecules, 29 (1996): 1091–1098 25, 26

[104] A.K. Khandpur, S. Förster, F.S. Bates, I.W. Hamley, A.J. Ryan, W. Bras, K. Almdal and K. Mortensen. Macromolecules, 28 (1995): 8796–8806 25, 26

[105] A.J. Meuler, M.A. Hillmyer and F.S. Bates. *Ordered Network Mesostructures in Block Polymer Materials.* Macromolecules, 42 (2009): 7221–7250 26

[106] M.R.J. Scherer, L. Li, P.M.S. Cunha, O.A. Scherman and U.Steiner. *Enhanced Electrochromism in Gyroid-Structured Vanadium Pentoxide.* Advanced Materials, 24 (2012): 1217–1221 26, 27, 83, 84, 87

[107] A. Okumura, Y. Nishikawa and T. Hashimoto. *Nano-fabrication of a double gyroid network structure via ozonolysis of matrix phase of polyisoprene in poly(2-vinylpiridine)-block-polyisoprene films.* Polymer, 47 (2006) 26

[108] S. Jin, J. Yoon, K. Heo, H.-W. Park, J. Kim, K.-W. Kim, T.J. Shin, T. Chang and M. Ree. *Detailed analysis of gyroid structures in diblock copolymer thin films with synchrotron grazing-incidence X-ray scattering.* Journal of Applied Crystallography, 40 (2007) 26

[109] S. Khlebnikov and H.W. Hillhouse. *Electronic Structure of double-gyroid nanostructured semiconductors: Perspectives for carrier multiplication solar cells.* Physical Review B, 80 (2009) 26

[110] D. Wei, M.R.J. Scherer, C. Bower, P. Andrew, T. Ryhänen and U. Steiner. *A Nanostructured Electrochromic Supercapacitor.* Nano Letters, 12 (2012) 27, 85

[111] P.M.S. Cunha, M.R.J. Scherer and U. Steiner. *Replication of nanoporous gyroid polymer films using Atomic Layer Deposition for use in dye-sensitised solar cells.* Talk, ECS Meeting (2011) 27

[112] *www.gwyddion.net* 30

[113] F.C. Spano. *Modeling disorder in polymer aggregates: The optical spectroscopy of regioregular poly(3-hexylthiophene) thin films.* The Journal of Chemical Physics, 122 (2005): 234701 31, 35, 36

[114] F.C. Spano. *The Spectral Signatures of Frenkel Polarons in H- and J-Aggregates.* Accounts of Chemical Research, 43 (2010): 429–439 31, 35, 68

[115] A. Köhler and H. Bässler. *Electronic Processes in Organic Semiconductors, An Introduction*, (Wiley-VCH, 2015) 31, 32, 33, 34

[116] S.D.D.V. Rughooputh, S. Hotta, A.J. Heeger and F. Wudl. *Chromism of Soluble Polythienylenes.* Journal of Polymer Science B: Polymer Physics, 25 (1987): 1071–1078 31, 32

[117] A. Amirav, U. Even and J. Jortner. *Spectroscopy of Large Molecules in Inert-Gas Clusters.* Chemical Physics Letters, 72 (1980): 16–20 32

[118] A. Elschner and H. Bässler. *Site-Selective Fluorescence and Hole-Burning Spectroscopy of MTHF Glasses Doped with Tetracene or Pentacene.* Chemical Physics, 112 (1987): 285–291 32

[119] R. Hesse, W. hofberger and H. Bässler. *Absorption Spectra of Disordered Solid Tetracene and Pentacene.* Chemical Physics, 49 (1980): 201–211 32

[120] W.R. Salaneck, O. Inganäs, B. Thémans, J.-O. Nilsson B. Sjögren, J.E. Österholm, J.-L. Brédas and S. Svensson. *Thermochromism in poly(-hexylthiophene) in the solid state: A spectroscopic study of temperature-dependent conformational defects.* The Journal of Chemical Physics, 89 (1988): 4613–4619 31

[121] J. Seixas de Melo, L.M. Silva, L.G. Arnaut and R.S. becker. *Singlet and triplet energies of α-oligothiophenes: A spectroscopic, theoretical and photoacoustic absorption study: Extrapolation to polythiophene.* The Journal of Chemical Physics, 111 (1999): 5427–5433 31, 36, 131

[122] A. Amirav, U. Even and J. Jortner. *Microscopic solvation effects on excited-state energetics and dynamics of aromatic-molecules in large van der Waals complexes.* The Journal of Chemical Physics, 75 (1981): 2489–2512 32

[123] P.J. Brown, D.S. Thomas, A. Köhler, J.S. Wilson, J.-S. Kim, C.M. Ramsdale, H. Sirringhaus and R.H. Friend. *Effect of interchain interactions on*

the absorption and emission of poly(3-hexylthiophene). Physical Review B, 67 (2003): 064203 33

[124] F.C. Spano and C. Silva. *H- and J-Aggregate Behaviour in Polymeric Semiconductors.* Annual Review of Physical Chemistry, 65 (2014): 477–500 33

[125] M. Kasha, H.R. Rawls and M. Ashraf El-Bayoumi. *The Exciton Model in Molecular Spectroscopy.* Pure and Applied Chemistry, 11 (1965): 371–392 33

[126] J. Clark, J.-F. Chang, F.C. Spano, R.H. Friend and C. Silva. *Determining exciton bandwidth and film microstructure in polythiophene films using linear absorption spectroscopy.* Applied Physics Letters, 94 (2009): 163306 35, 68, 69, 74, 117, 132, 160

[127] D. Spoltore, T. Vangerven, P. Verstappen, F. Piersimoni, S. Bertho, K. Vandewal, N. Van den Brande, M. Defour, B. Van Mele, A. De Sio, J. Parisi, L. Lutsen, D. Vanderzande, W. Maes and J.V. Manca. *Effect of molecular weight on morphology and photovoltaic properties in P3HT:PCBM solar cells.* Organic Electronics, 21 (2015): 160–170 35

[128] C. Scharsich, R.H. Lohwasser, M. Sommer, U. Asawapirom, U. Scherf, M. Thelakkat, D. Neher and A. Köhler. *Control of Aggregate Formation in Poly(3-hexylthiophene) by Solvent, Molecular Weight, and Synthetic Method.* Journal of Polymer Science B: Polymer Physics, 50 (2012): 442–453 35, 69

[129] J. Poplawski, E. Ehrenfreund, S. Glenis and A.J. Frank. *Photoexcitation Spectroscopy of Ploy(3-methylthiophene): Electronic Bands and Vibrational Modes.* Synthetic Metals, 28 (1989): C335–C340 35

[130] S. Brückner and W. Porzio. *The structure of neutral polythiophene. An application of the Rietveld method.* Die Makromolekulare Chemie, 189 (1988): 961–967 35

[131] S. Jin and G. Xue. *Interaction between Thiophene and Solvated Lewis Acids and the Low-Potential Electrochemical Deposition of a Highly Anisotropic Conducting Polythiophene Film.* Macromolecules, 30 (1997): 5753–5757 35

[132] S. Jin, S. Cong, G. Xue, H. Xiong, B. Mansdorf and S.Z.D. Cheng. *Anisotropic Polythiophene Films with High Conductivity and Good Mechanical Properties via a New Electrochemical Synthesis.* Advanced Materials, 14 (2002): 1492–1496 35, 56, 70

[133] H.T. Santoso, V. Singh, K. Kalaitzidou and B.A. Cola. *Enhanced Molecular Order in Polythiophene Films Electropolymerized in a Mixed Electrolyte of Anionic Surfactants and Boron Trifluoride Diethyl Etherate.* ACS Applied Materials and Interfaces, 4 (2012): 1697–1703 35, 55

[134] T.-A. Chen, X. Wu and R.D. Rieke. *Regiocontrolled Synthesis of Poly(3-alkylthiophenes) Mediated by Rieke Zinc: Their Characterization and Solid-State Properties.* Journal of the American Chemical Society, 117 (1995): 233–244 35

[135] F.C. Spano. *Absorption in regio-regular poly(3-hexyl)thiophene thin films: Fermi resonances, interband coupling and disorder.* Chemical Physics, 325 (2006): 22–35 36

[136] J. Clark, C. Silva, R.H. Friend and F.C. Spano. *Role of Intermolecular Coupling in the Photophysics of Disordered Organic Semiconductors: Aggregate Emission in Regioregular Polythiophene.* Physical Review Letters, 98 (2007): 206406 36, 111

[137] G. Louarn, M. Trznadel, J.P. Buisson, J. Laska, A. Pron, M. Lapkowski and S. Lefrant. *Raman Spectroscopic Studies of Regioregular Poly(3-alkylthiophenes).* Journal of Physical Chemistry, 100 (1996): 12532–12539 36

[138] J. Gierschner, Y.-S. Huang, B. Van Averbeke, J. Cornil, R.H. Friend and D. Beljonne. *Excitonic versus electronic couplings in molecular assemblies: The importance of non-nearest neighbor interactions.* Journal of Chemical Physics, 130 (2009): 044105 37, 38

[139] D. Beljonne, J. Cornil, R. Silbey, P. Millié and J.L. Brédas. *Interchain interactions in conjugated materials: The exciton model versus the supermolecular approach.* Journal of Chemical Physics, 112 (2000): 4749–4758 37, 38

[140] D. Beljonne, J. Cornil, R.H. Friend, R.A.J. Janssen and J.L. Brédas. *Influence of Chain Length and Derivatization on the Lowest Singlet and Triplet States and Intersystem Crossing in Oligothiophenes.* Journal of the American Chemical Society, 118 (1996): 6453–6461 37

[141] E.S. Manas and F.C. Spano. *Absorption and spontaneous emission in aggregates of conjugate dpolymers.* Journal of Chemical Physics, 109 (1998): 8087–8101 37

[142] S. Westenhoff, A. Abrusci, W.J. Feast, O. Henze, A.F.M. Kilbinger, A.P.H.J. Schenning and C. Silva. *Supramolecular Electronic Coupling in Chiral Oligothiophene Nanostructures.* Advanced Materials, 18 (2006): 1281–1285 37, 38

[143] P.R.L. Malenfant J.J. Apperloo, R.A.J. Janssen and J.M.J. Frechet. *Interchain Delocalization of Photoinduced Neutral and Charged States in Nanoaggregates of Lengthy Oligothiophenes.* Journal of the American Chemical Society, 123 (2001): 6916–6924 37, 38

[144] E.J.W. Crossland, K. Rahimi, G. Reiter, U. Steiner and S. Ludwigs. *Systematic Control of Nucleation Density in Poly(3-Hexylthiophene) Thin Films.* Advanced Functional Materials, 21 (2011): 518–524 37, 38, 95

[145] J. Clark. *Intermolecular Interactions in π-Conjugated Molecules: Optical Probes of Chain Conformation.* Ph.D. thesis, University of Cambridge (2007) 37

[146] T.J. Prosa, M.J. Winokur, J. Moulton, P. Smith and A.J. Heeger. *X-ray Structural Studies of Poly(3-alkylthiophenes): An Example of an Inverse Comb.* Macromolecules, 25 (1992): 4364–4372 38

[147] A. Hexemer and P. Müller-Buschbaum. *Advanced grazing-incidence techniques for modern soft-matter materials analysis.* IUCrJ, 2 (2015): 106–125 39, 40

[148] J.L. Baker, L.H. Jimison, S. Mannsfeld, S. Volkman, S. Yin, V. Subramanian, A. Salleo, A.P. Alivisatos and M.F. Toney. *Quantification of Thin*

Film Crystallographic Orientation Using X-ray Diffraction with an Area Detector. Langmuir, 26 (2010): 9146–9151 39

[149] *www.gisaxs.de* 39

[150] W.H. Bragg and W.L. Bragg. *The Reflection of X-Rays by Crystals.* Proceedings of the Royal Society A: Mathematical, Physical and Engineering Sciences, 88 (1913): 428–438 39

[151] G. Renaud, R. Lazzari and F. Leroy. *Probing surface and interface morphology with Grazing Incidence Small Angle X-Ray Scattering.* Surface Science Reports, 64 (2009): 255–380 40

[152] J.C. de Mello, H.F. Wittmann and R.H. Friend. *An Improved Experimental Determiation of External Photoluminescence Quantum Efficiency.* Advanced Materials, 9 (1997): 230–232 41

[153] J. Cabanillas-Gonzalez, G. Grancini and G. Lanzani. *Pump-Probe Spectroscopy in Organic Semiconductors: Monitoring Fundamental Processes of Relevance in Optoelectronics.* Advanced Materials, 23 (2011): 5468–5485 41, 42

[154] H. Ibach and H. Lüth. *Solid-State Physics: An Introduction to Principles of Materials Science*, (Springer, 2009) 44

[155] G.A. Marlor. *Space Charge Limited Currents in Cadmium Sulphide.* Ph.D. thesis, Durham University (1962) 45

[156] I.D. Parker. *Carrier tunneling and device characteristics in polymer light-emitting diodes.* Journal of Applied Physics, 75 (1994): 1656–1666 47

[157] R.H. Fowler and L. Nordheim. *Electron Emission in Intense Electric Fields.* Proceedings of the Royal Society A, 119 (1928): 173–181 47

[158] S. Cosnier and A. Karyakin. *Electropolymerization: Concepts, Materials and Applications*, (Wiley-VCH, 2010) 51, 57

[159] Erin L. Ratcliff, Judith L. Jenkins, Ken Nebesny and Neal R. Armstrong. *Electrodeposited, Textured Poly(3-hexyl-thiophene) (e-P3HT) Films*

for Photovoltaic Applications. Chemistry of Materials, 20 (2008): 5796–5806 51, 57, 117, 121

[160] W. Yu, B. Xu, Q. Dong, Y. Zhou, J. Zhang, W. Tian and B. Yang. *A two-step method combining electrodepositing and spin-coating for solar cell processing.* Journal of Solid State Electrochemistry, 14 (2010): 1051–1–56 51, 116, 117

[161] E. Nasybulin, J. Feinstein, M. Cox, I. Kymissis and K. Levon. *Electrochemically prepared polymer solar cell by three-layer deposition of poly(3,4-ethylenedioxythiophene)/poly(2,2'-bithiophene)/fullerene (PEDOT/PBT/C_60).* Polymer, 52 (2011): 3627–3632 51, 117

[162] Y. Tezuka, T. Yamamoto, Y. Kamikado and H. Tanaka. *Partially interpenetrating heterojunction on bilayer photovoltaic devices of electrodeposited polythiophene/methanofullerene.* Solar Energy Materials and Solar Cells, 105 (2012) 51, 116, 117, 121

[163] B. Fan, P. Weng, L. Wang and G. Shi. *Polythiophene/fullerene bulk heterojunction solar cell fabricated via electrochemical co-deposition.* Solar Energy Materials & Solar Cells, 90 (2006): 3547–3556 51, 117

[164] J. Roncali. *Conjugated Poly(thiophenes): Synthesis, Functionlaization, and Applications.* Chemical Reviews, 92 (1992): 711–738 52, 54, 55, 63

[165] J. Heinze, B.A. Frontana-Uribe and S. Ludwigs. *Electrochemistry of Conducting Polymers - Persistent Models and New Concepts.* Chemical Reviews, 110 (2010): 4724–4771 52, 53, 55, 57, 65, 75, 78

[166] J. Heinze, H. John, M. Dietrich and P. Tschuncky. *σ-"Dimers" - key intermediates and products during generation and redox switching of conjugated polymers and oligomers.* Synthetic Metals, 119 (2001): 49–52 52, 55

[167] C.P. Andrieux, P. Audebert, P. Hapiot and J.-M. Savéant. *Identification of the First Steps of the Electrochemical Polymerization of Pyrroles by Means of Fast Potential Step Techniques.* Journal of Physical Chemistry, 95 (1991): 10158–10164 52

[168] H. Yang and A.J. Bard. *The application of rapid scan cyclic voltammetry and digital simulation to the study of the mechanism of diphenylamine oxidation, radical cation dimerization, and polymerization in acetonitrile.* Journal of Electroanalytical Chemistry, 306 (1991): 87–109 52

[169] C.P. Andrieux, P. Hapiot, P. Audebert, L. Guyard, M. Nguyen Dinh An, L. Groenendaal and E.W. Meijer. *Substituent Effects on the Electrochemical Properties of Pyrroles and Small Oligopyrroles.* Chemistry of Materials, 9 (1997): 723–729 52

[170] D. Fichou, G. Horowitz, B. Xu and F. Garnier. *Stoichiometric control of the successive generation of the radical cation and dication of extended α-conjugated oligothiophenes: a quantitative model for doped polythiophene.* Synthetic Metals, 39 (1990): 243–259 52

[171] R. Schrebler, P. Grez, P. Cury, C. Veas, M. Merino, H. Gómez, R. Córdova and M.A. del Valle. *Nucleation and growth mechanisms of poly(thiophene) Part 1. Effect of elecrolyte and monomer concentration in dichloromethane.* Journal of Electroanalytical Chemistry, 430 (1997): 77–90 53, 63, 91

[172] J. Lukkari, M. Alanko, V. Pitkänen, K. Kleemola and J. Kankare. *Photocurrent Spectroscopic Study of the Initiation and Growth of Pol(3-methythiophene) Films on Electrode Surfaces with Different Adsorption Properties.* Journal of Physical Chemistry, 98 (1994): 8525–8535 53

[173] K. Meerholz and J. Heinze. *Electrochemical Solid-State Studies on Oligomeric p-Phenylenes as Model Compounds for Conductive Polymers.* Angewandte Chemie International Edition, 29 (1990): 692–695 54

[174] K. Meerholz and J. Heinze. *Electrochemical Solution and Solid-State Investigations on Conjugated Oligomers and Polymers of the α-Thiophene and and the p-Phenylene Series.* Electrochimica Acta, 41 (1996): 1839–1854 54, 55, 75, 76

[175] K. Meerholz and J. Heinze. *Influence of Chain Length and Defects on Electrical Conductivity of Conducting Polymers.* Synthetic Metals, 55-57 (1993): 5040–5045 54, 55, 75, 76, 78

[176] J.M. Pringle, M. Forsyth and D.R. MacFarlane. *Electrodeposition from Ionic Liquids*, (Wiley-VCH, 2008), chapter 7 54, 57

[177] M.S. Kiani and G.R. Mitchell. *The role of the counter-ion in the preparation of polypyrrole films with enhanced properties using a pulsed electrochemical potential.* Synthetic Metals, 48 (1992): 203–218 54, 73, 92, 121

[178] T.F. Otero and I. Boyano. *Comparative Study of Conducting Polymers by the ESCR Model.* The Journal of Physical Chemistry B, 107 (2003): 6730–6738 55, 66, 78

[179] G. Zotti, G. Schiavon, S. Zecchin, F. Sannicolo and E. Brenna. *Anion-Assisted Anodic Coupling of 2,2-Bipyrrole. Role of Tosylate Anion in the Electrochemical Synthesis of Polypyrrole.* Chemistry of Materials, 7 (1995): 1464–1468 55, 62

[180] G. Zotti, G. Schiavon, A. Berlin and G. Pagani. *The Role of Water in the Electrochemical Polymerization of Pyrroles.* Electrochimica Acta, 34 (1989): 881–884 55, 62

[181] A.J. Downard and D. Pletcher. *A Study of the Conditions for the Electrodeposition of Polythiophen in Acetonitrile.* Journal of Electroanalytical Chemistry and Interfacial Electrochemistry, 206 (1986): 147–152 55, 63

[182] M. Zhou and J. Heinze. *Electropolymerization of pyrrole and electrochemical study of polypyrrole: 1. Evidence for structural diversity of polypyrrole.* Electrochimica Acta, 44 (1999): 1733–1748 55

[183] S. Hotta, T. Hosaka and W. Shimotsuma. *Electrochemically Prepared Polythienylene Films.* Synthetic Metals, 6 (1983): 69–71 55

[184] C.C. Bof Bufon, T. Heinzel, P. Espindola and J. Heinze. *Influence of the Polymerization Potential on the Transport Properties of Polypyrrole Films.* The Journal of Physical Chemistry B, 114 (2010): 714–718 55

[185] K. Teshima, K. Yamada, N. Kobayashi and R. Hirohashi. *Effect of electropolymerization temperature on structural, morphological and conductive properties of poly(aniline) deposits prepared in 1,2-dichloroethane without a proton donor.* Journal of Electroanalytical Chemistry, 426: 97–102 55, 56

[186] K. Tanaka, T. Shichiri and T. Yamabe. *Influence of Polymerization Temperature on the Characteristics of Polythiophene Films.* Synthetic Metals, 16 (1986): 207–214 55, 56

[187] J. Roncali, M. Lemaire, R. Garreau and F. Garnier. *Enhancement of the Mean Conjugation Length in Conducting Polythiophenes.* Synthetic Metals, 18 (1987): 139–144 55, 56

[188] C.C. Bof Bufon, J. Vollmer, T. Heinzel, P. Espindola, H. John and J. Heinze. *Relationship between Chain Length, Disorder, and Resistivity in Polypyrrole Films.* The Journal of Physical Chemistry B, 109 (2005): 19191–19199 55, 78

[189] R.F. Curtis, D.M. Jones, G. Ferguson, D.M. Hawley, J.G. Sime, K.K. Cheung and G. Germain. *The Structures of the Trimer and Pentamer Obtained on Polymerization of Thiophen by Phosphoric Acid.* Journal of the Chemical Society D: Chemical Communications, 4 (1969): 165–166 56

[190] W. Wernet, M. Monkenbusch and G. Wegner. *On Structure and Properties of Polypyrrole Alkyl-Sulf(on)ates.* Molecular Crystals and Liquid Crystals, 118 (1985): 193–197 56, 79

[191] K.D. O'Neil and O.A. Semenikhin. *On the Origin of Mesoscopic Inhomogeneity of Conducting Polymers.* Journal of Physical Chemistry B, 111 (2007): 9253–9269 56

[192] K.D. O'Neil and O.A. Semenikhin. *AFM Phase Imaging of Electropolymerized Polybithiophene Films at Different Stages of Their Growth.* Journal of Physical Chemistry C, 111 (2007): 14823–14832 56, 73

[193] G. Tourillon and F. Garnier. *Stability of Conducting Polythiophene and Derivatives.* Journal of the Electrochemical Society, 130 (1983): 2042–2044 57

[194] F. Endres, D. MacFarlane and A. Abbott. *Electrodeposition from Ionic Liquids*, (Wiley, 2008) 58

[195] B. Huber and B. Roling. *Development of a Ag/Ag$^+$ micro-reference electrode for electrochemical measurements in ionic liquids.* Electrochimica Acta, (2011): 6569–6572 58

[196] F.C. Anson and J.J. Lingane. *Chemical Evidence for Oxide Films on Platinum Electrometric Electrodes.* Journal of the American Chemical Society, (1957): 4901–4904 58

[197] G.A. Snook, A.S. Best, A.G. Pandolfo and A.F. Hollenkamp. *Evaluation of a Ag—Ag$^+$ reference electrode for use in room temperature ionic liquids.* Electrochemistry Communications, 8 (2006): 1405–1411 58

[198] G. Gritzner and J. Kůta. *Recommendations on Reporting Electrode Potentials in Nonaqueous Solutions.* Pure and Applied Chemistry, 56 (1984): 461–466 58, 130

[199] E.P. Grishina, L.M. Ramenskaya, M.S. Gruzdev and O.V. Kraeva. *Water effect on physicochemical properties of 1-butyl-3-methylimidazolium based ionic liquids with inorganic anions.* Journal of Molecular Liquids, 177 (2013): 267–272 58

[200] H. Tokuda, S. Tsuzuki, M.A.B.H. Susan, K. Hayamizu and M. Watanabe. *How Ionic Are Room-Temperature Ionic Liquids? An Indicator of the Physicochemical Properties.* Journal of Physical Chemistry B, 110 (2006): 19593–19600 60

[201] T. Nishida, Y. Tashiro and M. Yamamoto. *Physical and electrochemical properties of 1-alkyl-3-methylimidazolium tetrafluoroborate for electrolyte.* Journal of Fluorine Chemistry, 120 (2003): 135–141 60

[202] www.sigmaaldrich.com 60, 103

[203] R.L. Gardas and J.A.P. Coutinho. *A group contribution method for viscosity estimation of ionic liquids.* Fluid Phase Equilibria, 266 (2008): 195–201 60

[204] S. Zhang, X. Lu, Q. Zhou, X. Li, X. Zhang and S. Li. *Ionic Liquids: Physicochemical Properties*, (Elsevier2009) 60

[205] D. Battisti, G.A. Nazri, B. Klassen and R. Aroca. *Vibrational Studies of Lithium Perchlorate in Propylene Carbonate Solutions.* Journal of Physical Chemistry, (1993): 5826–5830 60, 129, 131

[206] *www.chemguide.co.uk* 59

[207] *http://docs.scipy.org/doc/scipy/reference/* 60

[208] J.M. Pringle, M. Forsyth, G.G. Wallace and D.R. MacFarlane. *Solution-Surface Electropolymerization: A Route to Morphologically Novel Poly(pyrrole) Using an Ionic Liquid.* Macromolecules, 39 (2006): 7193–7195 63

[209] J. Heinze, A. Rasche, M. Pagels and B. Geschke. *On the Origin of the So-Called Nucleation Loop during Electropolymerization of Conducting Polymers.* Journal of Physical Chemistry B, 111 (2007): 989–997 63, 64

[210] J.M. Pringle, M. Forsyth, D.R. MacFarlane, K. Wagner, S.B. Hall and D.L. Officer. *The influence of the monomer and the ionic liquid on the electrochemical preparation of polythiophene.* Polymer, 46 (2005): 2047–2058 63, 90, 91

[211] S. Asavapiriyanont, G.K. Chandler, G.A. Gunawardena and D. Pletcher. *The Electrodeposition of Polypyrrole Films from Aqueous Solutions.* Journal of Electroanalytical Chemistry and Interfacial Electrochemistry, 177 (1984): 229–244 64, 90

[212] J.L. Brédas, B. Thémans, J.G. Fripiat, J.M. André and R.R. Chance. *Highly conducting polyparaphenylene, polypyrrole, and polythiophene chains: An ab initio study of the geometry and electronic-structure modifications upon doping.* Physical Review B, 29 (1984): 6761–6773 67

[213] M. Sato, S. Tanaka and K. Kaeriyama. *Electrochemical Preparation of Conducting Poly(3-Methylthiophene): Comparison with Polythiophene and Poly(3-Ethylthiophene).* Chemical Society Chemical Communications, 14 (1986): 279–288 67, 75

[214] K. Pichler, D.A. Halliday, D.D.C. Bradley, P.L. Burn, R.H. Friend and A.B. Holmes. *Optical spectroscopy of highly ordered poly(p-phenylene vinylene).* Journal of Physics: Condensed Matter, 5 (1993): 7155–7172 68

[215] S.T. Salammal, E. Mikayelyan, S. Grigorian, U. Pietsch, N. Koenen, U. Scherf, N. Kayunkid and M. Brinkmann. *Impact of Thermal Annealing on the Semicrystalline Nanomorphology of Spin-Coated Thin Films of Regioregular Poly(3-alkylthiophene)s as Observed by High-Resolution Transmission Electron Microscopy and Grazing Incidence X-ray Diffraction.* Macromolecules, 45 (2012): 5575–5585 68, 69

[216] W.R. Salaneck, O. Inganäs, J.-O. Nilsson, J.-E. Österholm, B. Thémans and J.-L. Brédas. *Thermochromism in the Poly(3-alkylthiophene)s: A Study of Conformational Defects by Photoelectron Spectroscopy.* Synthetic Metals, 28 (1989): C451–C460 68

[217] S. van Bavel, E. Sourty, G. de With, K. Frolic and J. Loos. *Relation between Photoactive Layer Thickness, 3D Morphology, and Device Performance in P3HT/PCBM Bulk-Heterojunction Solar Cells.* Macromolecules, 42 (2009): 7396–7403 69

[218] R.J. Waltman and J. Bargon. *Electrically conducting polymers: a review of the electropolymerization reaction, of the effects of chemical structure on polymer film properties, and of applications towards technology.* Canadian Journal of Chemistry, 64 (1986): 76–95 70

[219] C.M. Camaggi, R. Leardini, M. Tiecco and A. Tundo. *Homolytic Aromatic Substitution of Heterocyclic Compounds. Part IV. The Arylation of Thiophen.* Journal of the Chemical Society B: Physical Organic Chemistry, (1970): 1683–1687 70

[220] X.Q. Yang, J. Chen, P.D. Hale, T. Inagaki, T.A. Skotheim and M.L. den-Boer. *Orientational Behaviour of Thin Films of Poly(3-methylthiophene) on Platinum: A FTIR and NEXAFS Study.* Synthetic Metals, 28 (1989): 329–334 73, 121

[221] S. Osawa, T. Ogawa and M. Ito. *Molecular orientation of electrochemically synthesized polythiophene: effects of temperature, solvent and magnetic field.* Synthetic Metals, 90 (1997): 109–113 73, 75, 121

[222] B. Krische and M. Zagorska. *The Polythiophene Paradox.* Synthetic Metals, 28 (1989): C263–C268 75

[223] M. Slama and J. Tanguy. *Electrogravametrical Study of Polypyrrole.* Synthetic Metals, 28 (1989): C171–C176 78

[224] V. Ruiz, Á. Colina, A. Heras and J. López-Palacios. *Electropolymerization under potentiodynamic and potentiostatic conditions: Spectroelectrochemical study on electrosynthesis of poly[4,4′-bis(2-methylbutylthio)-2,2′-bithiophene].* Electrochimica Acta, 50 (2004): 59–67 78

[225] A.W. Taylor, P. Licence and A.P. Abbott. *Non-classical diffusion in ionic liquids.* Physical Chemistry Chemical Physics, 13 (2011): 10147–10154 79

[226] M.R.J. Scherer. *Nanostructured Materials via Self-Assembed Templates.* Master's thesis, Universität Konstanz (2009) 83, 84

[227] A.R. Hillman and E.F. Mallen. *Nucleation and Growth of Polythiophene Films on Gold Electrodes.* Journal of Electroanalytical Chemistry and Interfacial Electrochemistry, 220 (1987): 351–367 90

[228] R. Rodríguez-Amaro and J.J. Ruiz. *Handbook of Surfaces and Interfaces of Materials*, (Academic Press, 2001), volume 1, chapter 10 90

[229] F. Machui, S. Abbott, D. Waller, M. Koppe and C.J. Brabec. *Determination of Solubility Parameters for Organic Semiconductor Formulations.* Macromolecular Chemistry and Physics, 212 (2011): 2150–2165 97, 98, 99

[230] C.M. Hansen. *Hansen Solubility Parameters: A User's Handbook*, (CRC Press, 2007) 97, 98, 99

[231] C.M. Hansen and K. Skaarup. *The Three Dimensional Solubility Parameter - Key to Paint Component Affinities III.* Journal of Paint Technology, 39 (1967): 511–514 97

[232] A.L. Ayzner, C.J. Tassone, S.H. Tolbert and B.J. Schwartz. *Reappraising the Need for Bulk Heterojunctions in Polymer-Fullerene Photovoltaics: The Role of Carrier Transport in All-Solution-Based P3HT/PCBM Bilayer Solar Cells.* Journal of Physical Chemistry C, 46 (2009): 20050–20060 98

[233] C.W. Rochester, S.A. Mauger and A.J. Moulé. *Investigating the Morphology of Polymer/Fullerene Layers Coated Using Orthogonal Solvents.* Physical Chemistry C, 116 (2012): 7287–7292 98

[234] T.E. Kang, H.-H. Cho, C.-H. Cho, K.-H. Kim, H. Kang, M. Lee, S. Lee, B. Kim, C. Im and B.J. Kim. *Photoinduced Charge Transfer in DonorAcceptor (DA) Copolymer:Fullerene Bis-adduct Polymer Solar Cells.* ACS Applied Materials and Interfaces, 5 (2013): 861–868 101

[235] JCPDS International Centre for Diffraction Data. *021-1272* (1969) 108, 109

[236] JCPDS International Centre for Diffraction Data. *016-0617* (1964) 108

[237] M.W.B. Wilson. *Ultrafast Triplet Generation in Organic Semiconductors.* Ph.D. thesis, University of Cambridge (2012) 110

[238] I.F. Perepichka, D.F. Perepichka, H. Meng and F. Wudl. *Light-Emitting Polythiophenes.* Advanced Materials, 17 (2005): 2281–2305 111

[239] E.T. Hoke, K. Vandewal, J.A. Bartelt, W.R. Mateker, J.D. Douglas, R. Noriega, K.R. Graham, J.M.J. Fréchet, A. Salleo and M.D. McGehee. *Recombination in Polymer:Fullerene Solar Cells with Open-Circuit Voltages Approaching and Exceeding 1.0 V.* Advanced Energy Materials, 3 (2013): 220–230 111

[240] J. Guo, H. Ohkita, H. Benten and S. Ito. *Charge Generation and Recombination Dynamics in Poly(3-hexylthiophene)/Fullerene Blend Films with Different Regioregularities and Morphologies.* Journal of the American Chemical Society, 132 (2010): 6154–6164 114

[241] J. Piris, T.E. Dykstra, A.A. Bakulin, P.H.M. van Loosdrecht, W. Knulst, M.T. Trinh, J.M. Schins and L.D.A. Siebbeles. *Photogeneration and Ul-*

trafast Dynamics of Excitons and Charges in P3HT/PCBM Blends. The Journal of Physical Chemistry C, 113 (2009): 14500–14506 114

[242] H. Ohkita and S. Ito. *Transient absorption spectroscopy of polymer-based thin-film solar cells.* Polymer, 52 (2011): 4397–4417 114, 115

[243] T.W. Kee. *Femtosecond Pump-Push-Probe and Pump-Dump-Probe Spectroscopy of Conjugated Polymers: New Insight and Opportunities.* The Journal of Physical Chemistry Letters, 5 (2014): 3231–3240 115, 160

[244] C.G. Shuttle, A. Maurano, R. Hamilton, B. O'Regan, J.C. de Mello and J.R. Durrant. *Charge extraction analysis of charge carrier densities in a polythiophene/fullerene solar cell: Analysis of the origin of the device dark current.* Applied Physics Letters, 93 (2008): 183501 115

[245] A.J. Mozer and N.S. Sariciftci. *Conjugated polymer photovoltaic devices and materials.* Comptes Rendus Chimie, 9 (2006): 568–577 118

[246] Y.-H. Lin, Y.-T. Tsai, C.-C. Wu, C.-H. Tsai, C.-H. Chiang, H.-F. Hsu, J.-J. Lee and C.-Y. Cheng. *Comparative study of spectral and morphological properties of blends of P3HT with PCBM and ICBA.* Organic Electronics, 13 (2012): 2333–2341 118

[247] D. Gupta, S. Mukhopadhyay and K.S. Narayan. *Filll factor in organic solar cells.* Solar Energy Materials & Solar Cells, 94 (2010): 1309–1313 119

[248] G. Zhao, Y. He and Y. Li. *6.5% Efficiency of Polymer Solar Cells Based on poly(3-hexylthiophene) and Indene-*C_{60}*Bisadduct by Device Optimization.* Advanced Materials, 22 (2010): 4355–4358 119

[249] J. Roncali, R. Garreau, A. Yassar, P. Marque, F. Garnier and M. Lemaire. *Effects of Steric Factors on the Electrosynthesis and Properties of Conducting Poly(3-alkylthiophenes).* The Journal of Physical Chemistry, 91 (1987): 6706–6714 121

[250] J. Roncali. *Molecular Engineering of the Band Gap of* π*-Conjugated Systems: Facing Technological Applications.* Macromolecular Rapid Communications, 28 (2007): 1761–1775 121

[251] B. Kitchen, O. Awartani, R.J. Kline, T. McAfee, H. Ade and B.T. O'Connor. *Tuning Open-Circuit Voltage in Organic Solar Cells with Molecular Orientation.* ACS Applied Materials and Interfaces, 7 (2015): 13208–13216 121

[252] H.J. Snaith. *Perovskites: The Emergence of a New Era for Low-Cost, High Efficiency Solar Cells.* The Journal of Physical Chemistry Letters, 4 (2013): 3623–3630 125, 144

[253] S.D. Stranks and H.J. Snaith. *Metal-halide perovskites for photovoltaic and light-emitting devices.* Nature Nanotechnology, 10 (2015): 391–402 125

[254] P.J. Verlinden, R.M. Swanson and R.A. Crane. *7000 High-efficiency Cells for a Dream.* Progress in Photovoltaics: Research and Applications, 2 (1994): 143–152 126, 127

[255] G. Xing, N. Mathews, S. Sun, S.S. Lim, Y.M. Lam, M. Grätzel, S. Mhaisalkar and T.C. Sum. *Long-Range Balanced Electron- and Hole-Transport Lengths in Organic-Inorganic* $CH_3NH_3PbI_3$. Science, 342: 344–347 127, 141, 145

[256] S.D. Stranks, G.E. Eperon, G. Grancini, C. Menelaou, M.J.P. Alcocer, T. Leijtens, L.M. Herz and H.J. Snaith. *Electron-Hole Diffusion Lengths Exceeding 1 Micrometer in an Organometal Trihalide Perovskite Absorber.* Science, 342 (2013): 341–343 127, 141, 145

[257] Q. Dong, Y. Fang, Y. Shao, P. Mulligan, J. Qiu, L. Cao and J. Huang. *Electron-hole diffusion lengths* $> 175\,\mu m$ *in solution-grown* $CH_3NH_3PbI_3$ *single crystals.* Science, 347 (2015): 967–970 127

[258] L.M. Pazos-Outón, M. Szumilo, R. Lamboll, J.M. Richter, M. Crespo-Quesada, M. Abdi-Jalebi, H.J. Beeson, M. Vrucinic, M. Alsari, H.J. Snaith, B. Ehrler, R.H. Friend and F. Deschler. *Photon recycling in lead-iodide perovskite solar cells.* Science, 351 (2016): 1430–1433 128, 140, 141, 142, 145

[259] E. Poverenov, M. Li, A. Bitler and M. Bendikov. *Major Effect of Electropolymerization Solvent on Morphology and Electrochromic Properties of PEDOT Films.* Chemistry of Materials, 22 (2010): 4019–4025 129, 131

[260] R. Dehmel, A. Nicolas, M.R.J. Scherer and U. Steiner. *3D Nanostructured Conjugated Polymers for Optical Applications.* Advanced Functional Materials, 25 (2015): 6900–6905 129

[261] C. Kvarnström, H. Neugebauer, S. Blomquist, H.J. Ahonen, J. Kankare and A. Ivaska. *In situ spectroelectrochemical characterization of poly(3,4-ethylenedioxythiophene).* Electrochimica Acta, 44 (1999): 2739– 129

[262] A. Kumar, D.M. Welsh, M.C. Morvant, F. Piroux, K.A. Abboud and J.R. Reynolds. *Conducting Poly(3,4-alkylenedioxythiophene) Derivatives as Fast Electrochromics with High-Contrast Ratios.* Chemistry of Materials, 10 (1998): 896–902 131

[263] R. Chang, J.H. Hsu, W.S. Fann, K.K. Liang, C.H. Chang, M. Hayashi, J. Yu, S.H. Lin, E.C. Chang, K.R. Chuang and S.A. Chen. *Experimental and theoretical investigations of absorption and emission spectra of the light-emitting polymer MEH-PPV in solution.* Chemical Physics Letters, 317 (2000): 142–152 131

[264] M. Turbiez, P. Frère and J. Roncali. *Stable and Soluble Oligo(3,4-ethylenedioxythiophene)s End-Capped with Alkyl Chains.* Journal of Organic Chemistry, 68 (2003): 5357–5360 131

[265] J.F. Moulder, W.R. Stickle, P.E. Sobol and K.D. Bomben. *Handbook of X-ray photoelectron spectroscopy: A reference book of standard spectra for identification and interpretation of XPS data*, (Physical Electronics Division, Perkin-Elmer Corporation1992) 134, 136

[266] L. Groenendaal, F. Jonas, D. Freitag, H. Pielartzik and J.R. Reynolds. *Poly(3,4-ethylenedioxythiophene) and Its Derivatives: Past, Present and Future.* Advanced Materials, 12 (2000): 481–494 136

[267] S.A. Spanninga, D.C. Martin and Z. Chen. *X-ray Photoelectron Spectroscopy Study of Counterion Incorporation in Poly(3,4-ethylenedioxythiophene).* Journal of Physical Chemistry C, 113 (2009): 5585–5592 136, 137

[268] Y. Park, V. Choong, Y. Gao, B.R. Hsieh and C.W. Tang. *Work function of indium tin oxide transparent conductor measured by photoelectron spectroscopy.* Applied Physics Letters, 68 (1996): 2699–2701 137

[269] K.-Z. Xing, M. Fahlman, X.W. Chen, O. Inganäs and W.R. Salaneck. *The electronic structure of poly(3,4-ethylene-dioxythiophene): studied by XPS and UPS.* Synthetic Metals, 89 (1997): 161–165 137

[270] T.M. Brown, J.S. Kim, R.H. Friend, F. Cacialli, R. Daik and W.J. Feast. *Built-in field electroabsorption spectroscopy of polymer light-emitting diodes incorporating a doped poly(3,4-ethylene dioxythiophene) hole injection layer.* Applied Physics Letters, 75 (1999): 1679–1681 137

[271] H. Frohne, D.C. Müller and K. Meerholz. *Continuously Variable Hole Injection in Organic Light Emitting Diodes.* ChemPhysChem, 3 (2002): 707–711 138, 139

[272] H. Frohne, S.E. Shaheen, C.J. Brabec, D.C. Müller, N.S. Saraciftci and K. Meerholz. *Influence of the Anodic Work Function on the Performance of Organic Solar Cells.* ChemPhysChem, 3 (2002): 795–799 138, 139

[273] H. Wei, L. Scudiero and H. Eilers. *Infrared and photoelectron spectroscopy study of vapor phase deposited poly (3-hexylthiophene).* Applied Surface Science, 255 (2009): 8593–8597 138

[274] A.N. Jumabekov, E. Della Gaspera, Z.-Q. Xu, A.S.R. Chesman, J. van Embden, S.A. Bonke, Q. Bao, D. Vak and U. Bach. *Back-contacted hybrid organic-inorganic perovskite solar cells.* Journal of Materials Chemistry C, 4 (2016): 3125–3130 140, 161

[275] C. Wehrenfennig, M. Liu, H.J. Snaith, M.B. Johnston and L.M. Herz. *Homogeneous Emission Line Broadening in the Organo Lead Halide Perovskite* $CH_3NH_3PbI_{3x}Cl_x$. The Journal of Physical Chemistry Letters, 5 (2014): 1300–1306 141, 142

[276] F. Deschler, M. Price, S. Pathak, L.E. Klintberg, D.-D. Jarausch, R. Higler, S. Hüttner, T. Leijtens, S.D. Stranks, H.J. Snaith, M. Atatüre, R.T. Phillips and R.H. Friend. *High Photoluminescence Efficiency and Optically*

Pumped Lasing in Solution-Processed Mixed Halide Perovskite Semiconductors. Journal of Physical Chemistry Letters, 5 (2014): 1421–1426 142, 145

[277] J.M. Ball, M.M. Lee, A. Hey and H.J. Snaith. *Low-temperature processed meso-superstructured to thin-film perovskite solar cells.* Energy & Environmental Science, 6 (2013): 1739–1743 144

[278] D. Liu and T.L. Kelly. *Perovskite solar cells with a planar heterojunction structure prepared using room-temperature solution processing techniques.* Nature Photonics, 8 (2013): 133–138 144

[279] G.E. Eperon, V.M. Burlakov, P. Docampo, A. Goriely and H.J. Snaith. *Morphological Control for High Performance, Solution-Processed Planar Heterojunction Perovskite Solar Cells.* Advanced Functional Materials, 24 (2014): 151–157 144

[280] B. Conings, L. Baetan, C. De Dobbelaera, J. D'Haen, J. Manca and H.-G. Boyen. *Perovskite-Based Hybrid Solar Cells Exceeding 10% Efficiency with High Reproducibility Using a Thin Film Sandwich Approach.* Advanced Materials, 26 (2014): 2041–2046 144

[281] W. Zhang, M. Saliba, D.T. Moore, S.K. Pathak, M.T. Hörantner, T. Stergiopoulos, S.D. Stranks, G.E. Eperon, J.A. Alexander-Webber, A. Abate, A. Sadhanala, S. Yao, Y. Chen, R.H. Friend, L.A. Estroff, U. Wiesner and H.J. Snaith. *Ultrasmooth organic-inorganic perovskite thin film formation and crystallization for efficient planar heterojunction solar cells.* Nature Communications, 6 (2015): 6142 144

[282] H.S. Jung and N.-G. Park. *Perovskite Solar Cells: From Materials to Devices.* Small, 11 (2015): 10–25 144

[283] International Technology Roadmap for Photovoltaic. *International Technology Roadmap for Photovoltaic 2014 Results* (2015) 144

[284] B.A. Gregg, F. Pichot, S. Ferrere and C.L. Fields. *Interfacial Recombination Processes in Dye-Sensitized Solar Cells and Methods to Passivate the Interfaces.* Journal of Physical Chemistry B, 105 (2001): 1422–1429 144

[285] A. Robertson, U. Erb and G. Palumbo. *Practical Applications for Electrodeposited Nanocrystalline Materials.* NanoStructured Materials, 12 (1999): 1035–1040 144

[286] M. Berggren, A. Dodabalapur, R.E. Slusher, A. Timko and O. Nalamasu. *Oranic solid-state lasers with imprinted gratings on plastic substrates.* Applied Physics Letters, (1998): 410–411 145

[287] H. Cho, S.-H. Jeong, M.-H. Park, Y.-H. Kim, C. Wolf, C.-L. Lee, J.H. Heo, A. Sadhanala, N. Myoung, S. Yoo, S.H. Im, R.H. Friend and T.-W. Lee. *Overcoming the electroluminescence efficiency limitations of perovskite light-emitting diodes.* Science, 350 (2015): 1222–1225 145

[288] Y.C. Kim, H.N. You, S.K. Man, M.-S. Jang and P.H. Hur. *High-T_C Superconductor Bi-Sr-Ca-Cu-O Films Prepared by Electrodeposition Method.* Physica C: Superconductivity and its Applications, 185 (1991): 2303–2304 145

[289] C. Chaillout, J. Durr, C. Escribe-Filippini, T. Fournier, J. Marcus and M. Marezio. *Structure Determination of a New Perovskite Phase in the Ba-K-Bi-Na-O System.* Journal of Solid State Chemistry, 93 (1991): 63–68 145

[290] M.L. Norton. *Electrodeposition of $Ba_{.6}K_{.4}BiO_3$.* Materials Research Bulletin, 24 (1989): 1391–1397 145

[291] H. Konno, M. Takita and R. Furuichi. *Formation of Perovskite Structure $La_{1\text{-}x}Ca_xCrO_3$ Films with Electrodeposition.* Journal of the Electrochemical Society, 137 (1990): 361–362 145

[292] Y. Matsumoto, T. Sasaki and J. Hombo. *A New Preparation Method of $LaCoO_3$ Perovskite Using Electrochemical Oxidation.* Inorganic Chemistry, 31 (1992): 738–741 145

[293] Y. Matsumoto, T. Morikawa, H. Adachi and J. Hombo. *A New Preparation Method of Barium Titanate Perovskite Film Using Electrochemical Reduction.* Materials Research Bulletin, 27 (1992): 1319–1327 145

[294] V.K. Dwivedi, J.J. Baumberg and G. Vijaya Prakash. *Direct deposition of inorganic-organic hybrid semiconductors and their template-assisted microstructures.* Materials Chemistry and Physics, 137 (2013): 941–946 145, 146, 148, 151

[295] JCPDS International Centre for Diffraction Data. *72-2440* (2003) 149, 153

[296] JCPDS International Centre for Diffraction Data. *89-2805* (2003) 149

[297] X. Li, D. Pletcher and F.C. Walsh. *Electrodeposited lead dioxide coatings.* Chemical Society Reviews, 40 (2011): 3879–3894 149

[298] J. Burschka, N. Pellet, S.-J. Moon, R. Humphry-Baker, P. Gao, M.K. Nazeeruddin and M. Grätzel. *Sequential deposition as a route to high-performance perovskite-sensitized solar cells.* Nature, 499 (2013): 316–319 151, 154

[299] JCPDS International Centre for Diffraction Data. *079-0235* (2003) 153

[300] T. Baikie, Y. Fang, J.M. Kadro, M. Schreyer, F. Wei, S.G. Mhaisalkar, M. Graetzel and T.J. White. *Synthesis and crystal chemistry of the hybrid perovskite* $(CH_3NH_3)PbI_3$ *for solid-state sensitised solar cell applications.* Journal of Materials Chemistry A, 1 (2013): 5628–5641 153, 156

[301] K. Liang, D.B. Mitzi and M.T. Prikas. *Synthesis and Characterization of Organic-Inorganic Perovskite Thin Films Prepared Using a Versatile Two-Step Dipping Technique.* Chemistry of Materials, 10 (1998): 403–411 154, 155

[302] Q. Chen, H. Zhou, Z. Hong, S. Luo, H.-S. Duan, H.-H. Wang, Y. Liu, G. Li and Y. Yang. *Planar Heterojunction Perovskite Solar Cells via Vapor-Assisted Solution Process.* Journal of the American Chemical Society, 136 (2013): 622–625 154

[303] N. Onoda-Yamamuro, T. Matsuo and H. Suga. *Calorimetric and IR Spectroscopic Studies of Phase Transitions in Methylammonium Trihalogenoplumbates.* Journal of Physics and Chemistry of Solids, 51 (1990): 1383–1395 156

[304] A. Poglitsch and D. Weber. *Dynamic disorder in methylammoniumtrihalogenoplumbates (II) observed by millimeter-wave spectroscopy.* Journal of Chemical Physics, 87 (1987): 6373–6378 156

[305] Y. Kawamura, H. Mashiyama and K. Hasebe. *Structural Study on Cubic-Tetragonal Transition of* $CH_3NH_3PbI_3$. Journal of the Physical Society of Japan, 71 (2002): 1694–1697 156

[306] P. Scherrer. *Bestimmung der Grösse und der inneren Struktur von Kolloidteilchen mittels Röntgenstrahlen.* Nachrichten von der Gesellschaft der Wissenschaften zu Göttingen, 26 (1918): 98–100 156

[307] J.I. Langford and A.J.C. Wilson. *Seherrer after Sixty Years: A Survey and Some New Results in the Determination of Crystallite Size.* Journal of Applied Crystallography, 11 (1978): 102–113 156

[308] X.-P. Cui, K.-J. Jiang, J.-H. Huang, X.-Q. Zhou, M.-J. Su, S.-G. Li, Q.-Q. Zhang, L.-M. Yang and Y.-L. Song. *Electrodeposition of PbO and its in situ conversion to* $CH_3NH_3PbI_3$ *for mesoscopic perovskite solar cells.* Chemical Communications, 51: 1457–1460 157, 161

[309] H. Chen, Z. Wei, X. Zheng and S. Yang. *A scalable deposition route to the low-cost, versatile and controllable fabrication of perovskite solar cells.* Nano Energy, 15 (2015): 216–226 157, 161

[310] J.-H. Huang, K.-J. Jiang, X.-P. Cui, Q.-Q. Zhang, M. Gao, M.-J. Su, L.-M. Yang and Y. Song. *Direct Conversion of* $CH_3NH_3PbI_3$ *from Electrodeposited PbO for Highly Efficient Planar Perovskite Solar Cells.* Scientific Reports, 5 (2015): 15889 157, 158, 161

[311] V.D. Mihailetchi, J. Wildeman and P.W.M. Blom. *Space-Charge Limited Photocurrent.* Physical Review Letters, 94 (2005): 126602 160